Pathophysiological mechanisms of cortical spreading depolarisation and epileptic seizures in novel transgenic mouse models for hemiplegic migraine

Dissertation

zur Erlangung des Grades eines
Doktors der Naturwissenschaften

der Mathematisch-Naturwissenschaftlichen Fakultät
und
der Medizinischen Fakultät
der Eberhard-Karls-Universität Tübingen

vorgelegt
von

Daniela Miely
aus Ried im Innkreis, Österreich

2024

Tag der mündlichen Prüfung: 29.11.2024

Dekan der Math.-Nat. Fakultät: Prof. Dr. Thilo Stehle
Dekan der Medizinischen Fakultät: Prof. Dr. Bernd Pichler

1. Berichterstatter: Prof. Dr. Holger Lerche

2. Berichterstatter: Prof. Dr. Bernd Antkowiak

Prüfungskommission: Prof. Dr. Holger Lerche

Prof. Dr. Bernd Antkowiak

Prof. Dr. Cornelius Schwarz

Prof. Dr. Tobias Freilinger

Erklärung / Declaration:

Ich erkläre, dass ich die zur Promotion eingereichte Arbeit mit dem Titel:

„Pathophysiological mechanisms of cortical spreading depolarisation and epileptic seizures in novel transgenic mouse models for hemiplegic migraine“

selbständig verfasst, nur die angegebenen Quellen und Hilfsmittel benutzt und wörtlich oder inhaltlich übernommene Stellen als solche gekennzeichnet habe. Ich versichere an Eides statt, dass diese Angaben wahr sind und dass ich nichts verschwiegen habe. Mir ist bekannt, dass die falsche Abgabe einer Versicherung an Eides statt mit Freiheitsstrafe bis zu drei Jahren oder mit Geldstrafe bestraft wird.

I hereby declare that I have produced the work entitled “Pathophysiological mechanisms of cortical spreading depolarisation and epileptic seizures in novel transgenic mouse models for hemiplegic migraine”, submitted for the award of a doctorate, on my own (without external help), have used only the sources and aids indicated and have marked passages included from other works, whether verbatim or in content, as such. I swear upon oath that these statements are true and that I have not concealed anything. I am aware that making a false declaration under oath is punishable by a term of imprisonment of up to three years or by a fine.

Tübingen, den 11.12.2024 ....

Unterschrift / Signature

Statement of Contribution

Parts of this thesis were published in "Auffenberg, E.*****, Hedrich U.B.*****, Barbieri, R.*****, Miely, D.*****, Groschup, B., Wuttke, T.V., … & Freilinger, T. (2021). Hyperexcitable interneurons trigger cortical spreading depression in an *Scn1a* L1649Q migraine model. *The Journal of Clinical Investigation*, *131*(21)". The study was conceived by all the authors. The first authorship was shared by Eva Auffenberg, Ulrike Hedrich, Raffaella Barbieri and by me. The work was a collaborative project with participation of the Lerche, Hedrich, Plesnila and Pusch lab. The first author Eva Auffenberg performed all the *in vivo* work using the *Scn1a*$^{\mathrm{L1649Q/wt}}$ model to demonstrate an increased CSD susceptibility in heterozygous animals, whereas the second first author Ulrike Hedrich performed cortical and hippocampal whole-cell patch clamp recordings in slices of *Scn1a*$^{\mathrm{L1649Q/wt}}$ animals to verify the increased interneuron hyperexcitability on the single cell level. The third first author Raffaella Barbieri and her lab contributed with GS967 treatment of homozygous mice as well as electrophysiological data from the cerebellum, which is not included in this thesis.

The contribution of the other three first authors is indicated in the text and appropriate credit is given by providing the correct reference. Several figures from the publication are used and were adapted to be included in this dissertation, which is also stated in the respective figure descriptions.

I contributed a major part of the publication by performing the *in vitro* CSD and $[K^+]_e$ recordings in the *Scn1a* L1649Q migraine model, which are presented in this dissertation. As displayed in this thesis, I demonstrated a higher CSD susceptibility and increased propagation velocity during CSD in the FHM3 mouse model. Additionally, the $[K^+]_e$ recordings in the *Scn1a* L1649Q model that I performed revealed elevated K^+ levels during an early CSD phase, which provided the essential mechanistic link between the increased CSD susceptibility *in vivo* and the hyperexcitability of inhibitory interneurons, which had been observed beforehand. For this purpose, I newly established the method of recording CSD in acute brain slices using IOS imaging as well as K^+-sensitive microelectrode and DC potential recordings in our lab, which is delineated in this thesis. I also designed the tools to analyse the CSD recording data. Furthermore, I performed the CSD recordings using GS967 that verified the alleviating effect of the late sodium channel blocker on CSD susceptibility *in vitro*, which is also part of this dissertation. The statistical analysis of the FHM3 data that I gathered and that is presented within this thesis was also performed by me.

Some hypotheses and experimental designs with respect to the *Slc1a3* P290R mouse model for EA6 were established based on previously conducted, unpublished work performed by Prof. Christoph Fahlke and his colleagues, which is also stated accordingly in the text. The investigations of the *Slc1a3*$^{\mathrm{P290R/wt}}$ animal model that are presented in this dissertation contribute to a collaborative work on P290R-associated hemiplegic migraine pathophysiology with participation of the Hedrich and the Fahlke lab.

With respect to the EA6 mouse model, I performed the *in vitro* CSD and $[K^+]_e$ recordings, which are presented in this thesis. I demonstrated an increased CSD susceptibility and propagation velocity in the *Slc1a3* P290R mouse model using the beforementioned method that I had newly established in the Lerche/Hedrich lab. Moreover, I revealed accelerated K^+ dynamics during the early CSD phase and elevated $[K^+]_e$ during the re-uptake process in the EA6 mouse model, which verified a different pathophysiological mechanism for CSD induction and propagation compared to the FHM3 model. I also performed the cortical whole cell patch-clamp recordings demonstrating unaltered synaptic transmission and tonic inhibition in the *Slc1a3* P290R model, which are presented in this dissertation. As presented in this dissertation, I collected the growth/body weight data showing delayed growth during epileptogenesis as well as gender-related body weight differences in the EA6 model. Additionally, I performed the EEG transmitter implantations and *in vivo* EEG-video monitoring in the *Slc1a3* P290R model, which are also part of this thesis. The EEG recordings revealed high vulnerability to epileptic seizures and status epileptic in heterozygous animals during the peak period of seizures and during the compensatory phase. I also conducted the immunohistochemical c-fos stainings that are presented in this dissertation demonstrating an upregulation of c-fos expression in distinct brain regions after status epileptici in the EA6 model. All data that I gathered with respect to the *Slc1a3* P290R mouse model was analysed by me, which also includes the statistical calculations.

The CSD recordings using UCPH-101 were carried out by Caroline Kurth as part of a medical doctoral thesis, which has been explicitly specified in the text. During the realisation of her doctoral work, she was supervised by Dr. Ulrike Hedrich and by me. As already mentioned, I newly established the method of recording CSD in acute brain slices in our lab, which she used to investigate the effect of UCPH-101 on CSD susceptibility, propagation speed and K^+ parameters *in vitro*.

Acknowledgement

I would like to express my deepest gratitude to Dr. Ulrike Hedrich-Klimosch and Prof. Dr. Holger Lerche who made my dissertation possible and provided guidance as well as feedback during every step of my project.

Additionally, I am extremely thankful to Dr. Ulrike Hedrich-Klimosch for her continuous support in the laboratory, her precious advice and expertise, her endless patience and for proof-reading my work.

This dissertation would not have been possible without the assistance of my board members Prof. Dr. Bernd Antkowiak and Prof. Dr. Cornelius Schwarz. In this context, I also want to thank Prof. Dr. Tobias Freilinger, who accepted to complete my defence committee.

Furthermore, I would like to express my sincere thanks to the BMBF for financing my PhD position during the required time frame. My scientific research would not have been possible without the TreatION funding.

I could not have persevered and finished this work without the encouragement of Peter since he made me confident in my abilities, kept on motivating me during challenging times, and simply made every day a better one.

I am also grateful for my family and especially my uncle and my parents, who have always confided in my skills and supported every decision that I made along the way.

During my time in the Lerche/Hedrich lab I had the pleasure to work with some very kind and interesting people. I will be glad to remember the nice conversations distracting me from daily routine.

Abstract

Familial hemiplegic migraine (FHM) represents a severe monogenic subtype of migraine with aura and frequently includes specific neurological disorders as additional phenotypes. Cortical spreading depolarisation (CSD), the neurophysiological correlate for migraine aura, is a slowly migrating wave of depolarisation, which results in a long-lasting suppression of cortical activity. FHM3 is caused by gain-of-function (GOF) variants in the *SCN1A* gene encoding the voltage-gated sodium channel $Na_V1.1$ that is predominantly expressed in inhibitory neurons. Patients carrying the missense mutation L1649Q display a pure hemiplegic migraine (HM) phenotype. In contrast, the *SLC1A3* gene is associated with episodic ataxia type 6 (EA6) but has recently been implicated in HM. *SLC1A3* encodes the glial excitatory amino acid transporter 1 (EAAT1) functioning both as glutamate transporter and anion channel. The variant P290R was identified in a patient with an overlapping syndrome comprising HM, epilepsy, and ataxia and results in impaired glutamate transport but increased Cl^- (chloride) channel activity.

To unravel the largely unknown pathophysiological mechanisms of CSD and characterise additional HM phenotypes, the *Scn1a*$^{L1649Q/wt}$ and the *Slc1a3*$^{P290R/wt}$ knock-in mouse models were studied using a multimodal approach.

Combining intrinsic optical signal (IOS) imaging with extracellular and potassium (K^+)-sensitive electrode recordings in brain slices revealed increased extracellular K^+ concentration ($[K^+]_e$) levels during an early CSD phase in *Scn1a*$^{L1649Q/wt}$ animals likely representing the mechanistic link between interneuron hyperactivity and elevated CSD susceptibility *in vivo*, which had previously been demonstrated[1]. Additionally, the late sodium channel blocker GS967 alleviated CSD susceptibility *in vitro*[1]. The novel identified cascade expands the concepts of CSD pathophysiology[1], which had mainly focussed on glutamatergic neurotransmission.

In the *Slc1a3*$^{P290R/wt}$ model, CSD susceptibility and propagation velocity were increased, however, $[K^+]_e$ levels were exclusively elevated during late CSD phases. Additionally, K^+ dynamics were markedly accelerated during an early CSD phase.

Synaptic transmission and tonic GABAergic inhibition were investigated by performing whole-cell patch clamp recordings. However, as the balance between cortical excitation and inhibition in *Slc1a3*$^{P290R/wt}$ animals was preserved, the underlying cellular mechanisms leading to altered CSD characteristics remained unclear. Video-EEG monitoring during the period of maximum seizure susceptibility and the subsequent compensatory phase revealed that heterozygous animals were extremely vulnerable to seizures and status epileptici. The high seizure-associated lethality additionally confirmed the severe phenotype, with a peak during the 4th and 5th postnatal week. The expression of c-fos was markedly upregulated in the thalamus and hippocampus likely representing brain regions that are involved during seizures or status epileptici.

Keywords: cortical spreading depolarisation, (familial) hemiplegic migraine, potassium, sodium channels, glutamate transporters, epilepsy, episodic ataxia

Zusammenfassung

Bei der familiären hemiplegischen Migräne (FHM) handelt es sich um einen schweren monogenen Subtyp der Migräne mit Aura, welche häufig bestimmte neurologische Krankheitsbilder als zusätzliche Phänotypen einschließt. Die kortikale Streudepolarisation, das neurophysiologische Korrelat für die Migräneaura, stellt eine sich langsam ausbreitende Depolarisationswelle dar, die eine langanhalte Suppression kortikaler Aktivität zur Folge hat.

FHM3 wird durch Varianten mit Funktionsgewinn im *SCN1A* Gen verursacht, welches den vorwiegend in inhibitorischen Neuronen exprimierten, spannungsgesteuerten Natriumkanal $Na_V1.1$ kodiert. Phänotypisch weisen PatientInnen mit der Missense-Variante L1649Q eine reine hemiplegische Migräne (HM) auf. Im Gegensatz dazu wird das *SLC1A3* Gen mit episodischer Ataxie Typ 6 (EA6) assoziiert. Allerdings wurde das Gen kürzlich auch mit HM in Verbindung gebracht. *SLC1A3* kodiert für den glialen exzitatorischen Aminosäuretransporter 1 (EAAT1), der sowohl als Glutamat-Transporter als auch als Anionenkanal operiert. Die P290R Variante wurde in einem Patienten mit einem überlappenden Syndrom bestehend aus HM, Epilepsie sowie Ataxie identifiziert und führt zu einem beeinträchtigten Glutamat-Transport, jedoch gleichzeitig ebenso zu einer vermehrten Aktivität des Chloridkanals.

Um die weitgehend ungeklärten pathophysiologischen Mechanismen der kortikalen Streudepolarisation zu entschlüsseln, wurden die *Scn1a*$^{L1649Q/wt}$ und *Slc1a3*$^{P290R/wt}$ knock-in Mausmodelle anhand eines multimodalen Ansatzes untersucht.

Die Kombination aus einer Bildgebung mittels intrinsischem optischen Signal (IOS) und extrazellulären sowie Kalium (K^+)-sensitiven Mikroelektroden Ableitungen in Hirnschnitten zeigte eine erhöhte extrazelluläre K^+ Konzentration ($[K^+]_e$) während einer frühen Phase der kortikalen Streudepolarisation in *Scn1a*$^{L1649Q/wt}$ Tieren[1]. Dies stellt vermutlich den mechanistischen Zusammenhang zwischen der Übererregbarkeit von Interneuronen und der erhöhten Suszeptibilität gegenüber kortikalen Streudepolarisationen *in vivo* dar, was kürzlich demonstriert werden konnte[1]. Zusätzlich wurde nach Anwendung von GS967, einem Blocker des persistierenden Natriumstroms, eine verminderte Anfälligkeit gegenüber kortikalen Streudepolarisationen *in vitro* nachgewiesen[1]. Diese neu identifizierte Kaskade erweitert die Konzepte der Pathophysiologie kortikaler Streudepolarisationen maßgeblich[1], da der Fokus bisher hauptsächlich auf die glutamaterge Neurotransmission gelegt worden war.

Im *Slc1a3*$^{P290R/wt}$ Model zeigten sich die Anfälligkeit gegenüber kortikaler Streudepolarisationen sowie die Ausbreitungsgeschwindigkeit erhöht, jedoch verblieben die $[K^+]_e$-Level ausschließlich während später Phasen der Streudepolarisation erhöht. Zusätzlich zeigte sich eine deutlich beschleunigte K^+ Dynamik während der frühen Phase der kortikalen Streudepolarisation.

Mithilfe von Patch-Clamp Ableitungen wurden sowohl die synaptische Transmission als auch die tonische GABAerge Inhibition untersucht. Da sich das Gleichgewicht zwischen kortikaler Erregung und Hemmung in den *Slc1a3*$^{P290R/wt}$ Tieren jedoch als erhalten erwies, verblieben die zu Grunde liegenden zellulären Mechanismen, welche zu den jeweilig veränderten Charakteristika der Streudepolarisationen führen, ungeklärt.

Ein Video-EEG-Monitoring während der Episode mit der höchsten Anfälligkeit gegenüber epileptischen Anfällen sowie der daran anschließenden kompensatorischen Phase ergab eine äußerst hohe Vulnerabilität heterozygoter Tiere gegenüber Anfällen und Status epileptici. Die hohe Anfalls-assoziierte Letalität bestätigte zusätzlich den schweren Phänotyp, welcher ein Maximum während der vierten und fünften postnatalen Woche erreicht.

Eine gesteigerte c-fos Expression wurde sowohl im Thalamus als auch im Hippokampus nachgewiesen und deutet auf Regionen hin, die vermutlich während epileptischer Anfälle oder Status epileptici eine Rolle spielen.

Schlüsselwörter: kortikale Streudepolarisation, (familiäre) hemiplegische Migräne, Kalium, Natriumkanäle, Glutamat-Transporter, Epilepsie, episodische Ataxie

List of contents

List of figures

List of tables

List of abbreviations

FHM	familial hemiplegic migraine
CSD	cortical spreading depolarisation
FHM X	FHM type X
GOF	gain-of-function
SCN1A	gene encoding the voltage-gated sodium channel $Na_V1.1$
$Na_V1.1$	voltage-gated sodium channel 1.1
HM	hemiplegic migraine
SLC1A3	solute carrier family 1 member 3 gene, gene encoding the excitatory amino acid transporter 1
EA6	episodic ataxia type 6
EAAT1	excitatory amino acid transporter 1
Cl^-	chloride
IOS	intrinsic optical signal
K^+	potassium
$[K^+]_e$	extracellular potassium concentration
GABA	γ-aminobutyric acid
EEG	electroencephalography
IHS	International Headache Society
SHM	sporadic hemiplegic migraine
Na^+	sodium
Ca^{2+}	calcium
DC	direct current
SD	spreading depolarisation
$[Na^+]_e$	extracellular sodium concentration
$[Cl^-]_e$	extracellular chloride concentration
$[Ca^{2+}]_e$	extracellular calcium concentration
ATP	adenosine triphosphate
NMDA	N-methyl-D-aspartate
AMPA	α-amino-3-hydroxy-5-methyl-4-isoxazolepropionic acid
TTX	tetrodotoxin
$[Ca^{2+}]_I$	intracellular calcium concentration
NKA	Na^+/K^+-ATPase
CACNA1A	gene encoding the α1-subunit of the P/Q-type calcium channel $Ca_V2.1$
EA2	episodic ataxia type 2
$Ca_V2.1$	voltage-gated calcium channel 2.1
AP	action potential
E/I	excitatory/inhibitory
LOF	loss-of-function

ATP1A2	gene encoding the α2-subunit of the catalytic subunit of a T-type Na^+/K^+-ATPase
EAAT2	excitatory amino acid transporter 2
GLT-1	glutamate transporter 1
GEFS+	generalised epilepsy with febrile seizures plus
DS	Dravet syndrome
AIS	axon initial segment
PRRT2	gene encoding the proline rich transmembrane protein 2
SLC2A1	solute carrier family 2 member 1 gene, gene encoding glucose transporter 1
GLUT-1	glucose transporter 1
SLC4A4	solute carrier family 4 member 4 gene, gene encoding the Na^+-$HCO3^-$-cotransporter NBCe1
NBCe1	Na^+-$HCO3^-$-cotransporter 1
ATP1A4	gene encoding the α4-subunit of a Na^+/K^+-ATPase
EA	episodic ataxia
ASMs	anti-seizure medications
PV+	parvalbumin positive
BFIE	benign familial infantile epilepsy
Na_V	voltage-gated sodium channel
DX	domain X
SX	segment X
SCN5A	gene encoding the voltage-gated sodium channel $Na_V1.5$
tsA201	transformed human kidney cell line
C57Bl/6N	subline of the C57 black 6 mouse strain
PX	postnatal day X
KCl	potassium chloride
IPSC	inhibitory postsynaptic current
ECoG	electrocorticography
sIPSC	spontaneous inhibitory postsynaptic current
GLAST	glutamate aspartate transporter 1
TM	transmembrane domain/helix
HP	hairpin loop
KO	knock-out
HEK293T	human embryonic kidney cells
RGL	radial glia-like cells
DG	dentate gyrus
$[Cl^-]_i$	intracellular chloride concentration
GAT-3	GABA transporter 3
CGRP	calcitonin-gene related peptide
Slc1a2	solute carrier family 1 member 2 gene, gene encoding the excitatory amino acid transporter 2

129Sv/Tac	subline of the 129S6 mouse strain by Taconic Biosciences
PCR	polymerase chain reaction
DNA	deoxyribonucleic acid
Tris-HCl	Tris-(hydroxymethyl)-aminomethanhydrochlorid
EDTA	ethylenediaminetetraacetic acid solution
NaCl	sodium chloride
DTT	DL-Dithiothreitol or *threo*-1,4-Dimercapto-2,3-butanediol
SDS	sodium dodecyl sulfate
rpm	revolutions per minute
TBE	tris borate EDTA
bp	base pairs
aCSF	artificial cerebrospinal fluid
$NaHCO_3$	sodium hydrogen carbonate
$MgCl_2$	magnesium chloride 6-hydrate
$CaCl_2$	calcium chloride dihydrate
NaH_2PO_4	sodium phosphate monobasic
O_2	oxygen
CO_2	carbon dioxide
HCl	hydrochloric acid
G	Gauge
HEPES	4-(2-Hydroxyethyl)piperazine-1-ethanesulfonic acid
Ag	silver
AgCl	silver chloride
MEA	multi electrode array
LFP	local field potential
TTL	transistor-transistor logic
CCD	charge-coupled device
AUC	area under the curve
IPSC	inhibitory postsynaptic current
mIPSC	miniature inhibitory postsynaptic current
EPSC	excitatory postsynaptic current
sEPSC	spontaneous excitatory postsynaptic current
mEPSC	miniature excitatory postsynaptic current
A/D-converter	analog-to-digital converter
CsCl	cesium chloride
EGTA	ethylene glycol-*bis*(2-aminoethylether)-*N*,*N*,*N*',*N*'-tetraacetic acid
Mg-ATP	adenosine 5'-triphosphate magnesium salt
Li-GTP	guanosine 5'-triphosphate lithium salt
QX-314 bromide	lidocaine N-ethyl bromide

CsOH	caesium hydroxide
CNQX	cyanquixaline
AP-5	(2R)-amino-5-phosphovaleric acid
AMPA	α-amino-3-hydroxy-5-methyl-4-isoxazolepropionic acid
PTX	Picrotoxin
DSI	Data Sciences International
H_2O_2	hydrogen peroxide
PBS	phosphate buffered saline
PFA	paraformaldehyde
DAPI	4′,6-diamidino-2-phenylindole
NGS	Normal Goat Serum
IgG	Immunoglobulin G
AU	Airy Unit
wt	wildtype
nRT	nucleus reticularis of the thalamus
Hm1a	Heteroscodratoxin-1
Scn8a	gene encoding Na$_V$1.6
Na$_V$1.2	voltage-gated sodium channel 1.2
Na$_V$1.6	voltage-gated sodium channel 1.2
SCN2A	gene encoding Na$_V$1.2
(DL-)TBOA	DL-threo-β-Benzyloxyaspartic acid
iGluSnFR	glutamate-sensitive fluorescent reporter
iGlu$_f$	fast variant of the glutamate-sensitive fluorescent reporter
iGlu$_u$	ultrafast variant of the glutamate-sensitive fluorescent reporter
STCs	synaptically activated glutamate transporter currents
KCC1	potassium chloride cotransporter 1
KCC3	potassium chloride cotransporter 3
CLC2	chloride channel 2
NKCC1	sodium potassium chloride cotransporter 1
GAT-1	GABA transporter 1
SUDEP	sudden unexpected death in epilepsy
KCNQ2	gene encoding K$_V$7.2
K$_V$7.2	voltage-gated potassium channel 7.2

1 Introduction

1.1 Hemiplegic migraine (HM)

HM is a rare subtype of migraine with aura and is characterised by the occurrence of an aura phase comprising motor weakness of varying degree along with additional neurological deficits with respect to the visual, sensory or language system that are usually unilateral and fully reversible. In addition to a minimum number of two attacks, according to the International Headache Society (IHS) classification, at least three of the six following characteristics must be fulfilled to clinically diagnose HM: (i) a gradual spread of at least one aura symptom over at least 5 min, (ii) the occurrence of two or more aura symptoms in succession, (iii) a duration of 5-60 min for each aura symptom, (iv) the unilateral occurrence of at least one aura symptom, (v) the positive feature of at least one aura symptom and (vi) the appearance of a headache within 60 min[2].

HM can be further subdivided into a sporadic and a familial form with an autosomal dominant pattern of inheritance and high penetrance, which was already noticed decades ago[3, 4]. Whereas patients with sporadic hemiplegic migraine (SHM) do not have any affected family members[5], for classification of the familial subtype the affected patient is required to have at least one first- or second-degree relative with similar symptoms fulfilling the criteria for HM[2].

In contrast to more common forms of migraine, which are widespread among the general population and have a mean prevalence of 11 %[6, 7], HM only affects a small number of patients worldwide. Based on its rare occurrence, the number of studies determining the prevalence or incidence of HM is low resulting in a lack of transnational studies. In 2002, an epidemiological survey that exclusively included the Danish population observed a prevalence of 0.003 % for familial hemiplegic migraine (FHM) and of 0.002 % for SHM[8].

1.2 Cortical spreading depolarisation (CSD)

For decades, the phenomenon of CSD has been debated whether to represent the underlying neurophysiological correlate for migraine aura[9, 10, 11, 12]. Their correlation was strongly supported by the emergence of studies using newly available advanced imaging techniques[13], which enabled to correlate the observed phenomena with findings in human patients[14]. CSD is a wave of extensive neuronal and glial depolarisation that slowly propagates over the cortical areas and originates from the posterior cortex[15, 16, 17]. Concomitant disruption of the ion homeostasis and near-breakdown of the transmembrane ion gradients, including sodium (Na^+), K^+, calcium (Ca^{2+}) and Cl^-, result in a long-lasting silencing of cortical activity[17, 18, 19]. In 1944, Leão discovered the spreading depression of EEG activity after stimulating the cortical tissue of a rabbit, which was accompanied by a large negative deflection of the direct current (DC) potential[15]. Interestingly, a propagation speed of the wave-like phenomenon of approximately 3 mm/min had been postulated earlier by a physician by precisely observing the spread of his own scotomas during migraine auras over years[20].

At the same time, spreading depolarisation (SD) evokes complex changes in cerebral blood flow, initially inducing a short discrete hyperperfusion, which is followed by a first episode of hypoperfusion that temporally coincides with the negative DC potential shift and a second hyperemic phase, which evolves into a prolonged episode of oligemia[21].

Additionally, numerous studies have tried to discover the mechanistic link between Leão's CSD and the activation of specific pain pathways leading to headache in migraine patients. By now, it is widely assumed that the activation and sensitisation of meningeal nociceptors and the trigeminovascular system lead to headache that is characteristically perceived by patients during a migraine attack[22, 23]. Moreover, it has been demonstrated multiple times that CSD presumably plays a key role in the persistent activation of the trigeminovascular pain pathway, including meningeal nociceptors in the trigeminal ganglion as well as central neurons in the trigeminal *nucleus caudalis*[24, 25, 26]. Nevertheless, there is reasonable doubt that CSD as a key trigger in migraine attacks is solely involved in migraine with aura leading to the hypothesis that common migraine forms that lack aura symptoms may have distinct pathophysiological pathways.

CSD can be experimentally induced and has therefore been explored in numerous distinct animal models *in vitro* and *in vivo* using invasive and more recently also non-invasive techniques[16, 27, 28, 29]. Despite the widely debated role of the phenomenon in human migraine and aura pathophysiology, investigations of CSD, particularly by using transgenic animal models, have contributed significantly to our current knowledge of the involved disease mechanisms.
Although a lot of experimental evidence has already been collected over the last decades, the specific role of CSD in the context of migraine aura and headache pain remain to be unravelled in further detail.

1.3 Mechanisms of CSD initiation and propagation

To start with, recordings in the *stratum pyramidale* and *stratum radiatum* of the hippocampus provided first evidence for a depolarisation gradient between somata and dendrites of single neurons during CSD[30]. Performing simultaneous intrasomatic and intradendritic recordings during CSD revealed longitudinal depolarisation gradients along the somatodendritic axis of hippocampal pyramidal cells[31]. During CSD, a short phase with complete depolarisation of the apical dendrites but partial depolarisation of the soma is followed by a longer phase of complete depolarisation of the somatodendritic membrane lasting several seconds that proceeds to a late phase, in which only parts of the apical dendrites remain depolarised but the soma is already partially repolarised[31]. These findings indicate that specific ion channels that are localised in the apical dendrites may evoke the initial depolarisation within a single neuron and its subsequent spread by activating further ion channels along the somatodendritic membrane, whereas the terminating CSD phase may be induced by a centrifugal closure of ion channels towards the apical dendrites[31, 32].

Scientists were aware of the profound ionic changes during SD early[16, 17]. These are characterised by a rapid decrease in extracellular Na^+ ($[Na^+]_e$), Cl^- ($[Cl^-]_e$) and Ca^{2+} ($[Ca^{2+}]_e$) concentration together with a swift rise in extracellular K^+ concentration ($[K^+]_e$) and an intermittent increase in extracellular pH, which is succeeded by a reduction in extracellular pH[17]. In addition to extensive alterations in ionic homeostasis, certain amino acids are released from intracellular compartments during CSD, for example glutamate[17]. In general, CSD represents a highly energy-consuming phenomenon, as considerable amounts of adenosine triphosphate (ATP) are needed to restore the disrupted transmembrane ion gradients, which also explains why CSDs are associated with profound changes in blood flow lasting several hours[21, 33].

Although consensus with respect to CSD triggering factors is still lacking among experts in the field, some studies including both experimental and computational data strongly support the hypothesis that the interstitial K^+ accumulation after having exceeded its glial uptake results in neuronal depolarisation and finally initiates SD[16, 34]. Using computational modelling, it was demonstrated that K^+-induced depolarisation of the neuronal apical dendrite leads to the generation of an initial net inward current resulting in membrane depolarisation and local $[K^+]_e$ release, which consequently elicits a positive feedback cycle including the self-regenerative depolarisation of neurons[34]. Additionally, the data also confirmed the all-or-none principle of SD[34].
Nevertheless, experimental studies using transgenic models for FHM explicitly shifted the focus on the excitatory neurotransmitter glutamate to be the key factor in CSD initiation generating the glutamate-based hypothesis for CSD induction[35, 36]. Studying both the FHM1 and the FHM2 mouse model demonstrated that enhanced glutamatergic neurotransmission, either caused by an increased presynaptic glutamate release or a diminished synaptic removal of glutamate, represents the underlying cause for higher CSD susceptibility (see section 1.4)[27, 37].

Our knowledge on the involved ion channels and receptors during the different CSD phases is largely incomplete since distinct pharmacological mechanisms underlie the processes of CSD initiation and propagation. However, it is hardly possible to differentiate them as the single phases are highly connected and propagation directly supersedes CSD initiation.
To start with, both *in vivo* and *in vitro* studies using electrical or chemical stimulation to trigger CSD revealed the importance of NMDA-receptors in initiation or propagation of CSD, while the use of AMPA- and kainate-receptor antagonists verified the contrary and did not have any effect on CSD[38, 39, 40, 41]. The joint conclusion of these studies was that NMDA receptors are essential for CSD initiation or propagation, which was mostly not differentiated. One of the first publications to verify the role of NMDA-receptors during CSD *in vivo* demonstrated a dose-dependent effect of NMDA-receptor antagonists on CSD threshold, propagation velocity and the duration of ionic changes[38]. From the compelling evidence that NMDA-receptors are necessarily involved, one could directly infer the equal importance of glutamate during SD.

As outlined at the beginning of this section, there is evidence that specific ion channels in the membranes of apical dendrites finally lead to the spread of depolarisation within a single neuron[31]. The vast changes of distinct ion concentrations during SD that had been recognised early led to the hypothesis that Na^+ channels may be decisively involved in the initiation and propagation processes of CSD[17]. The discovery of *SCN1A* encoding the Na^+ channel $Na_V.1.1$ as the third

HM gene (see section 1.4) as well as the alleviating effect of the Na^+ channel blocker lamotrigine on migraine auras additionally contributed to this assumption. Therefore, the effect of Na^+ channel inhibition on CSD has been repeatedly studied mostly using tetrodotoxin (TTX), which blocks voltage-gated Na^+ channels that are present in the brain. However, the effect of TTX and consequently the inhibition of Na^+ channels on CSD has been slightly controversial. On the one hand, CSDs triggered by high K^+ dialysis/solution were not prevented by TTX *in vivo*[30] as well as *in vitro*[42]. On the other hand, experimental data from cortical slices demonstrating that the area of CSD and the IOS (intrinsic optical signal) intensity were reduced after applying TTX provided evidence that voltage-gated Na^+ channels may partly play a role[43].

In contrast to the inhibition of voltage-gated Na^+ channels, voltage-gated Ca^{2+} channels appear to be critical for CSD initiation in brain slices, because triggering of CSD was abolished by using Ca^{2+}-free medium or Ca^{2+} channel blockers[44]. Nevertheless, in rodent brain slices, SD was induced despite the inhibition of voltage-gated Na^+ and Ca^{2+} channels by generating glutamate release, activating presynaptic NMDA-receptors and highly increasing $[K^+]_e$, which demonstrated a Ca^{2+}-independent mechanism of CSD induction[45].

Furthermore, under more physiological conditions large increases in the intracellular Ca^{2+} concentration ($[Ca^{2+}]_i$) during CSD were not only observed for cortical neurons, but also for astrocytes[46, 47]. However, in the cortex neuronal $[Ca^{2+}]_i$ increase precedes the astrocytic Ca^{2+} rise indicating a less significant role of the glial cell type during CSD[47]. Nevertheless, variants in the astrocytic α2-subunit of the Na^+/K^+-ATPase (NKA) are associated with FHM2[37, 48]. As outlined in section 1.4, a diminished K^+ and glutamate clearance from the extracellular space is assumed to represent the main pathophysiological mechanism in FHM2[37, 48]. However, the astrocytic depolarisation during CSD is supposed to be induced passively via increased $[K^+]_e$ levels[17].

1.4 Genetics in HM

Advances in genomic sequencing techniques led to the identification of *CACNA1A* as the first FHM causing gene in 1996 (**Figure 1**) and simultaneously provided strong evidence for an additional association of the voltage-gated Ca^{2+}-channel gene with episodic ataxia type 2 (EA2)[49]. To provide a short explanation on the EA2 disorder, characteristic features include episodes of imbalance, vertigo and ataxia for several hours combined with an interictal nystagmus, which are provoked by stress and physical activity and respond well to acetazolamide[50]. *CACNA1A* encodes the pore-forming α1-subunit of the P/Q-type Ca^{2+} channel $Ca_V2.1$, which is localised in the presynaptic nerve terminals of neurons to participate in neurotransmitter release[51].

In FHM1, distinct GOF (gain-of-function) variants lead to an increase in action potential (AP)-induced Ca^{2+} influx, which results in an elevated glutamate release at pyramidal cell synapses (**Figure 1**), but simultaneously renders inhibitory synaptic transmission unaltered provoking a momentous excitation/inhibition (E/I) imbalance[52]. Using transgenic mouse models harbouring distinct pathogenic *CACNA1A* variants, a higher sensitivity to CSD due to enhanced glutamatergic neurotransmission was demonstrated[52, 53, 54]. Of note, depending on the specific variant, the phenotypic spectrum exceeds classic HM features and additionally includes ataxia, seizures, coma, and brain oedema evoked by mild head trauma[53, 55].

In 2003, heterozygous loss-of-function (LOF) variants in the *ATP1A2* gene were first associated with FHM2[56]. *ATP1A2* encodes the α2-subunit of the catalytic subunit of a T-type NKA, which is essential for restoring the electrochemical gradients across cell membranes[57] (**Figure 1**). In the adult brain, the respective isoform is predominantly found in astrocytes[58]. Studies using transgenic animals revealed an increased CSD susceptibility and propagation velocity caused by the dysfunctional synaptic clearance of glutamate and K^+ in association with diminished expression of the excitatory amino acid transporter 2 (EAAT2, former name: glutamate transporter 1 (GLT-1)), which results in an E/I imbalance favouring excitatory neurotransmission in the cortex[37, 48, 59]. FHM2 patients may present with epilepsy as frequent additional phenotype[60, 61, 62], which was reproduced using transgenic animals harbouring the respective variants[63].

The identification of *ATP1A2* was shortly followed by the discovery of pathogenic variants in *SCN1A* leading to HM in 2005, whereupon it was classified as the third FHM gene[64] (**Figure 1**). Of note, the *SCN1A* gene encoding the α-subunit of $Na_V1.1$ had already been established as causative gene for generalised epilepsy with febrile seizures plus (GEFS+)[65] and Dravet syndrome (DS), formerly known as severe myoclonic epilepsy of infancy[66]. To date, eleven missense mutations have been reported in the literature, showing that, in the context of (F)HM, the proportion of *SCN1A* variants is small compared to the broader mutational spectrum of *CACNA1A* and *ATP1A2* variants[64, 67, 68, 69, 70, 71, 72, 73, 74]. $Na_V1.1$ is predominantly expressed in fast-spiking inhibitory interneurons with a main localisation at the axon initial segment (AIS), where the channel plays a key role in AP initiation and propagation[75, 76]. Despite initial contradictory results of characterising *SCN1A* HM variants[77], the functional consequences of the discovered variants are overall consistent with a GOF effect leading to an increased firing frequency and thus, hyperexcitability of inhibitory neurons[71, 78, 79, 80]. Interestingly, *SCN1A* variants in HM mostly lead to pure HM phenotypes in the affected patients, however, the phenotypic spectrum was also found to comprise epilepsy in rare cases[81].

Since the identification of the three main HM genes, several candidate genes have been discovered to genetically increase the risk for HM or to possibly represent a novel FHM subtype. To name a few candidates, the *PRRT2* gene encoding the proline rich transmembrane protein 2 has been treated as the most promising nominee to account for a fourth autosomal dominant HM gene, with a recent genetic study undermining its importance in the context of the disorder[82]. In general, *PRRT2* is associated with a wide range of paroxysmal neurological disorders[83]. Another example is the solute carrier family 2 member 1 (*SLC2A1*) gene encoding the glucose transporter 1 (GLUT-1), which has also been linked to cause HM, although the migraine in the affected patients always occurred in combination with another neurological disorder[84, 85, 86]. Furthermore, homozygous variants in the solute carrier family 4 member 4 (*SLC4A4)* gene, which encodes the Na^+-$HCO3^-$-cotransporter 1 (NBCe1), have recently been identified in a family with migraine, also including family members with hemiplegic aura symptoms[87]. Most recently, a variant in *ATP1A4* encoding the NKA α4-subunit was identified in a family with pure HM, however, functional studies are still required to confirm its pathogenicity[88, 89].

In accordance with the clinical spectrum of the *CACNA1A* gene, the solute carrier family 1 member 3 (*SLC1A3*) gene is known to cause episodic ataxia type 6 (EA6)[90, 91, 92]. *SLC1A3* encodes the excitatory amino acid transporter 1 (EAAT1), a dual function protein, that couples glutamate reuptake from the extracellular space with the transport of Na$^+$, K$^+$ as well as pH gradients and additionally forms a Cl$^-$ channel during the glutamate transport cycle that is gated by two hydrophobic gates[93, 94, 95]. Interestingly, the first *SLC1A3* variant was discovered in a patient with a clinically complex overlapping syndrome, which did not only comprise episodic ataxia (EA), but also epileptic seizures as well as HM attacks[96]. The clinical presentation highly resembled one extremely severe phenotype caused by a HM variant in *CACNA1A*[53, 55]. In recent years, an increasing number of *SLC1A3* variants have been identified, providing further evidence for the specific overlap of EA and HM in the spectrum of *SLC1A3*-associated neurological disorders[97]. However, also a pure HM phenotype was described in one patient, turning the EA6-associated gene into a new HM candidate/risk gene[98, 99]. Functional characterisations of the identified *SLC1A3* variants have demonstrated varying effects on glutamate transport, anion currents and other EAAT1 properties depending on the respective variant[98, 100, 101].

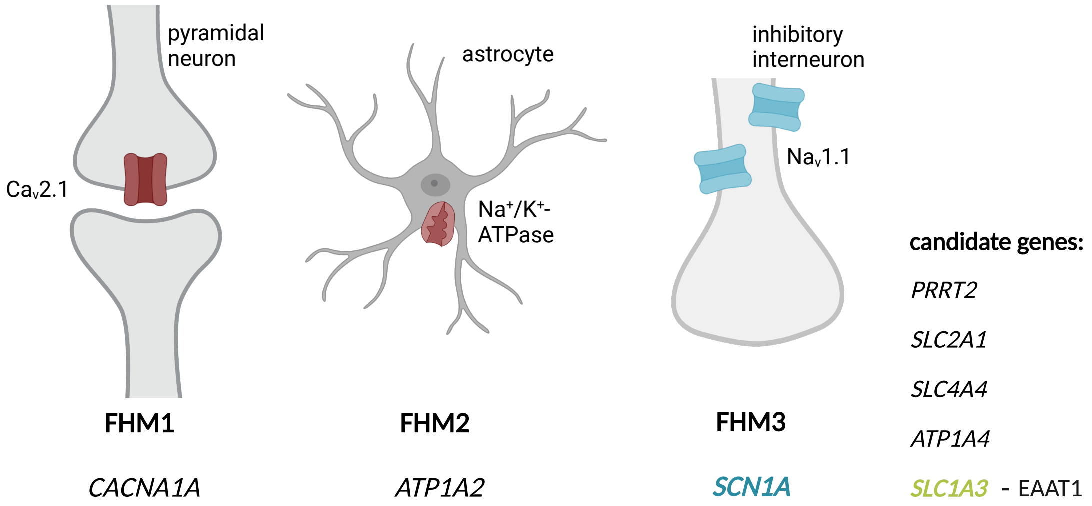

Figure 1. The genetic HM spectrum. FHM1 is associated with GOF variants in *CACNA1A* encoding the α1-subunit of the P/Q-type Ca^{2+} channel Ca$_V$2.1, which is important for AP-induced transmitter release in the presynaptic terminals of pyramidal neurons (left). LOF variants in *ATP1A2* encoding the catalytic subunit of an astrocytic NKA are associated with FHM2 (middle). FHM3 is caused by GOF variants in the *SCN1A* gene that encodes the α-subunit of the voltage-gated Na$^+$ channel Na$_V$1.1 being predominantly expressed in GABAergic interneurons (right). *PRRT2*, *SLC2A1*, *SLC4A4* and *ATP1A4* represent novel candidate/risk genes for HM. *SLC1A3* encoding the astrocytic glutamate transporter and anion channel EAAT1 is among those novel HM genes.

To summarise, several genes have been identified to be associated with HM, however, for most candidates the case number remains rather low. Supporting the rising number of genes linked to HM, a recent study in the Finnish population demonstrated that variants in the three main

HM genes do not account for most HM cases[102] and strongly indicates that additional, mostly unidentified variants may contribute to the genetically heterogeneous disease. Thus, multiple different genes, each slightly increasing the risk for the occurrence of HM in patients, rather than a major fourth HM gene remain to be established[103]. Moreover, there is a lack of studies that comprehensively characterise the functional effects of the discovered variants using cell culture techniques or transgenic animal models.

1.5 Common additional phenotypes in HM

The phenotypic spectrum of HM is characterised by a considerable overlap with different neurological disorders, with epilepsy and ataxia being on top of the list. Although epilepsy, migraine and ataxia appear to be heterogeneous disease entities at first sight, they share a remarkable amount of similarities[104]. From an epidemiologic point of view, the prevalence of epilepsy in migraineurs and of a migraine disorder in patients with epilepsy was increased according to a recent review shedding light on the relationship between migraine and epilepsy[105]. This co-occurrence and close correlation between seizures and HM attacks has already been noticed more than 150 years ago[106].

One rather obvious common feature is their episodic nature, which means that a certain pathologic state is evoked for a limited amount of time before restoring the physiological state[107]. Several triggering factors that have been identified are common among migraine, ataxia and epilepsy, for instance sleep deprivation or stress[108]. The exact mechanisms evoking the transition into the beforementioned pathologic state are largely unknown. However, once the pathophysiological processes have been identified, they offer the grand opportunity to specifically develop therapies that may counteract the transition and prevent seizures, migraine attacks and ataxic spells. Nevertheless, with respect to genetically caused, monogenic forms of the three specified disorders, the paroxysmal occurrences of migraine attacks, seizures and ataxic episodes contrast with the fact that the disease-causing variants are constantly present.

Furthermore, many disease-causing genes are shared between epilepsy syndromes, HM, and ataxia, which frequently encode transmembrane ion channels, pumps, or transporters. One historical example that was outlined earlier is the discovery of *CACNA1A* variants, which were on the one hand, associated with HM and on the other hand, linked to EA2[49]. In general, different variants in the same gene often lead to distinct phenotypes suggesting to some extent that certain pathophysiological pathways may be shared[109]. This connection raises the idea that similar pharmacological treatment may be applicable[110]. In fact, the use of certain substances as treatment for both migraine and epilepsy is already implemented in daily clinical praxis. For example, the German guidelines for migraine therapy recommend to use the anti-seizure medications (ASMs) lamotrigine and topiramate as prophylactic treatment to prevent migraine auras[111].

Both migraine attacks and epileptic seizures are considered to arise from hyperexcitability of a large neuronal population in different brain regions, which can be the result of genetic variants amongst other causes[112]. However, the critical factors that decide whether a hyperexcitable state induces a CSD or epileptiform activity have remained elusive to date.

1.5.1 Epilepsy and seizures

Epileptic seizures are defined as “a transient occurrence of signs or symptoms due to abnormal excessive or synchronous neuronal activity in the brain”[113]. Seizures are characterised by the generation of hypersynchronous network activity due to the involvement of a large population of neurons, during which the participating cells synchronously depolarise and fire APs[104]. They can be described based on a focal or generalised onset depending on whether they originate within neuronal networks of one hemisphere or whether they promptly engage networks of both hemispheres after originating at some point within networks[113, 114]. Additionally, focal, generalised, and unknown onset seizures can be further subdivided depending on the respective occurrence of motor or nonmotor classifiers[113].

The diagnosis of epilepsy is made if two unprovoked seizures occur more than 24 h apart, if one unprovoked seizure occurs in combination with a ≥ 60 % probability for further seizures over the following ten years or if an epilepsy syndrome is diagnosed[113]. In 2016, the lifetime prevalence of epilepsy estimated for the general population was 7.6 % per 1000 persons[115]. In a Norwegian population-based study from 2017, 41 % of the included children with epilepsy were diagnosed a specific genetic epilepsy syndrome[116].

To classify the epilepsy type of a patient, four different categories including “focal”, “generalised”, “combined generalised and focal”, and “unknown” epilepsies have been established[117]. According to the ILAE classification of the epilepsies, an aetiology among six different subgroups should be determined for every seizure and epilepsy including structural, genetic, infectious, metabolic, immune, and unknown aetiologies[117]. Defining an aetiologic subgroup is considered highly important, because different therapies are required depending on the respective aetiology. For example, epileptic seizures in the context of a bacterial central nervous system infection may primarily require antibiotic treatment. Moreover, the classification may proceed to defining a specific epilepsy syndrome, which comprises different characteristics such as seizure types, EEG features, imaging abnormalities, an age-dependent onset/progress, or the manifestation of comorbidities, for example intellectual disability. Since the ground-breaking discovery of the first gene in 1995, a growing number of epilepsy-associated genes have been described in literature[118]. Therefore, the focus of this thesis will entirely be on genes that are associated with genetic epilepsy syndromes and additionally play a role in HM genetics.

1.5.2 Epilepsy in the context of HM genes

As already mentioned, *CACNA1A* LOF variants are associated with EA2, whereas GOF variants lead to FHM1[49, 50]. However, as in several patients with epileptic encephalopathy that presented with distinct seizure types, *CACNA1A* LOF variants were discovered[119, 120, 121], it was recently adjudged to be an important gene in the context of epileptic encephalopathies[122]. Of note, in many cases, an overlap with additional phenotypic features was noticed, for instance cognitive

impairment, ataxic symptoms, or autism[121]. Furthermore, *CACNA1A* variants had been identified in tottering and leaner mice displaying absence epilepsy earlier[123].
For most epilepsy-related *ATP1A2* variants that have been published in literature, the epileptic phenotype usually occurred in association with HM[60, 61]. However, in a recent study the spectrum of *ATP1A2*-related disorders was expanded linking heterozygous mutations with a severe neurodevelopmental phenotype that comprised status epilepticus, early lethality, microcephaly, cortical malformation, and progressive brain atrophy[124].

In contrast, *SCN1A* represents the most important epilepsy-associated gene among the three main HM genes, as LOF variants do not only cause the extremely severe DS but also the milder GEFS+ phenotype[65, 66]. The broad spectrum of *SCN1A*-associated epilepsy syndromes clearly contrasts with the fact that the co-occurrence of epilepsy and seizures in FHM3 patients is relatively rare compared to FHM1 and FHM2. Whereas GEFS+ patients usually have well treatable seizures without additional cognitive or motor impairment[125], the developmental and epileptic encephalopathy DS is characterised by an early-onset epilepsy with prolonged seizures of various types that are mostly refractory to standard ASMs[126, 127]. Motor function, behaviour as well as cognitive development are additionally impaired in affected children[127]. $Na_V1.1$ LOF resulting in hypoexcitability of parvalbumin positive (PV+) inhibitory interneurons underlies both GEFS+ and DS, however, the severity and consequently the phenotype depend on the degree of interneuron impairment[75, 76]. Multimodal analysis of a GEFS+ mouse model harbouring the LOF variant R1648H revealed an impairment of the AP initiation at the AIS of cortical, hippocampal and thalamic GABAergic interneurons, which resulted in network hyperexcitability[76]. Of note, the R1648H variant directly neighbours the FHM3 variant L1649Q, which will be further discussed in section 1.6.

On the contrary, FHM3 is situated at the opposite end of the spectrum of *SCN1A*-related disorders as the underlying pathophysiological mechanism comprises $Na_V1.1$ GOF, which results in hyperexcitability of fast-spiking GABAergic interneurons[64, 78, 79]. The spectrum of GOF $Na_V1.1$ disorders has recently been extended due to the identification of a group of patients with neonatal onset epilepsy with tonic seizures and apnoeas, arthrogryposis, intellectual disability and movement disorders, a second group with later-onset early infantile developmental and epileptic encephalopathy also including movement disorders as well as one patient exclusively with developmental and epileptic encephalopathy[109, 128]. Interestingly, functional characterisation of *SCN1A* GOF variants leading to epilepsy and FHM3 revealed that epilepsy-associated variants cause a milder GOF effect on the channel[109]. In comparison, HM variants are characterised by a more pronounced GOF effect on $Na_V1.1$ as they evoke a relatively large change in the gating properties, especially with respect to an increased persistent Na^+ current[109]. Studies that further elucidate the specific role of $Na_V1.1$ persistent Na^+ current and that determine characteristic features to distinguish epilepsy causing GOF and LOF variants will be of great value, as the functional effect of an *SCN1A* variant has major consequences on therapy.

As already outlined in section 1.4, several candidate genes have recently been discussed in the context of HM. Of note, the majority have also been associated with epilepsy. For example, *PRRT2* variants are known to cause benign familial infantile epilepsy (BFIE)[129]. For the *SLC2A1* gene, a rather broad spectrum of different epilepsy syndromes has been described in literature including early onset absence epilepsy, childhood absence epilepsy, myoclonic astatic epilepsy, and focal epilepsy[130]. The discovery of an extremely severe homozygous *SLC4A4* variant has recently expanded the spectrum of *SLC4A4*-related disorders[131]. Interestingly, the syndrome concurrently comprises HM, migraine-associated epileptic seizures as well as status epilepticus[131].

In the context of *SLC1A3*-related disorders, an association with epilepsy has also been discovered. To date, epilepsy has only been reported in one case and the syndrome was characterised by an overlap with HM and EA[96]. However, due to the frequent overlap of EA6 with (hemiplegic) migraine[96, 97, 132] and the recent identification of a variant leading to pure HM, *SLC1A3* is considered a potential HM candidate/risk gene[96, 98]. Nevertheless, technical advances in genetic diagnostics may reveal a more significant role of *SLC1A3*-associated epilepsy in the future, considering that variants in the related gene *SLC1A2* lead to severe forms of epileptic encephalopathy[133]. However, the pathophysiological mechanisms leading to *SLC1A3*-associated epilepsy have not been explored and clarified so far.

1.5.3 Epileptiform activity versus CSD

In contrast to the synchronous nature of epileptiform activity and its rapid involvement of both hemispheres in case of a generalised onset[113], CSD as the correlate for migraine aura propagates much more slowly at a speed of 2-3 mm/min[20, 134]. A spread to the contralateral hemisphere as well as an involvement of subcortical structures, like the thalamus or the hippocampus, are frequently observed in the context of seizure-like activity[76, 123], whereas CSD propagation to areas other than the cortex have only been described for certain HM variants mostly yielding a more severe phenotype[29, 55, 135, 136].

Another feature that appears to be similar at first sight but turns out to be rather different is the phase of suppressed activity following a seizure-like or a CSD event. Each seizure-like event is usually followed by a short phase of post-ictal depression or slowing of EEG activity lasting seconds to minutes[137]. This term must be distinguished from the postictal state lasting minutes to days, during which neurological or psychiatric symptoms are observed in patients after an epileptic seizure[137]. In contrast, the depolarisation block following a CSD is rather long-lasting, with a duration of several minutes[15, 17].

Furthermore, an increase in $[K^+]_e$ is found during both phenomena. During epileptic discharges, the $[K^+]_e$ increase is usually moderate and does not exceed 13 mM[138], whereas during CSDs, the rise in $[K^+]_e$ is mostly abrupt and noticeably higher, often exceeding 25 mM[18, 19].

A recent study clarifying the connection between seizure-like activity and CSD presented the SD event in a completely different, evolution-based context[139]. Tamim and colleagues showed that seizures elicited SDs, which resulted in the termination of ictal activity and prevention of seizure generalisation suggesting that SD may act as an innate antiseizure mechanism[139].

Despite the numerous differences between the two hyperexcitable events, seizure-like activity and SDs still appear to be closely related, which makes the study of both phenomena and their correlation highly interesting.

1.6 *SCN1A*-specific prior knowledge

FHM3 causing variants in the *SCN1A* gene are consistent with a GOF of $Na_V1.1$ leading to hyperexcitability of PV+ fast-spiking interneurons, in which the Na^+ channel is predominantly expressed[75]. In general, Na_V channels are responsible for generating APs and regulating membrane permeability for Na^+ ions due to their rapid channel opening and closing following changes in membrane potential[140]. The nine identified pore-forming α-subunits usually assemble with auxiliary β-subunits to form an Na_V channel and each α-subunit comprises four domains (DI-IV)[140]. Each domain contains six transmembrane segments (S1-S6), of which the S4 segment carrying charged amino acid residues acts as voltage sensor[140] (**Figure 2**).

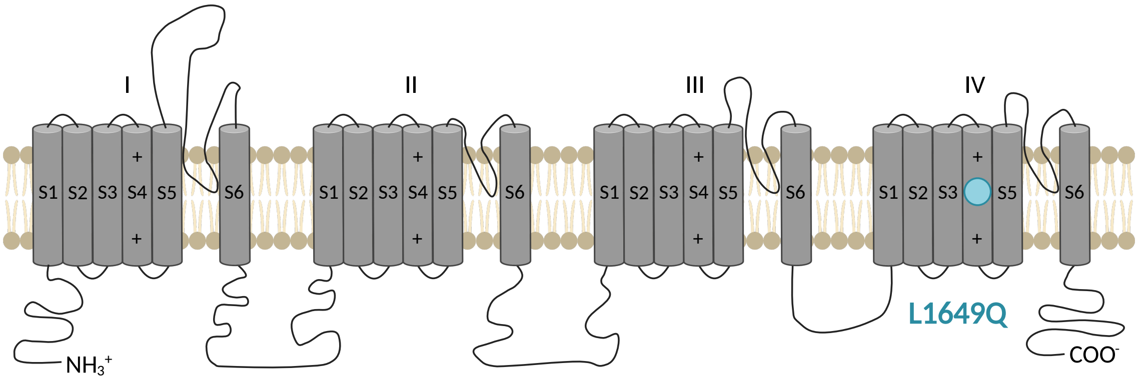

Figure 2. Scheme of the $Na_V1.1$ α-subunit. The α-subunit consists of four domains (DI-IV) and each domain comprises six transmembrane domains (S1-6). The S4 segment of each domain acts as voltage sensor. The GOF variant p.Leu1649Gln (L1649Q, blue dot) causing pure HM is located in the S4 segment of DIV[69].

The FHM3 phenotypic spectrum rarely includes epilepsy and mostly leads to pure HM[81], which also applies to the variant p.Leu1649Gln (L1649Q) being located in the voltage sensor of domain 4 of $Na_V1.1$ (**Figure 2**)[69]. First functional characterisation of L1649Q, which was introduced in the human *SCN5A* gene, overall revealed a GOF effect on $Na_V1.1$ and supported an interference with the process of inactivation[69]. On the contrary, expression of the mutant channel in tsA201 cells yielded a markedly reduced surface expression of $Na_V1.1$-L1649Q, thereby indicating a LOF effect[77]. However, after rescuing the folding-defective $Na_V1.1$-L1649Q mutant by incubation at lower temperatures, GOF properties were observed by expressing the mutant channel in tsA201 cells and transfected neurons[79]. Besides a slowed current activation/decay and a smaller current density, Cèstele and colleagues also demonstrated a depolarising shift of the voltage dependence of inactivation with an increase in persistent Na^+ current for $Na_V1.1$-L1649Q mutants, which resulted in an increased firing of the transfected neurons[79]. Overall, the previously published data on L1649Q strongly indicated a GOF effect on $Na_V1.1$, which leads to hyperexcitability of GABAergic inhibitory neurons and results in HM attacks in the affected patients. This was additionally supported by the first FHM3 mouse model harbouring the variant L263V, which displayed spontaneous CSDs *in vivo*[141].

In the following section, specific findings regarding the *Scn1a*$^{L1649Q/wt}$ knock-in mouse model that had been gathered by the Lerche, Hedrich, Plesnila and Pusch lab earlier will be shortly summarised to illustrate the previous knowledge on FHM3, on which the hypotheses and research questions of this thesis were built upon[1]. The FHM3-related results presented in this dissertation were recently published in the Journal of Clinical Investigation bearing the title "Hyperexcitable interneurons trigger CSD in an *Scn1a* mouse model" as part of a major collaborative work[1].

To elucidate the underlying pathophysiological mechanisms of FHM3 and explore how *SCN1A* GOF variants lead to higher CSD susceptibility and HM attacks, the *Scn1a*$^{L1649Q/wt}$ knock-in mouse line was generated on a C57Bl/6N background[1]. Whereas heterozygous mice did not differ from wildtype littermates in extensive phenotypic screenings, homozygous knock-in animals showed a markedly reduced survival, with a median age of 18 days, and rarely suffered from HM attacks characterised by circling behaviour (**Figure 3 A**)[1]. In contrast to an early time point at postnatal day 16 (P16), Western blot analysis at the age of two months revealed a reduction in $Na_V1.1$ protein levels in the cortex of *Scn1a*$^{L1649Q/wt}$ knock-in animals, which may indicate compensatory changes (**Figure 3 B**)[1].

To determine the consequences of the L1649Q variant *in vivo*, CSDs were triggered in anesthetised animals using topical KCl application and revealed a higher CSD frequency (**Figure 3 C, D**) and a lower latency until CSD onset in heterozygous 2 months-old mice (data not shown)[1]. Furthermore, using electrical stimulation a lower threshold for CSD induction in *Scn1a*$^{L1649Q/wt}$ animals was demonstrated (data not shown)[1].

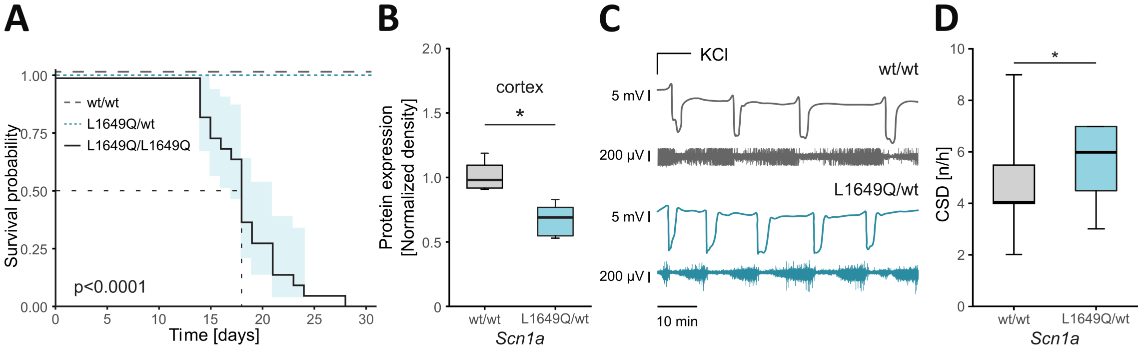

Figure 3. Reduced survival of homozygous mice and increased CSD susceptibility *in vivo* (adapted from Auffenberg et al., 2021)[1]. (**A**) In contrast to heterozygous and wildtype animals, homozygous mice died prematurely, with a median survival of 18 days, which is illustrated by the Kaplan-Meier-Plot (log rank test)[1]. (**B**) Western blot analysis revealed reduced $Na_V1.1$ protein levels in cortical tissue of heterozygous compared to wildtype animals at the age of 2 months (Mann-Whitney rank sum test)[1]. (**C**) Representative examples of CSD recordings in an anaesthetised wildtype (grey traces) and *Scn1a*$^{L1649Q/wt}$ (blue traces) animal after topical KCl application (top: DC potential, bottom: ECoG signal)[1]. (**D**) At the age of 2 months the frequency of elicited *in vivo* CSD events was increased in *Scn1a*$^{L1649Q/wt}$ mice (Mann-Whitney rank sum test)[1].

Whole-cell patch clamp recordings using acute brain slices from P14 to P20 mice were performed to comprehensively investigate the functional consequences of the L1649Q variant on the single cell level, with a focus on the hippocampal CA1 region and layer 4/5 of the cortex[1]. Whereas recordings of pyramidal neurons did not reveal any differences (data not shown), AP frequencies of fast-spiking inhibitory neurons in the hippocampus and cortical layer 4 were increased in slices of *Scn1a*$^{\text{L1649Q/wt}}$ animals compared to slices of wildtype littermates (**Figure 4 A, B**)[1]. Recordings from cortical and hippocampal excitatory neurons revealed an elevated frequency of spontaneous inhibitory postsynaptic currents (sIPSCs) in slices of heterozygous animals (**Figure 4 C**)[1]. Additionally, slow voltage ramp recordings in the CA1 region verified an increased steady-state Na^+ current of GABAergic interneurons in slices of *Scn1a*$^{\text{L1649Q/wt}}$ animals (**Figure 4 D, E**)[1].

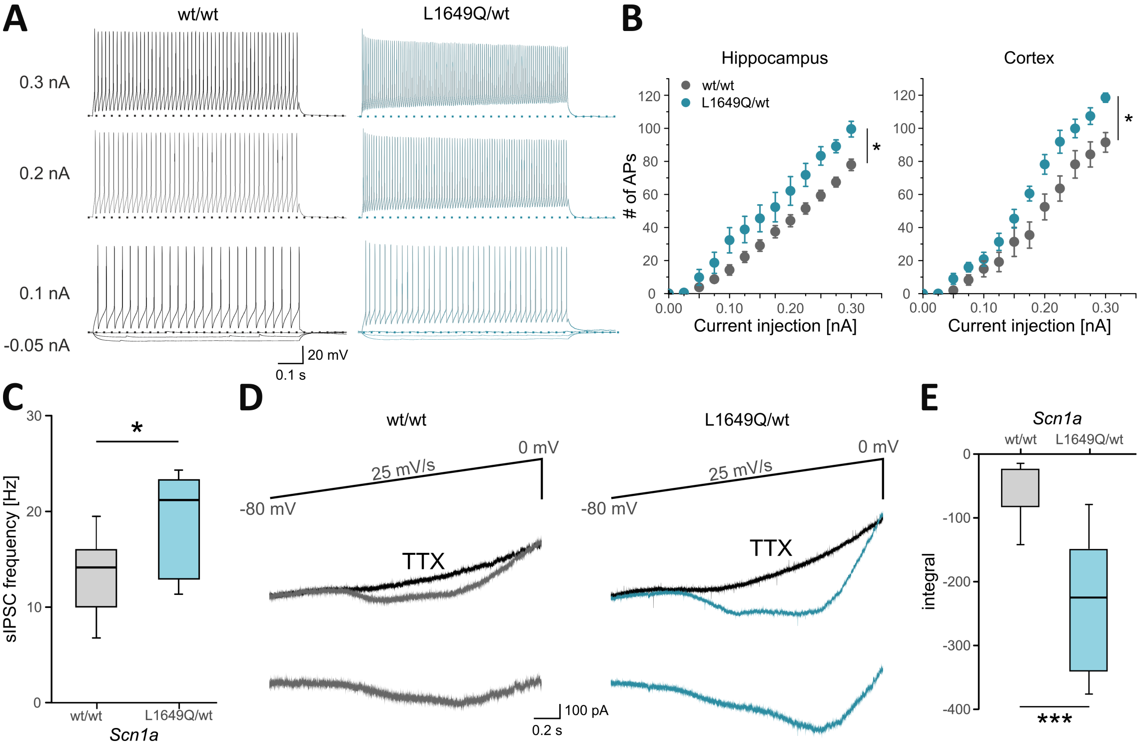

Figure 4. Hyperexcitability of cortical and hippocampal inhibitory neurons caused by increased firing rates and persistent Na^+ current (adapted from Auffenberg et al., 2021)[1]. (**A**) Representative AP series recorded from a hippocampal fast-spiking inhibitory neuron of a wildtype (left) and heterozygous (right) animal[1]. The distinct voltage traces were elicited upon different current injections[1]. (**B**) The frequency of AP firing was increased in fast-spiking interneurons in the hippocampus (left) and cortex (right) of heterozygous animals[1]. The number of APs was plotted against the respective current that had been injected (*Scn1a*$^{\text{wt/wt}}$: grey dots, *Scn1a*$^{\text{L1649Q/wt}}$: blue dots; Mann-Whitney rank sum test)[1]. (**C**) Accordingly, the sIPSC frequency was elevated in the cortex of *Scn1a*$^{\text{L1649Q/wt}}$ compared to wildtype mice (Mann-Whitney rank sum test)[1]. (**D**) Ramp Na^+ currents of hippocampal fast-spiking interneurons were elevated in *Scn1a*$^{\text{L1649Q/wt}}$ animals, which is exemplified in the illustrated traces that were recorded from a wildtype (left) and a heterozygous (right) mouse[1]. The net ramp current was estimated by subtracting the traces recorded with TTX from those without TTX application[1]. (**E**) The integral of the recorded ramp Na^+ currents was increased in fast-spiking neurons of *Scn1a*$^{\text{L1649Q/wt}}$ versus wildtype animals (Mann-Whitney rank sum test)[1].

To further strengthen the obtained results and pharmacologically reverse the effect of the variant, the persistent Na^+ current blocker GS967[142] was used to study its effect *in vivo* and *in vitro*[1].

GS967 did not only reduce the increased persistent Na^+ current and AP frequency (**Figure 4 B, C**), but also prolonged survival in homozygous *Scn1a*$^{L1649Q/wt}$ mice (**Figure 4 A**)[1].

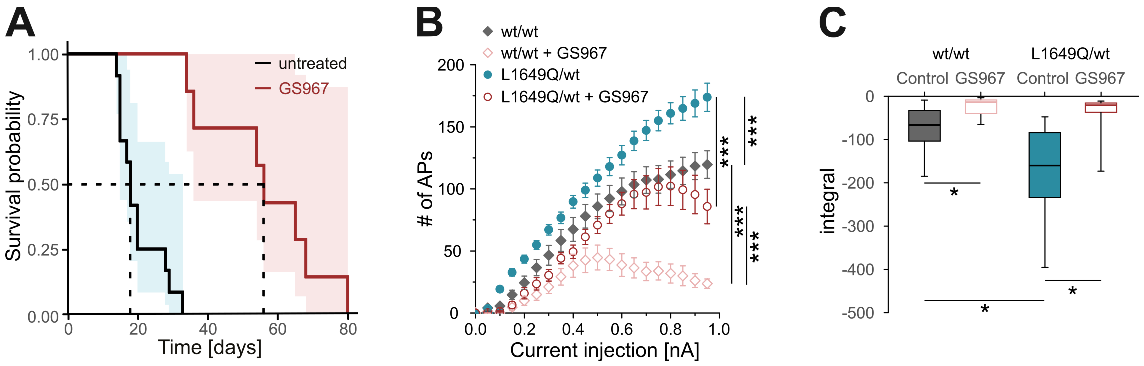

Figure 5. Beneficial effects of the persistent Na^+ channel blocker GS967 *in vivo* and *in vitro* (adapted from Auffenberg et al., 2021)[1]. (**A**) GS967 treatment prolonged the lifespan of homozygous mice, shown by the Kaplan-Meier-Plot (log rank test)[1]. (**B**) Application of GS967 decreased the AP number in hippocampal fast-spiking cells of wildtype and heterozygous animals that were elicited upon current injections (*Scn1a*$^{wt/wt}$: grey filled symbol, *Scn1a*$^{wt/wt}$ + GS967: pink empty symbol, *Scn1a*$^{L1649Q/wt}$: blue filled symbol, *Scn1a*$^{L1649Q/wt}$ + GS967: red empty symbol)[1]. The number of APs were plotted against the respective current injections (2-way ANOVA)[1]. (**C**) The boxplots visualise the integrals of the net (TTX-subtracted) ramp Na^+ currents (*Scn1a*$^{wt/wt}$: grey/filled, *Scn1a*$^{wt/wt}$ + GS967: pink/empty, *Scn1a*$^{L1649Q/wt}$: blue/filled, *Scn1a*$^{L1649Q/wt}$+ GS967: red/empty)[1]. The integral was significantly reduced after applying GS967 both for the cells of wildtype and heterozygous animals (2-way ANOVA)[1].

1.7 *SLC1A3*-specific prior knowledge

Closely resembling the *CACNA1A*-associated phenotypes, *SLC1A3* is associated with EA6[90, 91, 92] and has recently been considered as novel HM candidate/risk gene[143, 144]. In early studies, the dual function protein EAAT1 (former/rodent name: glutamate aspartate transporter (GLAST)) encoded by *SLC1A3* was linked to the regulation of extracellular glutamate levels and prevention of synaptic glutamate excitotoxicity[145, 146]. Of note, EAAT1 is mainly expressed in the astroglial cell population, for example astrocytes, retinal Mueller cells or radial glia-like cells[147, 148, 149, 150].

By utilising secondary-active transport mechanisms, EAAT1 couples the energy-consuming glutamate removal from the extracellular space with the downward flow of Na^+ and K^+ along their electrochemical gradients in addition to the use of the transmembrane pH gradient[151]. In general, EAAT1 assembles as a trimer that each comprises eight transmembrane domains (TM1-8) and two hairpin loops (HP1-2) interacting with the transport substrates (**Figure 6**)[151, 152] . The complex glutamate transport cycle is initiated in the outward-facing conformation by binding of the substrate to HP2, followed by a translocation into the inward-facing conformation, which is achieved by an elevator-like rotational-translational movement of the dynamic transport domain relative to the static trimerisation domain of the protein[151].

The function of EAAT1 to control glutamate homeostasis and its presumable role in HM pathophysiology may already point towards the excitatory neurotransmitter glutamate to elicit CSDs and to finally trigger migraine attacks in patients. On the contrary, an early study revealed that homozygous knock-out (KO) mice displayed defective motor coordination during more advanced tasks, impaired innervation of Purkinje cells by climbing fibers and an increased development of oedema after cerebellar injury[153]. The mild phenotype of EAAT1-deficient animals initially suggested a minor role of the astrocytic glutamate transporter in human disease.

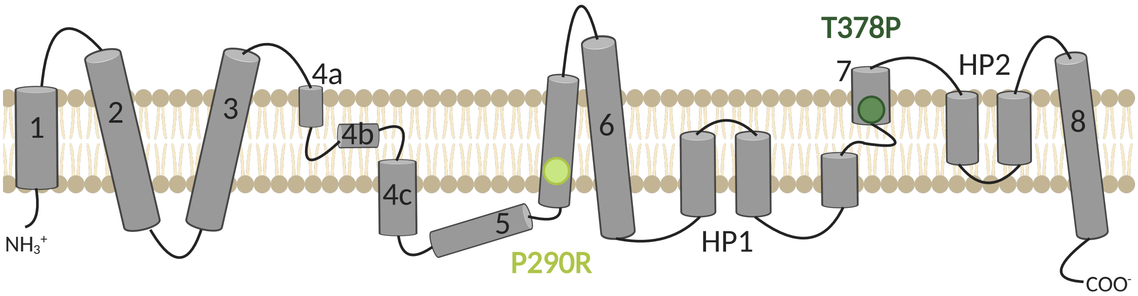

Figure 6. Scheme of the glutamate transporter and anion/Cl$^-$ channel EAAT1. EAAT1 comprises eight transmembrane domains (TM1-8) and two hairpin loops (HP1-2). EAAT1 usually assembles as trimer. The variant p.Pro290Arg (P290R, light green dot) is located in TM5 and was identified in a patient with HM, ataxia and epilepsy[96]. In contrast, the p.Thr387Pro (T387P, dark green dot) variant causing pure HM is located in TM7[98].

However, EAAT1 also contains an anion-selective conduction pathway, mainly functioning as a Cl$^-$ channel[154]. Both the glutamate transport rates as well as the anion currents depend on the specific EAAT isoform[155]. Whereas the outward- and inward-facing conformations are assumed to be non-conductive for anions/Cl$^-$, it was demonstrated that the anion-permeable pore is formed by a lateral movement of the transport domain from an intermediate conformational state, which is gated by two hydrophobic gates[93, 95]. As *SLC1A3* variants can exert effects on both functions, the pathophysiological mechanisms underlying the respective EAAT1-associated disorders appears to be more complex in nature.

This complexity also applies to the first case report by Jen and colleagues describing the severe phenotype of a ten-year old boy with EA, HM attacks and epileptic seizures[96]. The pathogenic variant p.Pro290Arg (P290R), which is localised in TM5, was identified to cause the overlapping syndrome (**Figure 6**)[96]. Although most *SLC1A3* variants are associated with EA6, one pure HM phenotype caused by the variant p.Thr387Pro (T387P) has recently been described supporting the role of *SLC1A3* in HM genetics and pathophysiology[98]. Comprehensive analyses of the functional effects of T387P demonstrated diminished glutamate removal and reduced EAAT1 surface expression, since K$^+$ binding to the inward facing transporter was abolished by the variant, which is consistent with a LOF EAAT1 effect[98]. Functional characterisation of the missense mutation P290R using HEK293T cells revealed decreased surface expression and reduced glutamate transport rates but increased EAAT1-associated anion/Cl$^-$ currents[100]. Therefore, the P290R variant simultaneously exerts a GOF and LOF effect on EAAT1[100].

Using the *Slc1a3*$^{P290R/wt}$ knock-in mouse model that closely resembles the human phenotype, a recent study investigated the cerebellar region to understand how the P290R variant causes ataxia[156]. On the one hand, heterozygous *Slc1a3*$^{P290R/wt}$ animals suffered from spontaneous seizures, peaking from P35 to P55[156]. On the other hand, the model exhibited distinct ataxic features, which were verified using the ledge and rotarod test[156]. Apoptosis of Bergmann glia cells was shown to be triggered by glutamate-activated Cl^- efflux during development, resulting in a reduction of cerebellar glutamate removal, impaired generation of cellular networks and consequently, cerebellar degeneration and ataxia[156].

To clarify the underlying mechanisms for the P290R-associated epilepsy, the collaborating lab of Prof. Christoph Fahlke focused on the hippocampal region of the *Slc1a3*$^{P290R/wt}$ knock-in model based on the high EAAT1 expression in radial glia-like cells (RGLs) of the dentate gyrus (DG) and the decisive role of the hippocampus in the context of epilepsies (unpublished data). It was discovered by Fahlke and colleagues that the tonic GABAergic inhibition of DG granule cells was decreased in heterozygous animals, while the phasic synaptic transmission mostly remained unchanged (unpublished data). Additionally, reduced internal Cl^- concentration ($[Cl^-]_i$) levels were observed in RGLs presumably related to an enhanced Cl^- efflux, which is caused by the P290R GOF effect on EAAT1 anion currents (unpublished data by Fahlke and colleagues). Simultaneously, a GABA transporter 3 (GAT-3) upregulation in the RGL population was discovered, which was hypothesised to evoke an increased GABA uptake, as the GAT-3 transport mechanism relies on transmembrane Na^+ and Cl^- gradients (unpublished data by Fahlke and colleagues). It was further speculated that the observed decreased tonic inhibition may be caused by the concomitant reduction in ambient GABA levels presumably resulting in hippocampal hyperexcitability and seizures both in mice and humans (**Figure 7**) (unpublished data by Fahlke and colleagues).

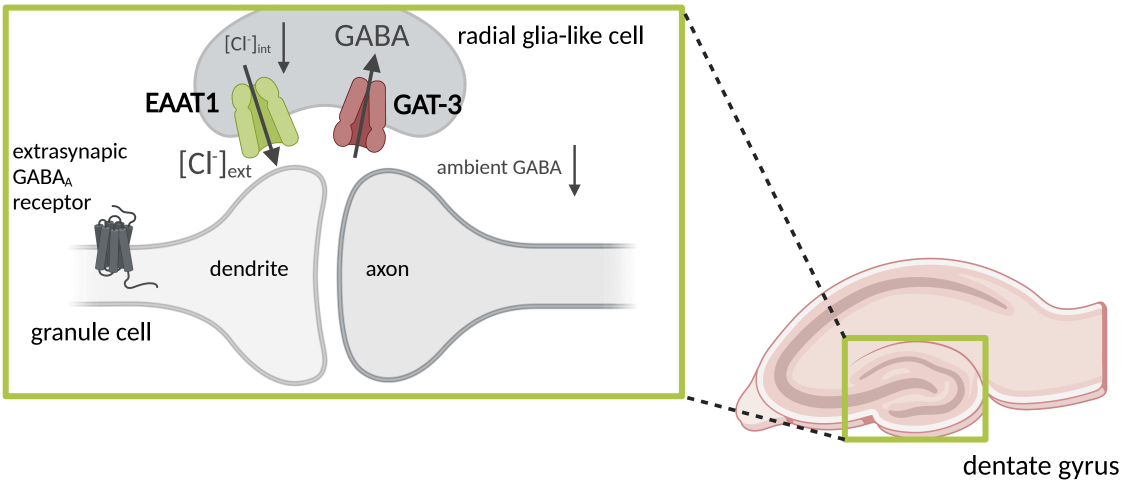

Figure 7. Representative scheme of the anticipated pathophysiological cascade of P290R-associated epilepsy (unpublished data by Fahlke and colleagues). Measurements of $[Cl^-]_i$ in the DG RGLs revealed lower internal Cl^- levels, presumably caused by P290R-associated increased Cl^- efflux (unpublished data by Fahlke and colleagues). Altered Cl^- (and Na^+) transmembrane gradients determine the driving force for extracellular GABA removal via GAT-3. A marked GAT-3 upregulation combined with an increased driving force for GABA uptake into RGLs may decrease ambient GABA levels, which decisively regulate tonic inhibition via extrasynaptic $GABA_A$-receptors (unpublished data by Fahlke and colleagues). This was confirmed by reduced tonic current amplitudes recorded from DG granule cells of *Slc1a3*$^{P290R/wt}$ animals (unpublished data by Fahlke and colleagues).

1.8 Research gap

Although CSD as correlate for migraine aura was first discovered 80 years ago, the exact initiating factors and underlying pathophysiological mechanisms have not been unravelled to date. A vast number of studies investigating distinct aspects that are involved in CSD have decisively contributed to our current understanding, however, several crucial elements with respect to the processes of CSD initiation and propagation or its relevance regarding migraine pathology in patients remain to be fully elucidated.

To start with, the more fundamental question if CSDs are mandatorily involved in the context of migraine with/without aura and initiate the pain pathway to evoke headache remains unanswered until now. Despite plenty of evidence supporting the theory that CSD is at the beginning of the pathophysiological cascade of each migraine attack, migraine with/without aura and HM may still represent different disease entities with distinct involved mechanisms. As the content of this thesis entirely focussed on HM, these questions were not touched upon.

Although transgenic animal models for FHM have significantly contributed to the field, studies exploring FHM1 and FHM2 pathophysiology have increasingly drawn the attention to the excitatory neurotransmitter glutamate as key component that elicits the CSD cascade[27, 37, 48, 53, 55]. On the contrary, K^+ has been implicated in initiating CSDs multiple times. Nevertheless, the specific role of K^+ as CSD triggering factor in the context of (F)HM pathophysiology has never been explored in detail so far. Moreover, experimental studies that directly compare different transgenic animal models for HM particularly regarding the key triggering factors and the role of K^+ in CSD initiation have never been performed to date. The direct comparison of distinct models may yield valuable elements that help to disentangle the phenomenon of CSD in HM.

The underlying causes for increased CSD susceptibility in *CACNA1A*- and *ATP1A2*-associated HM were already demonstrated using transgenic mouse models[1, 27, 37]. In contrast, the involved mechanisms in FHM3 have not been clarified until now. Of note, a major contribution of K^+ in triggering CSD was specifically proposed in the context of *SCN1A* GOF variants[79]. As already outlined in section 1.6, using the *Scn1a*$^{L1649Q/wt}$ knock-in model an increased persistent Na^+ current and AP frequency in GABAergic interneurons of heterozygous FHM3 animals as well as a higher susceptibility to CSDs *in vivo* have been demonstrated[1]. However, the underlying pathophysiological mechanisms connecting hyperexcitability of inhibitory neurons on the single cell level with an increased CSD susceptibility *in vivo* remained to be elucidated. Interestingly, in FHM3, the properties of GABAergic interneurons are altered[1], which clearly contrasts the affected cell populations in FHM1 and FHM2 and for the first time, suggests a pivotal role of inhibitory neurons in CSD and HM pathophysiology.

Additionally, exact knowledge about which ion channels, transporters and pumps contribute to CSD initiation and propagation is still lacking as previously performed studies frequently yielded controversial results[30, 34, 35, 36, 42, 43, 44, 45, 46]. The voltage-gated Na^+ channel $Na_V1.1$ as well as the glutamate transporter and anion channel EAAT1 are only two examples of a vast group of

channels, transporters and pumps that have not been investigated with respect to their specific contribution in the context of CSD.
However, the lack of profound understanding has hampered the development of novel pharmacological therapeutic options, especially for patients suffering from the severe HM subtype who do not benefit from calcitonin gene related peptide (CGRP)-related treatment. The neuropeptide CGRP, which is found in perivascular trigeminal sensory nerve endings[134, 157], is known to elicit the vasodilation during migraine attacks and is released upon stimulation of the trigeminal ganglion[158]. The discovery of CGRP (receptor) antagonists led to a breakthrough in migraine therapy more than a decade ago. In contrast to migraine patients with and without aura, CGRP did not elicit migraine attacks or aura symptoms in HM patients, which points towards distinct underlying disease mechanisms[159]. Therefore, there is a compelling need for additional therapeutic agents to treat the rarer, but also more severe and debilitating heterogeneous disorders of HM. However, the range of pharmacological treatment interfering with elements of the CSD cascade or directly targeting CSD initiation is extremely small. Thus, the identification of ion channels, transporters, and pumps as well as involved ions, neurotransmitters and other substances that affect CSD initiation or propagation are urgently required so that targeted therapeutic options can be developed in the future.

As the mutational spectrum in HM is relatively small, only three different transgenic mouse models, based on the underlying mutated gene, are currently available to study CSD and HM pathophysiology. This emphasises the need for establishing novel animal models with distinct underlying genetic causes to receive a more extensive insight and presumably cover new aspects. For instance, a novel mouse model harbouring an *Scn1a* GOF variant leading to severe epilepsy would enable to study the tight association between $Na_V1.1$-related HM and epilepsy in a different context[109]. The generation of an *Slc1a2* knock-in mouse model would enable to gain a more comprehensive knowledge on EAAT pathophysiology with respect to epilepsy and to further study the role of altered glutamate transport as well as Cl^- currents in seizure generation. Although a new major HM gene has not been established so far, the significance of many candidate/risk genes in the context of CSD and HM has not been investigated in further detail, especially by using transgenic animal models. *SLC1A3* is of particular interest among these identified genes, since it does not only represent an appropriate candidate to explore the glutamate-centred hypothesis for CSD initiation, but also allows to study alterations in Cl^- homeostasis and their involvement in CSD. Besides, due to the predominating astrocytic expression of EAAT1, the *SLC1A3* gene offers the opportunity to examine the widely debated significance of astrocytes in CSD initiation and propagation.

Additionally, studies that explore the occurrence of additional phenotypes in HM animal models and the pathophysiology of overlapping syndromes are rarely found, especially with respect to migraine, epilepsy, and ataxia. Nevertheless, the frequent presence of additional phenotypes in HM has been explicitly noticed in literature. Due to the marked similarities of CSD and epileptiform activity, which both represent pathological states of hyperexcitability, it is particularly intriguing to study the co-occurrence of both phenomena within one animal model. Variants in the *SLC1A3* gene can also cause epilepsy, however, the underlying mechanisms have not been clearly elucidated until now. Interestingly, variants in the *SCN1A* gene are simultaneously implicated in genetic epilepsy syndromes as well as FHM3.

1.9 Objectives

The main research question of this work referred to the significance of K^+ in CSD initiation and propagation with respect to HM pathophysiology. The objective was to clarify if alterations in K^+ levels are equally entitled to be considered a key factor in eliciting SD and migraine attacks compared to the excitatory neurotransmitter glutamate, thereby focusing on FHM3 and *SLC1A3*-associated overlapping syndrome. The second major question concerned additional HM phenotypes, especially the study of the co-occurrence of epileptiform activity. For answering both research questions two different novel mouse models for HM were studied.

In the first part of this thesis, the goal was to investigate the key role of K^+ in triggering CSDs in the *Scn1a*$^{L1649Q/wt}$ knock-in mouse model to establish a mechanistic link between interneuron hyperexcitability and a higher susceptibility to CSDs[1]. Additionally, a novel pharmacological treatment option for FHM3 patients specifically targeting persistent Na^+ currents should be tested[1]. In the second part of the thesis, the goal was to investigate if the *Slc1a3*$^{P290R/wt}$ knock-in model for EA6 was characterised by an increased CSD susceptibility and altered CSD characteristics, including potential changes in K^+ homeostasis and the assessment of K^+ as initiating factor. Finally, the findings of the *Scn1a*$^{L1649Q/wt}$ and the *Slc1a3*$^{P290R/wt}$ animal model for HM should be compared with respect to the identified ionic changes.

An additional goal was to identify anticipated changes in the cortical E/I balance on the single cell level of *Slc1a3*$^{P290R/wt}$ animals to comprehend the underlying pathomechanisms causing neuronal hyperexcitability and CSD generation.

The final goal was to study frequent HM phenotypes, specifically the co-occurrence of epilepsy in the *Slc1a3*$^{P290R/wt}$ model, and to identify the severity, the frequency and the duration of the seizures and status epileptici. Additionally, brain regions that are crucial for seizure origin and generation should be determined.

2 Methods

2.1 Study approval and ethics

The local animal care and use committee (Regierungspräsidium Tübingen, Germany) approved each animal experiment. For all *in vivo* and *in vitro* procedures, the 3R-principles (replace, reduce, refine) as fundamental ethical guidelines in animal research were followed.

2.2 Animals

The *Scn1a*$^{L1649Q/wt}$ knock-in mouse line was generated by Taconic Artemis (Köln, Germany)[1]. Generation of the *Slc1a3*$^{P290R/wt}$ knock-in mouse line was performed by Taconic Biosciences (Ejby, Denmark). *Scn1a*$^{L1649Q/wt}$ knock-in animals on a C57BL/6N genetic background, *Slc1a3*$^{P290R/wt}$ knock-in animals on a 129Sv/Tac genetic background and the respective wildtype control animals were maintained in a temperature- and humidity-controlled environment at the Core Facility Transgene Tiere (Tübingen, Germany). All animals were housed and bred under a 12-hour dark-light cycle and received water and food ad libitum. *In vitro* experiments were performed during the light period. Both sexes were used for the *in vitro* part of the studies since the animals were sacrificed before obtaining sexual maturity. In contrast, only male animals were used for *in vivo* EEG recordings and subsequent immunohistochemistry. Female animals were excluded from the *in vivo* part of the experiments, since their epileptic phenotype may be affected by fluctuating hormonal changes that depend on the phases of the female cycle. Breeding for both mouse lines was performed using one wildtype and one heterozygous animal, whereby the heterozygous mouse was chosen regardless of the gender. For the *Scn1a* L1649Q line the median litter size numbered seven animals, whereas for the *Slc1a3* P290R line the median litter size was 4.8 pups. Breeding was carefully planned to meet the demand for experimental animals and reduce the number of surplus mice. Health status of wildtype and heterozygous *Scn1a*$^{L1649Q/wt}$ and *Slc1a3*$^{P290R/wt}$ animals was continuously monitored to assess stress levels and identify severe conditions that fulfilled the human endpoint criteria (**Appendix A**). Additionally, heterozygous animals of both lines as well as their wildtype littermates were evaluated around the time of birth, usually at P3, and after weaning at P21 (**Appendix B, C**). Diseased animals were presented to a veterinarian. In case of an unexpected illness, which did not match the mouse line's phenotype, animals were excluded from any experimental procedures.

2.3 Genotyping

Genotyping of the *Scn1a* L1649Q and the *Slc1a3* P290R offspring was performed using standard polymerase chain reaction (PCR) techniques. For animals, that had been used for *in vitro* experiments, deoxyribonucleic acid (DNA) was acquired from post-mortem tail biopsies. Animals that were used for *in vivo* experiments or breeding were earmarked, whereby the DNA was acquired from earmark tissue. Earmarks were only taken from animals with a minimum age of P21. The specialised instruments used for this purpose were thoroughly disinfected before and after usage. After the biopsy, the mice were examined to check for bleeding complications. The tissue from the earmarks and tails were stored in Eppendorf tubes at -20°C until further usage. For

DNA extraction from earmarks of wildtype and heterozygous *Scn1a*$^{\text{L1649Q/wt}}$ animals and from tail biopsies of both mouse lines the tissue was incubated overnight in 500 µl lysis buffer and 10 µl Proteinase K (Meridian Bioscience Inc., Memphis, USA) at 56°C. The lysis buffer contained the following (in mM): 50 Tris-HCl (pH 7.5) (AppliChem GmbH, Darmstadt, Germany), 50 EDTA (pH 8.0) (AppliChem GmbH), 100 NaCl (VWR International GmbH, Darmstadt, Germany), 5 DTT (AppliChem GmbH), 0.5 Spermidin (Salmon Sperm DNA, 10mg/dl, Invitrogen/Thermo Fisher Scientific Inc., Waltham, USA), 347 SDS (Carl Roth GmbH + Co. KG, Karlsruhe, Germany). Next, the lysate was centrifuged at a speed of 12000 rpm for five minutes and the supernatant was transferred to a different Eppendorf tube. The rest of the lysate was stored at 4°C until the end of the procedure in case of genotyping failures. After adding 350 µl of 100 % isopropanol to the lysate and precipitating the DNA by gently shaking the tube, another centrifuging step at the same speed for 15 min took place. The supernatant was discarded, leaving the DNA pellet, and a washing step with 350 µl of 70 % ethanol followed by centrifuging the tubes again at 12000 rpm for 5 min. Subsequently, the supernatant was discarded, and the remaining DNA fragments were dried at room temperature for 45 min to one hour. As a last step of DNA extraction, the dried DNA fragments were diluted with Ampuwa water.

For DNA extraction from earmark tissue of wildtype and *Slc1a3*$^{\text{P290R/wt}}$ animals the MyTaq Extract-PCR Kit (Meridian Bioscience Inc.) was used. The tissue was incubated in 70 µl Ampuwa water, 20 µl buffer A and 10 µl buffer B with a duration of 15 min for each included temperature step, first at 75°C and then at 95°C. After centrifuging at maximum speed, 90 µl of the supernatant were carefully removed with a pipette and diluted with Ampuwa water at a 1:40 ratio.

For both procedures of DNA extraction, the DNA concentration was quantified using a NanoDrop ND-1000 UV-Vis spectrophotometer (Thermo Fisher Scientific Inc., Waltham, USA). If the concentration was > 300 ng/µl for the tail tissue and > 600 ng/µl for the earmark tissue, the amount of Ampuwa water needed to obtain the desired concentration was firstly calculated and then added to the diluted DNA.

For PCR amplification, 2 µl of the diluted DNA were added to a previously prepared master mix comprising 8.5 µl Ampuwa water, 1 µl of the first, 1 µl of the second primer and 12.5 µl MyTaq Red Mix (Meridian Bioscience Inc.), which included MyTaq DNA Polymerase and a buffer system with a red dye (**Table 1**). The included red dye served for visualising the results of the subsequently performed gel electrophoresis.

Table 1. Composition for polymerase chain reaction amplification.

Reagant	**Amount**
Primer A	1 µl
Primer B	1 µl
Mouse DNA	2 µl
MyTaq Red Mix	12.5 µl
Water	8.5 µl
Total	25 µl

Before performing PCR, each Eppendorf tube was shortly placed in a benchtop centrifuge to guarantee proper dissolution. PCR was performed using a Biometra T3 Thermocycler machine (Biometra biomedizinische Analytik GmbH, Göttingen, Germany) or a TurboCycler machine (TurboCycler 2 Thermal Cycler, Blue-Ray Biotech Corp., Taiwan). In **Table 2** the PCR protocol for the L1649Q knock-in mouse line is shown, whereas the PCR protocol for the P290R knock-in mouse line is visualised in **Table 3**.

Table 2. PCR protocol to perform genotyping of *Scn1a*$^{L1649Q/wt}$ and *Scn1a*$^{wt/wt}$ transgenic animals.

Protocol L1649Q		
Initial denaturation:	95°C	5 min
35 cycles:		
Denaturation:	95°C	0.50 min
Annealing:	60°C	0.50 min
Extension:	72°C	0.75 min
Final Extension:	72°C	10 min
Soak:	4°C	∞

Table 3. PCR protocol to perform genotyping of *Slc1a3*$^{P290R/wt}$ and *Slc1a3*$^{wt/wt}$ transgenic animals.

Protocol P290R		
Initial denaturation:	95°C	5 min
40 cycles:		
Denaturation:	95°C	0.50 min
Annealing:	57°C	0.50 min
Extension:	72°C	1 min
Final Extension:	72°C	5 min
Soak:	4°C	∞

After PCR, the samples were either stored at 4°C until further usage or directly applied onto an agarose electrophoresis gel to analyse the size of the DNA fragments. For the L1649Q knock-in mouse line, a 1.5 % agarose gel and for the P290R knock-in mouse line, a 1.0 % agarose gel were used respectively. The corresponding quantity of agarose basic (AppliChem GmbH) was dissolved in TBE-puffer (A348, AppliChem GmbH) and heated up in a conventional microwave for several minutes until complete dissolution could be visually confirmed. After a short cooling step, 7 µl of RedSafe nucleic acid staining solution (iNtRON Biotechnology, Jungwon-gu, Seongnam, Gyeonggi-do, Korea) were supplemented per 100 ml of the initially vicious agarose gel to later identify the nucleic acids. Subsequently, the vicious agarose gel was poured into an electrophoresis chamber. Gel hardening was usually achieved after 30 min. Before loading the small gel pockets with 10 µl of the samples, the entire chamber was flooded using TBE-buffer. A voltage of 120 V was used during electrophoresis leading to total duration of around 1.5 hours.
For genotyping *Scn1a* L1649Q offspring, the following primers purchased from Integrated DNA Technologies, BVBA (Leuven, Belgium) and Thermo Fisher Scientific Inc. were used: 5'- TAGTGTGCAAGCTTGAGAACG-3' and 5'-TCAGCTCCTTCAGTCCTTGC-3'[1]. Visualisation of the electrophoresis gel (1.5 % argarose) resulted in one fragment at 197 bp for wildtype DNA and two fragments at 197 bp and 298 bp for heterozygous DNA (**Figure 8 A**)[1].
Deletion of the neomycin cassette, which had been introducing the P290R knock-in, was used as a marker for genotyping *Slc1a3* P290R offspring and resulted in the following primers (Metabion International AG, Planegg, Germany): 5'-AAGAGGATCCCCAGGCGCGCATAC-3' and 5'-CAGGCTGTGGCATGGACAAC-3'[156]. Visualisation of the electrophoresis gel (1.0 % agarose) under

UV light gave rise to a single band at 478 bp for wildtype DNA and two bands at 478 bp and 739 bp for heterozygous DNA (**Figure 8 B**).

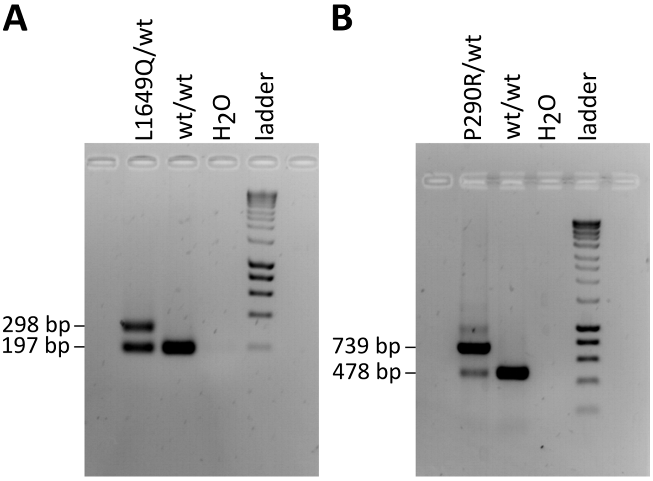

Figure 8. **Genotyping of the L1649Q and P290R mouse lines**. (**A**) Representative example of a gel electrophoresis result of one *Scn1a*$^{\mathrm{L1649Q/wt}}$ knock-in animal (left), one *Scn1a*$^{\mathrm{wt/wt}}$ animal (second left), a water containing control (second right) and a HyperLadder 1 kB with 100 lanes (Meridian Bioscience Inc.) (right)[1]. (**B**) Representative example of a gel electrophoresis result of one *Slc1a3*$^{\mathrm{P290R/wt}}$ knock-in animal (left), one *Slc1a3*$^{\mathrm{wt/wt}}$ animal (second left), a water containing control (second right) and a HyperLadder 1 kB with 100 lanes (Meridian Bioscience Inc.) (right).

2.4 Preparation of acute brain slices

For *in vitro* electrophysiology, P15-20 animals of both lines were sacrificed under isoflurane anaesthesia. For induction of anaesthesia, animals were maintained in their home cages, which had been transferred from the animal facility to the laboratory area. An isoflurane vaporiser (Eickemeyer IsoFlo) was used to apply 5 volume % isoflurane (CP-Pharma) with a flow of 1 l/min. During induction of anaesthesia, the mice were continuously monitored in terms of spontaneous movements, respiratory rate, and absence/presence of specific reflexes. After having reached the state of surgical anaesthesia, which was confirmed by a negative righting and toe pinch reflex, the mice were translocated from their home cage to a bench for slice preparation and promptly decapitated using scissors. Removal of the brains was performed in ice-cold cutting artificial cerebrospinal fluid (aCSF).

To prepare the cutting aCSF for *in vitro* CSD recordings, the following composition (in mM) was used: 125 NaCl (VWR International GmbH), 25 $NaHCO_3$ (Carl Roth GmbH + Co. KG), 2.5 KCl (AppliChem GmbH), 7 $MgCl_2$ (AppliChem GmbH), 2 $CaCl_2$ (Sigma-Aldrich/Merck, St. Louis, USA), 1.25 NaH_2PO_4 (Sigma-Aldrich/Merck, St. Louis, USA), 10 D(+)-glucose (Carl Roth GmbH + Co. KG) (pH 7.4, equilibrated with 95 % O_2/5 % CO_2)[1, 76]. For preparation of the cutting aCSF for *in vitro* patch-clamp recordings, a different composition (in mM) was utilised: 125 NaCl, 26 $NaHCO_3$, 2.5 KCl, 5 $MgCl_2$, 0.5 $CaCl_2$, 1.25 NaH_2PO_4, 20 Glucose (pH 7.4, osmolarity 305 mOsm/kg, equilibrated with 95 % O_2/5 % CO_2). For preparing both the cutting and the recording solutions, a Kern ABJ analytical balance (Ascuro AG, Reinach, Switzerland) was used. An osmometer (Löser Messtechnik, Berlin, Germany) and a pH meter (Mettler-Toledo GmbH, Gießen, Germany) served to check and adjust the osmolarity and the pH of a solution.

First, the skin of the animal was reversed to expose the skull, which was followed by a straight, careful cut along the midline with a scalpel. As a next step, a small forceps was used to lift the skull of each hemisphere and subsequently fold the bony parts to the sides without damaging the brain. The olfactory bulbs were carefully severed with a scalpel. A small spatula was gently moved between the inferior part of the brain and the skull so that the brain could be lifted to put it into a different dish filled with ice-cold cutting aCSF. If the cranial nerves were still intact, they were disconnected immediately. The most posterior part of the brain was usually cut off to create an even surface. Mounting of the brain was performed with a spatula. First, the brain surface that was subsequently used for gluing the brain onto a circular magnet was dried with a tissue. The brain was positioned next to a 4 % agarose cuboid to ensure additional stabilisation on the magnet. By dropping aCSF onto the brain, hardening of the glue was ensured. Finally, the circular magnet was connected to the bottom of the bathing chamber of a Microm HM 650V vibratome (Thermo Fisher Scientific Inc.). The bathing chamber was filled with cutting aCSF, whereby the recipe depended on the planned experiment, as mentioned before.

Coronal slices with a thickness of 350 µm were obtained with the beforementioned vibratome using a frequency of 90 Hz, an amplitude of 0.9 mm and a velocity of 7 mm/s. After cutting, the acute slices were stored for one hour at a temperature of 36.0°C to allow recovery from the slicing procedure. For storage, the brain slices were carefully positioned on a thin nylon net allowing aCSF exposure from the upper and lower side of the slice and avoiding any overlap with nearby slices. The extracellular solution for the storage of slices and the subsequent CSD recordings contained the following modified composition in (mM): 124 NaCl, 26 $NaHCO_3$, 3.5 KCl, 1 $MgCl_2$, 2 $CaCl_2$, 1.2 NaH_2PO_4, 20 Glucose (pH 7.4, osmolarity 305 mOsm/kg, equilibrated with 95 % O_2/5 % CO_2)[1, 160]. The extracellular solution for the storage of slices and the subsequent patch clamp recordings contained the following composition (in mM): 125 NaCl, 26 $NaHCO_3$, 2.5 KCl, 1 $MgCl_2$, 1.25 NaH_2PO_4, 2 $CaCl_2$, 25 Glucose (pH 7.4, osmolarity 305 mOsm/kg, equilibrated with 95 % O_2/5 % CO_2). After the recovery period, the slices were kept at room temperature. All *in vitro* experiments were completed within seven hours after brain removal.

2.5 Recording of CSD *in vitro*

As described previously, K^+-sensitive microelectrodes were built out of borosilicate glass micropipettes that did not comprise a filament inside (GB150-10, 0.86 x 1.50 x 100 mm, Science Products, Hofheim, Germany)[160]. The glass capillaries were washed overnight in a tube filled with 1 M hydrochloric acid (HCl) (AppliChem GmbH) that was put on a shaker[160]. After rinsing them with 70 % ethanol, the capillaries were dried at a temperature of 120°C and for the duration of seven to eight hours[160]. Subsequently, the washed capillaries were exclusively handled with gloves to avoid any contamination. For storage up to four weeks, they were deposited in a box containing anhydrous Ca^{2+} sulphate desiccant (W. A. Hammond DRIERITE Co. LTD, USA)[160].

After pulling the micropipettes with a Flaming/Brown Micropipette Puller (Model P-97, Sutter Instrument, Novato, USA), they were taped onto a conventional cover slip (Menzel GmbH + Co KG, Braunschweig, Germany) with the fine tips being slightly elevated from the bottom of a glass container[160]. Next, a nitrogen-filled balloon that was connected to a 1 ml syringe (Becton, Dickinson and Company (BD), Eysins, Switzerland) and 20 G needle (Sterican Gr. 1, G 20 x 1.5"/ ø 0,9 x 40 mm, B. Braun SE, Melsungen, Germany) was used to create the correct atmosphere to remove 1-2 ml of silanisation solution I (≈ 5 %, dimethyldichlorosilane in heptane, Sigma-Aldrich/Merck) from a container using a second syringe connected to a 20 G needle[160]. On each electrode tip, at least two droplets of silanisation solution were applied[160]. The electrodes were dried in an oven (HERAEUS oven, Thermo Fisher Scientific Inc.) at 220°C for 30 min[1, 160]. After that, the electrodes were either used directly in an experiment or stored in a container with Ca^{2+} sulphate desiccant for a maximum of one week.

Prior to the experimental use, the silanised electrodes were filled with an intracellular solution containing 300 mM NaCl buffered with 10 mM HEPES (AppliChem GmbH) (pH 7.4) by strictly avoiding any air bubbles[160]. The electrode tips were manually broken using a surgical blade and a small droplet (≈ 0.1 µl) of K^+ ionophore I-cocktail B (Sigma-Aldrich/Merck) was directly absorbed into the electrodes when applying it near the tip[160]. The microelectrodes were filled to 1-2 mm with the ionophore cocktail[160]. For magnification, the entire procedure was performed using a binocular.

Five different aCSF compositions containing different KCl concentrations (in mM: 0.1, 1, 3.5, 10, 100, pH 7.4, equilibrated with 95 % O_2/5 % CO_2) were used to calibrate each electrode[1, 160]. Each calibration solution was equal in osmolarity as NaCl quantity was adjusted according to the KCl quantity that was added[160]. The electrode tip was immersed into the bath, which was perfused at a rate of 6.5 ml/min and contained an Ag/AgCl ground electrode. To define a baseline, each calibration procedure started with aCSF comprising 3.5 mM K^{+1}, in which the electrode was provided several minutes to adjust before the aCSF solutions with different KCl concentrations were applied. Calibration solutions were applied stepwise to record the potential changes in mV starting with the lowest KCl concentration[160]. The calibration solution was changed to a higher concentration after the potential value had reached a stable plateau. Only electrodes with a slope between 52 and 58 mV per log change in $[K^+]$ were considered reliable for experimental use (**Figure 9**)[1, 160]. The aCSF comprising 3.5 mM K^+ was not used during the calibration procedure, but in a final step, for excluding those electrodes that were characterised by significant deviations compared to the baseline potential.

During experiments, each K^+-sensitive microelectrode was closely monitored for showing stable potential values and to immediately identify the sudden occurrence of air bubbles interfering with correct measurements. Instable potential values and the occurrence of air bubbles led rejecting the microelectrode in use. CSD recordings of slices from heterozygous *Scn1a*$^{L1649Q/wt}$ versus wildtype animals were followed by a re-calibration of the microelectrode after each recording[1]. This procedure was complied with to check that the self-made electrodes did not deviate more than 10 % from the original slope, which confirmed their reliability[1].

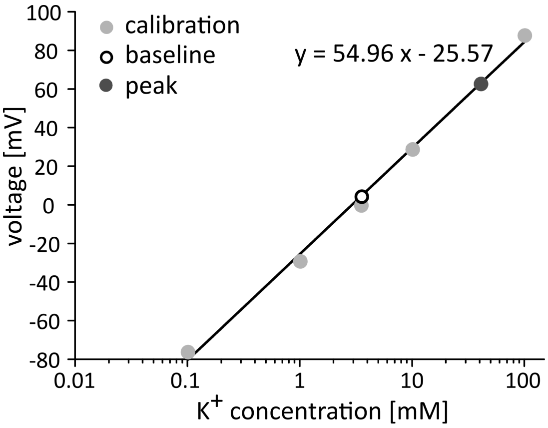

Figure 9. Representative calibration curve of a K$^+$-sensitive electrode (adapted from Auffenberg et al., 2021)[1]. The calibration curve has an acceptable slope of 54.96 (52-58 mV per log change in [K$^+$])[1]. The voltage/concentration values for the different $[K^+]_e$ aCSFs (light grey dots), the baseline value (white dot) and the recorded maximum value of a $[K^+]_e$ rise during a CSD (dark grey dot) are shown[1].

For CSD recordings, each brain slice was carefully placed onto the surface of a 256MEA chip (Multi Channel Systems MCS GmbH, Reutlingen, Germany), which was utilised as a submerged recording chamber. The chip was inserted into a MEA2100-256-headstage (Multi Channel Systems MCS GmbH) connected to an Interface Board (MCS-IFB 3.0 Multiboot, Multi Channel Systems MCS GmbH) and a computer. With respect to the CSD recordings, the MEA system was primarily used to better visualise and observe the propagation of the CSD via multi-unit activity during recordings. The MEA-headstage was placed in the centre of a platform belonging to a Sensapex uM workstation (Sensapex, Oulu, Finland) equipped with a Sensapex uMs microscope. To visualise the slices and position the electrodes, an Olympus UPlanFLN 4x objective was used. A self-made harp ensured that floating of the slice was permanently absent, particularly by positioning one harp string onto the cortical surface. During experiments, slices were perfused at a rate of 6.5 ml/min using a Peristaltic Perfusion System (PPS2, Multi Channel Systems MCS GmbH) and with recording aCSF containing a slightly elevated concentration of 3.5 mM KCl compared to the cutting aCSF, which has already been described before[1]. For each recording, the inflow and outflow were each placed at the same position inside the recording chamber to avoid confounding by alternating the supply and removal of substances, in particular K$^+$. Slices were kept at a constant temperature of 34°C using a perfusion cannula with a heating element and a sensor (PH01, Multi Channel Systems MCS GmbH) in combination with an internal heating element and a PT100 sensor belonging to the MEA headstage, that were both connected to a temperature controller (TC02, Multi Channel Systems MCS GmbH).

To elicit a CSD, a glass pipette (0.2 - 0.5 MΩ) containing a concentration of 200 mM KCl was placed onto the surface of cortical layer 2/3 of the motor or somatosensory cortex[1, 29, 161]. A single KCl injection with a duration of 400 ms was applied using a PDES-02DX pneumatic drug ejection system (npi electronic GmbH, Tamm, Germany), which ejected pulses at a pressure of 7 psi[1, 48, 162]. To visualise the injected volume and estimate its spread the puff solution was supplemented with 0.1 % Fast Green FCF (Sigma-Aldrich/Merck)[1, 162].

To record an elicited CSD, a K$^+$-sensitive microelectrode was placed onto the surface of cortical layer 2/3 with a distance of at least 800 µm to the beforementioned puff electrode[1, 48, 52, 162]. An extracellular local field potential (LFP) pipette having less than 100 µm to the K^+-sensitive electrode confirmed the presence or absence of a CSD[1]. The DC potential electrodes (≈ 0.5 MΩ) were built out of borosilicate glass micropipettes (Science Products) that were pulled using the beforementioned Flaming/Brown Micropipette Puller (Model P-97, Sutter Instrument, Novato, USA)[1]. Subsequently, the DC potential electrodes were filled with recording aCSF[1]. The tip of each DC potential electrode was manually broken using a surgical blade and a binocular for magnification. For grounding the DC and the K^+-sensitive electrodes, Ag/AgCl electrodes were put into the bath. Both the microelectrode as well as the DC electrode were tightly connected to Sensapex uMp micromanipulators to guarantee controlled movements with a rotary wheel controller and a touch screen unit (Sensapex). The electrophysiological traces were recorded with an EPC 10 USB Quadro System (HEKA Instruments Inc., Holliston, USA) and the Patchmaster next software (HEKA Instruments Inc.). Each CSD recording consisted of a 10 s-lasting baseline recording of the DC and K^+ trace, which was directly followed by a 400 ms-lasting TTL pulse transmitted by the Patchmaster next software. The TTL pulse triggered the pneumatic drug ejection system to elicit the K^+ puff, the Ocular Image Acquisition Software to start the CCD camera for IOS (intrinsic optical signal) recording and the acquisition of a series of three 100 s-lasting sweeps to record the DC and K^+ trace. Consequently, the DC and K^+ traces of each CSD recording had a total duration of 300 s. A sampling rate of 20 kHz was used. As the selection of a filter application was required by the software, a 10 kHz Bessel filter was chosen.

Each slice was only used once for the initiation and recording of a SD[1], since CSDs are followed by a long-lasting suppression of neuronal activity. After CSD induction, the slices usually require long recovering periods until they can be used for recurrent CSD inductions and recordings.

A CSD was determined as "local" CSD if the IOS signal exclusively occurred locally at the injection site and did not start to migrate (**Figure 10 A**)[1]. A CSD was defined as an "aborted" CSD if the IOS signal travelled less than 800 µm distance from the injection site (**Figure 10 B**). Aborted and local CSDs were both categorised as "failed" CSDs[1].

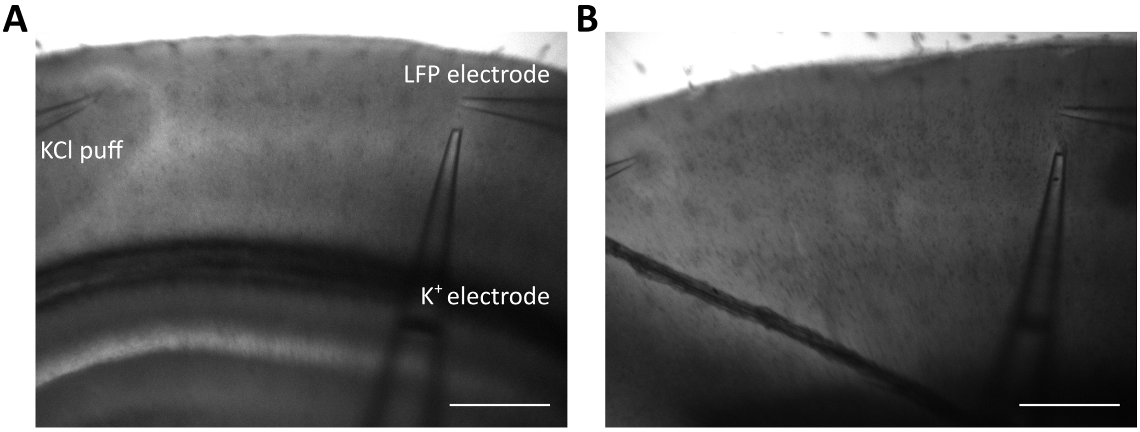

Figure 10. Failed CSD. (**A**) Representative example of an aborted CSD with a migration distance < 800 µm from the injection site. A KCl injection onto cortical layer 2/3 was used to elicit CSDs that were recorded by an LFP and K^+-sensitive electrode[1]. Scale bar: 500 µm. (**B**) Representative example of a local CSD recognisable by the white IOS ring around the puff pipette and the lack of any signs for migration[1]. Scale bar: 500 µm.

Additionally, a CCD camera (Retiga Electro, Teledyne Photometrics, Tucson, USA) was used to capture the IOS. Using an Ocular Image Acquisition Software (Teledyne Photometrics), the IOS picture sequences were acquired at a constant frame rate (10 per second) and with a fixed exposure time (100 ms), resulting in a varying duration of each movie (86.5 s to 89.0 s)[1]. To identify the propagating wave front and quantify the propagation speed, a custom-made ImageJ-Fiji Macro was generated for image processing[1], based on a previously published script[162]. The first step included a manual contrast adjustment of each picture sequence[1]. Background elimination and extraction of the wave were achieved by subtracting the first image that had been acquired prior to KCl microinjection[1]. The site of KCl injection was defined manually and used as a starting point for drawing a horizontal straight line[1]. Using the Plot Profile function, a data sheet including the pixel intensity values along the previously drawn line and for each IOS image of the sequence was created[1]. For each frame, the location of the CSD wave front was determined as the position of the values of maximum pixel intensity along the drawn line[1]. For identifying the maximum values and for further quantifying the propagation speed, a custom-made Matlab script (Matlab R2020, Matlab R2021, Matlab R2022 software) was used[1]. The calculation of the average propagation speed was achieved by plotting the location of the maximum pixel values, which represents the distance travelled by the wave, for each frame, representing the time[1]. For each IOS picture sequence, the velocity was estimated by dividing the travelled distance by ten consecutive time intervals and average the obtained values[1].

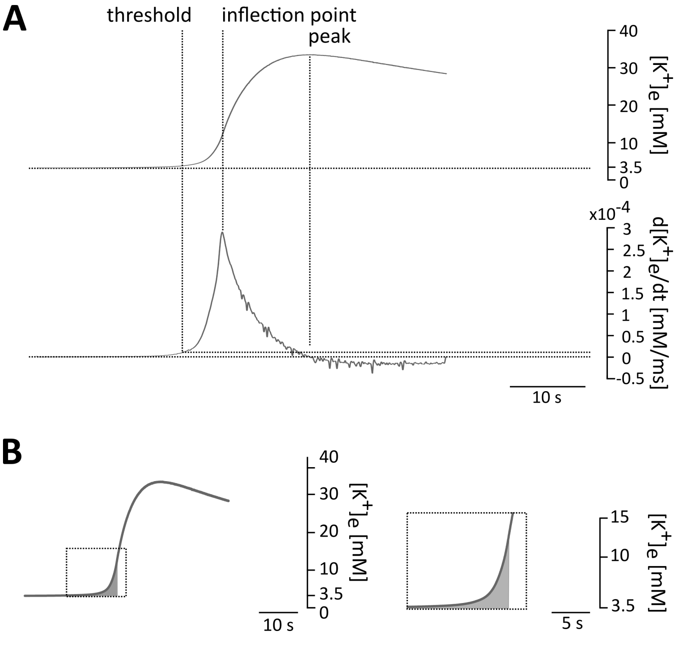

Figure 11. Visualisation of the threshold/inflection point, AUC and rise time/decay of the $[K^+]_e$ curve (adapted from Auffenberg et al., 2021)[1]. (**A**) Determination of the inflection point by calculating the first derivative and identifying its peak value[1]. The averaged $[K^+]_e$ curve for all K^+ recordings in slices of $\mathit{Scn1a}^{L1649Q/wt}$ animals (top) and the respective first derivative (bottom) are presented[1]. The threshold, inflection point, and peak are indicated in both curves[1]. (**B**) The averaged $[K^+]_e$ curve for all K^+ recordings in slices of $\mathit{Scn1a}^{L1649Q/wt}$ animals before and during a CSD including the AUC from K^+ threshold to the inflection point[1]. In the magnified box, the AUC, from the time point of a + 0.1 mM $[K^+]_e$ increase of the 10 s $[K^+]_e$ baseline to the inflection point, is shown in detail[1]. (**C**) Representative $[K^+]_e$ recording to visualise the time point of the KCl puff (arrow) to elicit the CSD, the 20 to 90 % rise time, the maximum $[K^+]_e$ at the peak of the curve and the $[K^+]_e$ 200 s after the peak value, termed as the decay[1].

For analysis of the K^+ electrode traces, a custom-made Matlab script was used to obtain the concentration changes (in mM) during CSD recordings via the recorded potential changes as well as the slope of calibration and to calculate further K^+-associated parameters[1]. The $[K^+]_e$ baseline was defined as the average of the first 10 s of the recording following KCl microinjection[1]. The beginning of the $[K^+]_e$ increase, which will also be referred to as the K^+ threshold, was defined as a 0.1 mM increase in average baseline concentration (**Figure 11 A**)[1]. The inflection point of the K^+ trace was calculated by estimating the peak of the first derivative of the K^+ recording (**Figure 11 A**)[1]. The area under the curve (AUC) was quantified by integrating the K^+ signal from the point of K^+ threshold until the inflection point (**Figure 11 B**)[1]. The maximum rising speed was determined as the peak value of the first derivative of the K^+ trace (**Figure 11 A**)[1]. The $[K^+]_e$ decay 200 s after the peak of the curve was defined as the relative $[K^+]_e$ compared to the $[K^+]_e$ value at the peak (**Figure 11 C**)[1]. For calculating $[K^+]_e$ at the peak, the 20 to 90 % rise time and the $[K^+]_e$ decay, the baseline concentration was subtracted respectively[1].

2.6 Administration of GS967

To test the effect of the persistent Na^+ channel blocker GS967 (Cayman Chemical, Ann Arbor, USA) on CSD initiation, a concentration of 5 µM was used[1, 142]. Aliquots containing stock solutions with a concentration of 10 mM were stored at -20°C and dilution was performed on the day of the experiment. Slices were perfused with recording aCSF supplemented with GS967. Before KCl application, slices were exposed to the inhibitor of the persistent Na^+ current for at least 25 min. Recording aCSF supplemented with GS967 was used for a maximum of 1.5 hours.

2.7 *In vitro* electrophysiology of the *Slc1a3*$^{P290R/wt}$ knock-in mouse line

As described previously, whole-cell patch clamp recordings (**Figure 12 A**, adapted from Hamill et al., 1981) were performed in a submerged chamber, in which the acute brain slices were continuously perfused with oxygenated recording aCSF[163]. For this purpose, a Gilson Minipuls 3 Peristaltic Pump (Gilson Incorporated, Middleton, USA) with a flow rate of 12.5 ml/min was used. The temperature was held at 34°C with a Scientifica heater and a LinLab2 software (Scientifica, Uckfield, United Kingdom). To ensure complete absence of movements of the cells during electrophysiological recordings, a self-made harp was used to keep the slices in place.

To visualise the targeted cells in the respective region of interest, an Olympus BX61WI microscope (Olympus Corporation, Tokyo, Japan) was used with the following objectives: LUMPlanFLN 60x objective, LMPlanFLN 5x objective. The software cellSens Dimension (Olympus Corporation) was used for controlling the microscope via the computer and for visualising the brain slice on screen. As layer 2/3 of the motor and somatosensory cortex were chosen for investigating CSDs, recordings of spontaneous and miniature inhibitory and excitatory postsynaptic currents (s/mIPSCs, s/mEPSCs) as well as tonic current recordings of pyramidal cells were performed in layer 2/3 of the somatosensory cortex. Pyramidal cells were selected according to their triangular shape, large size and specific localisation within the slice. A representative example is depicted in section 3.3.1 (**Figure 19 E, I**). Additionally, patched cells were filled with biocytin (Sigma-

Aldrich/Merck) and stained afterwards to confirm the correct cell type and position within the layers.

Patch clamp data were collected using a Multiclamp 700B amplifier, a DigiData 1420 and pClamp 10.6 software, which were all purchased from Molecular Devices (San Jose, USA) (**Figure 12 B**).

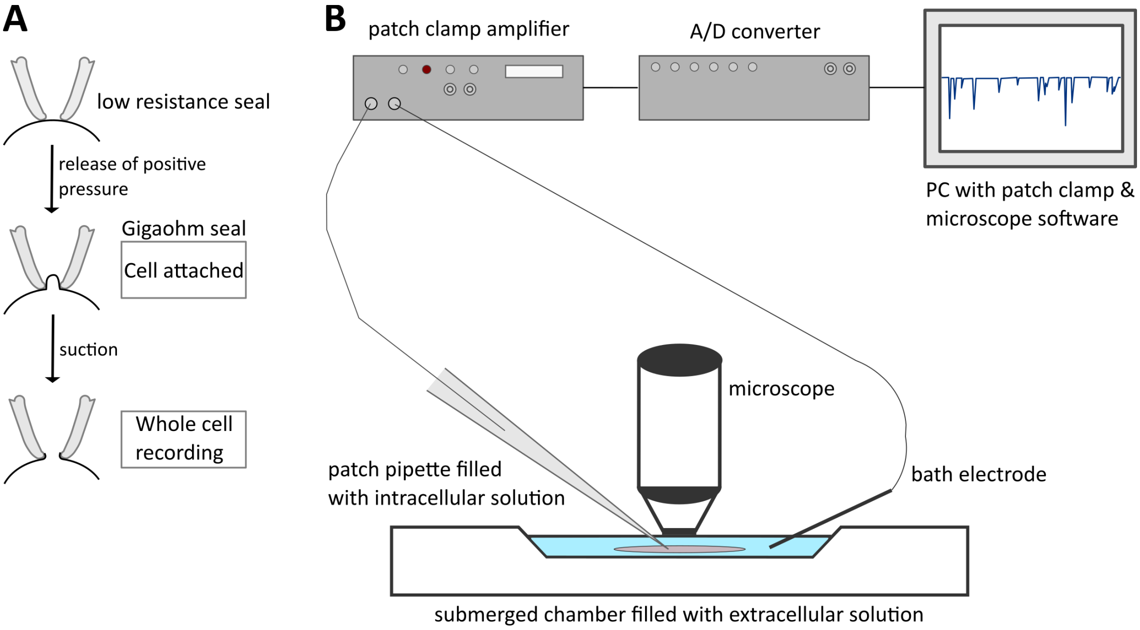

Figure 12. Representative schemes of the establishment of a whole-cell configuration and a recording setup. (**A**) Release of minimal positive pressure is essential to obtain a Gigaohm seal resulting in a cell-attached configuration. After carefully applying suction and gaining access to the cell, whole-cell patch clamp recordings can be initiated (adapted from Hamill et al., 1981)[163]. (**B**) Postsynaptic and tonic currents were recorded from cells of an acute brain slice using a pipette filled with intracellular solution containing Biocytin for subsequent identification and a bath electrode, while the submerged chamber was perfused with extracellular solution. Cells were visualised with a microscope. A patch clamp amplifier and A/D-converter were needed to record, visualise, and store the electrophysiological data on a PC.

The intracellular recording solution contained (in mM): 130 CsCl (Sigma-Aldrich/Merck), 8 NaCl, 0.2 $MgCl_2$, 2 EGTA (Sigma-Aldrich/Merck), 4 Mg-ATP (Sigma-Aldrich/Merck), 0.3 Li-GTP (Sigma-Aldrich/Merck), 1 QX-314, 10 HEPES/CsOH (Sigma-Aldrich/Merck) and 0.3 % Biocytin (pH 7.2, osmolarity 290 mOsm/kg). During recordings, the intracellular solution was stored in a container containing ice to avoid the breakdown of certain ingredients.

Patch electrodes were pulled out of borosilicate glass micropipettes (Science Products) using a Flaming/Brown Micropipette Puller (Model P-97, Sutter Instrument) until they had a final tip resistance of 2.5-4.0 MΩ.

The electrodes filled with intracellular solution were tightly connected to a Scientifica PatchStar micromanipulator on the mounting stage of a Scientifica SliceScope Pro 2000 electrophysiology system (Scientifica). Upon access to the extracellular solution, a small amount of positive pressure was applied using a 1 ml syringe (BD) to prevent the debris within the solution to occlude the pipette tip. Before establishing a gigaseal with the desired cell, the pipette current was adjusted to zero by using the Pipette Offset function provided by the pClamp software. After forming a gigaseal, the pipette capacitance was electronically eliminated and corrected for by using the Pipette Capacitance Compensation being split into a fast and a slow component by the program. Next, the membrane patch was broken by building up negative pressure with the syringe (BD) followed by stepwise Whole-Cell and Series Resistance compensation for each recorded cell. Series Resistance compensation was increased to at least 80 % to minimise the voltage error. Cells with a series resistance > 20 MΩ or with an unstable membrane potential were excluded. During IPSC, EPSC and tonic current recordings, cells were held at a membrane potential of -70 mV. Sampling rate for all recordings was 100 kHz.

IPSCs were recorded and analysed over a period of 5 min, whereas for EPSCs a shorter duration of 100 s was chosen. To record GABAergic IPSCs, 10 µM cyanquixaline (CNQX) (Sigma-Aldrich/Merck or Tocris Bioscience, Bristol, United Kingdom) and 50 µM (2R)-amino-5-phosphovaleric acid (AP-5) (Tocris Bioscience) were added to the recording solution. To isolate α-amino-3-hydroxy-5-methyl-4-isoxazolepropionic acid (AMPA) receptor-mediated EPSCs, the recording aCSF was supplemented with 50 µM AP-5 and 100 µM Picrotoxin (PTX) (Sigma-Aldrich/Merck). Recordings of miniature IPSCs (mIPSCs) and miniature EPSCs (mEPSCs) were performed in the presence of 1 µM TTX (Carl Roth GmbH + Co. KG). CNQX, AP-5, PTX and TTX were stored as stock solutions at -20°C. The toxins were diluted with recording solution on the day of recording, whereas the remaining aliquots were temporarily kept in an ice-filled container. During recordings, cells were filled with 0.3 % Biocytin for subsequent immunohistochemistry.

The analysis of spontaneous and miniature IPSCs and EPSCs was also performed with Clampfit software using the Template Search function. For each recorded trace, one or more representative events were identified to search for further templates within the respective trace generating a template file. Before the analysis, a threshold that specifically matched each template file was chosen manually and the template file was used to identify the IPSCs and EPSCs. Due to a minor signal-to-noise ratio for EPSC recordings, traces were filtered prior to Clampfit analysis by applying a 1 kHz Bessel filter. Each event, which was automatically detected by the template search function of the program, was checked, and confirmed manually. The relative amplitude, the interevent interval, the instantaneous frequency and the decay time constant were used as parameters for further statistical analyses.

For generating representative current traces, spontaneous and miniature IPSC and EPSC recordings were filtered applying a Bessel filter at 1 kHz (Clampfit 11.1 software, Molecular Devices, LLC.) (**Figure 19 A, Figure 20 A**).

For estimating the amplitude of $GABA_A$-receptor mediated tonic conductances, holding currents under baseline condition were recorded in the presence of 10 µM CNQX and 50 µM AP-5. During holding current recordings, cells were carefully monitored for maintaining a stable leak current over a period of at least 5 min. If instability was observed, the cells were discarded and not used for recordings. If the cells appeared to be highly stable, 50 µM PTX were added to the recording aCSF and subsequently washed in. After PTX arrival cells were recorded for at least another 10 min. Estimation of the $GABA_A$-receptor mediated tonic conductance was achieved by subtracting the average of a 30-second epoch of the holding current during constant PTX perfusion

(+ 6 min after PTX arrival) from the average of a 30-second epoch of the baseline holding current. Two representative examples of the analysis of the $GABA_A$-receptor mediated tonic conductance are shown in **Figure 20 G** (section 3.3.2), which depicts the holding current epoch as well as the 30-second interval after PTX perfusion. The Clampfit statistics function (mean measurement) provided by the Clampfit software (Clampfit 11.1 software, Molecular Devices, LLC.) was used for quantification of the absolute amplitude of each tonic conductance.

2.8 Implantation of EEG transmitters

Slc1a3$^{P290R/wt}$ and the respective wildtype animals were implanted with wireless EEG transmitters (ETA-F10 or HD-X02, Data Sciences International (DSI), St.Paul, USA) at two different time points, whereby the young group underwent surgery from P25 to P32 and the older group from P44 to P53 (**Figure 13 A**). Only male animals were used for EEG recordings. Female animals were excluded to avoid any confounding effect on seizures caused by the menstrual cycle. Animals of the young group were implanted with a minimum weight of 14 g and before the apparent onset of epileptic seizures, which was carefully monitored after weaning (≥ P21). Animals of the older group underwent surgery with a minimum weight of 20 g and after having passed the peak of seizures, which was also closely monitored.

Immediately before starting the procedure, the respective animals were checked with respect to their health status und weight. Temporary anaesthesia was induced in a whole-body chamber using an isoflurane vaporiser (3EX Precision Vaporiser, Patterson Scientific, Waukesha, USA), which was applying 5.0 % isoflurane (CP-Pharma) at a flow rate of 1.0 l/min. Adequate depth of anaesthesia was confirmed by the absence of righting and toe pinch reflexes. Subsequently, animals were administered a single intraperitoneal injection (BD Microlance 3 cannula, 27 G x ¾, 0.4 x 19 mm, BD, Heidelberg, Germany) with the long-term anaesthesia consisting of the following components and dosages: fentanyl (0.05 mg/kg bodyweight) (Fentadon 50 µl/ml, Dechra Veterinary Prodcuts Deutschland GmbH, Aulendorf, Deutschland), midazolam (5 mg/kg bodyweight) (Midazolam-hameln 5 mg/ml, hameln pharma gmbh, Hameln, Germany), medetomidine (0.50 mg/kg bodyweight) (Dorbene vet 1 mg/ml, Zoetis Inc., Parsippany, USA) and 0.9 % NaCl (Fresenius Kabi Deutschland GmbH, Bad Homburg, Germany). Additionally, all animals were applied carprofen (5 mg/kg bodyweight) (Rimadyl, Zoetis Deutschland GmbH, Berlin, Germany) subcutaneously to guarantee long-term postoperative analgesia. Bepanthen ointment (Bepanthen with 5 % dexpanthenol, Bayer AG, Leverkusen, Germany) was used to avoid drying of the eyes and to protect against the bright lights for surgery.

During the surgical procedure, the animals were safely fixed in a stereotaxic frame (Just for Mouse Stereotaxic Instrument, Stoelting Co., Wood Dale, USA) and were closely monitored with respect to respiration and cardiovascular condition. The animals were prevented from becoming hypothermic using an integrated warming pad (STOELTING Rodent Warmer X2, Stoelting Co.). After shaving the areas of surgery, the respective sites were disinfected thoroughly using an iodine containing solution (Betaisadona, Mundipharma GmbH, Frankfurt, Germany).

A first incision with a length of 1 cm was made on the right body side serving as access point for the transmitter. A second incision with a smaller diameter of 0.5-1.0 cm was made on the skull to remove the skin, which was followed by an application of 30 % H_2O_2 (Wasserstoffperoxidlösung 3 % Ph.Eur., Otto Fischar GmbH & Co. KG, Saarbrücken, Germany). Next, the surface of the skull was pre-treated with a primer and compressed air, followed by an adhesive component (OptiBond FL, Nobel Biocare Services AG - Kerr Business, Kloten, Switzerland) in combination with a dental curing light (BA Optima 10, B.A. International Ltd, Northampton, United Kingdom) to guarantee proper fixation of the cement afterwards. Using a fine drill (Proxxon Micromot GG12**,** PROXXON S.A., Wecker, Luxembourg) connected to a spherical diamond grinding pin (diameter: 1 mm, PROXXON S.A.), two holes with a diameter of 1 mm were drilled into the skull to obtain direct contact with the dura mater. Before surgery, the isolation of the electrode tips had been removed to uncover approximately 3-5 mm of the wires. Those wires were fixed bilaterally adjacent to the parietal cortex using dental cement (Tetric EvoFlow, Ivoclar Vivadent GmbH, Ellwangen, Germany) and a dental curing light. The two wires connecting the transmitter with the recording and reference electrode were retained in a subcutaneous tunnel. For stereotactic identification of the correct electrode positions, Bregma and Lambda served as bony landmarks, which are found at the intersection between the sagittal suture and the coronal and lambdoid suture, respectively (**Figure 13 B**). The reference as well as the recording electrode were placed 1 mm dorsal to bregma and 1 mm lateral to the sagittal suture. A stereo microscope (Stemi 305, Carl Zeiss Microscopy GmbH, Jena, Germany) was used to identify the correct electrode position on the skull and to continuously assess the depth of the holes during the drilling procedure (**Figure 13 B**). In case of small bleedings, ceasing was achieved by using absorbent cloths. The transmitter was placed subcutaneously posterior to the scapula and contralateral to the incision. Skin incisions were closed with simple interrupted stitches using absorbable sutures (Coated VICRYL undyed, 6-0, P-3, 13 mm, 3/8c, reverse cutting, 45 cm, Ethicon, LLC; Raritan, USA). The incisions on the skull were closed by applying enough dental cement to guarantee closing between the cement and the incision margins (**Figure 13 C**).

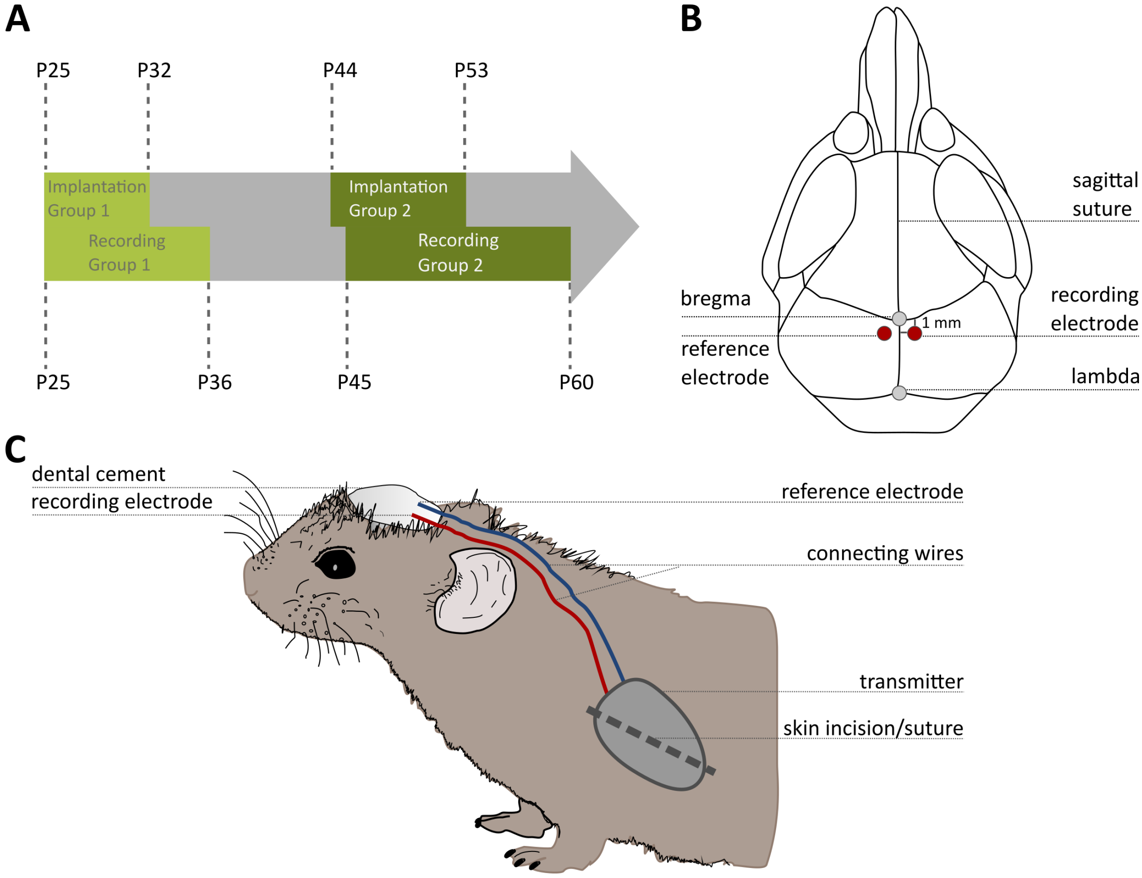

Figure 13. Timeline for video-EEG monitoring in *Slc1a3* animals as well as representative schemes of the skull and of an implanted mouse. (**A**) Visualisation of a timeline with chronologically arranged events comprising the implantation of a long-term wireless EEG recording system (P25-P30; P44-P53) and the simultaneous video-EEG monitoring period (P25-P36; P45-P60) in *Slc1a3*$^{P290R/wt}$ and wildtype animals before/during the episode of maximum seizure susceptibility and during the compensatory phase after seizure peak. (**B**) A representative scheme of the skull of a mouse during the surgical implantation procedure is shown including the essential landmarks of the sagittal suture, bregma as well as lambda and their intersections respectively (grey dots). After drilling two holes, the recording and reference electrodes were fixed 1 mm dorsal to bregma and 1 mm lateral to the sagittal suture using dental cement (red dots). (**C**) A representative drawing of an animal implanted with a wireless EEG transmitter. The reference and recording electrodes were fixed on the skull using dental cement and connected to the transmitter via a subcutaneous tunnel. The transmitter was positioned on the opposite side of the skin incision/suture.

After surgery, all animals received an antidote via subcutaneous injection consisting of the following components: naloxon (1.2 mg/kg body weight) (Naloxon-hameln, 0.4 mg/ml, hameln pharma gmbh, Hameln, Germany), flumazenil (0.5 mg/kg body weight) (Flumazenil Kabi 0.1 mg/ml, Fresenius Kabi Deutschland GmbH, Bad Homburg, Germany), atipamezole (2.5 mg/kg body weight) (Atipam 5 mg/ml, Dechra Veterinary Products Deutschland GmbH, Aulendorf, Germany). The administration of flumazenil was refrained for the young group to avoid pro-epileptic adverse effects in this high-risk group. To maintain body temperature and assess postoperative outcome, the animals were put in their home cages and monitored closely for several hours in front of an infrared heat lamp (Beurer GmbH, Ulm, Germany).

All animals received subcutaneous carprofen injections (5 mg/kg body weight) for two postoperative days as analgesic therapy and were provided additional milk powder as nutritional supplement. Additionally, animals of the post-seizure group were orally administered 25 µg enrofloxacin (Baytril 2.5 mg/ml, Bayer AG) per ml drinking water to reduce the risk of peri- and postoperative infections. Starting from the first postoperative day, animals that had received surgery were assessed with respect to their health status and the fulfilment of previously defined endpoint criteria at least once a day (**Appendix A**).

Until the start of chronic video-EEG recordings, animals of the older group were provided one week to recover from surgery, whereby the recovery period for mice of the pre-seizure group was shortened to three days. The purpose of decreasing recovery time was to avoid complications caused by continuous growth of the skull at this early age, which would have interfered with the non-expanding cement. Chronic EEG-recordings were initiated earlier than three/seven days after implantation if the occurrence of epileptic seizures or a status epilepticus was suspected or if there was unclear worsening of the general condition of the animal. It is necessary to highlight that an earlier start of the video-EEG recording before terminating the recovery period did not harm the animals or affect their well-being in any way.

2.9 EEG recordings and analysis

Video-EEG recordings of the older, “post-peak” group were performed from P45 to P60, whereas animals of the young, “pre-seizure” group were recorded from P25 to P36. As EEG signals were wirelessly transmitted to the Physio Tel Receiver (Model RPC-1, DSI), to the Matrix 2.0 (MX2, DSI) and subsequently to the acquisition computer, the animals were kept in the familiar environment of their home cages (cage type II long). EEG traces were digitally recorded using Ponemah software (Version 6.5, DSI). EEG data recorded with the ETA-F10 transmitter was sampled at 1 kHz, whereas EEG data recorded with the HD-X02 transmitter was sampled at 0.5 kHz. For simultaneous video recordings an Axis M1145-L network camera (Axis Communications AB, Lund, Sweden) and a Noldus Media Recorder software (Version 4.0, Noldus Information Technology BV, Wageningen, Netherlands) were used. Video recordings were acquired at 15 frames per second with a resolution of 800 x 600 pixels. Chronic video-EEG monitoring was performed for 48 h unless the animals died or reached the human endpoint, which was assessed by applying the already mentioned score sheet (**Appendix A**) defining the human endpoint as severe stress in the context of the conducted experimental procedure. EEG analysis was performed using Neuroscore software (DSI). The frequency and duration of epileptic seizures were assessed manually for every combined video-EEG recording. Semi-automatic identification of ictal or interictal events provided by the software used for analysis failed for most seizure events recorded from the *Slc1a3* P290R mouse line, since the traces were superimposed by spike-like breathing artefacts. The occurrence of an epileptic seizure was defined as the presence of an ictal EEG pattern consisting of rhythmic discharges > 10 s and < 5 min (sharp waves or spikes), a clear clinical presentation indicating a seizure or a combination of both. Power calculation for different frequency bands (Delta: 0.5-4 Hz; Theta: 4-8 Hz; Alpha: 8-12 Hz; Sigma: 12-16 Hz; Beta: 16-24 Hz, Gamma: 30-100 Hz) was performed automatically by the used software (**Table 4**).

The combination of a low-amplitude EEG, a dominating higher frequency > 8 Hz and an actively moving mouse during the dark phase were considered criteria for defining wake periods, whereas a high-amplitude EEG, dominating frequencies of < 4 Hz or 4-8 Hz, indicating delta and theta power, and sleep-like behaviour in the video sequences during the light phase were used as criteria for identifying sleep episodes. The application of these criteria to distinguish wake and sleep was exclusively used to identify representative EEG traces to show characteristic physiological EEG activity.

A status epilepticus was defined as a continuous seizure event or as at least two seizures with incomplete recovery of consciousness in between, whereby in each case a minimum duration of five minutes had to be exceeded[164].

Table 4. Decomposition of the EEG signal into distinct frequency power bands.

Power Bands	**Frequency**
Delta (δ)	0.5-4 Hz
Theta (θ)	4-8 Hz
Alpha (α)	8-12 Hz
Sigma (σ)	12-16 Hz
Beta (β)	16-24 Hz
Gamma (ɣ)	30-100 Hz

2.10 Perfusion

After completion of the recordings, the animals were maintained in their home cages to transfer them to the laboratory area, where an isoflurane vaporiser was used to apply 5 volume % isoflurane with a flow of 1 l/min. Induction of anaesthesia was followed by an intraperitoneal injection of a lethal dose of ketamine (150 mg/kg bodyweight) (Ketamin 10 %, 100 mg/ml, Wirtschaftsgenossenschaft deutscher Tierärzte eG, Garbsen, Germany) and xylazine (15 mg/kg bodyweight) (Sedaxylan, 20 mg/ml, Albrecht GmbH, Aulendorf, Germany).

When heartbeats were still present, but the animal had already reached a deep state of surgical anaesthesia, a ventral incision along the midline was made starting at the level of the bladder until the diaphragm was visible. A V-shaped incision was performed through both sides of the rib cage to lift the sternum and uncover the pleural cavity. The sternum and nearby parts of the rib cage were either removed or constantly kept out of the area of surgery.

A small cannula (Safety-Multifly-Needle, 23 G x ¾, 0.6 x 19 mm, Sarstedt, Nümbrecht, Germany) was placed in the left ventricle, while a small incision using fine scissors was made to open the right atrium. By perfusing 20-30 ml phosphate buffered saline (Dulbecco's PBS (1x), [-] $CaCl_2$, [-] $MgCl_2$, Gibco, Thermo Fisher Scientific Inc.,) and subsequently a similar amount of 4 % paraformaldehyde (PFA) (formaldehyde solution about 37 %, Merck KGaA, Darmstadt, Germany) through the needle, the blood was removed from the circulation. Clearing of the liver and an early presence of fixation tremors ensured good performance of the transcardial perfusion. After fixing the tissue, the skull was opened, and the brain was carefully removed avoiding any iatrogenic damage. Afterwards, the brain was put into 4 % PFA (Merck) overnight at 4°C and washed with PBS by changing the media three times at room temperature, for at least 15 min each, on the following day. For long-term storage the brains were preserved in PBS supplemented with 0.1 % sodium azide (Carl Roth GmbH + Co. KG) at 4°C.

2.11 Immunostaining of patched cells

Patched cells were filled with 0.3 % biocytin during recordings to retrospectively verify the correct cell type and localisation of the cell within the desired brain area. The brain slices were fixed at 4°C overnight using 4 % PFA (Merck). On the following day, three washing steps with PBS for 10-15 min were performed. Until initiation of the staining procedure, the slices were stored in PBS at 4°C. The staining protocol commenced with three washing steps using PBS for 15 min each, in which the slices were slightly agitated at room temperature. For permeabilising the intact cell membranes, the slices were incubated in PBS supplemented with 0.2 % Triton X-100 (Sigma-Aldrich) for one hour. Subsequently, incubation with Streptavidin (Streptavidin-Cy3 from *Streptomyces avidinii*, Sigma-Aldrich/Merck) at a 1:1000 ratio was performed for two hours, followed by three PBS washing steps, as described before. Next, the slices were incubated with 4′,6-diamidino-2-phenylindole (DAPI) (AppliChem GmbH) at a 1:5000 ratio for two minutes to identify the nuclei followed by three PBS washing steps. Finally, the slices were air-dried and mounted with Fluoromount-G (SouthernBiotech, Birmingham, USA) using conventional microscope slides (Menzel GmbH + Co KG/Thermo Fisher Scientific Inc.) and cover slips. Visualisation of the patched cells and storage of the data was performed with an Axiovert 200 M 2 microscope and a 20x objective (LD Achroplan 20x/0.40 Korr Ph2) or 40x objective (LD Achroplan 40x/0.60 Korr Ph 2) using ZEN 2.6 blue edition software (Carl Zeiss Microscopy GmbH). The image size was 1937 x 1460 µm. 14 bits were chosen as bit depth. Filters were chosen accordingly to fit the excitation and emission wavelengths of the two fluorophores DAPI and rhodamine.

2.12 Immunostaining of brain slices against c-fos after perfusion

For further immunohistochemical procedures, specifically the staining of c-fos protein, the brains of the previously perfused *Slc1a3*$^{\mathrm{P290R/wt}}$ and *Slc1a3*$^{\mathrm{wt/wt}}$ animals ranging from P25 to P60 that had been implanted with EEG electrodes and transmitters were used to obtain 100 µm thin coronal slices with a Leica VT 1000 S vibratome. For cutting, the mouse brain and a 4 % agarose cuboid for stabilisation were glued onto a circular metal plate that was screwed onto the bottom of the cutting chamber filled with PBS as medium. Each brain was cut following the same procedure, which enabled the identification of corresponding brain slices/regions between different animals. After cutting, the slices were either stored in PBS supplemented with 0.1 % sodium azide for a short period of time or directly used for immunohistochemistry.

On average, five slices per brain/mouse that comprised both hemispheres were used for immunochemical studies. The slices were chosen to depict different levels of cutting and to include distinct regions across the brain, with a focus on the cortex, thalamus, and hippocampus. However, the cutting levels and brain regions did not differ between the single included mouse brains.

First, the slices were washed with PBS supplemented with 0.2 % Triton X-100 (AppliChem GmbH) for 5 min, which was repeated three times. As a second step, blocking of the slices for at least one and a half hours at room temperature was performed using PBS that had been supplemented with 1.0 % Normal Goat Serum (NGS) (Immunopure Normal Goat Serum, Thermo Fisher

Scientific Inc.) and 0.2 % Triton X-100. Dilution of the primary antibody against c-fos (Cat.No. 226 308, Synaptic Systems GmbH, Göttingen, Germany) at a 1:1000 ratio was achieved using PBS supplemented with 2.0 % NGS and 0.2 % Triton X-100. A three hours-lasting incubation of the slices with the primary antibody was performed at room temperature, while the slices were gently agitated. Subsequently, the slices were washed three times using 0.2 % Triton X-100 supplemented PBS. As a next step, the slices were incubated for two hours at room temperature with the corresponding secondary antibody (Goat anti-Guinea Pig IgG (H+L) Highly Cross-Adsorbed Secondary Antibody, Alexa Fluor™ 568, Thermo Fisher Scientific Inc.) while protecting them from any light and gently agitating them. For diluting the secondary antibody, PBS supplemented with 1.0 % NGS and 0.2 % Triton X-100 served as a medium. The immunohistochemical protocol was continued with three PBS washing steps for 5 min each and with a DAPI staining, as described in section 2.10. Mounting of the stained slices was performed as outlined before.

The first step of imaging was performed with a Leica Microscope DMi8 and a Leica DFC9000 GTC sCMOS camera (Leica Microsystems GmbH, Wetzlar, Germany) to obtain an overview of the distribution of c-fos positive cells for each stained slice. During the primary imaging step, regions with c-fos expression that qualified for subsequent confocal imaging were identified using a 10x/0.32 FLUO objective (Leica Microsystems GmbH) and the fluorescence light source Lumencor Spectra X (Lumencor, Beaverton, USA) with DAPI and Alexa Fluor 546/555 filters. Images of the stained slices were captured with the software LAS X using the Spiral and Mosaic Merge functions to obtain an overview of the entire slice with a 10 % overlap of the single scans. For every round of immunohistochemistry, consistent intensity values and exposure times were chosen. The aim of the first imaging step was to identify the brain regions with maximum density of c-fos positive cells, which was performed manually. Subsequently, these areas were identified with the coronal Allen Mouse Brain Atlas (https://mouse.brain-map.org/experiment/thumbnails/100048576?image_type=atlas)[165].

The second step of imaging was performed using the confocal inverted microscope Zeiss LSM 710 with an Argon laser and a 25x oil immersion objective (Carl Zeiss Microscopy GmbH). The goal of the second step was to capture images of the previously identified regions with maximum upregulation of c-fos expression. One drop of immersion oil (Immersol™, 518 F, Carl Zeiss Microscopy GmbH) was applied onto the cover slip before the microscope slide was inserted. Using the software ZEN 2011 for data acquisition, as a first step, DAPI and Alexa 568 were chosen as dyes. The Best-signal-function was used for acquisition. Z-stacks of c-fos positive regions were captured having an interval of 1 µm. Each captured image had a size of 2048 x 2048 pixels and a bit depth of 8 bit. As pinhole diameter 1 Airy Unit (AU) was chosen. For every round of immunohistochemistry, consistent gain values and exposure times were chosen. Data processing was performed with the software ImageJ-Fiji.

2.13 Statistics

For the performance and analysis of all *in vitro* experiments, the investigator was blinded to the genotype of the animal. Blinding was not possible for the performance and analysis of *in vivo*

EEG implantations and recordings, as the genotype of the animal was easily recognizable due to the behaviour, the weight, size, and appearance of *Slc1a3*$^{\mathrm{P290R/wt}}$ animals.

Statistical analysis was carried out using GraphPad Prism 9.5.1 software (GraphPad Software, Boston, United States), QuickCalcs (GraphPad Software) and IBM SPSS Statistics software (IBM, Armonk, United States). Each statistical test that was performed is indicated in the main text and the respective figure legends. Deviation from normal distribution was determined using Shapiro-Wilk-test and Kolmogorov-Smirnov-test. If the datasets of wt/wt and L1649Q/wt or P290R/wt animals were normally distributed, a two-tailed unpaired t-test (parametric) was used. In this context, the abbreviation “wt” refers to the term wildtype. In case of unequal variances, a Welch-corrected unpaired t-test was used. If the datasets of two unpaired groups were not normally distributed, Mann-Whitney Rank Sum Test (non-parametric) was applied. To analyse contingency tables, Fisher’s exact test for smaller sample sizes or chi-square test without Yates’ correction for larger sample sizes were used. The Fisher’s exact test and the chi-square test without Yates’ correction were performed online using QuickCalcs provided by GraphPad Software (https://www.graphpad.com/quickcalcs/contingency1). To compare multiple groups with a non-parametric distribution, multiple Mann-Whitney rank sum tests were applied and the Holm-Šídák method was used to correct for multiple comparisons. A p-value less than 0.5 was considered statistically significant.

In each box-and-whisker plot, the median is shown as a line. Additionally, minimums, maximums, outliers, 25th percentiles and 75th percentiles are given. The significance for each statistical test with respect to control is specified within the figures. For this purpose, the following symbols are used * $p < 0.05$, ** $p < 0.01$, *** $p < 0.001$.

The letter “n” indicates the number of slices that were used to perform *in vitro* CSD recordings, whereas in the context of patch-clamp recordings the letter “n” refers to the number of patched cells. The number of animals that were used in each experimental group is provided in the square brackets or after the backslash following the number of slices/cells. In the context of *in vivo* EEG recordings, the letter “n” refers to the number of animals that were implanted and recorded. For each dataset, a table including the number of included slices/cells, the mean and standard deviation values of each experimental group is provided in the respective section.

2.14 Figures

The included box-and-whisker plots were initially generated using RStudio software and consequently edited with Inkscape software. The representative traces for all electrophysiological data were also edited using Inskcape software. **Figure 1**, **Figure 2**, **Figure 6**, **Figure 7** and **Figure 31** were created with BioRender.com. All microscope pictures were processed using ImageJ-Fiji software.

3 Results

3.1 *In vitro* CSD recordings in the *Scn1a*$^{L1649Q/wt}$ knock-in mouse model

For elucidating the pathophysiological mechanisms of CSD in HM focussing on the respective role of K^+, the *Scn1a*$^{L1649Q/wt}$ knock-in model served as a transgenic FHM3 model[1]. As already outlined in the introduction, distinct variants in *SCN1A* encoding $Na_V1.1$, which is primarily expressed in inhibitory neurons, are associated with FHM3. *Scn1a*$^{L1649Q/wt}$ mice harbour the human missense variant L1649Q that had been identified in a family with pure HM[69]. L1649Q is located in the voltage sensor domain of transmembrane segment 4 (S4) in the fourth domain (D4) of $Na_V1.1$ (**Figure 2**), which is supposed to play a key role in fast inactivation of the Na^+ channel[166]. Whole-cell patch clamp recordings from our and another group had already demonstrated a GOF effect of L1649Q with an increased persistent Na^+ current and a higher firing frequency resulting in hyperexcitability of cortical and hippocampal fast-spiking inhibitory neurons[1, 29]. Additionally, in *vivo* recordings had revealed an enhanced CSD susceptibility of *Scn1a*$^{L1649Q/wt}$ animals[1]. However, the pathophysiological link between the hyperexcitability of inhibitory neurons on the single cell level and a higher CSD susceptibility *in vivo*, including the specific role of K^+ within the cascade, had remained unknown. It had already been proposed earlier that interneuron hyperexcitability caused by $Na_V1.1$ GOF variants may lead to $[K^+]_e$ accumulation and an extensive GABA release with a depletion of the electrochemical gradient for Cl^-, which induces CSD[68].

Therefore, *in vitro* CSD recordings were performed, focusing on $[K^+]_e$ changes before, during and after CSD induction[1]. As described in section 2.4, CSDs were captured by combining $[K^+]_e$ recordings using a K^+-sensitive microelectrode, LFP recordings and IOS imaging with a CCD camera in acute cortical slices of heterozygous and wildtype animals from P15 to P20[1]. CSDs were elicited by applying 400 ms-lasting puff injections containing 200 mM KCl onto the surface of layer 2/3 of the somatosensory and motor cortex[1]. The KCl puff injection site and the localisation of both the K^+-sensitive and the DC potential electrode were at least 800 µm apart[1].

3.1.1 Higher CSD susceptibility and increased propagation velocity in slices of *Scn1a*$^{L1649Q/wt}$ animals

A successfully induced CSD was defined as the combined occurrence of a negative DC potential shift in the LFP recording, an increase in $[K^+]_e$ captured by the K^+-sensitive microelectrode and the presence of a slowly propagating IOS with a migration distance of at least 800 µm from the injection site (**Figure 14 A, B**)[1]. The category of "failed" CSDs included aborted CSDs, which initially started to migrate, but then ceased to propagate any further (**Figure 10 A**)[1]. The failure category also contained local CSDs that were identified by an absent migration indicated by the presence of a white ring around the injecting puff pipette (**Figure 10 B**)[1]. Successfully induced CSDs were elicited in 87.8 % (36/41 slices from 11 mice) of slices of heterozygous animals, whereby aborted or local CSDs were detected in 12.2 % (5/41)[1]. In contrast, successful CSD inductions were recorded in 48.8 % (21/43 slices from 12 mice) of the slices of wildtype animals, while the rate of failed CSDs was found to be noticeably higher at 51.2 % (22/43) ($P < 0.001$; Fisher's exact test; **Figure 14 C**)[1].

Additionally, using the same experimental setup, the captured IOS imaging sequences were used to estimate the speed of the propagating wavefront, which was significantly increased in slices of *Scn1a*$^{\mathrm{L1649Q/wt}}$ knock-in animals compared to wildtype littermates ($n_{\mathrm{wt/wt}}$ = 22 [10 mice], $n_{\mathrm{L1649Q/wt}}$ = 31 [11 mice]; $P < 0.001$; unpaired t-test; **Figure 14 D**)[1]. Descriptive statistics are shown in **Table 5**[1].

3.1.2 Altered K$^+$ levels in slices of heterozygous *Scn1a*$^{\mathrm{L1649Q/wt}}$ knock-in animals

During CSD, $[K^+]_e$ at the inflection point of the rising phase and at the maximum $[K^+]_e$ of the entire ion-sensitive recording, also termed the K$^+$ peak, was significantly elevated in slices of *Scn1a*$^{\mathrm{L1649Q/wt}}$ knock-in animals compared to slices of control animals ($n_{\mathrm{wt/wt}}$ = 22 [10 mice], $n_{\mathrm{L1649Q/wt}}$ = 31 [11 mice]; $P < 0.01$, $P < 0.01$; unpaired t-test, Mann-Whitney rank sum test; **Figure 14 B, E, F**)[1]. The inflection point was determined by using the peak of the first derivative indicating $[K^+]_e$ at the time point of maximum speed of the $[K^+]_e$ rise (**Figure 14 E, Figure 11 A**)[1]. The rationale for calculating the inflection point was to define a reproducible time point/time interval during the early phase of the CSD that would yield comparable parameters and results between different K$^+$ recordings[1]. The beginning of the $[K^+]_e$ rise, also termed the K$^+$ threshold, was arbitrarily defined as a + 0.1 mM increase in baseline $[K^+]_e$[1]. The $[K^+]_e$ baseline was calculated by averaging the first 10 s of the whole 300 s-lasting ion-sensitive recording and did not differ between the two genotypes (**Figure 14 G**)[1].

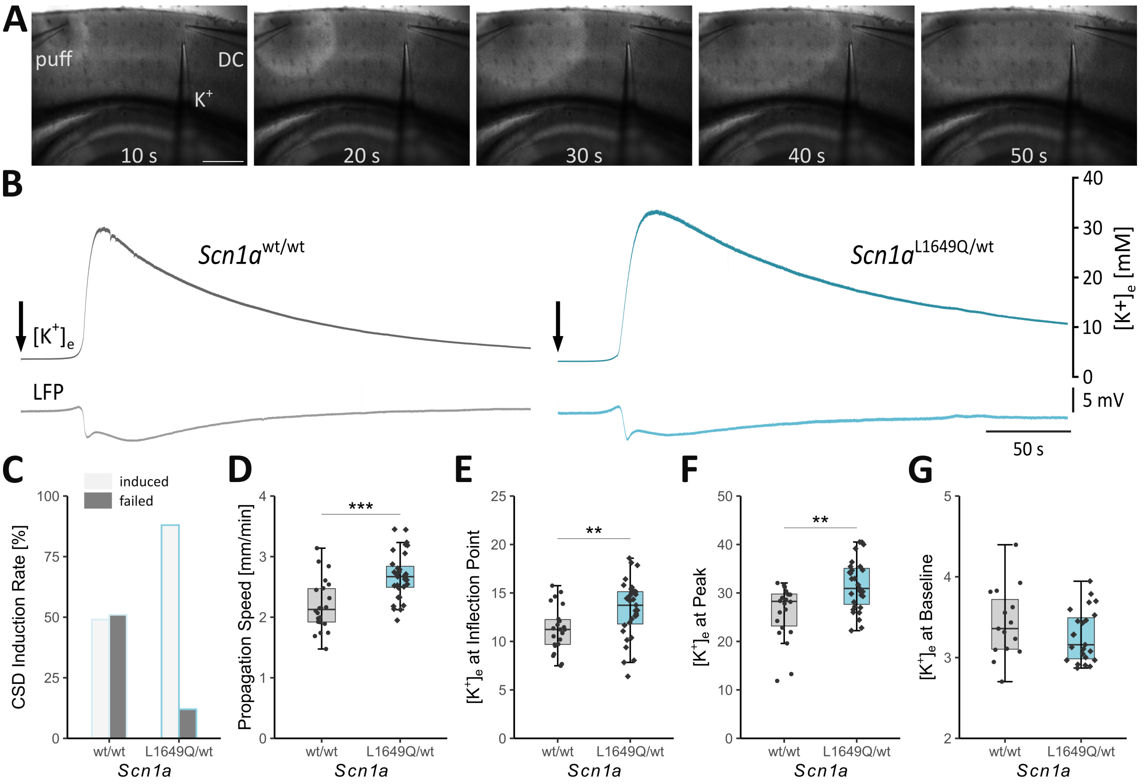

Figure 14. Higher susceptibility to CSDs, an increased propagation speed and elevated $[K^+]_e$ levels in slices of *Scn1a*$^{\mathrm{L1649Q/wt}}$ animals (adapted from Auffenberg et al., 2021)[1]. (**A**) Migration of the IOS signal

after KCl puff application (puff) onto a cortical slice of a wildtype animal and simultaneous recordings of CSD with a K^+-sensitive electrode (K^+) and an LFP electrode (DC)[1]. The images were captured 10-50 s after CSD induction[1]. Scale bar: 500 µm. (**B**) Representative traces of K^+-sensitive recording (top) and LFP recording (bottom) with a characteristic saddle-like configuration before and during CSD shown for a slice of a wildtype (left, grey) and an *Scn1a*$^{L1649Q/wt}$ (right, blue) animal[1]. The arrow marks the start of the CSD elicited by a KCl puff[1]. (**C**) The rate of successfully induced CSDs shows that slices of heterozygous versus wildtype mice were more susceptible to CSD triggering ($n_{wt/wt}$ = 43 slices of 12 animals [43/12], $n_{L1649Q/wt}$ = 41 slices of 11 animals [41/11]; $P < 0.001$; Fisher's exact test.)[1]. (**D**) The propagation velocity was elevated in slices of heterozygous compared to wildtype mice ($n_{wt/wt}$ = 22/10, $n_{L1649Q/wt}$ = 31/11; $P < 0.001$; unpaired t-test)[1]. (**E**) $[K^+]_e$ was increased at the inflection point in slices of heterozygous compared to wildtype animals ($n_{wt/wt}$ = 22/10, $n_{L1649Q/wt}$ = 31/11; $P < 0.01$; unpaired t-test)[1]. (**F**) At the peak of the whole ion-sensitive recording, $[K^+]_e$ was increased in slices of *Scn1a*$^{L1649Q/wt}$ versus wildtype mice ($n_{wt/wt}$ = 22/10, $n_{L1649Q/wt}$ = 31/11; $P < 0.01$; Mann-Whitney rank sum test)[1]. (**G**) $[K^+]_e$ baseline, defined as the averaged concentration of the recording's first 10 s, did not differ between the two genotypes ($n_{wt/wt}$ = 15/5, $n_{L1649Q/wt}$ = 23/8; unpaired t-test)[1].

Besides the changes in the absolute K^+ levels both at the inflection point and the peak, a comprehensive analysis of the K^+ dynamics was considered decisive to scrutinise the role of K^+ in CSD pathology[1]. In this context, the term $[K^+]_e$ dynamics did not only refer to velocity-related calculations, but also involved the identification of critical time intervals during CSD[1].

The time from the start of $[K^+]_e$ increase until the inflection point was significantly longer in slices of *Scn1a*$^{L1649Q/wt}$ animals compared to slices of *Scn1a*$^{wt/wt}$ mice ($n_{wt/wt}$ = 22 [10 mice], $n_{L1649Q/wt}$ = 31 [11 mice]; $P < 0.05$; Mann-Whitney rank sum test; **Figure 15 A**), whereas the time from the inflection point until the maximum $[K^+]_e$ was not different between the slices of the two genotypes (**Figure 15 B**), indicating an earlier increase in $[K^+]_e$ in slices of heterozygous animals[1].

In accordance with the overall elevated magnitude of the K^+ levels and the earlier $[K^+]_e$ increase during the first phase of the CSD, the 20 to 90 % rise time was also prolonged in slices of *Scn1a*$^{L1649Q/wt}$ compared to wildtype animals ($n_{wt/wt}$ = 22 [10 mice], $n_{L1649Q/wt}$ = 31 [11 mice]; $P < 0.05$; Mann-Whitney rank sum test; **Figure 15 C**, **Figure 11 C**)[1]. The verified $[K^+]_e$ shift exclusively during the early CSD phase was additionally supported by the fact that the $[K^+]_e$ decay was unaltered comparing slices of heterozygous and wildtype animals (**Figure 15 E**, **Figure 11 C**)[1]. The decay of $[K^+]_e$ was defined as the relative $[K^+]_e$ 200 ms after the maximum $[K^+]_e$ of the whole recording (**Figure 11 C**)[1].

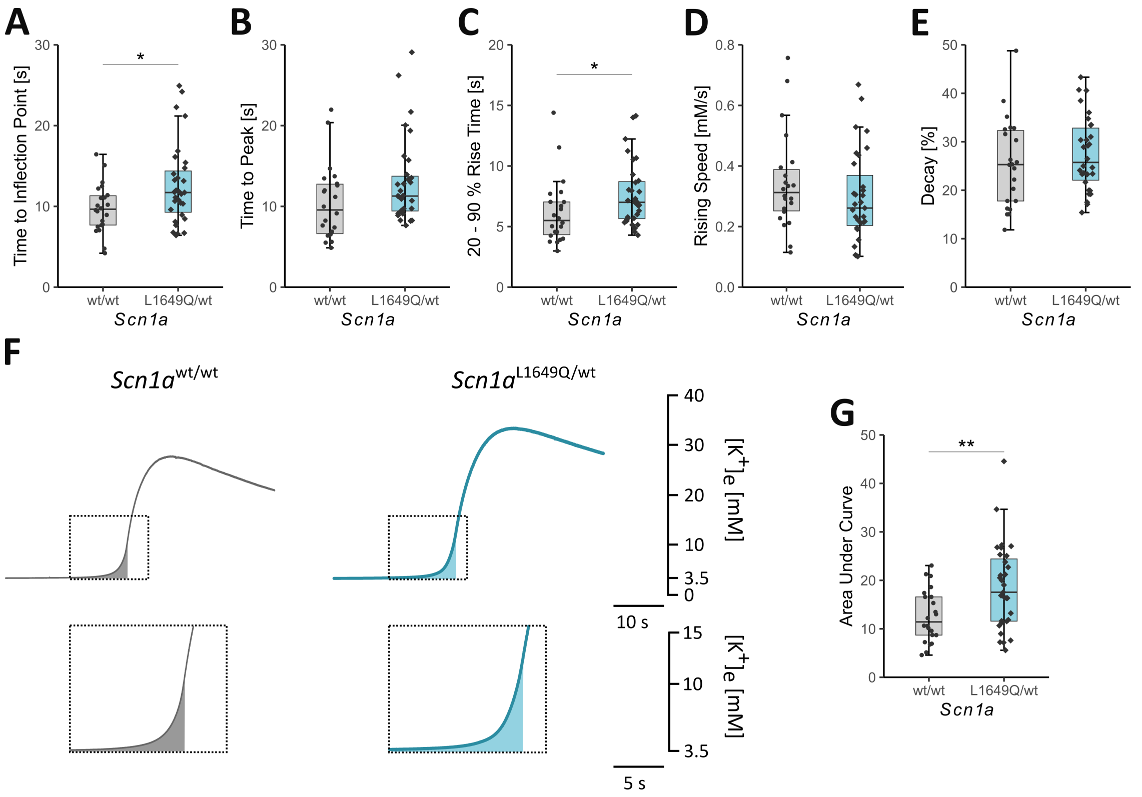

Figure 15. [K$^+$]$_e$ dynamics were altered in slices of heterozygous animals with an increase in [K$^+$]$_e$ early during CSD (adapted from Auffenberg et al., 2021)[1]. (**A**) The time interval from K$^+$ threshold, defined as the beginning of [K$^+$]$_e$ rise, until the inflection point was prolonged in slices of heterozygous versus wildtype animals due to an earlier start of [K$^+$]$_e$ increase ($n_{wt/wt}$ = 22 slices from 10 mice [22/10], $n_{L1649Q/wt}$ = 31/11; $P < 0.05$; Mann-Whitney rank sum test)[1]. (**B**) Alterations of K$^+$ dynamics were confined to an early interval during CSD, since the time from the inflection point to the peak did not differ between the genotypes ($n_{wt/wt}$ = 22/10, $n_{L1649Q/wt}$ = 31/11; Mann-Whitney rank sum test)[1]. (**C**) The 20 to 90 % rise time being affected by the K$^+$ dynamics of the incipient CSD phase and the magnitude of the overall K$^+$ levels was also prolonged in slices of *Scn1a*$^{L1649Q/wt}$ versus wildtype animals ($n_{wt/wt}$ = 22/10, $n_{L1649Q/wt}$ = 31/11; $P < 0.05$; Mann-Whitney rank sum test)[1]. (**D**) The maximum rising speed, calculated by the peak value of the first derivative, and (**E**) the K$^+$ decay, defined as the relative [K$^+$]$_e$ 200 s after the maximum concentration, did not reveal any differences between the genotypes ($n_{wt/wt}$ = 22/10, $n_{L1649Q/wt}$ = 31/11; Mann-Whitney rank sum test; Mann-Whitney rank sum test; unpaired t-test)[1]. (**F**) Averaged K$^+$ traces shown for all slices of *Scn1a*$^{wt/wt}$ (left, grey) and *Scn1a*$^{L1649Q/wt}$ (right, blue) mice before and during CSDs[1]. The magnified boxes illustrate the AUC calculation for both genotypes, performed from the beginning of K$^+$ rise (baseline + 0.1 mM) until the inflection point[1]. (**G**) The increased AUC in slices of heterozygous compared to wildtype animals indicated an early increase in [K$^+$]$_e$ ($n_{wt/wt}$ = 22/10, $n_{L1649Q/wt}$ = 31/11; $P < 0.01$; Welch-corrected unpaired t-test)[1].

Despite the increased propagation velocity during CSD in slices of *Scn1a*$^{L1649Q/wt}$ animals, the maximum rising speed of [K$^+$]$_e$, which was determined by the peak value of the first derivative, was not different between the genotypes (**Figure 15 D, Figure 11 A**)[1].

Moreover, the calculation of the AUC, which was defined from [K$^+$]$_e$ threshold until the inflection point (**Figure 11 B**), further indicated that the increase in [K$^+$]$_e$ was confined to an early time interval during CSD, since the AUC was significantly larger in slices of *Scn1a*$^{L1649Q/wt}$ compared to wildtype animals ($n_{wt/wt}$ = 22 [10 mice], $n_{L1649Q/wt}$ = 31 [11 mice]; $P < 0.01$; Welch-corrected unpaired t-test; **Figure 15 F, G**)[1]. Descriptive statistics are shown in **Table 5**[1].

Table 5. Descriptive statistics for the CSD recording data in *Scn1a*$^{L1649Q/wt}$ and *Scn1a*$^{wt/wt}$ animals[1].

	Mean (wt/wt)	**Mean (L1649Q/wt)**	**SD (wt/wt)**	**SD (L1649Q/wt)**	**t, df**	**p-value**
$[K^+]_e$ Baseline	3.4	3.3	0.4	0.3	t(36.0)=1.3	0.207
$[K^+]_e$ Decay	25.5	28.2	9.2	8.6	t(51.0)=1.1	0.280
$[K^+]_e$ at Inflection Point	11.3	13.3	2.3	3.0	t(51.0)=2.7	0.010
Area Under Curve	12.6	18.6	5.4	8.8	Welch-corrected t(50.2)=3.1	0.004
Maximum Rising Speed	0.3	0.3	0.2	0.2		0.192
$[K^+]_e$ at Peak	26.2	31.7	5.6	5.3		0.002
Propagation Velocity	2.2	2.7	0.4	0.4	t(51.0)=4.3	< 0.001
20 to 90 % Rise Time	6.2	7.6	2.7	2.6		0.015
Time Threshold-Inflection Point	9.8	12.6	3.0	5.0		0.035
Time Inflection Point-Peak	10.4	13.0	4.6	5.3		0.054

3.1.3 Effects of the persistent Na$^+$ channel blocker GS967 on CSD *in vitro*

To confirm that the elevated persistent Na$^+$ current and the associated increase in firing frequency recorded in fast-spiking inhibitory interneurons of *Scn1a*$^{L1649Q/wt}$ animals resulted in a higher CSD susceptibility, GS967 was used to eliminate the effect of an elevated ramp current caused by the L1649Q variant[1]. To do so, the effect of GS967 was investigated on the rate of successfully induced and failed CSDs *in vitro* using the same experimental setup as outlined before[1].

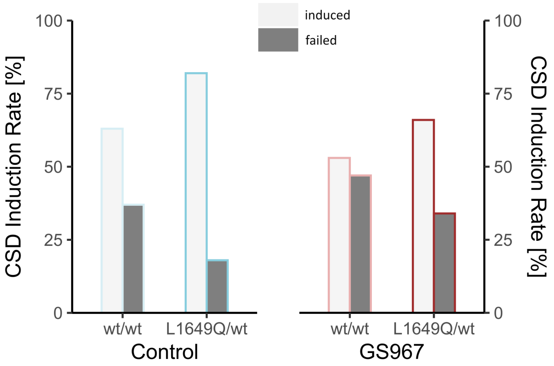

Figure 16. Alleviation of CSD susceptibility *in vitro* in the presence of the persistent Na$^+$ channel blocker GS967 (adapted from Auffenberg et al., 2021)[1]. The rate of successfully induced CSDs was increased in slices of heterozygous animals compared to wildtype littermates (left) ($n_{wt/wt}$ control = 54 slices from 28 mice [54/28], $n_{L1649Q/wt}$ control = 44 slices from 20 mice [44/20]; $P < 0.05$; χ^2 test without Yates correction)[1]. In the presence of 5 µM GS967, the induction and failure rates in slices of *Scn1a*$^{L1649Q/wt}$ knock-in mice approached the rates observed in slices of wildtype littermates (right) ($n_{wt/wt}$ GS967 = 60/28, $n_{L1649Q/wt}$ GS967 = 44/20; $P = 0.94$; χ^2 test without Yates correction)[1].

Without the application of 5 µM GS967, the rate of successfully induced CSDs was higher in slices of heterozygous animals (36/44 slices from 20 mice) compared to slices of wildtype littermates (34/54 slices from 28 mice)[1]. To be specific, CSDs were elicited in 81.8 % of slices of *Scn1a*$^{L1649Q/wt}$ animals, whereas the success rate was observed to be at 63.0 % in slices of wildtype animals[1]. Simultaneously, the rate of failed CSDs was lower in slices of *Scn1a*$^{L1649Q/wt}$ animals (18.2 %; 8/44) compared to slices of *Scn1a*$^{wt/wt}$ mice (37.0 %; 20/54)[1].

However, after GS967 perfusion of the slices at least 25 min before and during CSD recordings, the successful induction and failure rates of slices of *Scn1a*$^{L1649Q/wt}$ mice approached the respective rates found in slices of wildtype animals[1]. In the presence of GS967, successfully induced CSDs were observed in 53.3 % (32/60 slices from 28 mice) of the slices of *Scn1a*$^{wt/wt}$ and in 66.0 % (29/44 slices from 20 mice) of the slices of *Scn1a*$^{L1649Q/wt}$ animals[1]. Simultaneously, the rate of failed CSDs was increased to 46.7 % (28/60) in slices of wildtype and to 34.1 % (15/44) in slices of heterozygous mice ($n_{wt/wt}$ control = 54 slices from 28 mice [54/28], $n_{L1649Q/wt}$ control = 44/20; $P < 0.05$; χ^2 test without Yates correction; $n_{wt/wt}$ GS967 = 60/28, $n_{L1649Q/wt}$ GS967 = 44/20; $P = 0.94$; χ^2 test without Yates correction; **Figure 16**)[1].

3.2 *In vitro* CSD recordings in the *Slc1a3*$^{P290R/wt}$ knock-in mouse model

For unravelling CSD pathophysiology in the context of distinct HM causing variants and further elucidating the role of K^+ and other possible initiating factors in the CSD cascade, the *Slc1a3*$^{P290R/wt}$ knock-in mouse model for EA6 served as a novel HM model. The *SLC1A3* gene encodes the combined glutamate transporter and anion channel EAAT1, which is mainly expressed in astrocytes and RGLs, but is also found in retinal Muller cells, microglia, oligodendrocytes, and oligodendrocyte precursor cells[147, 148, 149, 150]. *SLC1A3* has recently been speculated to be also involved in common and rare hemiplegic types of migraine[96, 97, 98, 99]. Jen and colleagues had identified the missense mutation p.(Pro290Arg) (P290R) in a boy with a complex clinical phenotype not only including HM attacks, but also epileptic seizures and ataxic episodes[96], which are both common additional phenotypes in the HM spectrum[167]. *Slc1a3*$^{P290R/wt}$ knock-in animals harbour the P290R variant, which is located in the transmembrane helix 5 (TM5) of the glutamate transporter (**Figure 6**). The P290R variant leads to a marked reduction in glutamate transport and cell surface expression, but at the same time increases EAAT1-associated anion currents[100].

However, the pathophysiological mechanisms linking a LOF of the glutamate transport and a simultaneously occurring GOF of the anion conductance with CSDs and HM attacks had not been identified so far. Additionally, to emphasise the role of K^+ in CSD pathophysiology, especially with respect to the FHM3 model, the goal was to investigate $[K^+]_e$ alterations in the context of CSD pathology in the EA6 model. Nevertheless, due to the P290-related impaired glutamate transport, the excitatory neurotransmitter glutamate was hypothesised to be the key factor in CSD initiation in the *Slc1a3*$^{P290R/wt}$ mouse model. Comparing different HM models with distinct underlying genetic alterations was anticipated to provide an even more detailed insight into CSD pathophysiology.

As outlined in sections 2.4 and 3.1[1], CSD recordings comprised simultaneous LFP and $[K^+]_e$ recordings as well as the acquisition of IOS picture sequences using slices of *Slc1a3*$^{P290R/wt}$ and wildtype animals from P15 to P20. KCl puff injections onto the surface of layer 2/3 of the somatosensory and motor cortex, which had a distance of at least 800 µm to the DC potential and K^+-sensitive electrodes, were performed to trigger CSDs *in vitro*.

3.2.1 Higher CSD susceptibility and increased propagation velocity in slices of *Slc1a3*$^{P290R/wt}$ animals

Successful CSD inductions including a negative LFP shift, a $[K^+]_e$ rise (**Figure 17 A**) and an IOS propagation distance greater than 800 µm from the injection site were observed in 87.1 % (27/31 slices from 5 mice) of the slices of *Slc1a3*$^{P290R/wt}$ knock-in animals. In contrast, the rate of successful CSD inductions was lower in slices of wildtype mice, as CSDs were elicited in only 52.5 % (31/59 slices from 10 mice). Simultaneously, the rate of aborted and local CSDs was found to be at 47.5 % (28/59) in slices of wildtype animals, whereas the rate of failed CSDs was observed to be at only 12.9 % (4/31) in slices of heterozygous animals, overall indicating a higher susceptibility to CSDs *in vitro* ($n_{wt/wt}$ = 59 slices from 10 mice, $n_{P290R/wt}$ = 31 slices from 5 mice; $P < 0.01$; Fisher's exact test; **Figure 17 B**). An elevated CSD susceptibility has been demonstrated in numerous transgenic (F)HM models and is therefore considered to be a distinguishing feature for HM mouse models.

In the same setting, the propagation velocity, which was estimated by using the migrating wavefront captured in the IOS images, was significantly increased in slices of *Slc1a3*$^{P290R/wt}$ knock-in animals compared to wildtype animals ($n_{wt/wt}$ = 34 from 10 mice, $n_{P290R/wt}$ = 28 [5 mice]; $P < 0.001$; Welch-corrected unpaired t-test; **Figure 17 C**). Descriptive statistics are shown in **Table 6**.

3.2.2 Altered K^+ dynamics in slices of *Slc1a3*$^{P290R/wt}$ animals

To determine the role of K^+ in the pathophysiological cascade of the novel *Slc1a3*$^{P290R/wt}$ knock-in model and to compare the results to the *Scn1a*$^{L1649Q/wt}$ model for FHM3[1], $[K^+]_e$ was recorded in slices of heterozygous and wildtype animals before and during CSD using K^+-sensitive electrodes. All parameters based on the ion-sensitive recordings were calculated in accordance with the previously conducted CSD recordings using the FHM3 mouse model[1]. Further details are also provided in sections 3.1.1. and 3.1.2.

In contrast to the *Scn1a*$^{L1649Q/wt}$ model[1], $[K^+]_e$ at the inflection point was significantly lower in slices of *Slc1a3*$^{P290R/wt}$ animals compared to slices of wildtype littermates, whereas the maximum $[K^+]_e$ of the whole K^+ curve did not differ between the genotypes ($n_{wt/wt}$ = 34 [10 mice], $n_{P290R/wt}$ = 28 [5 mice]; $P < 0.05$; $P = 0.67$; Mann-Whitney rank sum test; **Figure 17 D, E**). Thus, the maximum speed of the $[K^+]_e$ rise was already reached at lower concentrations in the *Slc1a3*$^{P290R/wt}$ mouse model, but overall K^+ levels were not altered with respect to a $[K^+]_e$ increase or decrease during CSD. Baseline $[K^+]_e$ did not differ between the genotypes (**Figure 17 F**).

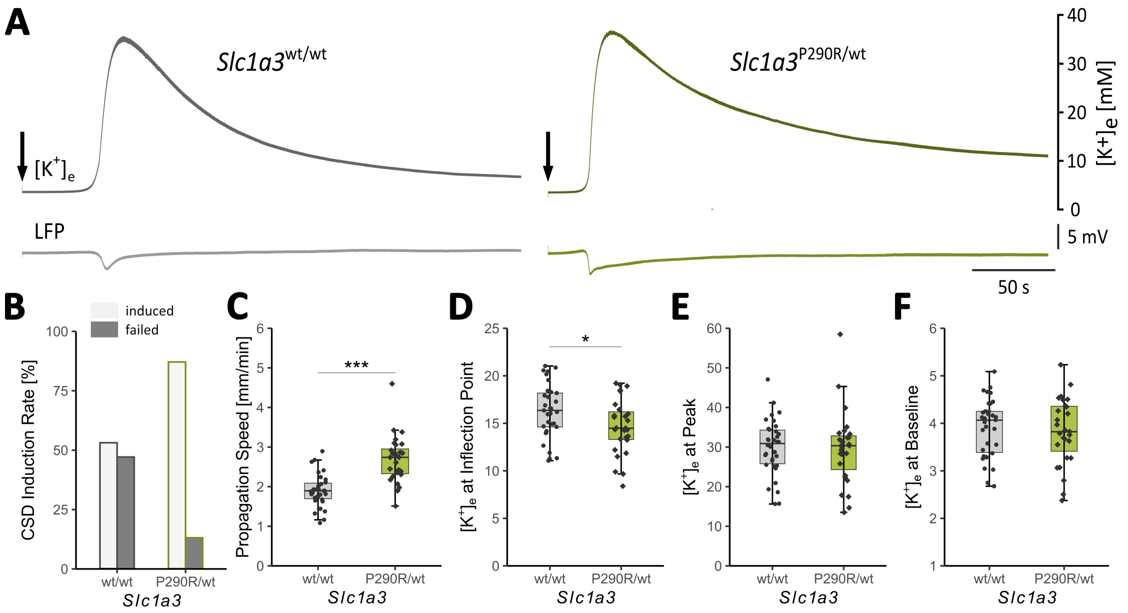

Figure 17. Increased CSD susceptibility and propagation speed as well as decreased $[K^+]_e$ levels at the inflection point in slices of *Slc1a3*$^{P290R/wt}$ animals. (**A**) Representative traces of K^+-sensitive microelectrode recording (top) and CSD-confirming LFP recording (bottom) before and during CSD illustrated for the slice of a wildtype (left, grey) and a heterozygous animal (right, green). The arrow marks the start of the CSD elicited by a KCl puff. (**B**) The success rate of CSDs was higher in slices of *Slc1a3*$^{P290R/wt}$ versus wildtype mice ($n_{wt/wt}$ = 59 slices from 10 mice [59/10]; $n_{P290R/wt}$ = 31 slices from 5 mice [31/5]; $P < 0.01$; Fisher's exact test). (**C**) The speed of the propagating wavefront was increased in slices of heterozygous versus wildtype animals ($n_{wt/wt}$ = 34/10, $n_{P290R/wt}$ = 28/5; $P < 0.001$; Welch-corrected unpaired t-test). (**D**) $[K^+]_e$ at the inflection point was decreased in slices of *Slc1a3*$^{P290R/wt}$ compared to wildtype animals ($n_{wt/wt}$ = 34/10, $n_{P290R/wt}$ = 28/5; $P < 0.05$; Mann-Whitney rank sum test), whereas (**E**) the maximum $[K^+]_e$ at the peak of the ion-sensitive recording did not differ between the genotypes ($n_{wt/wt}$ = 34/10, $n_{P290R/wt}$ = 28/5; Mann-Whitney rank sum test). (**F**) There was no difference in the $[K^+]_e$ baseline, calculated by the average of the first 10 s of the recording ($n_{wt/wt}$ = 34/10, $n_{P290R/wt}$ = 28/5; unpaired t-test).

In accordance with the analysis of the CSD recordings performed in the FHM3 model[1], a major interest was on comprehensively exploring K^+ dynamics. As already indicated by the lower $[K^+]_e$ at the inflection point, the time from the beginning of the $[K^+]_e$ increase until the inflection point was significantly shortened in slices of *Slc1a3*$^{P290R/wt}$ animals compared to slices of control mice ($n_{wt/wt}$ = 34 [10 mice], $n_{P290R/wt}$ = 28 [5 mice]; $P < 0.05$; Mann-Whitney rank sum test; **Figure 18 A**). In contrast, the time from the inflection point until the maximum $[K^+]_e$ was unaltered between the genotypes (**Figure 18 B**). The reduced time interval during the early phase of the CSD was contrary to what had been observed in the *Scn1a*$^{L1649Q/wt}$ model, in which an earlier and prolonged $[K^+]_e$ rise had been shown[1]. These findings indicated a less significant role of $[K^+]_e$ during the initiation phase of the CSD.

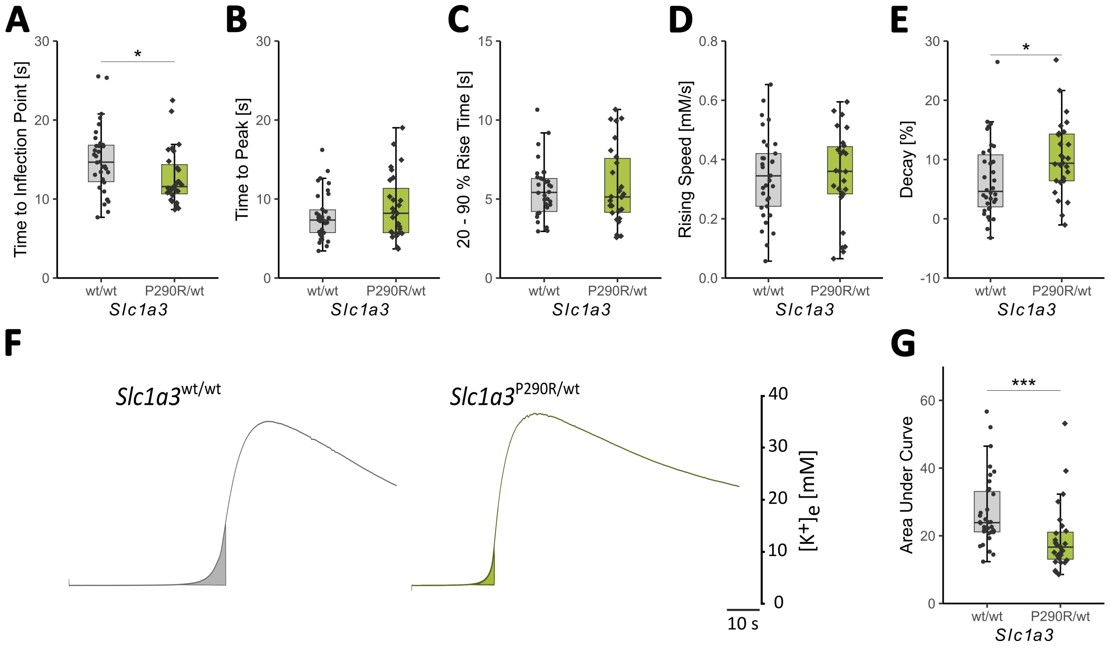

Figure 18. Altered dynamics of $[K^+]_e$ with a more rapid increase during the early CSD phase in slices of *Slc1a3*$^{P290R/wt}$ animals. (**A**) The time from the beginning of $[K^+]_e$ increase (baseline + 0.1 mM) until the inflection point was shortened in slices of heterozygous versus wildtype animals ($n_{wt/wt}$ = 34/10, $n_{P290R/wt}$ = 28/5; $P < 0.05$; Mann-Whitney rank sum test). (**B**) The time from the inflection point until the peak did not reveal any differences between the genotypes confirming that the changes in $[K^+]_e$ dynamics were confined to an early CSD interval ($n_{wt/wt}$ = 34/10, $n_{P290R/wt}$ = 28/5; Mann-Whitney rank sum test). (**C**) The 20 to 90 % rise time and (**D**) the maximum rising speed were unaltered comparing slices of wildtype and heterozygous mice ($n_{wt/wt}$ = 34/10, $n_{P290R/wt}$ = 28/5; Mann-Whitney rank sum tests). (**E**) The relative $[K^+]_e$ 200 s after the peak was elevated in slices of *Slc1a3*$^{P290R/wt}$ compared to wildtype mice ($n_{wt/wt}$ = 34/10, $n_{P290R/wt}$ = 28/5; $P < 0.05$; Mann-Whitney rank sum test). (**F**) Representative examples of K^+ traces illustrating the AUC analysis recorded from the slice of a wildtype (left, grey) and a heterozygous (right, green) animal. The AUC was calculated from the beginning of the $[K^+]_e$ rise until the inflection point. (**G**) The smaller AUC observed for slices of heterozygous compared to wildtype animals further confirmed the early changes of $[K^+]_e$ dynamics with an acceleration of the K^+ rise during CSD ($n_{wt/wt}$ = 34/10, $n_{P290R/wt}$ = 28/5; $P < 0.001$; Mann-Whitney rank sum test).

In addition, the 20 to 90 % rise time and the maximum rising speed did not differ between the genotypes (**Figure 18 C, D**). These findings overall indicated that the acceleration of the K^+ rise in slices of heterozygous animals was indeed confined to a very early phase of the CSD. The early acceleration of the $[K^+]_e$ increase was further confirmed by the AUC analysis showing a significantly reduced AUC in slices of *Slc1a3*$^{P290R/wt}$ compared to control animals ($n_{wt/wt}$ = 34 [10 mice], $n_{P290R/wt}$ = 28 [5 mice]; $P < 0.001$; Mann-Whitney rank sum test; **Figure 18 F, G**).

As opposed to the *Scn1a* mouse model[1], the relative $[K^+]_e$ 200 s after the maximum concentration of the curve, also termed the decay, was elevated in slices of *Slc1a3*$^{P290R/wt}$ animals ($n_{wt/wt}$ = 34 [10 mice], $n_{P290R/wt}$ = 28 [5 mice]; $P < 0.05$; Mann-Whitney rank sum test; **Figure 18 E**). The increased $[K^+]_e$ decay demonstrated that the K^+ levels in the *Slc1a3*$^{P290R/wt}$ model were exclusively altered during late phases of the CSD. Descriptive statistics are shown in **Table 6**.

Table 6. Descriptive statistics for the CSD recording data in *Slc1a3*$^{P290R/wt}$ and *Slc1a3*$^{wt/wt}$ animals.

	Mean (wt/wt)	**Mean (P290R/wt)**	**SD (wt/wt)**	**SD (P290R/wt)**	**t, df**	**p-value**
$[K^+]_e$ Baseline	3.9	3.8	0.6	0.7	t(59.0)=0.5	0.641

$[K^+]_e$ Decay	6.7	10.3	6.4	6.3		0.022
$[K^+]_e$ at Inflection Point	16.6	14.6	3.6	2.9		0.029
Area Under Curve	27.1	19.0	10.5	9.9		< 0.001
Maximum Rising Speed	0.4	0.4	0.2	0.2		0.746
$[K^+]_e$ at Peak	30.0	29.6	7.0	9.3		0.671
Propagation Speed	1.9	2.7	0.4	0.6	Welch-corrected t(45.6) =6.0	< 0.001
20 to 90 % Rise Time	5.5	6.2	1.8	3.0		0.823
Time Threshold-Inflection Point	14.9	12.8	4.3	3.5		0.025
Time Inflection Point-Peak	7.8	9.0	3.0	4.1		0.375

3.3 Whole-cell patch clamp recordings in the *Slc1a3*$^{P290R/wt}$ knock-in mouse model

To further unravel the functional effect of the P290R variant and determine the underlying cause for a higher CSD susceptibility, an increased propagation velocity and an accelerated $[K^+]_e$ rise during the early CSD phase, whole-cell patch clamp recordings were performed to investigate the inhibitory and excitatory synaptic transmission in the cortex. As already shown for distinct HM models, cortical hyperexcitability can be either caused by an excess of excitation or a deficit in inhibition, consequently resulting in a higher CSD susceptibility, a lower CSD threshold and an accelerated propagation velocity[1, 27, 29, 48, 53]. To investigate the E/I imbalance on the single cell level, the whole-cell patch clamp technique was used to record postsynaptic currents from cortical pyramidal neurons (**Figure 19**). In accordance with the CSD recordings described before, cortical slices from wildtype and *Slc1a3*$^{P290R/wt}$ animals from P15 to P20 were prepared and layer 2/3 of the somatosensory cortex was specifically chosen as target area, as CSD pathology was also explored and recorded in the same region.

As excitatory neurons constitute approximately 87 % of the entire cortical neuron population and thus, represent the predominant cell type in the cortex, pyramidal neurons were chosen to study the E/I balance. In the cortex, EAAT1 is predominantly expressed in astrocytes, which are known to be electrically active cells[168], but do not have the capability of generating APs under physiological conditions[169]. Therefore, despite being the main population expressing the defective protein, the glial cell subtype was not chosen to be directly investigated using electrophysiological techniques. It was hypothesised that the defective astrocytic glutamate transporters may disrupt synaptic glutamate clearance, which is known to directly affect the performance of the pyramidal cell population around those synapses[145], presumably uncovering the consequences of an altered glutamate/ Cl$^-$ homeostasis.

To detect alterations in excitatory input, sEPSCs as well as mEPSCs were studied. To characterise changes in inhibitory input, sIPSCs and mIPSCs were recorded. AMPA-receptor mediated EPSCs were recorded in the presence of the NMDA-receptor-antagonist AP-5 and the $GABA_A$-receptor antagonist PTX, whereas for IPSC recordings, AP-5 and the AMPA-/kainate-receptor antagonist CNQX were used. For mIPSCs/mEPSCs, the slices were additionally perfused with the Na^+ channel blocker TTX to block AP-driven inputs. For detecting the anticipated deficiencies in E/I balance, the instantaneous frequency, the relative amplitude, and the time constant of the decay were analysed. The time constant of the decay was exclusively investigated for the sEPCS and mEPSC recordings, since an impairment of synaptic glutamate removal was anticipated based on the P290R-associated LOF effect on astrocytic glutamate transport, which was initially hypothesised to result in longer decay time constants.

3.3.1 Unaltered phasic glutamatergic transmission at cortical synapses of *Slc1a3*$^{P290R/wt}$ animals *in vitro*

Recordings of spontaneous EPSCs did not reveal any significant differences in the relative amplitude and in the instantaneous frequency recorded from layer 2/3 cortical pyramidal neurons (**Figure 19 E, I**) in slices of *Slc1a3*$^{P290R/wt}$ versus those of wildtype animals (**Figure 19 A, B, C**). Also, the analysis of the sEPSC decay time constant did not show any differences between the two genotypes (**Figure 19 A, D**).

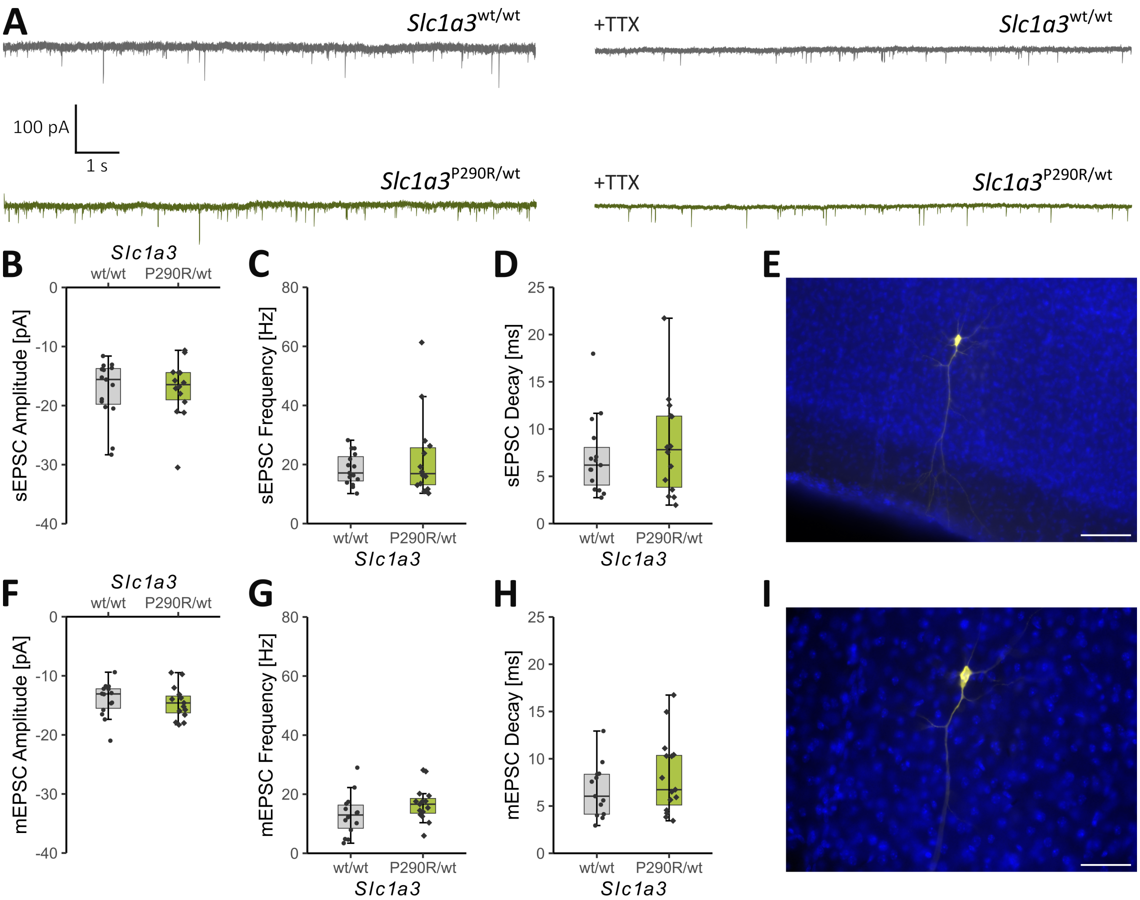

Figure 19. Unaltered excitatory (glutamatergic) synaptic transmission in slices of *Slc1a3*$^{P290R/wt}$ animals. (**A**) Representative traces of excitatory postsynaptic currents recorded from layer 2/3 pyramidal neurons in slices of wildtype (top, grey) versus heterozygous (bottom, green) animals. Spontaneous EPSCs were recorded in the presence of AP-5 and PTX (left traces). For mEPSCs, slices were additionally perfused with

TTX to block AP-driven inputs (right traces). (**B**) Analysis of the sEPSC amplitude, (**C**) the instantaneous frequency of the sEPSCs and (**D**) the time constant of the sEPSC decay did not reveal any differences between the genotypes ($n_{wt/wt}$ = 15/7, $n_{P290R/wt}$ = 14/6; Mann-Whitney rank sum tests). (**E**) Representative example of a biocytin filled pyramidal cell in layer 2 of the somatosensory cortex combined with a DAPI staining (20x magnification). Scale bar: 100 µm. (**F**) Analysis of the mEPSC amplitude, (**G**) the instantaneous frequency of the mEPSCs and (**H**) the mEPSC decay time constant were unaltered comparing pyramidal cells recorded from slices of heterozygous versus wildtype animals ($n_{wt/wt}$ = 14/6, $n_{P290R/wt}$ = 15/6; unpaired t-test; unpaired t-test; Mann-Whitney rank sum test). (**I**) 40x magnification of the biocytin filled pyramidal cell in E. Scale bar: 50 µm.

To isolate mEPSCs, 1 µM TTX was additionally added to the recording aCSF to block Na^+ channels and consequently APs. The mEPSC amplitude and instantaneous frequency recorded from pyramidal neurons in slices of *Slc1a3*$^{P290R/wt}$ animals were not distinct from pyramidal neurons in slices of wildtype littermates (**Figure 19 A, F, G**). Furthermore, the mEPSC decay time constants were unaltered between the genotypes (**Figure 19 A, H**). Descriptive statistics are provided in **Table 7**.

Table 7. Descriptive statistics for the whole-cell patch clamp data (m/sEPSC recordings) in *Slc1a3*$^{P290R/wt}$ animals and wildtype littermates.

	Mean (wt/wt)	**Mean (P290R/wt)**	**SD (wt/wt)**	**SD (P290R/wt)**	**t, df**	**p-value**
mEPSC Amplitude	-14.0	-14.5	2.9	2.7	t(27.0)=0.5	0.627
mEPSC Decay Tau	8.3	8.2	6.6	4.0		0.533
mEPSC Frequency	13.0	16.7	7.1	5.8	t(27.0)=1.5	0.136
sEPSC Amplitude	-17.4	-17.2	5.1	5.0		0.747
sEPSC Decay Tau	7.0	8.3	4.1	5.4		0.561
sEPSC Frequency	18.5	22.2	5.4	14.3		0.983

3.3.2 Unaltered phasic GABAergic transmission at cortical synapses of *Slc1a3*$^{P290R/wt}$ animals *in vitro*

Likewise, analysis of the sIPSC amplitude did not reveal any differences between layer 2/3 pyramidal neurons recorded in slices of heterozygous versus those of wildtype animals (**Figure 20 A, B**). Furthermore, the instantaneous frequency of the sIPSCs were unaltered between layer 2/3 pyramidal neurons of both genotypes (**Figure 20 A, C**).

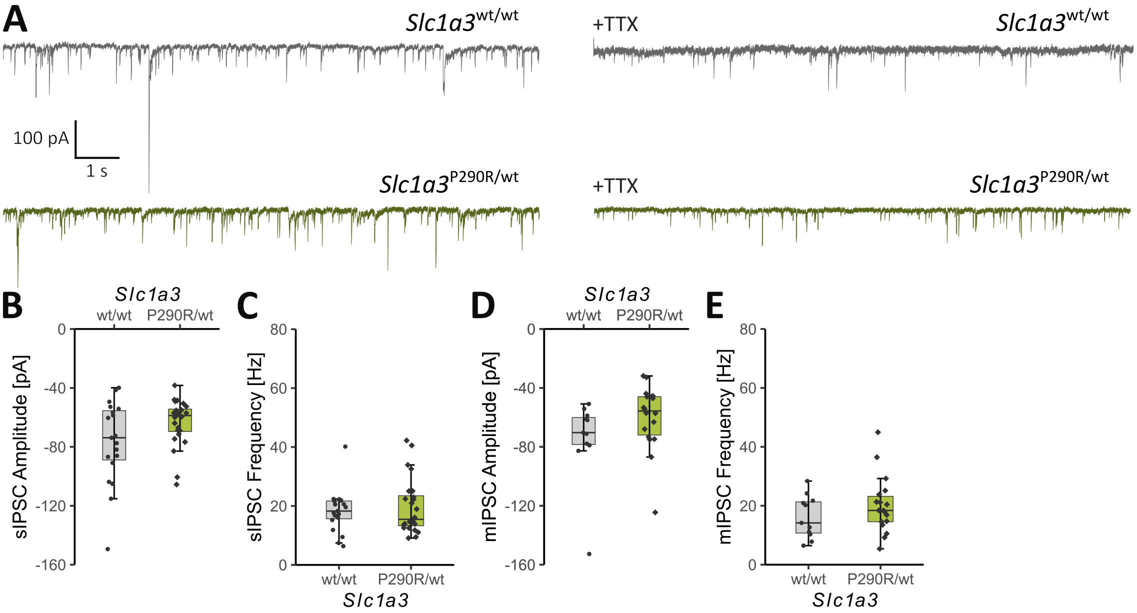

Figure 20. Unaltered inhibitory (GABAergic) synaptic transmission in slices of *Slc1a3*$^{\mathrm{P290R/wt}}$ animals. (**A**) Representative traces of inhibitory postsynaptic currents recorded from layer 2/3 excitatory neurons of the somatosensory cortex in slices of wildtype (top, grey) and heterozygous (bottom, green) animals. Spontaneous IPSCs were recorded during continuous perfusion with AP-5 and CNQX (left traces), whereas for the mIPSC recordings, TTX was additionally applied to the recording solution (right traces). (**B**) Analysis of the sIPSC amplitude and (**C**) the instantaneous frequency of the sIPSCs did not reveal any differences between excitatory neurons in slices of wildtype versus *Slc1a3*$^{\mathrm{P290R/wt}}$ mice ($n_{\mathrm{wt/wt}}$ = 19/8, $n_{\mathrm{P290R/wt}}$ = 24/11; Mann-Whitney rank sum tests). (**D**) Analysis of the mIPSC amplitude and (**E**) the instantaneous frequency of the mIPSCs did not show any differences between the genotypes ($n_{\mathrm{wt/wt}}$ = 11/4, $n_{\mathrm{P290R/wt}}$ = 18/10; Mann-Whitney rank sum tests).

TTX perfusion of the acute slices enabled the isolation of miniature IPSCs recorded from layer 2/3 pyramidal cells in the somatosensory cortex. However, mIPSC recordings did not reveal any significant differences in the amplitude or in the instantaneous frequency, when recorded from excitatory neurons in slices of *Slc1a3*$^{\mathrm{P290R/wt}}$ versus those of wildtype animals (**Figure 20 A, D, E**). Descriptive statistics are found in **Table 8**.

Table 8. Descriptive statistics for the whole-cell patch clamp data (m/sIPSC recordings) in *Slc1a3*$^{\mathrm{P290R/wt}}$ animals and wildtype littermates.

	Mean (wt/wt)	**Mean (P290R/wt)**	**SD (wt/wt)**	**SD (P290R/wt)**	**t, df**	**p-value**
mIPSC Amplitude	-74.6	-60.0	27.9	22.0		0.068
mIPSC Frequency	16.2	20.1	7.2	9.6	t(27.0)=1.2	0.254
sIPSC Amplitude	-76.7	-63.6	28.1	16.0		0.121
sIPSC Frequency	18.3	19.8	7.3	9.4		0.913

3.3.3 Unchanged cortical tonic inhibition in slices of *Slc1a3*$^{\mathrm{P290R/wt}}$ animals

As mentioned in section 1.7, Fahlke and colleagues had recently proposed that a decreased tonic GABAergic inhibition of the granule cell population in the DG may be the underlying pathophysiological mechanism for the development of hippocampal hyperexcitability and consequently, of epileptic seizures in *Slc1a3*$^{\mathrm{P290R/wt}}$ animals (**Figure 7**) (unpublished data). It was concluded that an increased P290R-associated EAAT1 Cl^- efflux would result in an enhanced driving force for GABA uptake via GAT-3, which would simultaneously reduce the ambient GABA levels and diminish tonic inhibition (unpublished data by Fahlke and colleagues).

As HM pathophysiology is assumed to primarily originate from cortical regions, it was hypothesised that the mechanistic cascade supposedly leading to epilepsy in the *Slc1a3*$^{P290R/wt}$ mouse model could be directly transferred from the hippocampal to the cortical region causing cortical hyperexcitability and CSD pathology. However, in the cortex, EAAT1 is predominantly expressed in astrocytes that surround cortical pyramidal neurons as opposed to the hippocampal region, where the RGL cell populations surround DG granule cells. Therefore, tonic GABAergic currents were investigated in layer 2/3 pyramidal neurons of the somatosensory cortex, which was also in accordance with the previously performed recordings of CSD and synaptic transmission. In general, tonic inhibition, as opposed to phasic inhibition, is exerted via extrasynaptic $GABA_A$ receptors modulating the excitability of the entire neuronal network[170, 171].

For estimating the $GABA_A$-receptor mediated tonic conductance, the average of a 30 seconds-lasting holding current after continuous PTX perfusion was subtracted from the averaged holding current that had been recorded in the exclusive presence of AP-5 and CNQX. Cells were held at a membrane potential of -70 mV.

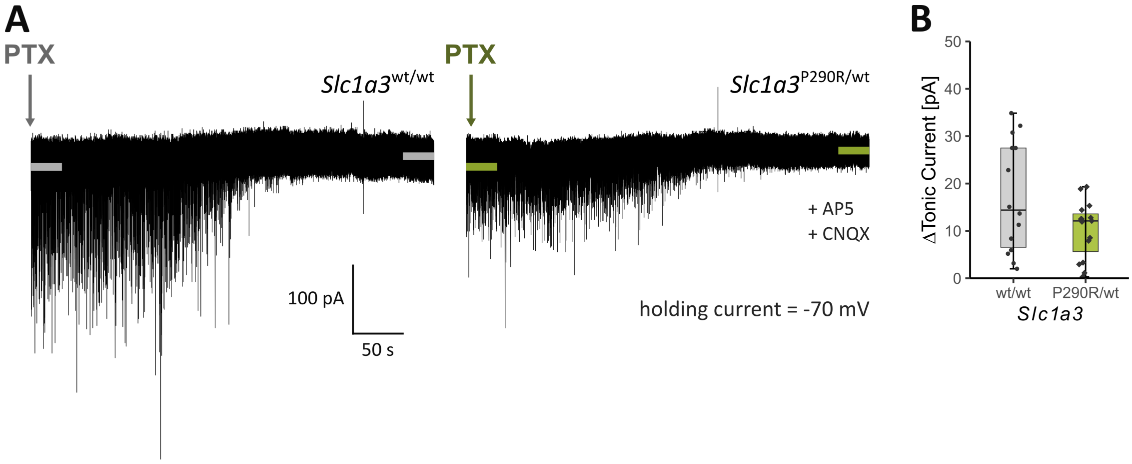

Figure 21. Unchanged tonic GABAergic currents in slices of *Slc1a3*$^{P290R/wt}$ animals. (**A**) Representative traces of tonic current recordings from layer 2/3 pyramidal cells of the somatosensory cortex in the presence of AP-5 and CNQX. To estimate of the amount of the $GABA_A$-receptor mediated conductance, the average of a 30 s current epoch during continuous PTX perfusion was subtracted from the average of a 30 s PTX-free baseline holding current. Cells were held at -70 mV. (**B**) The magnitude of the tonic GABAergic currents did not reveal significant alterations between the genotypes ($n_{wt/wt}$ = 14/7, $n_{P290R/wt}$ = 15/9; *P* = 0.063; Welch-corrected unpaired t-test).

Although tonic inhibitory currents recorded from layer 2/3 pyramidal cells did not reveal any statistical difference between the two genotypes, a trend towards a diminished tonic inhibition of pyramidal cells in the cortex of *Slc1a3*$^{P290R/wt}$ mice was observed ($n_{wt/wt}$ = 14 [7 mice], $n_{P290R/wt}$ = 15 [10 mice]; *P* = 0.06; t-test with Welch correction; **Figure 21 A, B**). Descriptive statistics are given in **Table 9**.

Table 9. Descriptive statistics for tonic current recordings in *Slc1a3*$^{\text{P290R/wt}}$ animals and wildtype littermates.

	Mean (wt/wt)	Mean (P290R/wt)	SD (wt/wt)	SD (P290R/wt)	t, df	p-value
ΔTonic Current	17.2	10.3	11.7	6.1	Welch corrected t(19.2)=2.0	0.063

3.4 Additional P290R-associated phenotypes and *in vivo* recordings of epileptic seizures in *Slc1a3*$^{\text{P290R/wt}}$ animals

The *Slc1a3*$^{\text{P290R/wt}}$ mouse model was used to study HM-associated additional phenotypes. First, the growth of *Slc1a3*$^{\text{P290R/wt}}$ versus wildtype animals as well as gender-related differences were explored in detail. Moreover, to investigate the frequent co-occurrence of epilepsy in HM patients, the presence of epileptic seizures as well as their neurophysiological features were analysed using the EA6 model.

The *Scn1a*$^{\text{L1649Q/wt}}$ mouse model was not used for this purpose as, firstly, patients carrying the L1649Q variant are known to have a pure HM phenotype without epilepsy, and, secondly, heterozygous animals did not show any signs of epileptic seizures during the initial phenotypic screening[1] as well as during regular observations and handling. Basically, heterozygous animals did not differ from their wildtype littermates with respect to behaviour[1]. Nevertheless, to rule out a rare co-occurrence or subclinical presentation of spontaneous epileptic seizures, *Scn1a*$^{\text{L1649Q/wt}}$ animals would have to be comprehensively analysed using video-EEG-monitoring.

3.4.1 Weight reduction of *Slc1a3*$^{\text{P290R/wt}}$ animals during a critical time window

Slc1a3$^{\text{P290R/wt}}$ animals were studied with respect to basic body measures, as an unequivocal correlation between the occurrence of epileptic seizures and a stagnation of further weight gain or a reduction in body weight was noticed. In general, heterozygous animals and wildtype littermates were evaluated on a regular basis with respect to appearance, behaviour, health status and weight using score sheets. The body weight was continuously recorded from P3 to P50, which is the time interval coinciding with disease onset, the period of highest seizure susceptibility and the compensatory period characterised by a diminishing seizure frequency. Furthermore, the gender was observed to have an impact on the phenotype of *Slc1a3*$^{\text{P290R/wt}}$ animals and specifically the severity of the epileptic phenotype.

As the genotype was not determined until the weaning period, differences in growth and body weight were statistically evaluated starting at P21. At P21, the body weight/growth curve of heterozygous *Slc1a3*$^{\text{P290R/wt}}$ knock-in animals was noticed to deviate from the curve of wildtype littermates (**Figure 22 A, B**). Weight loss or stagnation of weight gain were exclusively observed during seizure occurrence. After reaching a maximum in body weight difference at P29 to P31, body weight gain for all heterozygous and wildtype animals was found to be similar again (**Figure 22 A**). Nevertheless, heterozygous animals stayed underweight in comparison to their wildtype littermates during the period of highest seizure susceptibility and persistently during an assumed compensatory phase after having passed the period of highest seizure vulnerability (**Figure 22 A, C, D**).

To eliminate confounding factors and unravel potential gender differences, weight gain was evaluated separately for female and male heterozygous versus wildtype animals. The body weight analyses specifically for each gender also revealed differences between the male and female population (**Figure 22 C, D, E, F**).

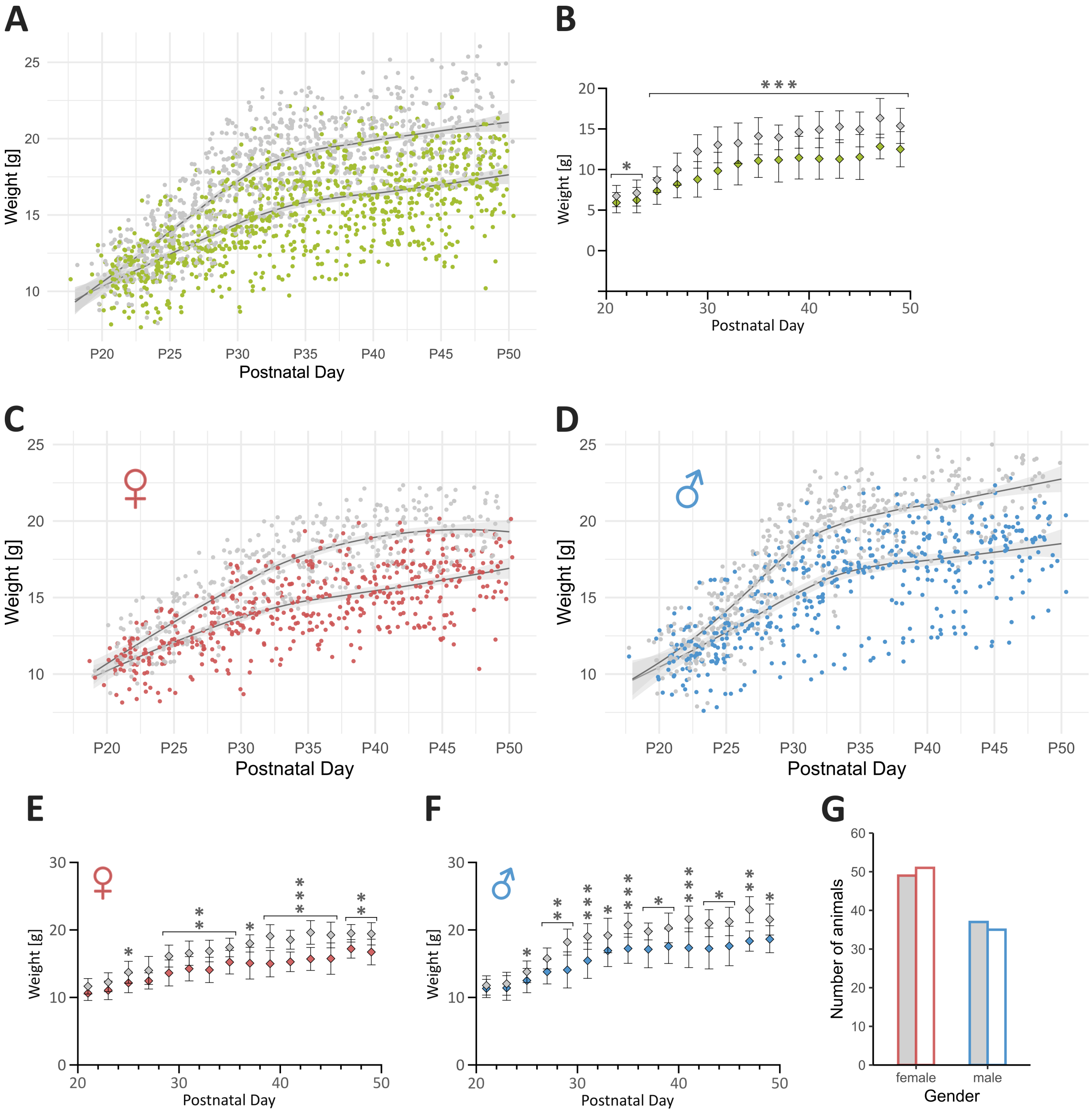

Figure 22. Delayed growth during epileptogenesis and gender-related differences in *Slc1a3*$^{P290R/wt}$ animals. (**A**) Weight gain/growth was diminished in heterozygous (green dots) versus wildtype (grey dots) animals during epileptogenesis. Statistical analysis started after weaning (P21). Trend lines for the growth curve of wildtype (top) and heterozygous (bottom) animals were implemented in the chart to optimise visualisation. (**B**) Starting at P21, the weight of *Slc1a3*$^{P290R/wt}$ animals was decreased in comparison to wildtype littermates, which is shown for the odd days until P49. Body weight difference was maximum around P30 (P21-P49: $n_{wt/wt}$ = 17-50, $n_{P290R/wt}$ = 26-42; P21-P23: $P < 0.05$; P25-P49: $P < 0.001$; Multiple Mann-Whitney rank sum tests) (also see **Table 10**). (**C**) A difference in body weight gain was observed for female heterozygous (red dots) compared to female wildtype (blue dots) mice from P20 to P50. The lines for the weight of female *Slc1a3*$^{P290R/wt}$ animals (bottom) and female wildtype littermates (top) were graphically implemented to visualise the respective trend. (**D**) Male heterozygous animals (blue dots) were underweight compared to male wildtype littermates (grey dots) starting at P20, which is shown until P50. Trend lines are drawn for the growth curve of male heterozygous (bottom) and male wildtype mice (top). (**E**) Starting at P25, the growth of female heterozygous *Slc1a3*$^{P290R/wt}$ animals was reduced compared to female wildtype animals, peaking from P39 to P45. The means and standard errors of the means (SEMs)

were calculated from the dataset shown in Figure C. Only the odd days, from P21 to P49, are shown. (P21-P49: $n_{wt/wt} = 8\text{-}19$, $n_{P290R/wt} = 9\text{-}22$; P25/P37: $P < 0.05$; P29-P35/P47-P49: $P < 0.01$; P39-45: $P < 0.001$; Multiple Mann-Whitney rank sum tests) (also see **Table 11**). (**F**) From P25 to P49, the weight gain of male heterozygous animals was diminished in comparison to male wildtype littermates, which is exclusively shown for the odd days. The means and SEMs were calculated from the dataset shown in Figure D. The difference in growth between male wildtype and male heterozygous mice was observed to be undulating during epileptogenesis (P21-P49: $n_{wt/wt} = 7\text{-}30$, $n_{P290R/wt} = 11\text{-}23$; P25/P33/P37-P39/P43-45/P49: $P < 0.05$; P27-P29/P47: $P < 0.01$; P31/35/41: $P < 0.001$; Multiple Mann-Whitney rank sum tests) (also see **Table 12**). (**G**) The number of born male animals was lower in comparison to born female animals, applying to both genotypes (♀ $n_{wt/wt} = 49$, ♂ $n_{wt/wt} = 37$, ♀ $n_{P290R/wt} = 51$, ♂ $n_{wt/wt} = 35$).

The growth/body weight gain was diminished in female heterozygous animals in comparison with female control mice during the analysed time interval from P20 until P50 (**Figure 22 C, E**). Similarly, during epileptogenesis and the subsequent compensatory phase, the growth/body weight gain of male heterozygous animals was reduced compared to male wildtype littermates (**Figure 22 D, F**). However, the maximum difference in body weight for female *Slc1a3*$^{P290R/wt}$ versus wildtype animals was found later in comparison to the male population, approximately from P39 to P45, overall indicating a later onset of the epileptic phenotype (**Figure 22 E**). In contrast, the differences in body weight observed for the male heterozygous versus male wildtype animals appeared to be undulating during a large time interval from P25 to P49, indicating a more variable onset and occurrence of epileptic seizures (**Figure 22 F**). Furthermore, curve progression of the female *Slc1a3*$^{P290R/wt}$ animals implied a potential re-gain of body weight during the late compensatory phase (**Figure 22 C**).

Additionally, male animals made the impression to be affected more severely by the epileptic phenotype. As exclusively male animals were implanted, this difference was only observational and could not be confirmed based on the acquired EEG recording data. Of note, the rate of male animals that were born during breeding was lower compared to the number of born female animals. However, interestingly, this distinction was not only evident for the heterozygous, but also for the wildtype male mice. Despite not reaching statistical significance a clear trend was observed (♀ $n_{wt/wt} = 49$, ♂ $n_{wt/wt} = 37$, ♀ $n_{P290R/wt} = 51$, ♂ $n_{wt/wt} = 35$, **Figure 22 G**). Of all *Slc1a3*$^{P290R/wt}$ and *Slc1a3*$^{wt/wt}$ animals that were born during breeding 58.14 % were female, whereas only 41.86 % were male. Descriptive statistics of the body weight data for both genders as well as the male and female heterozygous and wildtype animals are, in addition to **Figure 22**, shown in **Table 10**, **Table 11** and **Table 12**.

Table 10. Descriptive statistics for the growth/body weight data in all *Slc1a3*$^{P290R/wt}$ animals and wildtype littermates.

	n (wt/wt)	**n (P290R/wt)**	**Mean (wt/wt)**	**Mean (P290R/wt)**	**SD (wt/wt)**	**SD (P290R/wt)**	**p-value**
P21	30	30	11.7	10.9	1.3	1.3	0.034
P23	36	34	12.1	11.2	1.6	1.6	0.034
P25	50	42	13.8	12.4	1.6	1.7	< 0.001
P27	39	29	15.1	13.2	2.0	1.7	< 0.001
P29	34	34	17.2	13.8	2.1	2.2	< 0.001
P31	40	39	17.8	14.9	2.4	2.3	< 0.001
P33	42	30	18.3	15.7	2.5	2.6	< 0.001
P35	35	32	19.1	16.1	2.3	2.1	< 0.001

P37	26	26	19.0	16.2	1.5	2.7	< 0.001
P39	23	30	19.6	16.5	2.0	2.6	< 0.001
P41	25	37	19.9	16.4	2.2	2.5	< 0.001
P43	21	29	20.3	16.3	2.0	2.4	< 0.001
P45	23	35	20.0	16.5	2.2	2.8	< 0.001
P47	17	20	21.4	17.9	2.4	1.5	< 0.001
P49	16	25	20.4	17.5	2.2	2.2	0.001

Table 11. Descriptive statistics for the growth/body weight data in female *Slc1a3*$^{\text{P290R/wt}}$ animals and female wildtype littermates.

	n (wt/wt)	**n (P290R/wt)**	**Mean (wt/wt)**	**Mean (P290R/wt)**	**SD (wt/wt)**	**SD (P290R/wt)**	**p-value**
P21	12	16	11.7	10.6	1.2	1.1	0.112
P23	11	17	12.3	11.1	1.4	1.4	0.112
P25	19	19	13.7	12.2	1.6	1.5	0.021
P27	16	13	14.0	12.5	2.1	1.2	0.112
P29	16	22	16.1	13.6	1.6	1.9	0.002
P31	16	20	16.6	14.3	1.8	1.8	0.005
P33	17	13	16.9	14.1	1.6	1.9	0.002
P35	17	21	17.4	15.2	1.4	1.8	0.003
P37	12	12	18.0	15.1	1.3	2.4	0.013
P39	13	13	19.1	15.0	1.7	2.0	< 0.001
P41	14	18	18.6	15.3	1.4	1.5	< 0.001
P43	11	18	19.6	15.7	1.8	1.7	< 0.001
P45	15	20	19.3	15.8	1.9	2.3	< 0.001
P47	8	9	19.5	17.2	1.3	1.4	0.013
P49	9	15	19.4	16.7	1.7	1.9	0.013

Table 12. Descriptive statistics for the growth/body weight data in male *Slc1a3*$^{\text{P290R/wt}}$ animals and male wildtype littermates.

	n (wt/wt)	**n (P290R/wt)**	**Mean (wt/wt)**	**Mean (P290R/wt)**	**SD (wt/wt)**	**SD (P290R/wt)**	**p-value**
P21	18	15	11.8	11.3	1.4	1.4	0.377
P23	25	15	12.0	11.4	1.7	1.8	0.358
P25	30	23	13.8	12.5	1.6	1.8	0.037
P27	23	16	15.8	13.8	1.6	1.8	0.009
P29	18	12	18.2	14.1	1.9	2.7	0.001
P31	24	19	19.0	15.5	1.9	2.6	< 0.001
P33	25	17	19.2	17.0	2.6	2.4	0.037
P35	18	12	20.7	17.3	1.8	2.2	< 0.001
P37	14	14	19.8	17.1	1.3	2.7	0.014
P39	10	17	20.3	17.6	2.2	2.6	0.037
P41	11	19	21.6	17.4	1.9	2.9	< 0.001
P43	10	11	21.0	17.3	2.0	3.0	0.037
P45	8	16	21.3	17.6	2.1	2.9	0.024
P47	9	11	23.0	18.4	1.9	1.5	0.001
P49	7	11	21.6	18.6	2.3	2.0	0.085

3.4.2 High vulnerability to status epileptici in young *Slc1a3*$^{\text{P290R/wt}}$ animals

Male *Slc1a3*$^{\text{P290R/wt}}$ knock-in animals and their wildtype littermates underwent surgery before the apparent onset of epileptic seizures and with a minimum weight of 14 g, corresponding to an age of P25 to P32. Five heterozygous and an equal number of wildtype animals were implanted with single channel EEG electrodes and connected wireless transmitters under general anaesthesia (see section 2.8). Major complications, for example cardiorespiratory arrest or massive intracranial haemorrhage, did not occur during the surgical procedures. Minor complications in the younger group comprised an increased likelihood of prolonged minor bleeding and a higher fragility of the skull during iatrogenic manipulations in comparison with older animals. All heterozygous and wildtype mice survived the one-hour recovery period after surgery. As described in section 2.9, the favoured duration of recovery time numbered approximately three days for animals implanted before seizure onset. However, as seizure-like behaviour was observed in four of five heterozygous animals on the day of implantation, video-EEG monitoring was initiated several hours following the surgical procedure. As a heating lamp was used to maintain body temperature in the first few hours postoperatively, especially in the younger mice, monitoring was not started earlier than six hours postoperatively. For one heterozygous animal, the start of the combined video-EEG recording was rescheduled to the first postoperative day, also due to an observed seizure occurrence. In contrast, the recovery time averaged 2.4 days for wildtype animals. The average duration of the combined video-EEG recordings was 38.0 hours in *Slc1a3*$^{P290R/wt}$ and 37.0 hours in wildtype animals that were implanted before seizure onset.

Video-EEG monitoring of heterozygous P25 to P32 animals contained numerous distinct seizure events, defined by the occurrence of rhythmic epileptiform discharges in the EEG trace, an unequivocal behaviour indicating a seizure or the combination of both features. The ictal events varied with respect to the severity, the duration, and the electrographic pattern, which applied to the comparison of seizure events within one *Slc1a3*$^{P290R/wt}$ animal, but also between individual heterozygous mice. Seizure events were usually introduced with a short episode of tail lifting/stiffing and occasionally a rotational head movement, followed by a tonic whole-body stretch that further proceeded to repetitive head nodding and unilateral or bilateral forelimb cloni. Most seizures ceased directly thereafter, or they were followed by an additional episode of rearing and sometimes falling, whereas a relatively small number of epileptic events was characterised by wild running and jumping of the heterozygous animals. Furthermore, numerous ictal-like events exclusively consisted of a behavioural arrest, characterised by the absence of any movements. If an epileptic seizure exceeded a duration of 5 min, either as a continuous seizure event or as two/more seizure events without complete recovery of consciousness in between, the term status epilepticus was used[164].

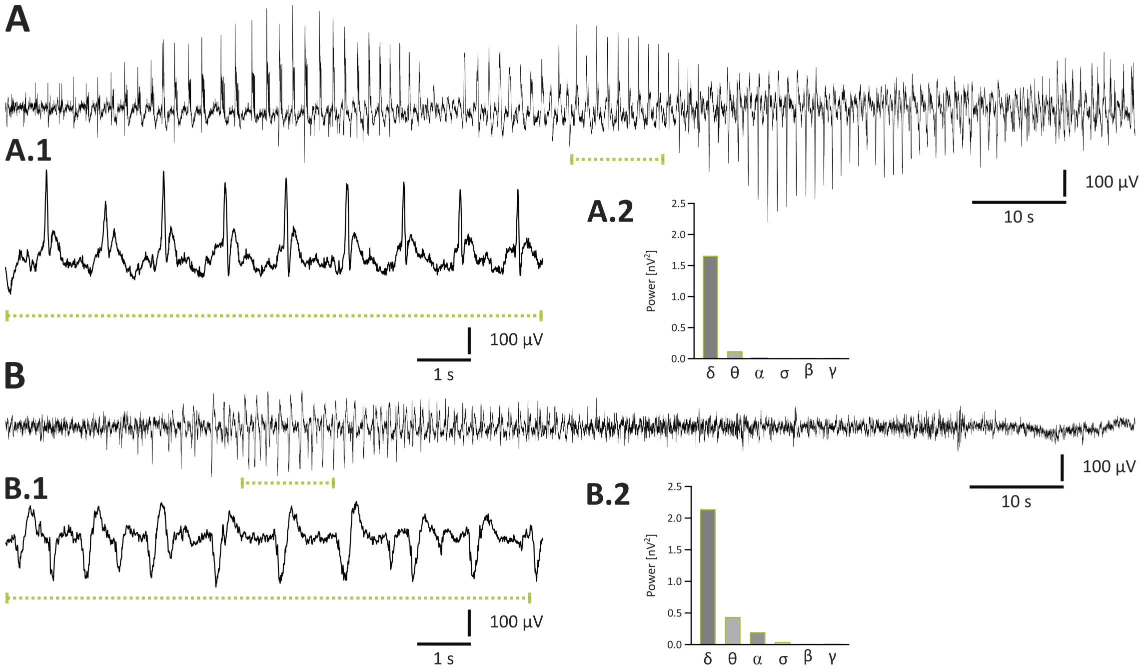

Figure 23. High vulnerability of *Slc1a3*$^{\mathrm{P290R/wt}}$ animals to ictal events during the period of maximum seizure susceptibility. (**A**) Representative example of a 50 s-epoch of an epileptic seizure with rhythmically occurring epileptiform discharges recorded in a heterozygous animal during the period of highest seizure vulnerability. (**A.1**) 10 s-cut-out of the ictal event in Figure A magnifying the epileptiform discharges. (**A.2**) During the seizure event shown in Figure 22 A.1, the power was dominated by frequencies in the lower range < 8 Hz, whereas frequencies in the upper range > 8 Hz were relatively underrepresented. (**B**) Representative EEG trace (50 s-epoch) displaying an ictal event recorded from a different heterozygous animal during the phase of maximum seizure occurrence. (**B.1**) Rhythmic spike-and-wave discharges are magnified in the 10 s-cut-out of the ictal event in Figure 22 B. (**B.2**) During the epileptiform discharges in the 10 s-epoch of Figure B.1, the delta and theta frequency ranges dominated in the power spectrum.

Representative examples for ictal events recorded from two *Slc1a3*$^{\mathrm{P290R/wt}}$ animals at P29 (**Figure 23 A, A.1, A.2**) and P26 (**Figure 23 B, B.1, B.2**) during maximum seizure susceptibility are shown in **Figure 23 A** and **Figure 23 B**, in which the rhythmically occurring spike-and-wave complexes indicated the presence of an epileptic seizure. The magnifications of two 10 s-epochs are shown in **Figure 23 A.1** and **B.1**, respectively. These ictal events during the period of highest seizure vulnerability were characterised by a predominating delta power band in the low frequency range (0.5-4 Hz) followed by the theta power band (4-8 Hz), whereas the remaining frequency bands were underrepresented (**Figure 23 A.2, A.3**).

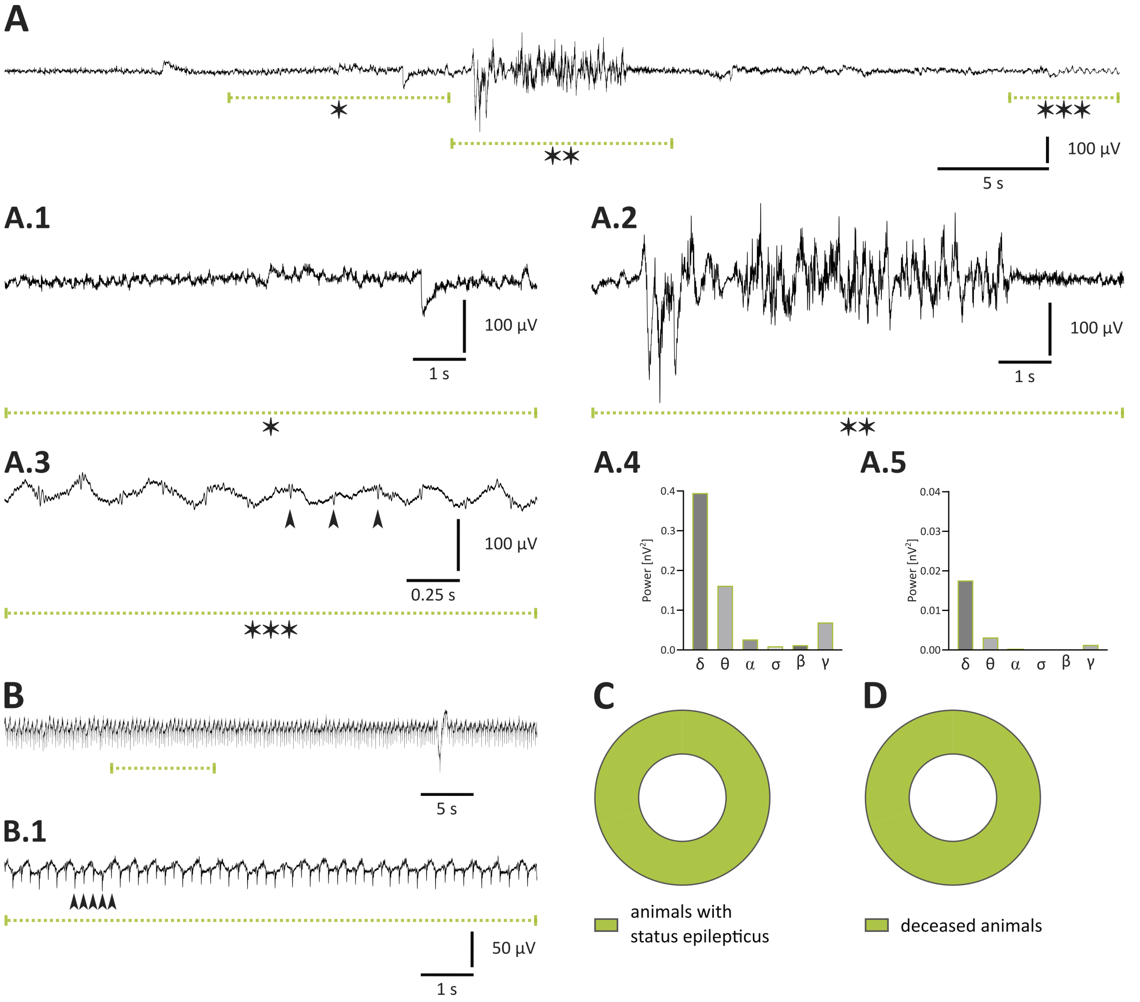

Figure 24. High susceptibility of heterozygous animals to status epileptici and frequent occurrence of suppressed electrographic activity during the fourth and fifth postnatal week. (**A**) Representative trace recorded from a young *Slc1a3*$^{P290R/wt}$ animal during the phase of highest seizure activity displaying a flat EEG signal interspersed with wave-like components and one seizure-like event, especially indicated by the behaviour of the mouse. The ictal event was not classified as a seizure mostly due to the lack of fulfilling the time criterion (duration < 10 s). (**A.1**) 10 s-cut-out of the flat EEG signal shown in Figure A preceding the ictal event, with ✶ indicating the location of the cut-out. (**A.2**) 10 s-cut-out of the EEG trace displayed in Figure A to magnify the seizure-like event < 10 s, with ✶✶ indicating the location of the epoch. (**A.3**) 2.5 s-cut-out of the electrographic signal shown in Figure A to magnify the suppressed electrographic activity after the seizure-like event, with ✶✶✶ indicating the location of the cut-out. The arrowheads (➤) mark breathing artefacts that were uncovered due to the flatness of the signal. (**A.4**) The power of the seizure-like event in Figure A.2 was dominated by frequencies in the delta and theta range (< 4 Hz, 4-8 Hz). (**A.5**) During post-ictal suppression of the EEG signal, shown in Figure A.3, delta and theta frequency ranges dominated in the power spectrum. (**B**) Representative example of a suppressed EEG signal between two seizure events recorded in a young *Slc1a3*$^{P290R/wt}$ animal that also comprised one spike-and-wave discharge. (**B.1**) Due to the flat electrographic signal breathing artefacts were uncovered, as shown in a 10 s-cut-out of the EEG trace in Figure B. The arrowheads (➤) mark 5 consecutive artefacts caused by respiration. (**C**) Video-EEG monitoring of all five implanted heterozygous animals during seizure peak revealed continuous status epileptici and consisted of numerous ictal events without full recovery of consciousness in between the seizures. (**D**) All five implanted *Slc1a3*$^{P290R/wt}$ animals reached the human endpoint or died during video-EEG monitoring.

EEG traces of all heterozygous animals that were implanted before the onset of the epileptic phenotype and recorded during seizure peak were overall characterised by flat EEG signals interspersed with many electrographically ictal events and single spikes or waves. In **Figure 24 A,** a short seizure-like event, which did not fulfil the time criterion for being classified as a seizure (**Figure 24 A.2**) but showed similar predominance of delta and theta power (**Figure 24 A.4**), was preceded by a relatively flat EEG trace comprising single sharp wave components (**Figure 24 A.1**). The short seizure-like event was succeeded by suppressed electrographic activity (**Figure 24 A.3**) with predominating delta and theta power (**Figure 24 A.5**), which was additionally interspersed with breathing artefacts. During ictal events, *Slc1a3*$^{\mathrm{P290R/wt}}$ animals usually displayed characteristic seizure-indicating behaviour, as described before. However, during episodes with suppressed EEG activity the behaviour of implanted heterozygous animals was mainly characterised by the absence of movements and an altered state of consciousness (**Figure 24 B, B.1**). The phase of postictal depression ranged from unresponsiveness to a coma-like state in the *Slc1a3*$^{\mathrm{P290R/wt}}$ mouse model. Of note, the presence of suppressed EEG activity in the heterozygous animals uncovered rhythmically occurring artefacts that were correlated with the respiratory rate of the mice using simultaneous video-monitoring (**Figure 24 A.3, B, B.1**).

All young *Slc1a3*$^{\mathrm{P290R/wt}}$ animals displayed numerous fulminant ictal events in combination with the absence of full recovery of consciousness in between the single seizures. Therefore, chronic video-EEG monitoring revealed that status epileptici were continuously present in the five implanted *Slc1a3*$^{\mathrm{P290R/wt}}$ knock-in animals (**Figure 24 C**). In contrast, the five recorded wildtype animals did not show any behavioural or rhythmically occurring electrographic signs for epileptic seizures during the monitoring period.

Of five heterozygous animals, one *Slc1a3*$^{\mathrm{P290R/wt}}$ mouse died during continuous recording and four animals reached the human endpoint requiring termination of the experiment and killing of the respective animal (**Figure 24 D**). The time, until *Slc1a3*$^{\mathrm{P290R/wt}}$ animals that were implanted before the onset of seizures reached the human endpoint, averaged 40.28 hours per animal. Due to the lack of continuous electrographic monitoring, it is not possible to directly compare the data of implanted with non-implanted heterozygous animals during the period of maximum seizure vulnerability. Nevertheless, the severity and frequency of seizures/status epileptici appeared to be increased in heterozygous mice that had received surgery beforehand, indicating that either the surgical procedure itself or the impact of the applied general anaesthesia or antidot may play a role in worsening the epileptic phenotype in the *Slc1a3*$^{\mathrm{P290R/wt}}$ mouse line. To summarise, video-EEG monitoring clearly revealed that *Slc1a3*$^{\mathrm{P290R/wt}}$ animals recorded during the peak period of seizure susceptibility were highly vulnerable to seizures and status epileptici.

3.4.3 Increased vulnerability to epileptic seizures in *Slc1a3*$^{\mathrm{P290R/wt}}$ animals after the peak period of seizures

The requirements for implanting *Slc1a3*$^{\mathrm{P290R/wt}}$ and wildtype mice with EEG recording systems comprised the survival of the period of maximum seizure susceptibility as well as a minimum weight of 20 g, corresponding to an age of P44 to P53. All implanted animals survived the immediate post-surgical period of one hour. Of the eight implanted wildtype mice, one animal died during the first postoperative night. Despite a comprehensive post-mortem examination, the cause of death remained unclear. As outlined in detail in section 2.7, the preferable duration of recovery following surgery was set to be seven days for the animal group that was implanted after having passed the time of highest seizure vulnerability. For all seven wildtype and four of ten heterozygous animals, the planned one-week postoperative recovery period was complied with. However, in six of ten *Slc1a3*$^{P290R/wt}$ animals, chronic video-EEG monitoring was initiated earlier within the first postoperative days either because of a suspected occurrence of epileptic seizures or due to unclear worsening of the animal's health status.

For heterozygous animals implanted after the peak period of seizures, the average duration of one video-EEG monitoring was 37.84 hours per animal, whereas the recording duration for wildtype littermates averaged 49.65 hours per animal. As six of ten heterozygous animals reached the human endpoint or died during monitoring, the average recording duration per animal was shorter for *Slc1a3*$^{P290R/wt}$ compared to wildtype animals. Due to a higher number of implanted and recorded *Slc1a3*$^{P290R/wt}$ animals, overall recording duration numbered 378.43 hours for *Slc1a3*$^{P290R/wt}$ mice and 347.58 hours for *Slc1a3*$^{wt/wt}$ mice.

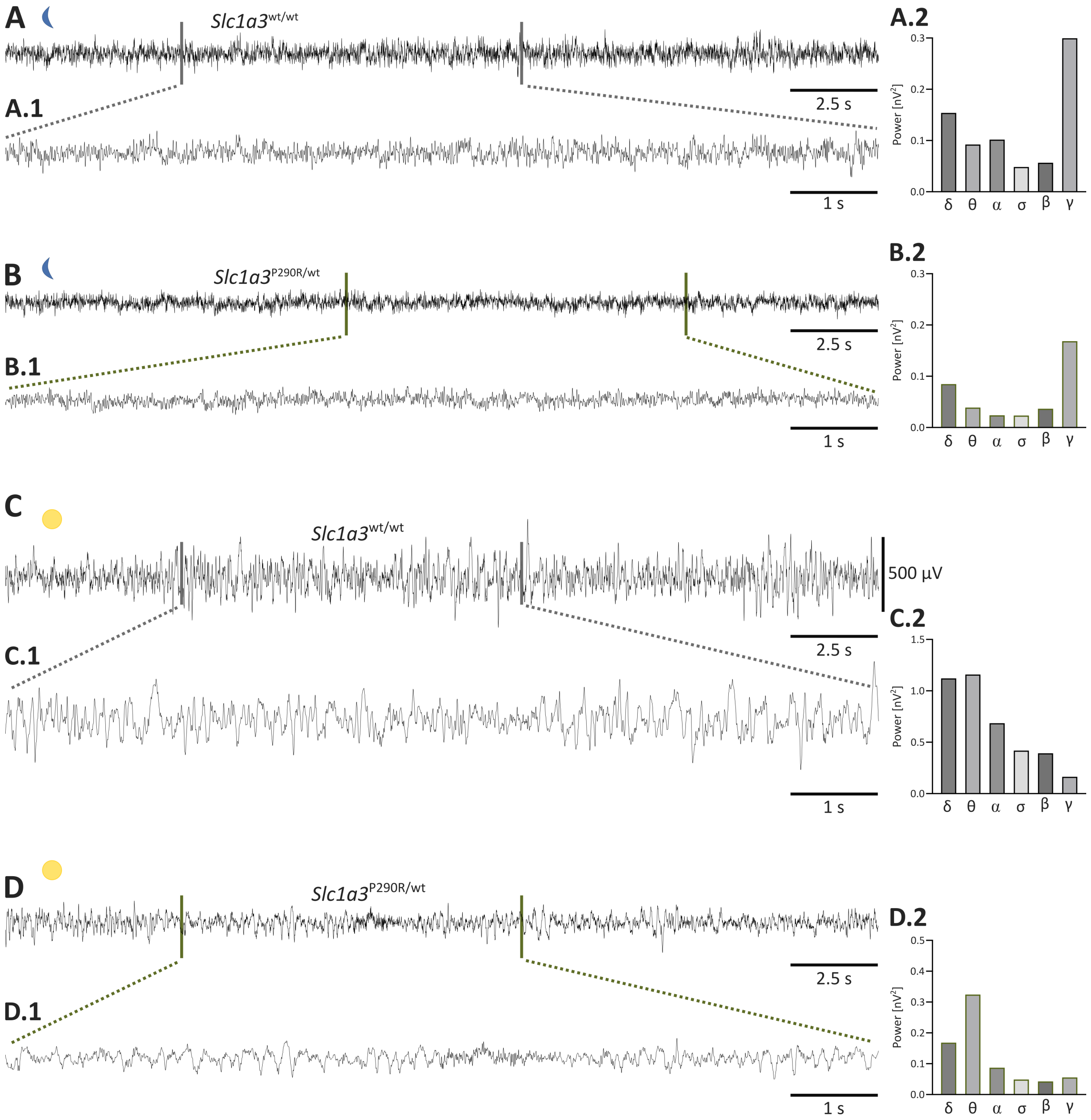

Figure 25. Physiological baseline activity during wake and sleep episodes in *Slc1a3*$^{P290R/wt}$ and wildtype animals during video-EEG monitoring in the compensatory phase. (**A**) Representative example of baseline EEG activity in an awake, moving *Slc1a3*$^{wt/wt}$ animal during the dark phase as indicated by the moon

sign. (**A.1**) 10 s-epoch to magnify the physiological EEG activity shown in Figure A. (**A.2**) In the EEG trace shown in Figure A.1, all frequency ranges were represented in the power spectrum, with a dominance of the gamma band. (**B**) Representative example recorded from an awake *Slc1a3*$^{\mathrm{P290R/wt}}$ mouse during the dark phase displaying physiological baseline activity while the animal was freely moving in the cage. (**B.1**) 10 s-cut-out to magnify the physiological activity in the EEG trace shown in Figure B. (**B.2**) The gamma band dominated in the power spectrum, but all frequency ranges were represented in the cut-out shown in Figure B.1. (**C**) Representative example of physiological baseline activity with high amplitudes during the light phase, as indicated by the sun sign, recorded from a sleeping *Slc1a3*$^{\mathrm{wt/wt}}$ mouse. (**C.1**) 10 s-cut-out of the EEG trace in Figure C to magnify the electrographic activity during sleep. (**C.2**) During sleep (Figure C.1), the power spectrum was characterised by dominating frequencies in the lower range, in particular delta and theta, relative to the remaining frequency bands. (**D**) Representative example of an EEG trace recorded from a sleeping *Slc1a3*$^{\mathrm{P290R/wt}}$ mouse during the light phase. High EEG amplitudes, dominating frequency ranges < 8 Hz and sleeping behaviour were used to identify sleep episodes. (**D.1**) Magnification of a 10 s-cut-out of the EEG trace in Figure D for better visualisation of the electrographic activity during sleep (**D.2**) In the power spectrum, frequencies in the theta followed by the delta range dominated the 10 s-epoch shown in Figure D.1.

In contrast to *Slc1a3*$^{\mathrm{P290R/wt}}$ animals recorded during the period of highest seizure susceptibility, video-EEG monitoring of heterozygous animals recorded after the peak of seizures comprised normal baseline activity during wake and sleep episodes (**Figure 25 B, B.1, D, D.1**) as well as pathological brain activity including seizure events or status epileptici. Recordings of older animals revealed that, depending on the individual animal, the traces consisted of exclusive physiological activity, exclusive pathological activity, or a combination of both. In contrast, EEG traces of wildtype *Slc1a3*$^{\mathrm{wt/wt}}$ mice only showed physiological activity during wake and sleep episodes, with an absence of seizures and status epileptici (**Figure 25 A, A.1, C, C.1**). As already outlined in section 2.8, a low-amplitude EEG (**Figure 25 A, A.1, B, B.1**), a dominating higher frequency (**Figure 25 A.2, B.2**) and an actively moving mouse during the dark phase were considered criteria for defining wake periods, whereas a high-amplitude EEG (**Figure 25 C, C.1, D, D.1**), dominating frequencies of < 4 Hz or 4-8 Hz (**Figure 25 C.2, D.2**) and sleep-like behaviour in the video sequences during the light phase were used as criteria for identifying sleep episodes.

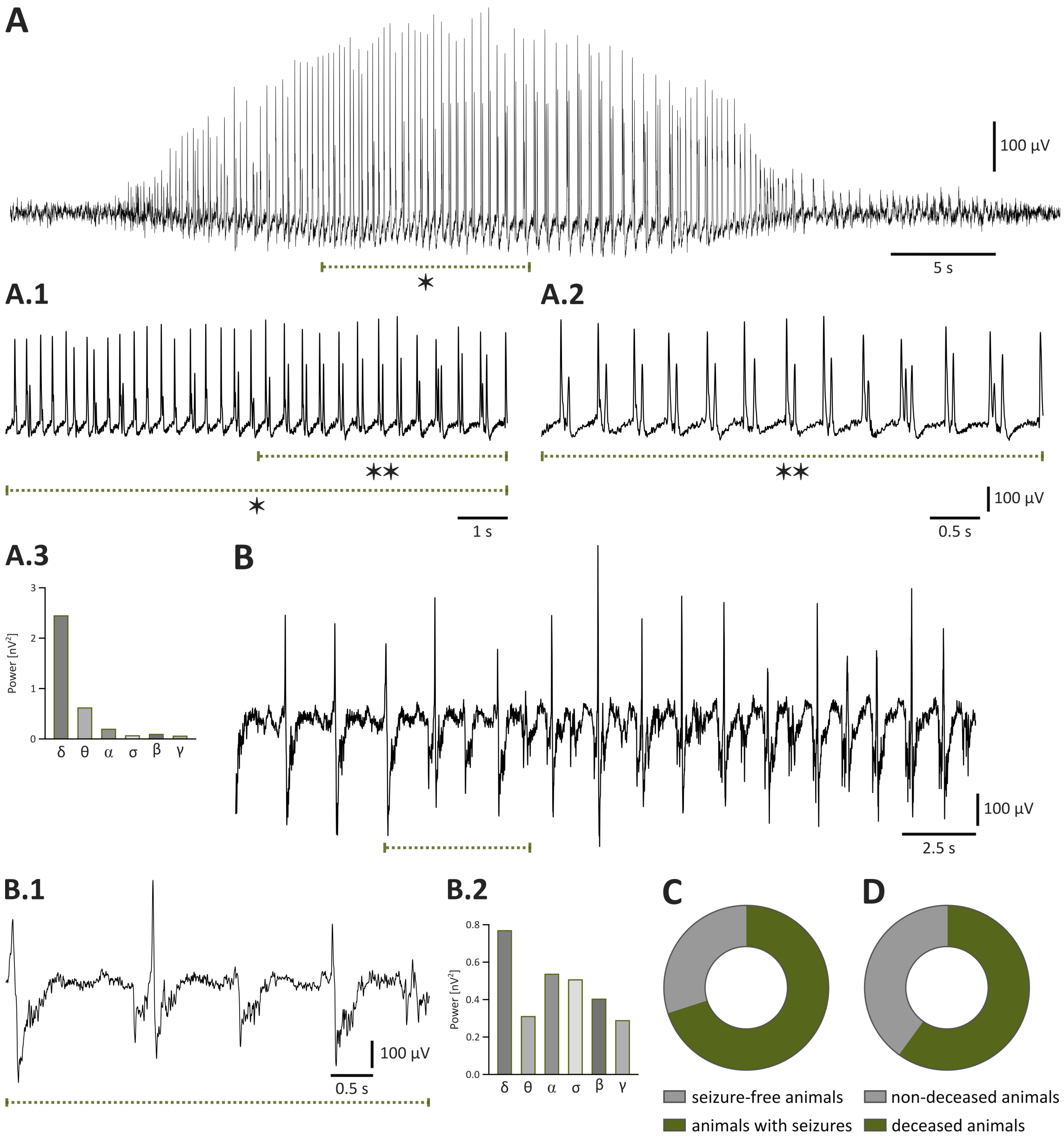

Figure 26. Persisting susceptibility of *Slc1a3*$^{\text{P290R/wt}}$ animals to epileptic seizures during the compensatory phase. (**A**) Representative example of a 50 s-epoch of an ictal event displaying rhythmic epileptiform discharges recorded in a heterozygous animal after having passed the period of highest seizure vulnerability. The amplitudes of the spikes and spike-and-wave complexes were slowly building up and gradually returning to baseline. (**A.1**) 10 s-cut-out of the ictal event in Figure A magnifying the epileptiform discharges, with ✶ indicating the location of the cut-out. (**A.2**) 5 s-cut-out of the ictal event in Figure A.1 to better visualise the single rhythmic discharges, with ✶✶ indicating the location of the cut-out. (**A.3**) The power spectrum for the EEG trace in Figure A.2 was dominated by frequencies in the lower range, particularly the delta band (< 4 Hz). (**B**) Representative example of an EEG signal with rhythmic epileptiform discharges (25 s-epoch) that were depicted from an ictal event classified as a status epilepticus due to the long duration. The trace was recorded in a different heterozygous animal after seizure peak. (**B.1**) Magnification of the epileptiform discharges in a 5 s-cut-out of the ictal pattern visualised in Figure B. (**B.2**) The delta frequency range dominated in the power spectrum during the occurrence of the epileptiform discharges in Figure B.1, however, also higher frequency bands were represented, particularly alpha, sigma and beta. (**C**) Seven of ten implanted *Slc1a3*$^{\text{P290R/wt}}$ animals had at least one seizure/status epilepticus during continuous video-EEG monitoring, whereas three animals stayed seizure-free. (**D**) Six of ten implanted heterozygous animals reached the human endpoint or died during video-EEG recording.

Of the ten implanted heterozygous animals, seven had one or more epileptic seizure(s) or one or more status epilepticus(-i), whereas three *Slc1a3*$^{\mathrm{P290R/wt}}$ animals stayed seizure-free and exclusively displayed physiological activity during the respective monitoring episodes (**Figure 26 C**). In accordance with the EEG analysis of the younger heterozygous mice, ictal events were identified by the presence of rhythmic discharges (spikes or sharp waves) with a duration > 10 s and < 5 min. Representative examples recorded from two different mice having passed the time of highest seizure vulnerability are shown in **Figure 26 A** and **Figure 26 B**. The slow build-up of a characteristic seizure event followed by its gradual return to baseline was depicted in a 50 s-lasting epoch (**Figure 26 A**). Magnifications of a 10 s-epoch and a 5 s-epoch respectively were used to visualise the clustering of the rhythmic discharges (**Figure 26 A.1, A.2**), with predominating lower frequencies in the delta and theta power range (**Figure 26 A.3**).

The 25 s-cut-out in **Figure 26 B** was depicted from a rather long ictal event classified as a status epilepticus due to its duration > 5 min, which comprised rhythmically arising spike-and-wave complexes. These epileptiform discharges are shown in more detail in **Figure 26 B.1**, uncovering a combination of spike-and-wave as well as sharp-wave discharges, with a predominating frequency in the delta band (**Figure 26 B.2**).

The death rate of implanted *Slc1a3*$^{\mathrm{P290R/wt}}$ animals during the compensatory phase was lower compared to the mice recorded at an earlier time point. Of ten implanted *Slc1a3*$^{\mathrm{P290R/wt}}$ animals, four reached the human endpoint and two died during video-EEG recordings (**Figure 26 D**).

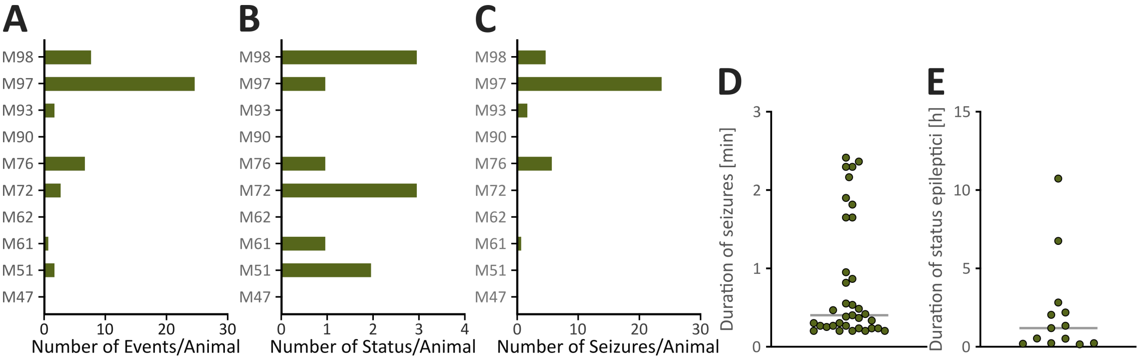

Figure 27. Frequency of ictal events and duration of epileptic seizures/status epileptici in *Slc1a3*$^{\mathrm{P290R/wt}}$ mice. (**A**) The number of seizure-like events varied between the different *Slc1a3*$^{\mathrm{P290R/wt}}$ animals ($n_{\mathrm{P290R/wt}}$ = 10), ranging from one seizure/status to 25 seizure-like events. In this context, the category of seizure-like events comprised epileptic seizures and status epileptici. (**B**) The frequency of status epileptici ranged from one to three in the recorded heterozygous animals ($n_{\mathrm{P290R/wt}}$ = 10) during the compensatory phase. (**C**) The number of seizure events in *Slc1a3*$^{\mathrm{P290R/wt}}$ animals ($n_{\mathrm{P290R/wt}}$ = 10) implanted after the period of maximum seizure susceptibility was low, except for one animal with a frequency of 25 seizures during monitoring. (**D**) The average duration of epileptic seizures recorded in heterozygous animals during the compensatory phase was 0.8 min. Rhythmic epileptiform discharges with a duration > 10 s and < 5 min were classified as epileptic seizures. (**E**) The duration of a status epilepticus averaged 2.2 h in *Slc1a3*$^{\mathrm{P290R/wt}}$ animals. Seizures with a duration > 5 min and an episode > 5 min of two or more seizures without full recovery of consciousness in between were classified as status epilepticus.

As already mentioned, the number of ictal events or status epileptici had a high variation between *Slc1a3*$^{\mathrm{P290R/wt}}$ knock-in animals that were recorded during the compensatory phase after having passed the period of maximum seizure susceptibility. The frequency of seizure-like events varied from one to eight epileptic seizures/status epileptici, with one animal displaying a comparatively elevated frequency of 25 seizure events (**Figure 27 E**). On average, each heterozygous animal had a frequency of 4.8 seizure-like events per recorded monitoring period, however, it is important to highlight that this value was substantially influenced by the beforementioned high number of ictal events observed for one mouse and by the varying recording duration of the different animals. Of note, at least one seizure-like event of each of the seven *Slc1a3*$^{\text{P290R/wt}}$ knock-in animals fulfilled the criteria for a status epilepticus, with a > 5 min duration of a single seizure or the occurrence of at least two seizures > 5 min without full recovery of consciousness in between the ictal events. For the occurrence of a status epilepticus, the frequency was rather consistent among P290R-harbouring animals and varied from one to three status per animal (**Figure 27 F**). During the compensatory phase, each heterozygous animal displayed on average 3.8 epileptic seizures (**Figure 27 G**).

The average duration of an epileptic seizure, assessed by an ictal-like behaviour in the video recording > 10 s or rhythmically arising epileptiform discharges with a duration > 10 s, numbered 48.8 s (**Figure 27 H**). The duration of a status epilepticus varied from 0.1 h to 10.8 h, with an average of 2.2 h (**Figure 27 I**).

3.4.4 Upregulation of c-fos after seizure occurrence in different regions of the brain

After completing the video-EEG monitoring, heterozygous and wildtype animals ranging from P25 to P60 were transcardially perfused using 4 % PFA to fix the brain tissue and to subsequently perform immunohistochemical studies. Details are provided in section 2.10. One heterozygous animal recorded during the period of maximum seizure susceptibility as well as two *Slc1a3*$^{\text{P290R/wt}}$ animals implanted during the compensatory phase could not be perfused due to unexpected deaths at night leading to severe damage of the brain tissue by autolytic processes. Four heterozygous and four wildtype animals recorded during the period of maximum seizure vulnerability were included to perform immunochemical staining. However, one heterozygous animal had to be excluded from further analyses because of an insufficient perfusion quality. Accordingly, four heterozygous and four wildtype animals that had been implanted and recorded during the compensatory phase were included. In two heterozygous animals, epileptic seizures or status epileptici had been recorded before sacrificing the animals, whereas two heterozygous animals had remained seizure-free during the entire recording period. An overview over the animals that were used for immunohistochemical studies is provided in **Table 13** also including crucial information on the respective mice.

Table 13. Overview and important information on the *Slc1a3*$^{\text{P290R/wt}}$ and wildtype animals that were perfused after video-EEG monitoring and used for immunohistochemical studies.

Animal	Genotype	Age during recording	Result of video-EEG recording	Premature death	Insufficient perfusion quality	Region with high c-fos expression
1	wt/wt	P25-36	seizure-free			none
2	wt/wt	P25-36	seizure-free			none
3	wt/wt	P25-36	seizure-free			none

4	wt/wt	P25-36	seizure-free		none
5	P290R/wt	P25-36	continuous status epilepticus	x	excluded
6	P290R/wt	P25-36	continuous status epilepticus		thalamus
7	P290R/wt	P25-36	continuous status epilepticus		DG
8	P290R/wt	P25-36	continuous status epilepticus		CA1, CA3
9	wt/wt	P45-60	seizure-free		none
10	wt/wt	P45-60	seizure-free		none
11	wt/wt	P45-60	seizure-free		none
12	wt/wt	P45-60	seizure-free		none
13	P290R/wt	P45-60	seizure-free		none
14	P290R/wt	P45-60	seizure-free		none
15	P290R/wt	P45-60	seizures/ status epilepticus		none
16	P290R/wt	P45-60	seizures/ status epilepticus		none

After preparing coronal slices with a thickness of 100 µm, staining against the early immediate gene c-fos was performed to discover brain regions with high cellular activity[172]. The aim of performing c-fos staining was to identify specific brain regions in the *Slc1a3*$^{P290R/wt}$ knock-in model that were implicated in seizure generation and epileptogenesis, since the seizure origin was unknown[172]. Additionally, DAPI staining was used to visualise neuronal and non-neuronal cells, which consequently also included astrocytes and radial glia-like cells. Distinct regions across the brain were chosen for studying c-fos expression, with a focus on the cortex, thalamus, and hippocampus. The first imaging step was implemented to obtain an overview of the entire stained slice enabling the identification of brain regions with maximum density of c-fos positive cells. Subsequently, z-stacks of the respective areas were captured with a confocal microscope to ensure optimal quality and higher resolution, as comprehensively outlined in section 2.12.

The brain regions showing maximum c-fos expression varied substantially between the three included heterozygous animals that had been recorded during the period of maximum seizure vulnerability. In the first *Slc1a3*$^{P290R/wt}$ mouse, staining against c-fos revealed a pronounced upregulation in the nucleus reticularis of the thalamus (nRT), which was absent in the stained slices of wildtype control animals (**Figure 28 A**). For the second heterozygous animal, the maximum upregulation of c-fos expression was localised within the hippocampal DG, whereas in the stained slices of the wildtype animals no brain region with highly upregulated c-fos expression could be identified (**Figure 28 B**).

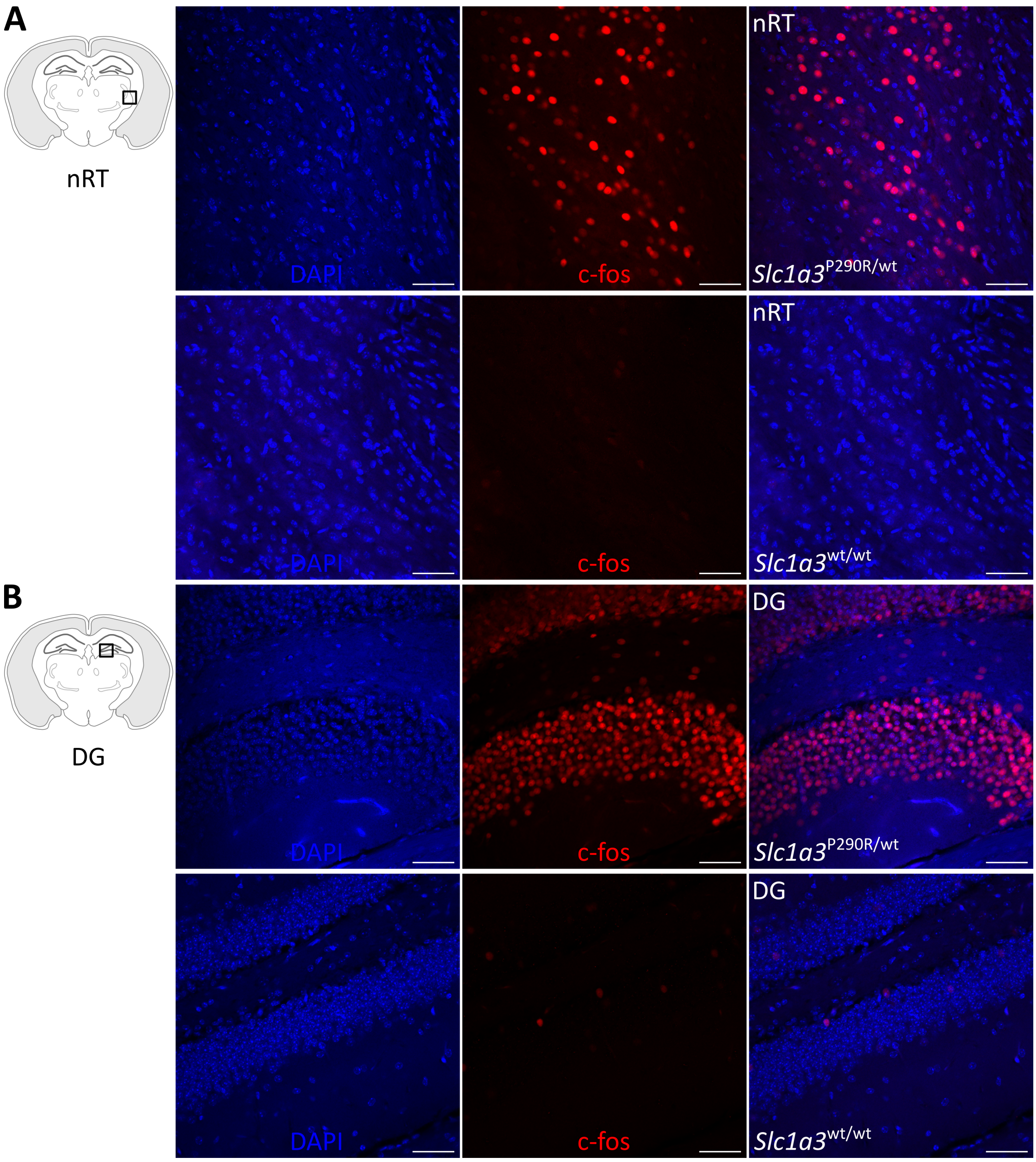

Figure 28. Upregulation of c-fos expression in the nucleus reticularis (nRT) and the hippocampal DG. (**A**) In the first *Slc1a3*$^{\text{P290R/wt}}$ animal, the maximum density of c-fos expressing cells was localised in the nRT (top row; left: DAPI staining in blue, middle: c-fos staining in red, right: merged image). A representative example of a wildtype animal is depicted at the bottom. Scale bar: 50 µm. The drawing on the left indicates the location of the nRT within the coronal brain slice. (**B**) In the second heterozygous mouse, the highest upregulation of c-fos expression was found in the DG (top row; left: DAPI staining in blue, middle: c-fos staining in red, right: merged image). Scale bar: 50 µm. The drawing on the left indicates the location of the DG. A representative example of a wildtype animal is given in the bottom row.

Staining against c-fos using slices of the third *Slc1a3*$^{\text{P290R/wt}}$ animal revealed highly elevated c-fos expression levels in the CA1 and CA3 region of the hippocampus, which were not detected in c-fos stained slices of wildtype littermates (**Figure 29 A, B**). Due to the marked interindividual variability among the included heterozygous animals, it was not possible to perform reasonable statistical analyses.

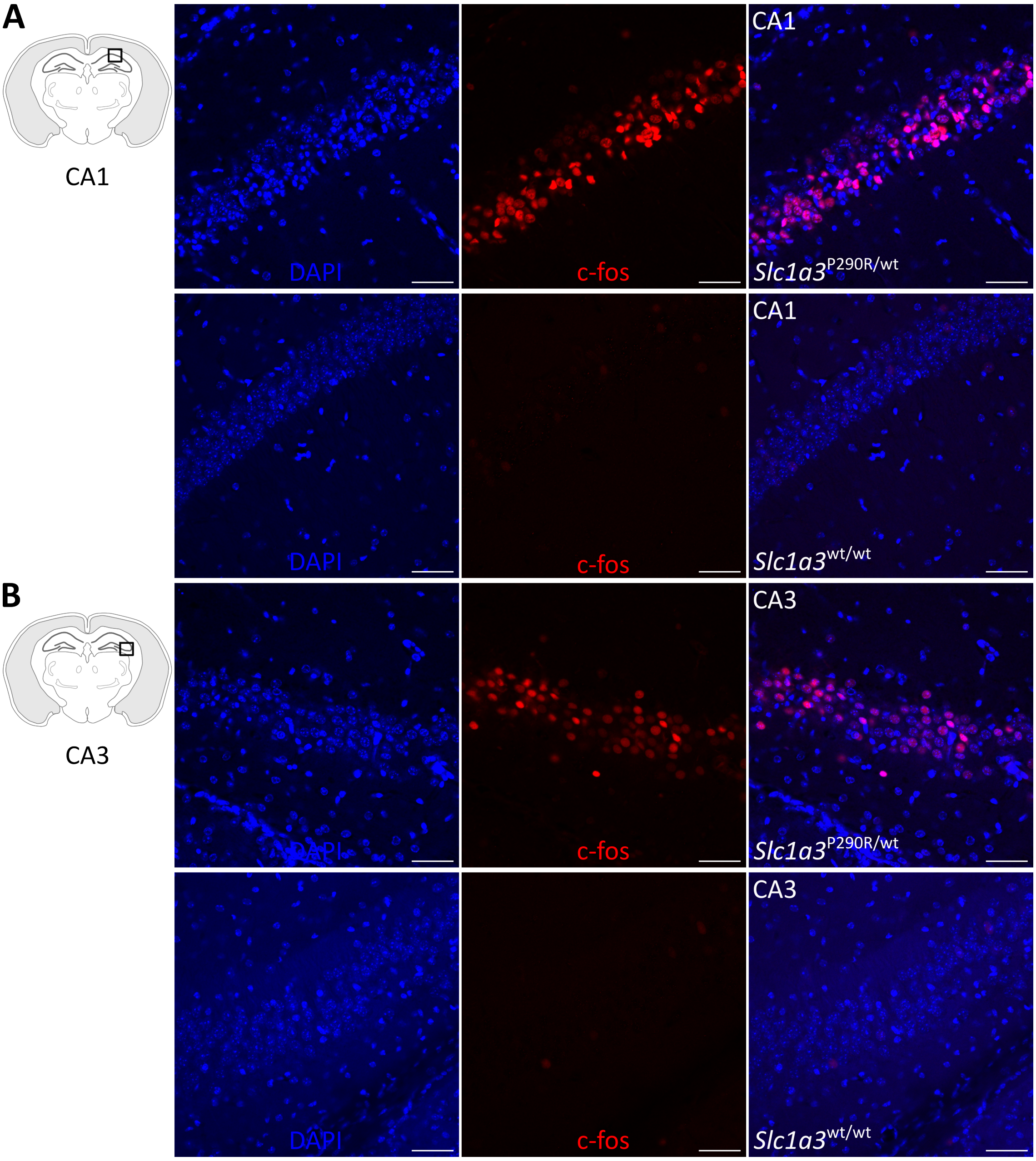

Figure 29. Upregulation of c-fos expression in the hippocampal CA1 and CA3 regions. (**A**) In the third *Slc1a3*$^{\mathrm{P290R/wt}}$ animal, the maximum density of c-fos expressing cells was localised the CA1 and (**B**) CA3 region of the hippocampus (top row; left: DAPI staining in blue, middle: c-fos staining in red, right: merged image). Representative examples of a wildtype animal are depicted at the bottom (left: DAPI staining in blue, middle: c-fos staining in red, right: merged image). Scale bar: 50 µm. The drawings on the left indicate the location of the CA1 and CA3 regions, where the images were captured within the stained slice.

In contrast, a marked upregulation of c-fos expression in specific areas of the brain was absent in the four heterozygous animals that had been implanted and recorded during the compensatory phase. As the expression of c-fos positive cells did not differ between the genotypes in the overview images, confocal microscopy scans were not performed with respect to the compensatory period.

4 Discussion

4.1 The pre-existing research gap and arising research problems

Despite intense scientific research over several decades, the exact pathophysiological mechanisms involved in CSD and HM have remained elusive to date. The generation of transgenic animal models have significantly expanded our understanding of the involved factors and processes. However, experimental data from FHM1 and FHM2 mouse models have given rise to focus on the excitatory neurotransmitter glutamate as the key triggering factor and to establish a glutamate-based hypothesis in CSD initiation. Although an increase in K^+ levels was implicated in eliciting the CSD cascade in some studies, the exact role of K^+ as main element to trigger CSD in HM has never been investigated so far.

The underlying molecular and cellular causes for hyperexcitability and increased CSD susceptibility are already elucidated for *CACNA1A*- and *ATP1A2*-associated FHM models[27, 37, 53]. In contrast, the mechanisms of FHM3 pathology have stayed rather unclear having to reconcile hyperexcitability of inhibitory neurons on the single cell level with a higher CSD susceptibility *in vivo*[1]. Of note, the role of GABAergic cells as CSD elicitors has not been studied in detail, as the inhibitory cell population was assumed to play a rather insignificant role during the CSD processes.

Comprehensive knowledge about which types of ion channels, transporters and pumps are specifically involved both during the initiation and propagation phase is still missing, which also applies to $Na_V1.1$ and EAAT1. This research gap has also complicated the development of novel pharmacological treatment targeting specific components within the CSD cascade, which is particularly important for the more severely affected HM patients.

Furthermore, the three major HM genes only constitute a minor part of the whole mutational spectrum. Therefore, the number of risk/candidate genes is growing nowadays, which should be accompanied by the generation of novel animal models to investigate their significance. These models may contribute with new aspects and expand our current knowledge.

The frequent occurrence of additional phenotypes such as epileptic seizures or psychiatric conditions as well as the high number of reported overlapping syndromes between HM and other disorders, for example ataxia or epilepsy syndromes, make it necessary to further study the nature of these correlations. For instance, CSDs and epileptiform activity particularly share numerous similarities and appear to be closely connected.

To sum up, a comparison of different pathophysiological aspects between distinct HM models is rarely observed in literature but may add further information to unravel CSD and HM pathophysiology.

4.1.1 The pivotal role of K^+ in CSD pathophysiology of FHM3

The first objective of this work was to identify the role of K^+ as key factor triggering CSD in FHM3 and to determine the mechanistic link between a higher CSD susceptibility *in vivo* and the hyperexcitability of fast-spiking inhibitory neurons[1].

For addressing this first research question, the *Scn1a*$^{L1649Q/wt}$ knock-in model was used harbouring the human L1649Q GOF variant that causes pure HM in affected patients[1, 69]. CSD was elicited and recorded in acute cortical slices demonstrating both an increased rate of successful CSD inductions as well as an elevated propagation velocity in slices of heterozygous animals[1]. Additionally, K^+-sensitive microelectrode recordings identified higher K^+ levels during CSD and demonstrated that the increased $[K^+]_e$ shift was confined to an early CSD phase[1]. These key findings led to the identification of a completely new cascade for CSD initiation, which comprises GOF properties of $Na_V1.1$ leading to hyperexcitable GABAergic neurons and an early rise and accumulation of $[K^+]_e$ acting as the main triggering factor for CSD[1].

Previous and new concepts of the cellular and molecular mechanisms underlying CSD

Significant advances in understanding CSD and HM pathophysiology and the included single processes have been made since the possibility of studying (F)HM mouse models. However, cortical hyperexcitability in the established FHM1 and FHM2 animal models was mostly linked to enhanced glutamatergic transmission resulting in increased glutamate levels that were considered as the key factor for triggering CSD[27, 37, 48, 55]. However, the observed early $[K^+]_e$ increase and accumulation in FHM3 could not be reconciled with the already established hypothesis for CSD initiation that entirely focused on glutamate[1].

Moreover, inducing a hyperexcitable state during CSD has mostly been attributed to pyramidal cells which are responsible for excitatory neurotransmission. Of note, in FHM2, the mutant NKA is expressed in the astrocytic cell population[37]. However, impaired astrocytic function directly affects the pyramidal cell population due to their tight connection with respect to neuronal activity and energy metabolism at cortical synapses[48].

Therefore, the identified pathophysiological cascade in FHM3 linking interneuron hyperexcitability and increased CSD susceptibility via an accumulation of $[K^+]_e$ represents a novel mechanism to elicit CSD in HM and clearly expands the previously established concepts[1]. The extension of the hypothesis for CSD initiation did not only apply to the pivotal role of $[K^+]_e$ during the process, but also referred to the significance of inhibitory interneurons, which have never been related to decisively affect CSD triggering in experimental studies so far[1].

Computational and experimental data support the novel CSD cascade and pivotal role of K^+

Profound ionic changes including a near-breakdown of ion homeostasis during CSD were noticed early[16, 17]. These identified alterations also comprised a rapid increase in $[K^+]_e$ and the release of amino acids like glutamate[17]. A computational study suggested early that CSD was elicited in an all-or-none principle if $[K^+]_e$ accumulation together with current injections initiated a depolarisation of the modelled neuron that spread to the apical dendrite to activate persistent Na^+ current among others[34]. The pivotal role of hyperexcitable inhibitory interneurons leading to $[K^+]_e$ increase was already proposed by Cestèle and colleagues as the likely L1649Q-associated FHM3 pathomechanism that facilitates CSD generation[81].

A different, more recent computational model of a cortical microcircuit, including a pyramidal cell and a GABAergic interneuron, provided additional evidence that CSD can be elicited by high frequency firing of inhibitory neurons[173]. Modulation of the spiking frequency demonstrated that spiking-induced K^+ efflux from the inhibitory and pyramidal cells were required for CSD triggering, whereas synaptic transmission was not mandatory for CSD induction but positively affected its facilitation[173]. Furthermore, an increased persistent Na^+ current promoted CSD induction and resulted in a larger elevation of K^+ efflux possibly indicating an accelerating effect on the process of CSD propagation in the vicinity of larger circuits and networks[173].

Chever and colleagues demonstrated that both the acute pharmacological activation of $Na_V1.1$, using the spider toxin Hm1a, as well as the exclusive optogenetic activation of GABAergic interneurons initiated CSD specifically in the neocortex, which was caused by spiking-induced interstitial increase and accumulation of $[K^+]_e$[29]. Hm1a was reported to act as specific $Na_V1.1$ enhancer and to induce a 12-fold increase in steady-state Na^+-current yielding hyperexcitability of GABAergic neurons[29, 174]. Thus, the toxin pharmacologically imitates the functional effects of GOF *SCN1A* variants including L1649Q[69, 78, 79] and provides an acute model to study FHM3 consequences[29]. By restoring the firing deficits of GABAergic interneurons, while sparing the function of excitatory cells, the efficacy of the selective $Na_V1.1$ activator Hm1a has recently been demonstrated in a DS mouse model leading the an alleviation of seizure severity and a diminished mortality[175]. The experimental and computational data provided by Chever and colleagues[29] perfectly complemented our accompanying study, which investigated the chronic genetic model for FHM3 using a multimodal approach, including the data presented in this thesis[1]. The results by Chever and colleagues further verify the newly established mechanism of CSD induction that includes $Na_V1.1$ GOF, early hyperactivity of neocortical inhibitory neurons and a concomitant progressive rise of $[K^+]_e$ at the site of CSD induction[29].

Using the beforementioned optogenetic and pharmacological techniques, SD was not initiated in different areas than the neocortex[29]. Nevertheless, the functional changes on the single cell level underlying increased CSD susceptibility were comprehensively studied in the cortex and the hippocampus using the *Scn1a*$^{L1649Q/wt}$ knock-in model[1]. These results may indicate that the presence of $Na_V1.1$ GOF-associated alterations in the hippocampal region lack a significant contribution to HM pathophysiology, which clearly contrasts with the pivotal role of the hippocampus in numerous models for epilepsy.

Of note, CSD generation was prevented by optogenetically stimulating slices of heterozygous *Scn1a* KO animals demonstrating the importance of $Na_V1.1$ activation and hyperactive interneurons during the process of CSD emergence[29].

Technical limitations and advantages of the CSD and K^+-sensitive recordings

The use of KCl puff applications prevented K^+-sensitive microelectrode recordings of $[K^+]_e$ changes directly at the CSD initiation site. In this study, a minimum distance of at least 800 µm between the puff and the K^+-sensitive electrode was established to avoid any interference of the KCl containing puff with the measurement[1]. However, by using different techniques of spatial optogenetic illumination, the spike-generated $[K^+]_e$ increase at the CSD induction site was demonstrated in the study by Chever and colleagues[29]. Thus, $[K^+]_e$ levels were emphasised as key component in CSD generation associated with an $Na_V1.1$. GOF mechanism, thereby supporting the observed pivotal role of $[K^+]_e$ increase to elicit CSD within this work[1, 29]. The consistency of the results of both studies strongly supports the applicability of the presented technique. Nevertheless, $[K^+]_e$ recordings at the initiation site would have been more precise and remain to be performed to verify the results by Chever and colleagues in the transgenic FHM3 model.

KCl puff applications represent a classical experimental model for *in vivo* and *in vitro* CSD generation that is widely found in literature. In this work, a noticeably lower KCl concentration of 300 mM was used[1] compared to most studies that induce CSD with stronger stimuli usually ranging from 1 M to 3 M of KCl[48, 52, 176, 177]. These high K^+ concentrations do not correspond to levels that are found under physiological and pathological conditions, which usually range from a minimum of 2.3 mM at resting levels to 30-40 mM during CSD and sometimes peak at 60-65 mM[1, 17, 18, 19]. CSD initiation is a dynamic, continuously evolving process, which contrasts with the abrupt, rapid CSD onset triggered by KCl puff applications. To completely avoid the use of artificial stimuli, the most accurate method would be to record spontaneously occurring CSDs, which are extremely rare in slices of heterozygous FHM animals and are usually not generated in slices of wildtype animals.

Implications for future research using the Scn1a$^{L1649Q/wt}$ model

Moreover, it was shown that neither glutamatergic nor GABAergic synaptic transmission was required for eliciting CSD in the acute model mimicking FHM3 variants which provided important details with respect to the concerned pathophysiological mechanisms[29]. Pharmacological modulation to disclose the involvement of additional ion channels and receptors was not performed using the *Scn1a*$^{L1649Q/wt}$ knock-in model[1]. As the FHM3 animal model represents a more appropriate model to mimic the condition of L1649Q-carrying patients and may also involve secondary changes, a comprehensive investigation thereof could be extremely useful to identify further pharmacological targets that interfere with crucial components of CSD generation or the chronification processes during HM episodes. To name an example for an attractive future target, scientists have increasingly focused on the processes of myelination and oligodendrogenesis in recent years, which were discovered to be pathologically altered in various epilepsy mouse models and peculiarly in the context of Na^+ channelopathies[178, 179]. In an *Scn8a* mouse model of generalised epilepsy, activity-dependent and consequently malfunctioning myelination was found to significantly contribute to epilepsy progression, while simultaneously providing a promising target for treatment[178]. Considering that there are ample similarities between CSDs and seizure-like activities, related mechanisms may also apply in the context of HM and represent an additional option for the development of targeted treatment.

A recent article largely expanded the GOF spectrum of *SCN1A*-associated disorders describing newly identified GOF $Na_V1.1$-related phenotypes with developmental and epileptic encephalopathy that may be associated with additional features[109]. However, HM attacks were not reported in these epilepsy cases[109]. A detailed study on the consequences of these newly identified *SCN1A* GOF variants on neuronal microcircuits and networks will be of great value to better understand how *SCN1A* variants with similar functional effects differentially lead to epilepsy or HM. Furthermore, the novel identification of severely affected epilepsy patients has emphasised the importance for discovering suitable pharmacological treatment options in *SCN1A* GOF-related disorders.

4.1.2 Beneficial effects of the persistent Na^+ channel blocker GS967 in FHM3

To evaluate potential pharmacological treatment options in FHM3 and further confirm the mechanistic concepts of L1649Q-associated CSD pathophysiology, the effect of GS967 on the rate of successfully induced CSDs was explored *in vitro*[1]. GS967 application during CSD recordings demonstrated an alleviation of CSD susceptibility in slices of *Scn1a*$^{L1649Q/wt}$ animals[1].
Additionally, our study revealed a reduction in persistent Na^+ current elicited by slow voltage ramps as well as a decrease in AP frequency recorded from fast-spiking inhibitory neurons[1]. The more prominent effect of GS967 in the range of higher frequencies was attributed to the use-dependent mode of action, which may further highlight its reasonable application in the context of preventing or stopping CSD right after its initiation[1]. Moreover, the presumably beneficial effect of GS967 in *SCN1A* GOF-related disorders was revealed by applying the persistent Na^+ channel blocker to homozygous *Scn1a*$^{L1649Q/L1649Q}$ animals, as it substantially prolonged the lifespan of treated mice[1].
The value of GS967 as specific pharmacological treatment in FHM3 was already proposed earlier in an experimental study investigating its effect on the increased persistent Na^+ current of seven different *SCN1A* GOF variants causing FHM3, which overall indicated specific binding of GS967 to $Na_V1.1$[142]. Whereas the persistent Na^+-current was largely reduced in the seven mutant channels, the effect on peak currents was revealed to be comparably small[142].

Expansion of GS967 targets and its relevance in neurological disorders

GS967 was also demonstrated to substantially decrease elevated persistent Na^+-currents of $Na_V1.2$ and $Na_V1.6$ caused by epileptic encephalopathy variants in *SCN2A* and *SCN8A* respectively[180, 181]. Hence, the beneficial effect on CSD susceptibility, as shown here for *Scn1a*$^{L1649Q/wt}$ knock-in animals[1], may not only be attributed to diminishing increased $Na_V1.1$-associated Na^+ ramp currents but may additionally be caused by exerting a modulatory effect on other channels of the Na_V family. On the contrary, TTX did not prevent CSD initiation *in vivo* and *in vitro*[30, 42] despite blocking the entire Na_V channel family and only yielded minor effects on specific CSD characteristics[43].

Of note, favourable outcomes with GS967 application were not only observed for *SCN2A*- and *SCN8A*-related epilepsy syndromes but rather unexpectedly also for DS, in which *SCN1A* LOF variants cause hypoexcitability of PV+ fast-spiking interneurons[182]. GS967 was shown to improve survival, decrease seizure frequency, normalise Na^+ current density of pyramidal cells, and diminish protein levels of $Na_V1.6$ in *Scn1a* KO mice, which was attributed to potential secondary changes of $Na_V1.6$ by the authors[182]. On the one hand, these studies indicate that the effect of GS967 may be even broader and more complex than anticipated initially. On the other hand, they suggest that, besides FHM3, GS967 may be applicable to a more expanded spectrum of channelopathies converting the substance into a promising treatment option that may succeed in clinical trials in the future. The comparison of GS967 (PRAX-562) with conventional Na^+ channel blockers has already revealed its reasonable efficacy combined with an improved preclinical tolerability[183].

Referring to the previous section, exploring the effects of the persistent Na^+ channel blocker on *SCN1A* GOF variants that lead to extremely severe epilepsy phenotypes will be highly relevant for the development of promising treatment options in the affected patients.

To sum up, the potential of GS967 to reverse the L1649Q-associated consequences on survival of homozygous mice, Na^+ ramp currents, AP frequency and CSD susceptibility, as demonstrated here and in our study, suggests a significant role in generating targeted treatment options of FHM3-related migraine attacks[1].

4.1.3 Altered CSD characteristics and K^+ dynamics in CSD pathophysiology of EA6

Based on the expanding genetic spectrum in HM, first investigations of the *Slc1a3*$^{P290R/wt}$ model for EA6 with respect to CSD pathophysiology and the related importance of K^+ within the CSD cascade are reported in this thesis. Both a higher CSD susceptibility as well as an increased propagation velocity were demonstrated *in vitro*, which are characteristic features for HM mouse models[1, 27, 37]. In addition, altered $[K^+]_e$ dynamics and levels were shown during the early and very late phases of CSD, with however different characteristics compared to the *Scn1a* model[1].

Based on the glutamate hypothesis for CSD initiation, it was speculated that the P290R LOF effect on EAAT1-associated glutamate transport would result in elevated glutamate levels triggering CSD and would be combined with overall unaltered $[K^+]_e$ levels[100]. In accordance with the initial hypothesis, K^+-sensitive recordings revealed that the absolute K^+ levels *in vitro* were not increased in the *Slc1a3*$^{P290R/wt}$ model. These findings indicate that $[K^+]_e$ does not play a key role in facilitating CSD initiation in the context of *SLC1A3*-related HM pathophysiology. On the contrary, $[K^+]_e$ levels were increased during late CSD phases, which may have an impact on facilitating the process of CSD propagation.

Establishment of the glutamate hypothesis in CSD pathophysiology

The glutamate-based theory mainly emerged from supportive findings in FHM1 and FHM2 animal models since an excessive glutamatergic transmission was demonstrated to facilitate CSD generation and provided evidence for the presumable key role of glutamate as CSD trigger. In

FHM1, *CACNA1A* GOF variants cause an increased Ca^{2+} influx through mutant $Ca_V2.1$ channels in response to APs which leads to an enhanced release probability at the synapses of pyramidal cells[52]. In contrast, reduced synaptic glutamate and $[K^+]_e$ removal by astrocytes depending on the magnitude of neuronal activity was demonstrated in FHM2[48]. Simultaneously, a tight coupling between EAAT2 and the mutant α_2 NKA was revealed, as expression levels of both proteins were equally decreased in the perisynaptic astrocytic processes[48]. Consequently, glutamate appears to be the common denominator for both HM mouse models, which clearly contrasts with the newly established hypothesis in FHM3[1].
Additional evidence for the significance of glutamate in CSD generation or propagation derived from early *in vivo* and *in vitro* studies verifying that NMDA receptors are indispensable to elicit a CSD event that is followed by its propagation[38, 39]. Conversely, one could argue that any pathological alteration that increases glutamatergic neurotransmission or delays glutamate re-uptake at cortical synapses concurrently increases the risk to elicit CSD, which also applies to *SLC1A3* variants that exert a LOF effect on EAAT1-related glutamate transport.

Additionally, an increased propagation velocity and a lower CSD threshold were observed in the presence of the EAAT1/2 inhibitor DL-*threo*-β-benzyloxyaspartic acid (TBOA) partially resembling the quantitative changes found in the FHM2 model[45, 48, 184]. Using the FHM2 model, it was shown that the defective glutamate clearance largely accounted for the facilitation of CSD induction but only partially for the increased CSD propagation velocity[48]. Furthermore, the rate of CSD propagation was demonstrated to be proportional to the levels of glutamate[45]. Importantly, TBOA non-specifically inhibits glial glutamate transporters and simultaneously blocks glutamate transport performed by EAAT1 and EAAT2. Therefore, TBOA application clearly represents a more impactful alteration in glutamate homeostasis than heterozygous LOF variants in one of the two genes.

Contradictory results from EAAT1 KO models

On the contrary, neither heterozygous nor homozygous EAAT1 KO animals displayed an increased CSD frequency, whereas a higher number of CSDs was observed in EAAT2 conditional KO mice[185]. However, the beforementioned study lacked a comprehensive exploration of further CSD features as for instance the CSD threshold, the frequency in response to electrical stimulation, the latency, or the frequency of spontaneous CSDs[185]. The difference in CSD frequency between EAAT1 and EAAT2 KO animals may be partly explained by the fact that EAAT2 accomplishes the major part in removing glutamate in the brain. Therefore, EAAT2 elimination may yield a stronger effect. KO models, which were used in the beforementioned study, usually represent rather simplified models that frequently resemble the phenotype inadequately and incorrectly reproduce the functional consequences of specific genetic variants. Moreover, compared to the generation of knock-in mouse models harbouring missense variants, the complete or partial knockdown of a gene usually results in an up- and downregulation of a vast number of genes, which was not investigated in the beforementioned study. These unknown secondary changes may also partly account for the missing effect on CSD frequency in the EAAT1 KO lines. To genuinely disclose the importance of both glutamate transporters in CSD pathophysiology, knock-in mouse models harbouring specific variants that have been identified in HM patients should be preferred.

A possible link between P290R-related impaired glutamate removal and accelerated K^+ dynamics

Despite the absent increase in absolute $[K^+]_e$ levels during the rising phase of CSD, a pronounced $[K^+]_e$ shift was identified during an early CSD phase in slices of *Slc1a3*$^{P290R/wt}$ animals, which comprised accelerated $[K^+]_e$ dynamics. The acceleration of the $[K^+]_e$ rise was identified by a shortened initial time interval, a decreased $[K^+]_e$ at the inflection point and a smaller AUC.
As outlined in the introduction, an early computational model indicated that the positive feedback cycle constituting the all-or-none characteristics of CSD comprises a net self-sustaining inward current as well as a regenerative local K^+ release, which results in neuronal depolarisation[34]. Evidence points towards an important involvement of NMDA-receptors in these two crucial components for CSD induction[186]. If impaired glutamate removal represented the mechanism to induce CSD in the *Slc1a3*$^{P290R/wt}$ knock-in model, NMDA-receptors would be activated, which would directly result in substantial K^+ efflux through these NMDA-receptors and a rapid rise in $[K^+]_e$ early during CSD[187, 188]. The observed acceleration of $[K^+]_e$ dynamics may therefore be caused by enhanced glutamate-induced NMDA-receptor activation. This mechanism of accelerated neuronal K^+ efflux would also explain an inflection point at lower $[K^+]_e$ ranges and a smaller AUC. Nevertheless, the hypothesis of glutamate being the key trigger for CSD in the EA6 model as well as the mechanistic link to the demonstrated acceleration of $[K^+]_e$ dynamics during an early CSD phase remain to be verified.

To provide unquestioned evidence for the anticipated decisive role of glutamate in triggering CSD in *SLC1A3*-associated HM, recordings of the glutamate levels before and during CSD should be performed. Although the genetically encoded glutamate sensor iGluSnFR has been available for some time now to visualise and optically quantify glutamate release and removal at the synapses, glutamate dynamics during high-frequency bursts exceeding $\sim$ 10 Hz, which are usually observed before and during CSD generation[189], cannot be resolved by iGluSnFR[190, 191]. Therefore, recent advances in developing fast (iGlu $_f$) and ultrafast (iGlu $_u$) variants will be of substantial help to decipher the significance of glutamate in CSD induction in the *Slc1a3*$^{P290R/wt}$ knock-in model in the future.

The effect of pharmacologically mimicking a pure EAAT1 LOF variant on CSD characteristics

In addition, experimental data has recently been gathered by Caroline Kurth as content of a medical doctoral thesis in attempt to mimic a pure LOF of the EAAT1-associated glutamate transport, thereby imitating the LOF effect of the P290R variant (unpublished data by Kurth, Miely and Hedrich). To do so, the highly selective EAAT1 inhibitor UCPH-101, which blocks both the associated anion/Cl^- currents and the glutamate transport[192, 193, 194], was applied to slices of wildtype animals with the same background than the *Slc1a3*$^{\mathrm{P290R/wt}}$ mouse strain, while CSD recordings were performed (unpublished data by Kurth, Miely and Hedrich). The primary hypothesis was that UCPH-101 application would yield equal findings as in the *Slc1a3*$^{\mathrm{P290R/wt}}$ model if the changes in CSD induction, propagation and $[K^+]_e$ dynamics were exclusively caused by the impaired EAAT1-related glutamate transport.

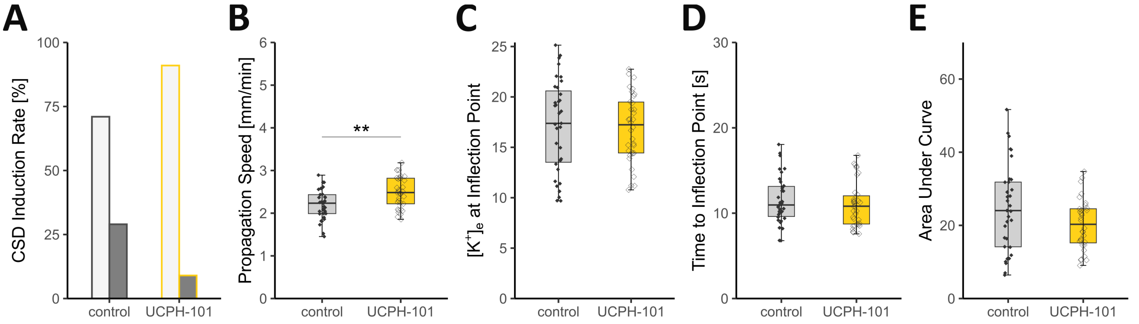

Figure 30. Increased CSD susceptibility and propagation velocity but unaltered $[K^+]_e$ dynamics in UCPH-101 perfused slices (unpublished data by Kurth, Miely and Hedrich). (**A**) The rate of successfully induced CSDs was significantly increased in UCPH-101 perfused compared to control slices (Fisher's exact test) (unpublished data by Kurth, Miely and Hedrich). (**B**) The propagation velocity was enhanced by 11.8 % in slices after UCPH-101 application (Mann-Whitney rank sum test) (unpublished data by Kurth, Miely and Hedrich). (**C**) The $[K^+]_e$ at the inflection point, (**D**) the time from the beginning of $[K^+]_e$ increase until the inflection point as well as (**E**) the area under the curve did not reveal any differences between control and UCPH-101 perfused slices, overall indicating unaltered $[K^+]_e$ dynamics (Mann-Whitney rank sum tests) (unpublished data by Kurth, Miely and Hedrich).

The rate of successful CSD inductions in the presence of UCPH-101 (90.9 %) was highly comparable to the CSD success rate observed in slices of *Slc1a3*$^{\mathrm{P290R/wt}}$ animals (87.1 %) (**Figure 30 A**) and the propagation velocity was also significantly increased after UCPH-101 application (**Figure 30 B**) (unpublished data by Kurth, Miely and Hedrich). However, the relative increase in CSD propagation velocity of UCPH-101 perfused slices was 11.8 %, whereas the propagation velocity in slices of heterozygous *Slc1a3*$^{\mathrm{P290R/wt}}$ animals was increased by 41.5 % (unpublished data by Kurth, Miely and Hedrich). The quantitative comparison revealed some difference in the magnitude of the relative increase in propagation velocity possibly implying that additional factors may play a role in the *Slc1a3*$^{\mathrm{P290R/wt}}$ model.

Furthermore, $[K^+]_e$ dynamics in slices after UCPH-101 application did not differ from control slices possibly indicating that the dynamics during the early phase of CSD may not be accelerated enough to alter the $[K^+]_e$ dynamics at the beginning of CSD (**Figure 30 C, D, E**) (unpublished data by Kurth, Miely and Hedrich). This finding additionally emphasises that further components may contribute to facilitate CSD propagation in the P290R-associated model. For instance, UCPH-101 was acutely applied to the slices preventing the system to adapt to the EAAT1 LOF and GOF and initiate compensatory mechanisms.

These results appear to resemble FHM2-related findings, which demonstrated that impaired glutamate transport only yields a fraction of the facilitation of CSD propagation[48].

Impaired astrocytic K^+ buffering as a possible connection between EAAT1-related HM and FHM2

Considering the detailed clinical characterisation of the P290R-associated disorder[96], the phenotype appears to closely resemble the S218L *CACNA1A* syndrome, which includes HM attacks, progressive EA, epileptic seizures, coma and cerebral oedema induced by mild head trauma[53, 195, 196]. These highly related phenotypes may, in general, indicate a shared underlying pathophysiological mechanism. However, shared pathways between *ATP1A2*- and *SLC1A3*-associated HM also become highly plausible considering the proposed mechanistic concepts as well as the affected cell type expressing the mutant protein[37, 48]. In FHM2, reduced astrocytic K^+ clearance following neuronal activity was demonstrated, which is why the involvement of K^+, especially during the process of CSD propagation, was never entirely ruled out[48]. Nevertheless, delayed $[K^+]_e$ clearance is probably not contributing substantially to the facilitation of CSD induction but may be decisive during the process of propagation and later CSD phases in FHM2[48].

Despite the primary hypothesis assuming absent $[K^+]_e$ alterations during all phases of CSD, K^+ levels were increased in slices of *Slc1a3*$^{P290R/wt}$ animals during the re-uptake process following the CSD peak. As already mentioned, EAAT1 is predominantly expressed in astrocytes in the cortical region, which are considered to substantially contribute to K^+ buffering[197]. Impaired astrocytic K^+ buffering was linked to increased propagation velocity of hippocampal SD in a rodent model, in which the gap junction protein connexin-43 had been inactivated in an astrocyte-directed manner[198]. Of note, general gap junction inhibition was shown to prevent SD generation[199]. On the one hand, delayed $[K^+]_e$ removal following the CSD peak may indeed indicate a potential involvement in facilitating CSD propagation in the EA6 model, highlighting a shared pathomechanism with the FHM2 model. In fact, the CSD propagation velocity in *Slc1a3*$^{P290R/wt}$ animals was markedly increased. On the other hand, the observed $[K^+]_e$ alterations during late CSD phases may also be related to P290R-associated secondary changes that alter important astrocytic properties. To further verify a defect in astrocytic K^+ buffering in the *Slc1a3*$^{P290R/wt}$ model, recordings of the slowly decaying inward current in cortical astrocytes after extracellularly stimulating pyramidal cells in the vicinity may provide an estimation of the rate of astrocytic K^+ clearance and therefore represent a valuable investigation[48]. The astrocytic inward current elicited upon neuronal stimulation largely represents a K^+ current and can be used to evaluate $[K^+]_e$ accumulation[48].

The role of P290R-associated increased Cl^- currents in CSD pathophysiology

It is important to consider that the P290R variant also comprises a GOF effect on the anion/Cl^- currents. Hence, substantial alterations in the Cl^- homeostasis that significantly affect the processes of CSD initiation and propagation cannot be excluded as of now. The largely increased anion/Cl^- currents were already proven to contribute significantly to the cerebellar pathology in *Slc1a3*$^{P290R/wt}$ animals and to represent the primary cause for ataxia[156]. The anticipated changes in the Cl^- homeostasis may also evoke abundant secondary changes that could partly evoke the CSD-related alterations observed in the *Slc1a3*$^{P290R/wt}$ model.

Evidence that the exclusive impairment of synaptic glutamate removal by EAAT1 is sufficient to increase CSD susceptibility also derives from the T387P variant causing a pure HM phenotype[98]. T387P is functionally characterised by a LOF of glutamate transport as well as a reduction in cell surface expression due to an impaired K^+ binding to the transporter in its inward facing conformation[98].

4.1.4 Comparison of the *Scn1a*$^{L1649Q/wt}$ and the *Slc1a3*$^{P290R/wt}$ knock-in mouse models

At first appearance the *Slc1a3*$^{P290R/wt}$ and the *Scn1a*$^{L1649Q/wt}$ knock-in model for HM seem to differ with respect to numerous aspects. Whereas EAAT1 is predominantly expressed in astrocytes in the cortex and represents the second most important transporter to remove synaptically released glutamate during phases of neuronal activity[200], $Na_V1.1$ is predominantly expressed in the AIS of fast-spiking PV+ interneurons and plays a major role in AP initiation and propagation[75]. Functional characterisation of the P290R variant revealed a mixed effect on the dual function protein comprising a LOF of glutamate transport and a strong GOF of EAAT1-associated anion/Cl^- currents, which indicates that CSD pathophysiology may be based on enhanced glutamatergic neurotransmission at cortical synapses related to diminished glutamate re-uptake[98, 100]. In contrast, the L1649Q variant was functionally characterised by an incomplete inactivation process leading to increased persistent Na^+-current and firing frequency, which overall results in hyperexcitability of GABAergic interneurons[1].

With respect to the phenotypic spectrum, the L1649Q variant was identified in patients with pure HM[69], whereas the P290R variant yielded a highly complex overlapping syndrome consisting of EA, epileptic seizures and HM[96]. *SCN1A* represents one of the major genes causing genetic epilepsy syndromes such as DS or GEFS+, although FHM3 patients usually do not display additional epileptic seizures. However, the mutational spectrum of the *SLC1A3*-related neurological disorder EA6 is rather small. In general, FHM3 and especially *SLC1A3*-related syndromes are extremely rare, which challenges the significance of the results presented in this thesis. So far, only one patient carrying the *SLC1A3* P290R variant has been identified. Additionally, FHM3 only represents a minor fraction of all genetically caused HM cases[102]. Considering the rareness of both genetic disorders, it appears precarious to draw any conclusions to all HM forms from the obtained results or even generalise the findings to more common types of migraine. Nevertheless, investigating rare disorders holds the great potential to identify decisive molecular and cellular pathways. For example, the exploration of *SLC1A3*-associated disorders generates important knowledge on the role of glutamate homeostasis, which is implicated in a vast number of neurological diseases like glioblastoma[201] or amyotrophic lateral sclerosis[202].

Despite the vast number of differences, the *SLC1A3*- and *SCN1A*-related HM syndromes strikingly lead to a common final path within their individual pathophysiological cascades. Both syndromes do not only result in the same neurophysiological phenomenon, which is the CSD, but also trigger the activation of specific pain pathways like the trigeminovascular system that evoke the typical migraine headache in the patients[22, 23].

Altered absolute K^+ levels in the Scn1a$^{L1649Q/wt}$ model during the early CSD phase

To start with, in contrast to the *Slc1a3*$^{P290R/wt}$ animal model, overall $[K^+]_e$ levels were substantially increased in the *Scn1a*$^{L1649Q/wt}$ knock-in model[1]. The $[K^+]_e$ increase at the inflection point as well as the peak indicated a major role of K^+ during the CSD cascade of FHM3[1]. In contrast, absolute $[K^+]_e$ levels at the peak remained unaltered in the P290R-associated model primarily pointing towards a less significant role of K^+ during the process of CSD induction and highlighting the presumable importance of other factors like glutamate.

Delayed $[K^+]_e$ clearance in the Slc1a3$^{P290R/wt}$ model

The removal of $[K^+]_e$ occurring during later CSD phases was unchanged in the FHM3 model[1]. In contrast, $[K^+]_e$ re-uptake was delayed in slices of *Slc1a3*$^{P290R/wt}$ animals, as K^+ levels remained elevated during the descending phase of the curve, which is consistent with the phase of K^+ clearance (**Figure 18 E**). This finding possibly indicates that the astrocytic function of K^+ buffering may be altered, which is either a direct consequence of the *SLC1A3* variant on astrocytic function or related to secondary modifications caused by changes in the glutamate or Cl^- homeostasis within the astrocytes. Referring to the FHM2-related CSD pathomechanism, synaptic $[K^+]_e$ removal related to defective astrocytic K^+ clearance may have an impact on facilitating the process of CSD propagation. In fact, the propagation velocity was increased in *in vitro* CSD recordings of the P290R-associated model.

Changed $[K^+]_e$ dynamics in both models

In both transgenic HM models, $[K^+]_e$ dynamics were altered and the $[K^+]_e$ shifts were mainly confined to an early phase of the CSD[1]. This may imply that the most essential processes needed for CSD generation occur at the initial phase, during which mutant channels, transporters and pumps interfere with the net self-sustaining inward current and local $[K^+]_e$ release, which are required for inducing the self-regenerative depolarisation of neurons[34, 186]. Additionally, the fact that the main alterations are confined to this initial phase emphasises the all-or-nothing principle of CSD. Therefore, identifying those ion channels, transporters and pumps that are crucial during early CSD states may reveal new targets for treatment, which may primarily lead to preventing the self-regenerative cycle of CSD.

Whereas our recordings in slices of *Scn1a*$^{L1649Q/wt}$ animals suggested an earlier $[K^+]_e$ increase[1], the *Slc1a3*$^{P290R/wt}$ knock-in model displayed a marked acceleration of $[K^+]_e$ rise during the early phase of CSD. In the *Scn1a*$^{L1649Q/wt}$ model, the earlier $[K^+]_e$ rise was associated with a prolonged time from K^+ threshold until the inflection point as well as an increased AUC during the early CSD interval and was additionally verified by an unaltered time from inflection point to peak[1]. Furthermore, $[K^+]_e$ levels were elevated, which was demonstrated by an increase of $[K^+]_e$ at the inflection point as well as the peak[1]. Related to the overall increased magnitude of K^+ levels, the

20 to 90 % rise time was also prolonged in slices of *Scn1a*$^{L1649Q/wt}$ animals, however, the maximum rising speed remained unaltered[1].

In the FHM3 model, the early increase and accumulation of $[K^+]_e$ was associated with the increased persistent Na^+ current and firing frequency of fast-spiking interneurons, which represented the mechanistic link between interneuron hyperexcitability and a higher CSD susceptibility[1]. Therefore, $[K^+]_e$ was considered the decisive factor initiating CSD in the *Scn1a*$^{L1649Q/wt}$ model[1].

In contrast, $[K^+]_e$ was attributed a minor role in the pathophysiological CSD cascade of the P290R-associated model, especially during the process of initiation. K^+-sensitive microelectrode recordings before and during CSD highlighted the significance of additional factors and supported the hypothesis of glutamate playing the key role in triggering CSD. In the *Slc1a3*$^{P290R/wt}$ model, the time from the K^+ threshold until the inflection point was shortened, which was confirmed by the AUC analysis revealing a smaller AUC. The accelerated $[K^+]_e$ increase resulted in a more rapid approach of the inflection point leading to diminished $[K^+]_e$ levels at this specific time point. The unchanged time from inflection point to peak, maximum rising speed and 20 to 90 % rise time emphasised that the accelerated dynamics were confined to a very early CSD interval. In accordance with the rapid $[K^+]_e$ rise at the incipient CSD phase, the propagation velocity was clearly increased in the P290R-associated model, which may additionally be affected by the delayed $[K^+]_e$ removal. In fact, the relative increase in propagation velocity was 42.1 % in the *Slc1a3*$^{P290R/wt}$ model, whereas the propagation velocity was only increased by 22.7 % in the FHM3 model[1].

4.1.5 Excitation and inhibition in the cortex of the *Slc1a3*$^{P290R/wt}$ knock-in mouse model

Emerging from the altered *in vitro* CSD characteristics in the *Slc1a3*$^{P290R/wt}$ model, the goal was to investigate if an imbalance between cortical excitation and inhibition underlies the observed changes. It was primarily hypothesised that the *Slc1a3*$^{P290R/wt}$ model would present with an enhanced glutamatergic synaptic transmission. However, under physiological conditions synaptic transmission as well as tonic inhibition in the cortex remained unaltered and did not account for the CSD-associated abnormalities.

Cortical E/I balance in P290R-associated CSD pathophysiology and comparison with FHM models

The absent changes in absolute $[K^+]_e$ levels and the differential alterations of $[K^+]_e$ dynamics during CSD verified that the *Slc1a3*$^{P290R/wt}$ model does not share the CSD-associated pathophysiological concepts of FHM3[1]. This speculation was further confirmed by the unaltered inhibition at cortical synapses of heterozygous animals. In contrast, the inhibitory input recorded from cortical pyramidal cells of heterozygous *Scn1a*$^{L1649Q/wt}$ animals was enhanced and represented one of the major findings, on which the hypothesis of interneuron hyperexcitability was built on (**Figure 31**)[1]. One possible explanation for the lacking verification of an impaired cortical E/I balance in the *Slc1a3*$^{P290R/wt}$ model may be due to focusing on the wrong cell type. Despite the well-known significance of pyramidal cells in CSD initiation, it was recently proven that inhibitory interneurons can play an important role in triggering CSD[1]. In the FHM1 model, inhibitory neurotransmission, which also depends on $Ca_V2.1$ channels, was found to be unaltered, showing that distinct cell types may be differentially sensitive to the functional effects of a variant[203]. Nevertheless, sIPSC and mIPSC recordings have been performed in this work verifying that the inhibitory input on cortical pyramidal cells is unaltered.

As already outlined, the phenotypic spectrum of FHM1 patients carrying the S218L variant highly resembles the P290R *SLC1A3* overlapping syndrome[53, 195, 196]. This may indicate shared underlying pathophysiological concepts. However, enhanced glutamatergic neurotransmission at pyramidal synapses based on increased AP-evoked Ca^{2+} influx was demonstrated in the FHM1 model[52], whereas synaptic excitatory neurotransmission remained unaltered in the *Slc1a3*$^{P290R/wt}$ model (**Figure 31**). This finding clearly contradicts an equal mechanism of CSD induction and propagation. Furthermore, *CACNA1A*-related HM pathophysiology is based on a presynaptic mechanism increasing the AP- and Ca^{2+}-dependent release probability of glutamate[52]. In contrast, deficient glutamate removal from the synaptic cleft presumably implies postsynaptic alterations in the *Slc1a3*$^{P290R/wt}$ model.

In FHM2, CSD pathophysiology is based on the impaired clearance of glutamate and K^+ during neuronal activity (**Figure 31**). The mutant α_2 NKA is predominantly expressed in cortical astrocytes, which explicitly highlights similar mechanisms between the two models[58]. Due to a tight coupling between the α_2 NKA and EAAT2 representing the main glutamate transporter in the mammalian brain, EAAT2 expression levels were substantially reduced in FHM2[48]. Although EAAT1 only accounts for a minor fraction of the synaptic glutamate removal, similar functions of the highly related transporters emphasise that the CSD cascade may be shared. As the P290R-related LOF effect on glutamate transport suggested an impaired glutamate removal associated with prolonged presence of glutamate in the synaptic cleft, an alteration of the EPSC decay time constant by performing whole-cell patch clamp recordings of pyramidal neurons was primarily hypothesised. However, this initial theory could not be verified as the respective mechanism underlying increased CSD susceptibility and altered CSD characteristics.
To date, recordings exploring excitatory and inhibitory transmission in the *ATP1A2* mouse model have not been performed impeding to draw sound conclusions from an unaltered E/I balance in the *Slc1a3*$^{P290R/wt}$ model. Instead, enhanced glutamatergic transmission was verified by performing recordings of synaptically activated glutamate transporter currents (STCs) that were either elicited by single pulse stimulation or high frequency trains of APs in cortical layer 1[48]. Similar experiments were conducted to investigate the rate of K^+ clearance in the FHM2 model[48]. Recordings to determine the efficacy of glutamate clearance in the *Slc1a3*$^{P290R/wt}$ model were not performed in this work, however, may bear the most promising potential to solve important aspects of the *SLC1A3*-related CSD cascade. Furthermore, sEPSC and mEPSC recordings depict a rather physiological presentation of excitatory synaptic transmission, as they are recorded during baseline neuronal activity. As already discussed before, the reduction of glutamate clearance based on the genetic defect in FHM2 depends on the magnitude of neuronal activity[48].

Additionally, EAAT1 represents the second most important transporter to perform synaptic glutamate re-uptake during neuronal activity. Therefore, dysfunctional EAAT1-associated glutamate removal may be exclusively revealed during enhanced neuronal activity, for example during high frequency stimulation.

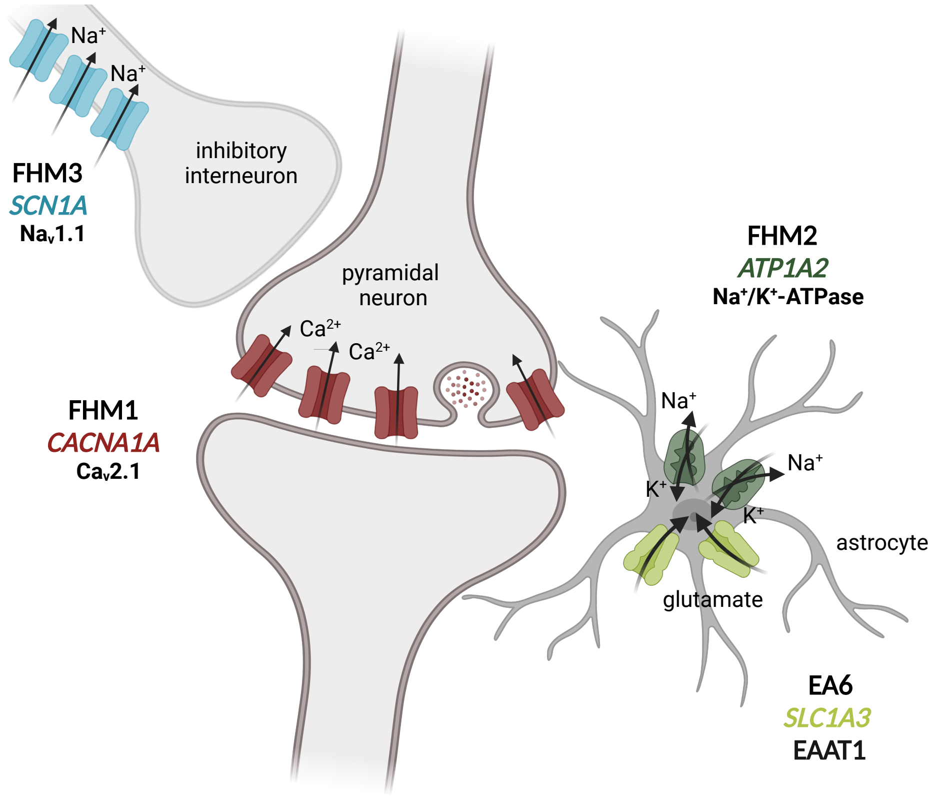

Figure 31. Cortical E/I imbalance as the common pathophysiological mechanism of genetic HM subtypes. FHM1 is caused by *CACNA1A* GOF variants encoding Ca$_V$2.1, which lead to increased AP-evoked Ca^{2+} influx resulting in enhanced glutamatergic neurotransmission at pyramidal synapses (middle, dark red). LOF variants in *ATP1A2* encoding the astrocytic α2 NKA cause FHM2 and evoke an impaired clearance of synaptically released glutamate and K$^+$ (right, dark green). Hyperexcitability of fast-spiking inhibitory neurons in FHM3 is based on an increase in persistent Na$^+$ current and AP frequency and is generated by GOF variants in *SCN1A*, which encodes Na$_V$1.1 (left, light blue)[1]. The P290R variant in *SLC1A3* encoding the astroglial EAAT1 exerts a LOF on glutamate transport and a GOF on anion currents, however, cortical E/I balance was preserved under physiological conditions (right, light green).

Cortical tonic inhibition in P290R-associated CSD pathophysiology

Moreover, tonic GABAergic inhibition was studied, as the lab Fahlke and colleagues had previously demonstrated that tonic GABA$_A$-receptor mediated currents were decreased in the DG granule cells causing hippocampal hyperexcitability in the EA6 model (unpublished data). Tonic current recordings of cortical pyramidal cells revealed a trend with respect to a reduction in the tonic current amplitude, which is unlikely to cause the HM phenotype.

It was hypothesised by Fahlke and colleagues that the diminished magnitude of DG tonic inhibition may be the consequence of an increased Cl$^-$ efflux through EAAT1 P290R-associated anion channels, which was based on [Cl$^-$]$_i$ measurements in RGLs (unpublished data). The reduced astrocytic [Cl$^-$]$_i$ was speculated to increase the Na$^+$/Cl$^-$-dependent GABA uptake performed by the GABA-transporter 3 (GAT-3) into astrocytic processes and to simultaneously decrease the

ambient GABA levels required for tonic inhibition (unpublished data by Fahlke and colleagues)[204]. So far, the mechanism leading to hippocampal hyperexcitability and epileptic seizures has mainly been associated with the P290R GOF effect on EAAT1 anion channels (unpublished data by Fahlke and colleagues).
As cortical tonic inhibition did not differ between the genotypes and the effect of UCPH-101 reproducing a complete EAAT1 KO accounted for most of the facilitation of CSD induction and propagation, EAAT1 anion channel GOF possibly represents a minor role in *SLC1A3*-related CSD pathophysiology. Nevertheless, these hypotheses remain to be verified.

In summary, synaptic neurotransmission and tonic inhibition were demonstrated to be balanced under physiological conditions despite the P290R-related LOF on EAAT1 glutamate transport (**Figure 31**). However, the rate of glutamate and K^+ clearance by cortical astrocytes, especially during increased neuronal activity, has not been explored so far and may be a promising future investigation to determine the underlying causes for an enhanced facilitation of CSD induction and propagation and to link *SLC1A3*-related HM pathophysiology to the proposed enhanced glutamatergic neurotransmission.

4.1.6 Occurrence of additional phenotypes with a focus on epileptic seizures in HM

The *Slc1a3*$^{\mathrm{P290R/wt}}$ knock-in model was used to identify additional phenotypes that frequently overlap with HM. In this regard, the co-occurrence of epileptic seizures and the development during epileptogenesis, which also involved gender-associated differences, were studied. Kovermann and colleagues previously elucidated the EA phenotype in *Slc1a3*$^{\mathrm{P290R/wt}}$ animals and will not be covered in this thesis[156]. In contrast, *Scn1a*$^{\mathrm{L1649Q/wt}}$ animals were not characterised by any additional phenotypes, which was anticipated beforehand since L1649Q carrying patients display pure HM characterised by the absence of epilepsy and other disorders[1, 69].

4.1.6.1 Impaired growth in *Slc1a3*$^{\mathrm{P290R/wt}}$ animals

After the weaning period, stagnation of weight gain or weight loss were observed in *Slc1a3*$^{\mathrm{P290R/wt}}$ mice, which coincided with the period of highest seizure vulnerability. Thus, these features appear to represent an adverse effect of the epilepsy. Nevertheless, heterozygous animals frequently stayed at an underweight level compared to wildtype littermates despite starting to re-gain weight during the compensatory phase.

Association between the P290R-associated epileptogenesis and delayed growth

Body weight differences and delayed growth are usually not observed in HM mouse models that lack an additional co-occurring epileptic phenotype and they mostly develop normally compared to their wildtype littermates[1, 27, 205]. Considering the phenotypic spectrum of human HM, concomitant symptoms characteristically lack weight loss. Furthermore, the first HM attack frequently occurs during adolescence between 12 and 17 years of age, when the most important developmental time periods have already been completed suggesting an absent correlation between CSD/HM attacks and altered growth in the *Slc1a3*$^{\mathrm{P290R/wt}}$ knock-in model[8].

However, the coincidence of seizures and weight changes in *Slc1a3*$^{\mathrm{P290R/wt}}$ mice as well as the perfectly parallel progress of weight loss/stagnation of weight gain during epileptogenesis point towards a close association. As opposed to (F)HM, delayed growth and body weight loss are often observed in distinct mouse models for genetic epilepsy syndromes indicating that these features are tightly connected to the occurrence of severe epileptic phenotypes[206, 207]. Despite the great relevance of physical development and metabolism in the daily care of patients with genetic epilepsy syndromes, little attention has been paid to these accompanying phenotypic features so far. Scientific data supporting and investigating the co-occurrence of growth issues in HM overlapping syndromes, like the *CACNA1A*-S218L mouse model, are not available.

Gender-related differences in the Slc1a3$^{P290R/wt}$ *knock-in model*

A separate evaluation of male and female *Slc1a3*$^{\mathrm{P290R/wt}}$ animals confirmed that the diminished growth occurred for both genders. However, the maximum difference in body weight was found later in the female heterozygous population overall suggesting a later onset of the epileptic phenotype compared to the male group. Furthermore, in the female population a re-gain in body weight was observed during the late compensatory phase. These slight differences indicated the presence of gender-related differences, with a less severe phenotype in female animals with respect to epilepsy and development. Of note, it was similarly observed in DS that female mice recovered faster from weight loss/stagnation of weight gain compared to male animals and displayed normal body weight after having passed the disease-specific peak period of epileptic seizures[207]. However, a minor number of experimental studies has focused on investigating HM models with overlapping syndromes and most lack an exploration of potential gender-related differences.

The milder epileptic phenotype in female heterozygous animals may be related to an upregulation of the GABA$_A$R δ subunit expression during defined phases of the ovarian cycle, as δ subunits are implicated in mediating tonic inhibition[208, 209]. As already discussed in section 4.1.5, the pivotal role of diminished hippocampal tonic inhibition causing the epileptic phenotype of *Slc1a3*$^{\mathrm{P290R/wt}}$ animals has recently been hypothesised by Fahlke and colleagues (unpublished data). GABA$_A$R δ subunits are upregulated in the high-progesterone late diestrus phase during the female ovarian cycle leading to enhanced tonic inhibition and decreased neuronal excitability, which is accompanied by a decreased seizure susceptibility[209].

Absent gender-related differences in the FHM3 mouse model

In contrast to the milder epileptic phenotype in female *Slc1a3*$^{\mathrm{P290R/wt}}$ mice, familial as well as sporadic HM disorders have a remarkably higher prevalence among women compared to men[210, 211]. These epidemiological observations are additionally supported by experimental data from transgenic FHM models demonstrating an increased CSD susceptibility in female mutant animals, which was abolished by neutralising the impact of female ovarian hormones[54]. Nevertheless, *in vivo* CSD recordings of male and female *Scn1a*$^{\mathrm{L1649Q/wt}}$ animals did not reveal any gender-related differences indicating that the more pronounced HM phenotype in females may not apply to FHM3[1].

4.1.6.2 The co-occurrence of epileptic seizures in the *Slc1a3*$^{P290R/wt}$ knock-in model

To start with, one common feature of *CACNA1A*, *ATP1A2*, *SCN1A* and *SLC1A3* is given by the fact that variants in all four genes can cause HM as well as epilepsy. However, the *CACNA1A* gene as well as the *ATP1A2* gene currently play a minor role in the context of genetic epilepsy syndromes and are rarely linked to severe epileptic encephalopathies, whereas most identified variants have been associated with HM[119, 120, 121, 124]. Nevertheless, *CACNA1A*- and *ATP1A2*-related HM phenotypes are frequently characterised by an overlap with epileptic seizures/epilepsy[61, 119, 120, 121, 212]. Additionally, *CACNA1A* LOF variants are known to cause EA2, which also represents a large fraction of the phenotypic spectrum[50].

Similarly, the largest fraction of *SLC1A3* variants was associated with ataxia-related, cerebellar symptoms followed by migraine attacks with or without aura[90, 91, 92, 97, 99, 132]. EA6 represents an extremely rare neurological disorder, which is highlighted by the fact that *SLC1A3* variants have only been reported in seven different families. Pure HM was exclusively observed in one patient carrying the LOF variant T387P[98]. Considering the recurrent association of *SLC1A3* with (H)M, the gene has already been claimed to expand the genetic HM spectrum[213].

Despite the rareness of overlapping syndromes between EA, epilepsy and HM, seizures are a frequent phenotypic feature of several EA subtypes[214]. However, the additional occurrence of epileptic seizures was exclusively reported in the first P290R carrying EA6 patient, which remained by far the most severe among all the variants that have been identified to date[96]. Nevertheless, studying the functional consequences of altered glial glutamate/Cl$^-$ homeostasis and the included epilepsy causing pathways is extremely useful. The acquired knowledge may additionally help to understand the pathophysiology of epileptic encephalopathies caused by variants in the highly related glutamate transporter gene *SLC1A2*[133].

The anticipated relevance of increased anion/Cl$^-$ currents in P290R-associated epilepsy

The remaining six identified *SLC1A3* variants were functionally characterised in a recent study demonstrating distinct impairments of EAAT1 properties that mainly affected glutamate transport, trafficking, and surface expression and mostly resulted in mild alterations, however, the consequences in patients remained difficult to predict[101]. Nevertheless, the absent pronounced increase in EAAT1-associated anion currents in all included EA6 variants stood out and differentiated the epilepsy causing P290R variant from the remaining *SLC1A3* variants that lead to EA6 and occasionally HM[100]. Therefore, the mixed P290R effect on EAAT1 function uniquely comprises largely altered Cl$^-$ currents that may yield the additional epileptic phenotype in the respective patient. This theory is additionally supported by the recent functional characterisation of three *SLC1A2* variants that cause an extremely severe epileptic encephalopathy, since enhanced anion channel function and impaired glutamate transport capability were equally demonstrated to be the major alterations[133]. Increased glutamate-activated Cl$^-$ efflux through mutant EAAT1 anion channels of Bergmann glia cells was shown to cause apoptosis, cerebellar degeneration and ataxia in *Slc1a3*$^{\mathrm{P290R/wt}}$ animals indicating that the hypothesis for developing *SLC1A3*-related ataxia is also based on the increase in anion currents[156].

On the contrary, one EA6 variant identified in a child with truncal ataxia and strabismus was consistent with a LOF of EAAT1 glutamate transport and anion currents corresponding with the functional effect of T387P, which instead leads to pure HM in the respective patient[98]. This example should emphasise that it is hardly possible to draw any sound conclusions exclusively from the functional characterisation of *SLC1A3* variants. Due to these ambiguous results from functional characterisation studies, an in-depth investigation of the epileptic phenotype using *Slc1a3*$^{\mathrm{P290R/wt}}$ knock-in animals is essential to clarify the underlying pathophysiology.

High interindividual variability in epilepsy-associated features

Whereas Bergmann glia cell degeneration underlying the ataxia occurred during the second and third postnatal week, the epilepsy onset was observed after the weaning period[156]. As *Slc1a3*$^{\mathrm{P290R/wt}}$ animals do not display spontaneous attacks of hemiplegia, it was not possible to verify the HM phenotype *in vivo* and to define its onset. However, the seizure onset and the period of highest susceptibility were characterised by high interindividual variability. As the onset widely ranged from the third to the sixth postnatal week, a correlation with the upregulation of EAAT1 or other implicated proteins either in the whole brain or in certain regions seems to be rather unlikely. A slightly differing genetic background between single animals also appears implausible to cause the strong variation since *Slc1a3*$^{\mathrm{P290R/wt}}$ knock-in animals were generated on the same 129Sv/Tac background. Additionally, the duration and frequency of ictal events, the lethality and seizure severity also differed remarkably between individual animals.

Heterozygous animals that were implanted during the sixth or seventh postnatal week showed an alleviation of the epileptic phenotype including a reduced seizure frequency, which is presumably caused by seizure-induced secondary changes leading to the up- or downregulation of specific proteins. The identification of secondary changes may be an interesting target for future studies.

Slc1a3$^{\mathrm{P290R/wt}}$ animals were initially generated on a C57BL/6N background yielding high seizure-induced lethality, which was reduced by ~ 70 % after changing the background[156]. This emphasises that a different genetic background with changes in the expression level of certain genes can result in a largely altered phenotype. The significant difference between the C57BL/6N and the 129Sv/Tac background may be based on the differential expression of certain GABA receptor subunits in distinct strains. Due to a single base pair deletion, the C57BL/6J mouse strain expresses a brain-wide reduced amount of the GABA$_{\mathrm{A}}$-receptor $\alpha 2$ subunit, which may be the cause for an enhanced seizure susceptibility in mouse models generated on this background[215].

Reduced hippocampal tonic inhibition as the proposed mechanism of P290R-related epilepsy

In this thesis, the first *in vivo* EEG recordings of seizures in *Slc1a3*$^{\mathrm{P290R/wt}}$ knock-in animals are presented. The recordings during highest seizure susceptibility revealed continuous status epileptici characterised by numerous ictal events that were interspersed with coma-like episodes.

In contrast, the epileptic phenotype was slightly milder during the compensatory phase. The explicit severity including the occurrence of status epilepticus- and seizure-associated lethality represent outstanding features of the P290R-associated epilepsy. Fahlke and colleagues have previously linked the epileptic phenotype of the *Slc1a3*$^{\mathrm{P290R/wt}}$ model to hippocampal hyperexcitability caused by decreased tonic inhibition but unaltered synaptic transmission (unpublished data). On the one hand, these apparently small changes may not be sufficient to cause the devastating epileptic phenotype observed in mice and human. On the other hand, the $\mathrm{GABA_A}$ receptor subunits mediating tonic inhibition are persistently activated by very low concentrations of ambient GABA ranging from tens of nanomolar to a few micromolar, which contrasts with the large amount of GABA during synaptic transmission peaking in the millimolar range[171, 216]. Hence, tonic inhibition is delicately regulated in the brain and small changes may yield large consequences.

It was hypothesised that enhanced P290R-related $\mathrm{Cl^-}$ efflux from RGLs resulting in reduced $[\mathrm{Cl^-}]_i$ and increased GABA uptake via GAT-3 underlies the diminished DG tonic inhibition (unpublished data by Fahlke and colleagues). Thus, the large heterogeneity in $[\mathrm{Cl^-}]_i$ in highly similar glial cell types during physiological as well as pathological states must be considered[217]. For example, $[\mathrm{Cl^-}]_i$ in cortical astrocytes is rather low, whereas $[\mathrm{Cl^-}]_i$ in DG astrocytes is relatively high[218]. Additionally, the role of EAAT1 and EAAT2 in determining the internal $\mathrm{Cl^-}$ levels varies substantially depending on the cell type and region. Moreover, $[\mathrm{Cl^-}]_i$ is differentially affected by the expression of KCC1, KCC3, CLC2 and NKCC1[218]. As EAAT1 distinctly contributes to setting $[\mathrm{Cl^-}]_i$ and $\mathrm{Cl^-}$ levels largely differ depending on the specific glial cell type, the brain regions may be differentially sensitive to $[\mathrm{Cl^-}]_i$ changes. In the hippocampal RGL population EAAT1 contributes to regulating $[\mathrm{Cl^-}]_i$, which also applies to astrocytes of cortical layer 2/3[218]. This finding supports the hypothesis that the comparably higher $[\mathrm{Cl^-}]_i$ of RGLs is substantially changed by the P290R variant and results in a major impact on RGL pathophysiology and presumably the whole DG region.

Hippocampal upregulation of c-fos expression during status epileptici

Furthermore, in two heterozygous animals, c-fos expression was highly upregulated in the hippocampus. In one heterozygous animal, the maximum density of c-fos positive cells was mapped to the DG supporting the hypothesis proposed by Fahlke and colleagues (unpublished data). However, in the second mouse an increased density of c-fos positive cells was observed in the CA1 and CA3 regions contradicting the minor changes that have recently been found in CA1 (unpublished data by Fahlke and colleagues). The CA3 region has not been investigated to date. Upregulated c-fos expression during increased neuronal activity may hold a great potential to identify areas that are important during seizure generation or even determine the seizure origin. However, the density of c-fos positive cells is also elevated in brain regions that get involved during secondary seizure generalisation or during a status epilepticus. The brain areas, which are activated most during seizure generation and epileptic seizures, may already be silenced during prolonged status epileptici. Instead, distinct brain regions may be characterised by excessive epileptic discharges if the status epilepticus persists. The three heterozygous animals used for c-fos staining were killed during prolonged status epileptici markedly exceeding a duration of 24 hours. Therefore, the high interindividual variability of c-fos expression may indicate that the areas of seizure origin are silenced during prolonged status epileptici and that distinct areas are involved during status activity, which depends on the single animal.

Potential involvement of the thalamic brain region

Studies demonstrated the co-localisation of GAT-3 with EAAT1 and EAAT2 on astrocytic process surrounding excitatory synapses[219, 48]. As already outlined in section 4.1.5, a marked GAT-3 upregulation has recently been identified in the hippocampus of *Slc1a3*$^{P290R/wt}$ animals (unpublished data by Fahlke and colleagues). However, profound changes in GAT-3 expression levels may be also found in other brain areas that have not been identified so far but may still be involved in epileptogenesis. For example, in a genetic epilepsy model, GAT-1 (GABA transporter 1) impairment in thalamic astrocytes leading to abnormal ambient GABA levels was associated with enhanced tonic inhibition and absence seizure generation[220]. Conversely, increased thalamic tonic inhibition was shown to result in enhanced seizure susceptibility caused by GAT-3 downregulation[221]. Although an alteration of thalamic tonic inhibition has the opposite effect on brain excitability compared to the hippocampus, the thalamus clearly represents a region of interest for further investigations, which is based on several observations presented in this work.

First, various ictal events were characterised by a sudden behavioural arrest of the animal, which is typically observed during absence seizures that are generated in the thalamus. However, during several of these freezing episodes electrographic features indicating a seizure were not present. Therefore, many of these events were not classified as seizures. Secondly, in one heterozygous animal the maximum density of c-fos positive cells was mapped to the reticular nucleus of the thalamus indicating a recent involvement in increased neuronal activity and possibly in seizure generation or generalisation. To further assess, if the seizures originate from the thalamus, deep electrode recordings monitoring thalamic activity in *Slc1a3*$^{P290R/wt}$ animals are essential. Thirdly, the thalamus is implicated in controlling alertness, which was not only impaired during disease exacerbations described in the P290R-carrying patient but also in *Slc1a3*$^{P290R/wt}$ animals during prolonged postictal depression episodes.

The role of diminished P290R-associated glutamate removal during epileptic seizures

As increased anion currents distinguish the P290R variant from other *SLC1A3* variants, the epilepsy-related discussion has so far focused on the GOF effect on the Cl^- channel. However, the LOF of EAAT1-associated glutamate transport may not only result in enhanced CSD susceptibility, as hypothesised in this work, but may also be involved in causing epilepsy. A study has recently revealed that neural activity bursts are dampened by the synchronous activity of glial cells that compensate excessive glutamate levels via EAAT2 and consequently prevent seizure generation[222]. Despite being responsible for the minor fraction of synaptic glutamate removal, diminished EAAT1 glutamate transport may also have an impact on the astrocytic function of dampening preictal neuronal activity. Moreover, using *eaat2a*$^{-/-}$ mutant zebrafish larvae it was demonstrated that reduced glutamate clearance results in hyperexcitability, however, during interictal states both neuronal and astroglial networks remained hypoactive[223]. The authors hypothesised that the observed hypoactivity was caused by seizure-induced depletion of presynaptic glutamate storages and an impaired glutamate-glutamine cycle to restore the presynaptic glutamate pool[223]. The pronounced prolongation of postictal states in the *Slc1a3*$^{\mathrm{P290R/wt}}$ model may be caused by a similar mechanism related to reduced availability of presynaptic glutamate. Therefore, glutamate imaging techniques would be highly valuable to unravel potential alterations in the P290R-related glutamate homeostasis during ictal and interictal states.

Limitations with respect to the video-EEG recordings

The ictal events during video-EEG monitoring were assessed manually, which is prone to misinterpretations by the analyst and represents an important limitation of this work. However, as the traces were superimposed by spike-like breathing artefacts in *Slc1a3*$^{\mathrm{P290R/wt}}$ animals, the usually applied semi-automated identification of ictal events mostly yielded wrong results. Additionally, some seizures were not clearly visible in the EEG recordings but were reliably verified by the characteristic behaviour of the respective mouse. On the contrary, EEG recordings from human patients are also assessed by experienced physicians of the respective specialties.

Another important limitation of this work is that exclusively male *Slc1a3*$^{\mathrm{P290R/wt}}$ animals were used for video-EEG monitoring. Although the phenotype of male mice may not be influenced by cyclic hormonal changes, they display a more severe epileptic phenotype compared to female *Slc1a3*$^{\mathrm{P290R/wt}}$ animals preventing to receive a representative picture of the entire population. Additionally, the sole use of male animals may partly account for the increased seizure severity and lethality of implanted compared to non-implanted animals.

Increased seizure-associated mortality in implanted Slc1a3$^{P290R/wt}$ *animals*

Epileptic seizures of implanted *Slc1a3*$^{\mathrm{P290R/wt}}$ animals were associated with high lethality, which was more pronounced in the younger animal group. Although the rate of deaths among implanted mice was increased compared to age-matched non-implanted heterozygous animals, a direct comparison between implanted and non-implanted mice must be handled with care. For example, implanted animals were closely monitored several times a day, whereas epileptic seizures of non-implanted animals that would also have fulfilled the human endpoint criteria may have been missed more easily due to a lower monitoring frequency.

The increased lethality may also be related to the surgical procedure although intraoperative monitoring of the general health status and the vital signs did not reveal any differences between wildtype and heterozygous animals. On the contrary, homozygous EAAT1-KO mice displayed increased oedema after cerebellar injury[153], which may also occur in the *Slc1a3*$^{\mathrm{P290R/wt}}$ knock-in model and contribute to increased lethality after surgical procedures. Additionally, enhanced formation of brain oedema combined with larger lesion volumes following traumatic brain injury were observed in the highly related *CACNA1A* S218L model[224].

Furthermore, the used anaesthetic substances or components of the antidot may also have a considerable impact on worsening the phenotype. In a mouse model for *SCN8A* epileptic encephalopathy, which is characterised by an increased risk for sudden unexpected death in epilepsy (SUDEP), non-fatal seizures were converted to fatal seizures by inhibiting adrenergic receptors[225]. The implanted animals were applied an antidot including atipamezole, which is a widely used adrenergic receptor antagonist. A similar mechanism that increases seizure-induced death by adrenergic receptor inhibition may also apply to the *Slc1a3*$^{\mathrm{P290R/wt}}$ knock-in model. However, the exact underlying mechanisms remain to be explored in detail.

Association between epileptiform activity and CSD in Slc1a3$^{P290R/wt}$ *animals*

Substantially protracted intervals of postictal depression, which were observed in most implanted *Slc1a3*$^{\mathrm{P290R/wt}}$ animals, represent a characteristic feature in P290R-associated epilepsy and closely resemble the human phenotype. In the respective patient, the two major episodes with documented seizure activity during EEG recordings were also characterised by a considerably reduced alertness lasting several days[96]. However, the classic postictal depression or slowing of EEG activity that directly follows an ictal event mostly lasts seconds to minutes[137]. On the one hand, the specific prolongation of postictal periods may be merely the result of severe, long-lasting seizure activities. However, on the other hand, the observed episodes of greatly diminished consciousness may also be caused or aggravated by CSD events that are triggered by seizures and directly emerge from ictal events. This is supported by the fact that depolarisation blocks in the context of CSD are known to last considerably longer[104].

During seizure activity, $[K^+]_e$ frequently rises to a peak level of approximately 12-13 mM[138, 226], which was verified to already exceed the threshold to trigger CSD[17, 227]. As shown in this work, the maximum $[K^+]_e$ during CSD is considerably higher, surpassing the peak $[K^+]_e$ during an epileptic seizure on average by three orders of magnitude[1]. A recent study suggested that the threshold for seizure-SD coupling may be controlled by different, so far unidentified molecular determinants, since not every epileptic seizure is followed by a CSD[228]. Thus, it seems rather unrealistic to exclusively attribute CSD induction following an epileptic seizure to the $[K^+]_e$ magnitude, although an involvement may be conceivable. It was demonstrated that the epilepsy causing gene *KCNQ2* encoding the axonal K^+ channel subunit $K_V7.2$ represents one of the genes that substantially interfere with the threshold of seizure-SD transition[228]. In the P290R carrying patient, seizure activity co-occurred with signs for HM[96]. Therefore, EAAT1-P290R may have similar modulatory effects resulting in the emergence of a long-lasting CSD-associated suppression of cellular activity after seizure events and may explain the prolonged postictal states of *Slc1a3*$^{\mathrm{P290R/wt}}$ animals. To verify this theory, chronic DC-band EEG recordings of *Slc1a3*$^{\mathrm{P290R/wt}}$ mice, preferably during the period of highest seizure susceptibility, are needed. Of note, the silencing effect of CSD may also provide an explanation why the areas with maximum c-fos expression among the heterozygous animals with status epileptici were inconsistent and did not reveal the seizure-generating brain regions.

On the contrary, novel experimental data suggests that CSD represents an innate antiseizure mechanism counteracting arising seizure activity and preventing the generation of ictal events[139]. However, if CSDs exclusively result from ictal activity to protect the brain against dangerous hyperexcitable states, as suggested by this concept, a more frequent co-occurrence of CSDs and epileptic seizures would have probably been noticed in literature.

To sum up, the *Slc1a3*$^{\mathrm{P290R/wt}}$ model is suited to investigate frequent additional phenotypes in HM and especially qualifies for studying a severe epileptic phenotype, which is verified in this work. However, the pathophysiological mechanisms have not been fully elucidated and further explorations are needed. This work provides important results that support the identification of critical aspects for future research.

4.1.6.3 The pure HM phenotype in *Scn1a*$^{\mathrm{L1649Q/wt}}$ animals versus the large spectrum of *SCN1A*-associated epilepsy syndromes

In contrast to the complex phenotypes of certain FHM1/2 variants and the *SLC1A3* P290R syndrome, FHM3 patients usually do not display overlapping epileptic seizures and variants have rarely been reported to simultaneously cause epilepsy and HM[77, 81]. This somehow contrasts with the vast number of *SCN1A* variants causing distinct genetic epilepsy syndromes ranging from mild and treatable to extremely severe epilepsy phenotypes that do not respond to ASMs[65, 66, 76, 126, 127]. Whereas FHM3 is associated with strong GOF effects and hyperexcitability of fast-spiking PV+ interneurons[1], GEFS+ and DS are caused by Na$_V$1.1 LOF leading to interneuron hypoexcitability[75, 76]. The concept of *SCN1A* GOF variants leading to FHM3 and *SCN1A* LOF variants resulting in epilepsy had to be rejected recently since mild GOF variants were demonstrated to cause different types of epileptic encephalopathy syndromes[109].

Pure HM caused by the L1649Q variant

Scn1a$^{\mathrm{L1649Q/wt}}$ animals harbour the human L1649Q variant[1], which was identified in a family with pure HM without epileptic seizures[69]. The seizure-free phenotype was confirmed by the initial, comprehensive phenotypic screening[1] and during frequent handling and monitoring of *Scn1a*$^{\mathrm{L1649Q/wt}}$ mice. Although the co-occurrence of subclinical epileptic seizures in heterozygous animals can only be excluded by performing chronic video-EEG monitoring of *Scn1a*$^{\mathrm{L1649Q/wt}}$ animals, an overlap with epilepsy seems rather unlikely. Further evidence supporting the absence of epilepsy was provided by the study by Chever and colleagues demonstrating that the activation of Na$_V$1.1 or PV+ GABAergic interneurons by distinct techniques induced CSD but never ictal-like epileptiform activities[29].

A computational model connecting a GABAergic to an excitatory neuron that included the dynamics of ion concentrations was used to generate FHM3 conditions by increasing the persistent Na^+ current and epileptogenic conditions by decreasing the Na^+ conductance in the involved interneuron[189]. Spike-induced alterations of extracellular ion concentrations were amplified by the increased persistent Na^+ current leading to a $[K^+]_e$ accumulation and facilitation of CSD induction, which represent the key effects in FHM3[189]. In contrast, $Na_V1.1$ LOF variants increased the susceptibility to enter long-lasting depolarisation blocks, however, both pathways resulted in hyperexcitable states of the connected pyramidal neuron[189]. The model once again emphasises the significance of $[K^+]_e$ accumulation and enhanced persistent Na^+ current in CSD triggering in FHM3. Of note, the absent increased persistent Na^+ current of mild *SCN1A* GOF variants that cause devastating epileptic phenotypes was shown to be the exclusive distinguishing factor from FHM3 *SCN1A* variants[109].

4.2 Recommendations for future research

In the *Scn1a*$^{L1649Q/wt}$ model for FHM3, $[K^+]_e$ recordings have never been performed directly at the CSD initiation site since K^+-sensitive microelectrodes were combined with KCl puff applications as CSD triggering technique[1]. Although the study by Chever and colleagues provided experimental evidence for the spike-elicited $[K^+]_e$ increase at the induction site by applying optogenetic tools, an acute model mimicking FHM3 pathology was used[29]. Besides this missing piece, the CSD cascade in FHM3 was successfully elucidated by demonstrating an early increased $[K^+]_e$ shift in this work, which provided the mechanistic link between interneuron hyperexcitability and increased CSD susceptibility[1].

The initial hypothesis was that P290R-associated CSDs are triggered based on the LOF effect that leads to impaired astrocytic glutamate clearance and enhanced glutamatergic neurotransmission. However, the mechanistic link between the dysfunctional EAAT1-assoicated glutamate transport and increased CSD susceptibility has not been demonstrated so far. One decisive future objective would be to measure the capacity of glutamate clearance of cortical astrocytes providing evidence for an enhanced synaptic glutamatergic transmission[48]. In this regard, the *Slc1a3*$^{P290R/wt}$ model would perfectly qualify for applying the great, newly available techniques of glutamate imaging to decipher the role of glutamate during CSDs and epileptiform activity. Despite extensively investigating phasic synaptic transmission and tonic inhibition, it was not possible to demonstrate an E/I imbalance underlying increased facilitation of CSD generation and propagation. These findings led to the conclusion that the impaired astrocytic glutamate removal may not be apparent under physiological conditions. Therefore, another future recommendation comprises the study of synaptic excitation under more pathological conditions, for example by presynaptic stimulation. In addition, CSD pathophysiology has only been investigated *in vitro*, using acute brain slices. However, the CSD and HM phenotype also need to be demonstrated *in vivo*.

Another interesting aspect for future studies is the gender-specific difference in the phenotype related to *SLC1A3*- and *SCN1A*-associated HM (and epilepsy) pathophysiology. Additionally, high interindividual variability between single *Slc1a3*$^{P290R/wt}$ animals regarding seizure onset, lethality or the frequency and duration of ictal events was observed in this thesis. However, the determining factors have not been identified so far. Furthermore, after having passed the period of highest seizure susceptibility *Slc1a3*$^{\mathrm{P290R/wt}}$ animals enter a compensatory phase characterised by a substantially reduced seizure frequency. As already suggested, this alleviation of the epileptic phenotype may be the result of the up- and downregulation of certain genes, however, the involved expression changes remain entirely unknown. Single-cell RNA-sequencing would represent an optimal tool to identify crucial genes that are up- or downregulated during epileptogenesis or the compensatory phase and to elucidate important differences in the gene expression levels between female and male animals.

As single-channel EEG recordings were performed in *Slc1a3*$^{\mathrm{P290R/wt}}$ animals, with the recording and reference electrodes being placed onto the brain surface, it was neither possible to determine if seizures are focal or generalised nor to identify the seizure origin. Therefore, it is recommended to use deep-electrode recordings in brain areas that are highly suspected to be implicated in seizure generation, like the thalamus or the hippocampus. Their selection is further supported by the observed pronounced c-fos upregulation indicating a participating role during epileptic seizures. Additionally, *Slc1a3*$^{\mathrm{P290R/wt}}$ animals represent a highly interesting model to further explore the seizure-SD coupling and to discover the correlation between these different, but similar hyperexcitable states. For studying the simultaneous occurrence of CSD and seizure-like activity chronic DC-band EEG recordings would be required.

One crucial step to decipher the detailed pathways of CSD pathophysiology comprises the identification of decisive ion channels, transporters and pumps that are implicated in the processes of CSD initiation and propagation. However, to avoid randomly picking different genes, proteins that are primarily located in apical dendrites or axonal processes may be highly interesting for detailed future studies. Although glutamate as well as K^+ have been identified to represent the two key triggering factors in HM, additional factors interfering with CSD initiation as well as the determinants of CSD propagation remain to be unravelled.

In conclusion, despite intensive research on CSD mechanisms and HM pathophysiology over the last decades, the subjects discussed within this work remain highly captivating for future investigations. As outlined in this section, recommendations for future explorations do not only concern general concepts of CSD and HM that have not been unravelled so far but also relate to very specific questions with respect to *SLC1A3*- and *SCN1A*-associated pathophysiology.

5 References

1. Auffenberg E, Hedrich UB, Barbieri R, Miely D, Groschup B, Wuttke TV, et al. Hyperexcitable interneurons trigger cortical spreading depression in an Scn1a migraine model. The Journal of Clinical Investigation. 2021;131(21).
2. Olesen J. The international classification of headache disorders. Headache: The Journal of Head and Face Pain. 2008;48(5):691-3.
3. Clarke JM. On recurrent motor paralysis in migraine, with report of a family in which recurrent hemiplegia accompanied the attacks. British Medical Journal. 1910;1(2582):1534.
4. Blau J, Whitty C. Familial hemiplegic migraine. The Lancet. 1955;266(6900):1115-6.
5. Thomsen LL, Ostergaard E, Olesen J, Russell MB. Evidence for a separate type of migraine with aura: sporadic hemiplegic migraine. Neurology. 2003;60(4):595-601.
6. Stovner L, Hagen K, Jensen R, Katsarava Z, Lipton R, Scher A, et al. The global burden of headache: a documentation of headache prevalence and disability worldwide. Cephalalgia. 2007;27(3):193-210.
7. Lipton RB, Bigal ME, Diamond M, Freitag F, Reed ML, Stewart WF. Migraine prevalence, disease burden, and the need for preventive therapy. Neurology. 2007;68(5):343-9.
8. Thomsen LL, Eriksen MK, Romer SF, Andersen I, Ostergaard E, Keiding N, et al. An epidemiological survey of hemiplegic migraine. Cephalalgia. 2002;22(5):361-75.
9. Lauritzen M. Pathophysiology of the migraine aura: the spreading depression theory. Brain. 1994;117(1):199-210.
10. Ayata C. Cortical spreading depression triggers migraine attack: pro. Headache: The Journal of Head and Face Pain. 2010;50(4):725-30.
11. Charles A. Does cortical spreading depression initiate a migraine attack? Maybe not. Headache: The Journal of Head and Face Pain. 2010;50(4):731-3.
12. Tfelt-Hansen PC, Koehler PJ. One hundred years of migraine research: major clinical and scientific observations from 1910 to 2010. Headache: The Journal of Head and Face Pain. 2011;51(5):752-78.
13. Hadjikhani N, Sanchez del Rio M, Wu O, Schwartz D, Bakker D, Fischl B, et al. Mechanisms of migraine aura revealed by functional MRI in human visual cortex. Proceedings of the national academy of sciences. 2001;98(8):4687-92.
14. Woods RP, Iacoboni M, Mazziotta JC. Bilateral spreading cerebral hypoperfusion during spontaneous migraine headache. New England Journal of Medicine. 1994;331(25):1689-92.
15. Leao AA. Spreading depression of activity in the cerebral cortex. Journal of neurophysiology. 1944;7(6):359-90.
16. Grafstein B. Mechanism of spreading cortical depression. Journal of neurophysiology. 1956;19(2):154-71.
17. Somjen GG. Mechanisms of spreading depression and hypoxic spreading depression-like depolarization. Physiological reviews. 2001;81(3):1065-96.
18. Kraig R, Nicholson C. Extracellular ionic variations during spreading depression. Neuroscience. 1978;3(11):1045-59.
19. Enger R, Tang W, Vindedal GF, Jensen V, Johannes Helm P, Sprengel R, et al. Dynamics of ionic shifts in cortical spreading depression. Cerebral Cortex. 2015;25(11):4469-76.
20. Lashley KS. Patterns of cerebral integration indicated by the scotomas of migraine. Archives of Neurology & Psychiatry. 1941;46(2):331-9.
21. Ayata C, Shin HK, Salomone S, Ozdemir-Gursoy Y, Boas DA, Dunn AK, et al. Pronounced hypoperfusion during spreading depression in mouse cortex. Journal of Cerebral Blood Flow & Metabolism. 2004;24(10):1172-82.
22. Moskowitz MA. The neurobiology of vascular head pain. Annals of Neurology: Official Journal of the American Neurological Association and the Child Neurology Society. 1984;16(2):157-68.

23. Pietrobon D, Striessnig J. Neurobiology of migraine. Nature Reviews Neuroscience. 2003;4(5):386-98.
24. Bolay H, Reuter U, Dunn AK, Huang Z, Boas DA, Moskowitz MA. Intrinsic brain activity triggers trigeminal meningeal afferents in a migraine model. Nature medicine. 2002;8(2):136-42.
25. Zhang X, Levy D, Noseda R, Kainz V, Jakubowski M, Burstein R. Activation of meningeal nociceptors by cortical spreading depression: implications for migraine with aura. Journal of Neuroscience. 2010;30(26):8807-14.
26. Zhang X, Levy D, Kainz V, Noseda R, Jakubowski M, Burstein R. Activation of central trigeminovascular neurons by cortical spreading depression. Annals of neurology. 2011;69(5):855-65.
27. van den Maagdenberg AM, Pietrobon D, Pizzorusso T, Kaja S, Broos LA, Cesetti T, et al. A Cacna1a knockin migraine mouse model with increased susceptibility to cortical spreading depression. Neuron. 2004;41(5):701-10.
28. Chung DY, Sadeghian H, Qin T, Lule S, Lee H, Karakaya F, et al. Determinants of optogenetic cortical spreading depolarizations. Cerebral Cortex. 2019;29(3):1150-61.
29. Chever O, Zerimech S, Scalmani P, Lemaire L, Pizzamiglio L, Loucif A, et al. Initiation of migraine-related cortical spreading depolarization by hyperactivity of GABAergic neurons and Na V 1.1 channels. The Journal of clinical investigation. 2021;131(21).
30. Herreras O, Somjen GG. Propagation of spreading depression among dendrites and somata of the same cell population. Brain Res. 1993;610(2):276-82.
31. Canals S, Makarova I, Lopez-Aguado L, Largo C, Ibarz JM, Herreras O. Longitudinal depolarization gradients along the somatodendritic axis of CA1 pyramidal cells: a novel feature of spreading depression. J Neurophysiol. 2005;94(2):943-51.
32. Makarova J, Gomez-Galan M, Herreras O. Variations in tissue resistivity and in the extension of activated neuron domains shape the voltage signal during spreading depression in the CA1 in vivo. Eur J Neurosci. 2008;27(2):444-56.
33. Busija DW, Bari F, Domoki F, Horiguchi T, Shimizu K. Mechanisms involved in the cerebrovascular dilator effects of cortical spreading depression. Prog Neurobiol. 2008;86(4):379-95.
34. Kager H, Wadman WJ, Somjen GG. Conditions for the triggering of spreading depression studied with computer simulations. J Neurophysiol. 2002;88(5):2700-12.
35. Ferrari MD, Klever RR, Terwindt GM, Ayata C, van den Maagdenberg AM. Migraine pathophysiology: lessons from mouse models and human genetics. Lancet Neurol. 2015;14(1):65-80.
36. Pietrobon D, Brennan KC. Genetic mouse models of migraine. J Headache Pain. 2019;20(1):79.
37. Leo L, Gherardini L, Barone V, De Fusco M, Pietrobon D, Pizzorusso T, et al. Increased susceptibility to cortical spreading depression in the mouse model of familial hemiplegic migraine type 2. PLoS genetics. 2011;7(6):e1002129.
38. Marrannes R, Willems R, De Prins E, Wauquier A. Evidence for a role of the N-methyl-D-aspartate (NMDA) receptor in cortical spreading depression in the rat. Brain Res. 1988;457(2):226-40.
39. Lauritzen M, Hansen AJ. The effect of glutamate receptor blockade on anoxic depolarization and cortical spreading depression. J Cereb Blood Flow Metab. 1992;12(2):223-9.
40. Kruger H, Heinemann U, Luhmann HJ. Effects of ionotropic glutamate receptor blockade and 5-HT1A receptor activation on spreading depression in rat neocortical slices. Neuroreport. 1999;10(12):2651-6.
41. Petzold GC, Windmuller O, Haack S, Major S, Buchheim K, Megow D, et al. Increased extracellular K+ concentration reduces the efficacy of N-methyl-D-aspartate receptor antagonists to block spreading depression-like depolarizations and spreading ischemia. Stroke. 2005;36(6):1270-7.

42. Zhou N, Gordon GR, Feighan D, MacVicar BA. Transient swelling, acidification, and mitochondrial depolarization occurs in neurons but not astrocytes during spreading depression. Cereb Cortex. 2010;20(11):2614-24.
43. Tozzi A, de Iure A, Di Filippo M, Costa C, Caproni S, Pisani A, et al. Critical role of calcitonin gene-related peptide receptors in cortical spreading depression. Proc Natl Acad Sci U S A. 2012;109(46):18985-90.
44. Footitt DR, Newberry NR. Cortical spreading depression induces an LTP-like effect in rat neocortex in vitro. Brain Res. 1998;781(1-2):339-42.
45. Zhou N, Rungta RL, Malik A, Han H, Wu DC, MacVicar BA. Regenerative glutamate release by presynaptic NMDA receptors contributes to spreading depression. J Cereb Blood Flow Metab. 2013;33(10):1582-94.
46. Peters O, Schipke CG, Hashimoto Y, Kettenmann H. Different mechanisms promote astrocyte Ca2+ waves and spreading depression in the mouse neocortex. J Neurosci. 2003;23(30):9888-96.
47. Chuquet J, Hollender L, Nimchinsky EA. High-resolution in vivo imaging of the neurovascular unit during spreading depression. J Neurosci. 2007;27(15):4036-44.
48. Capuani C, Melone M, Tottene A, Bragina L, Crivellaro G, Santello M, et al. Defective glutamate and K+ clearance by cortical astrocytes in familial hemiplegic migraine type 2. EMBO Molecular Medicine. 2016;8(8):967-86.
49. Ophoff RA, Terwindt GM, Vergouwe MN, Van Eijk R, Oefner PJ, Hoffman SM, et al. Familial hemiplegic migraine and episodic ataxia type-2 are caused by mutations in the Ca2+ channel gene CACNL1A4. Cell. 1996;87(3):543-52.
50. Jen J, Kim G, Baloh R. Clinical spectrum of episodic ataxia type 2. Neurology. 2004;62(1):17-22.
51. Catterall WA. Structure and function of neuronal Ca2+ channels and their role in neurotransmitter release. Cell Calcium. 1998;24(5-6):307-23.
52. Tottene A, Conti R, Fabbro A, Vecchia D, Shapovalova M, Santello M, et al. Enhanced excitatory transmission at cortical synapses as the basis for facilitated spreading depression in CaV2. 1 knockin migraine mice. Neuron. 2009;61(5):762-73.
53. Maagdenberg AM, Pizzorusso T, Kaja S, Terpolilli N, Shapovalova M, Hoebeek F, et al. High cortical spreading depression susceptibility and migraine-associated symptoms in Ca (v) 2.1 S218L mice. Annals of Neurology. 2010;67(1):85-98.
54. Eikermann-Haerter K, Dilekoz E, Kudo C, Savitz SI, Waeber C, Baum MJ, et al. Genetic and hormonal factors modulate spreading depression and transient hemiparesis in mouse models of familial hemiplegic migraine type 1. J Clin Invest. 2009;119(1):99-109.
55. Eikermann-Haerter K, Yuzawa I, Qin T, Wang Y, Baek K, Kim YR, et al. Enhanced subcortical spreading depression in familial hemiplegic migraine type 1 mutant mice. J Neurosci. 2011;31(15):5755-63.
56. Fusco MD, Marconi R, Silvestri L, Atorino L, Rampoldi L, Morgante L, et al. Haploinsufficiency of ATP1A2 encoding the Na+/K+ pump α2 subunit associated with familial hemiplegic migraine type 2. Nature genetics. 2003;33(2):192-6.
57. Kaplan JH. Biochemistry of Na,K-ATPase. Annu Rev Biochem. 2002;71:511-35.
58. Gritz SM, Radcliffe RA. Genetic effects of ATP1A2 in familial hemiplegic migraine type II and animal models. Human genomics. 2013;7(1):1-7.
59. Unekawa M, Ikeda K, Tomita Y, Kawakami K, Suzuki N. Enhanced susceptibility to cortical spreading depression in two types of Na(+),K(+)-ATPase alpha2 subunit-deficient mice as a model of familial hemiplegic migraine 2. Cephalalgia. 2018;38(9):1515-24.
60. Deprez L, Weckhuysen S, Peeters K, Deconinck T, Claeys KG, Claes LR, et al. Epilepsy as part of the phenotype associated with ATP1A2 mutations. Epilepsia. 2008;49(3):500-8.
61. Costa C, Prontera P, Sarchielli P, Tonelli A, Bassi MT, Cupini LM, et al. A novel ATP1A2 gene mutation in familial hemiplegic migraine and epilepsy. Cephalalgia. 2014;34(1):68-72.
62. Merwick A, Fernandez D, McNamara B, Harrington H. Acute encephalopathy in familial hemiplegic migraine with ATP1A2 mutation. BMJ Case Rep. 2013;2013.

63. Kros L, Lykke-Hartmann K, Khodakhah K. Increased susceptibility to cortical spreading depression and epileptiform activity in a mouse model for FHM2. Sci Rep. 2018;8(1):16959.
64. Dichgans M, Freilinger T, Eckstein G, Babini E, Lorenz-Depiereux B, Biskup S, et al. Mutation in the neuronal voltage-gated sodium channel SCN1A in familial hemiplegic migraine. The Lancet. 2005;366(9483):371-7.
65. Escayg A, MacDonald BT, Meisler MH, Baulac S, Huberfeld G, An-Gourfinkel I, et al. Mutations of SCN1A, encoding a neuronal sodium channel, in two families with GEFS+ 2. Nature genetics. 2000;24(4):343-5.
66. Claes L, Del-Favero J, Ceulemans B, Lagae L, Van Broeckhoven C, De Jonghe P. De novo mutations in the sodium-channel gene SCN1A cause severe myoclonic epilepsy of infancy. The American Journal of Human Genetics. 2001;68(6):1327-32.
67. Castro MJ, Stam AH, Lemos C, de Vries B, Vanmolkot KR, Barros J, et al. First mutation in the voltage-gated Nav1.1 subunit gene SCN1A with co-occurring familial hemiplegic migraine and epilepsy. Cephalalgia. 2009;29(3):308-13.
68. Cestèle S, Labate A, Rusconi R, Tarantino P, Mumoli L, Franceschetti S, et al. Divergent effects of the T 1174S SCN1A mutation associated with seizures and hemiplegic migraine. Epilepsia. 2013;54(5):927-35.
69. Vanmolkot KR, Babini E, de Vries B, Stam AH, Freilinger T, Terwindt GM, et al. The novel p. L1649Q mutation in the SCN1A epilepsy gene is associated with familial hemiplegic migraine: genetic and functional studies. Human mutation. 2007;28(5):522-.
70. Domitrz I, Kosiorek M, Zekanowski C, Kaminska A. Genetic studies of Polish migraine patients: screening for causative mutations in four migraine-associated genes. Hum Genomics. 2016;10:3.
71. Fan C, Wolking S, Lehmann-Horn F, Hedrich UB, Freilinger T, Lerche H, et al. Early-onset familial hemiplegic migraine due to a novel SCN1A mutation. Cephalalgia. 2016;36(13):1238-47.
72. Vahedi K, Depienne C, Le Fort D, Riant F, Chaine P, Trouillard O, et al. Elicited repetitive daily blindness: a new phenotype associated with hemiplegic migraine and SCN1A mutations. Neurology. 2009;72(13):1178-83.
73. Weller CM, Pelzer N, de Vries B, Lopez MA, De Fabregues O, Pascual J, et al. Two novel SCN1A mutations identified in families with familial hemiplegic migraine. Cephalalgia. 2014;34(13):1062-9.
74. Chastan N, Lebas A, Legoff F, Parain D, Guyant-Marechal L. Clinical and electroencephalographic abnormalities during the full duration of a sporadic hemiplegic migraine attack. Neurophysiol Clin. 2016;46(4-5):307-11.
75. Ogiwara I, Miyamoto H, Morita N, Atapour N, Mazaki E, Inoue I, et al. Nav1.1 localizes to axons of parvalbumin-positive inhibitory interneurons: a circuit basis for epileptic seizures in mice carrying an Scn1a gene mutation. J Neurosci. 2007;27(22):5903-14.
76. Hedrich UB, Liautard C, Kirschenbaum D, Pofahl M, Lavigne J, Liu Y, et al. Impaired action potential initiation in GABAergic interneurons causes hyperexcitable networks in an epileptic mouse model carrying a human NaV1. 1 mutation. Journal of Neuroscience. 2014;34(45):14874-89.
77. Kahlig KM, Rhodes TH, Pusch M, Freilinger T, Pereira-Monteiro JM, Ferrari MD, et al. Divergent sodium channel defects in familial hemiplegic migraine. Proc Natl Acad Sci U S A. 2008;105(28):9799-804.
78. Cestele S, Scalmani P, Rusconi R, Terragni B, Franceschetti S, Mantegazza M. Self-limited hyperexcitability: functional effect of a familial hemiplegic migraine mutation of the Nav1.1 (SCN1A) Na+ channel. J Neurosci. 2008;28(29):7273-83.
79. Cestele S, Schiavon E, Rusconi R, Franceschetti S, Mantegazza M. Nonfunctional NaV1.1 familial hemiplegic migraine mutant transformed into gain of function by partial rescue of folding defects. Proc Natl Acad Sci U S A. 2013;110(43):17546-51.

80. Dhifallah S, Lancaster E, Merrill S, Leroudier N, Mantegazza M, Cestele S. Gain of Function for the SCN1A/hNa(v)1.1-L1670W Mutation Responsible for Familial Hemiplegic Migraine. Front Mol Neurosci. 2018;11:232.
81. Cestele S, Labate A, Rusconi R, Tarantino P, Mumoli L, Franceschetti S, et al. Divergent effects of the T1174S SCN1A mutation associated with seizures and hemiplegic migraine. Epilepsia. 2013;54(5):927-35.
82. Riant F, Roos C, Roubertie A, Barbance C, Hadjadj J, Auvin S, et al. Hemiplegic Migraine Associated With PRRT2 Variations: A Clinical and Genetic Study. Neurology. 2022;98(1):e51-e61.
83. Ebrahimi-Fakhari D, Saffari A, Westenberger A, Klein C. The evolving spectrum of PRRT2-associated paroxysmal diseases. Brain. 2015;138(12):3476-95.
84. Mohammad SS, Coman D, Calvert S. Glucose transporter 1 deficiency syndrome and hemiplegic migraines as a dominant presenting clinical feature. J Paediatr Child Health. 2014;50(12):1025-6.
85. Weller CM, Leen WG, Neville BG, Duncan JS, de Vries B, Geilenkirchen MA, et al. A novel SLC2A1 mutation linking hemiplegic migraine with alternating hemiplegia of childhood. Cephalalgia. 2015;35(1):10-5.
86. Gardiner AR, Jaffer F, Dale RC, Labrum R, Erro R, Meyer E, et al. The clinical and genetic heterogeneity of paroxysmal dyskinesias. Brain. 2015;138(Pt 12):3567-80.
87. Suzuki M, Van Paesschen W, Stalmans I, Horita S, Yamada H, Bergmans BA, et al. Defective membrane expression of the Na+-HCO3− cotransporter NBCe1 is associated with familial migraine. Proceedings of the National Academy of Sciences. 2010;107(36):15963-8.
88. Palumbo P, Palumbo O, Operto FF, Castellana S, Di Muro E, Leone MP, et al. Familial Hemiplegic Migraine: A new gene in an Italian family. Archives of Clinical and Medical Case Reports. 2019;3(6):534-43.
89. Coppola G, Pastorino GMG, Vetri L, D’Onofrio F, Operto FF. Familial hemiplegic migraine with an ATP1A4 mutation: clinical spectrum and carbamazepine efficacy. Brain Sciences. 2020;10(6):372.
90. Choi KD, Kim JS, Kim HJ, Jung I, Jeong SH, Lee SH, et al. Genetic Variants Associated with Episodic Ataxia in Korea. Sci Rep. 2017;7(1):13855.
91. Choi KD, Jen JC, Choi SY, Shin JH, Kim HS, Kim HJ, et al. Late-onset episodic ataxia associated with SLC1A3 mutation. J Hum Genet. 2017;62(3):443-6.
92. Pyle A, Smertenko T, Bargiela D, Griffin H, Duff J, Appleton M, et al. Exome sequencing in undiagnosed inherited and sporadic ataxias. Brain. 2015;138(Pt 2):276-83.
93. Chen I, Pant S, Wu Q, Cater RJ, Sobti M, Vandenberg RJ, et al. Glutamate transporters have a chloride channel with two hydrophobic gates. Nature. 2021;591(7849):327-31.
94. Reyes N, Ginter C, Boudker O. Transport mechanism of a bacterial homologue of glutamate transporters. Nature. 2009;462(7275):880-5.
95. Machtens JP, Kortzak D, Lansche C, Leinenweber A, Kilian P, Begemann B, et al. Mechanisms of anion conduction by coupled glutamate transporters. Cell. 2015;160(3):542-53.
96. Jen J, Wan J, Palos T, Howard B, Baloh R. Mutation in the glutamate transporter EAAT1 causes episodic ataxia, hemiplegia, and seizures. Neurology. 2005;65(4):529-34.
97. De Vries B, Mamsa H, Stam AH, Wan J, Bakker SL, Vanmolkot KR, et al. Episodic ataxia associated with EAAT1 mutation C186S affecting glutamate reuptake. Archives of neurology. 2009;66(1):97-101.
98. Kovermann P, Hessel M, Kortzak D, Jen JC, Koch J, Fahlke C, et al. Impaired K+ binding to glial glutamate transporter EAAT1 in migraine. Scientific reports. 2017;7(1):1-10.
99. Iwama K, Iwata A, Shiina M, Mitsuhashi S, Miyatake S, Takata A, et al. A novel mutation in SLC1A3 causes episodic ataxia. Journal of human genetics. 2018;63(2):207-11.
100. Winter N, Kovermann P, Fahlke C. A point mutation associated with episodic ataxia 6 increases glutamate transporter anion currents. Brain. 2012;135(11):3416-25.
101. Chivukula AS, Suslova M, Kortzak D, Kovermann P, Fahlke C. Functional consequences of SLC1A3 mutations associated with episodic ataxia 6. Hum Mutat. 2020;41(11):1892-905.

102. Hiekkala ME, Vuola P, Artto V, Häppölä P, Häppölä E, Vepsäläinen S, et al. The contribution of CACNA1A, ATP1A2 and SCN1A mutations in hemiplegic migraine: a clinical and genetic study in Finnish migraine families. Cephalalgia. 2018;38(12):1849-63.
103. Pelzer N, Haan J, Stam AH, Vijfhuizen LS, Koelewijn SC, Smagge A, et al. Clinical spectrum of hemiplegic migraine and chances of finding a pathogenic mutation. Neurology. 2018;90(7):e575-e82.
104. Mantegazza M, Cestele S. Pathophysiological mechanisms of migraine and epilepsy: Similarities and differences. Neurosci Lett. 2018;667:92-102.
105. Keezer MR, Bauer PR, Ferrari MD, Sander JW. The comorbid relationship between migraine and epilepsy: a systematic review and meta-analysis. Eur J Neurol. 2015;22(7):1038-47.
106. Liveing E. Observations on Megrim or Sick-Headache. Br Med J. 1872;1(588):364-6.
107. Ryan DP, Ptacek LJ. Episodic neurological channelopathies. Neuron. 2010;68(2):282-92.
108. Ptacek LJ. Episodic disorders: channelopathies and beyond. Annu Rev Physiol. 2015;77:475-9.
109. Brunklaus A, Brunger T, Feng T, Fons C, Lehikoinen A, Panagiotakaki E, et al. The gain of function SCN1A disorder spectrum: novel epilepsy phenotypes and therapeutic implications. Brain. 2022;145(11):3816-31.
110. Mantegazza M, Curia G, Biagini G, Ragsdale DS, Avoli M. Voltage-gated sodium channels as therapeutic targets in epilepsy and other neurological disorders. Lancet Neurol. 2010;9(4):413-24.
111. Diener H-C, Förderreuther S, Kropp P. Therapie der Migräneattacke und Prophylaxe der Migräne, S1-Leitlinie. DGN und DMKG, in: Deutsche Gesellschaft für Neurologie (Hrsg), Leitlinien für Diagnostik und Therapie in der Neurologie. 2022.
112. Vecchia D, Pietrobon D. Migraine: a disorder of brain excitatory-inhibitory balance? Trends Neurosci. 2012;35(8):507-20.
113. Fisher RS, Cross JH, D'Souza C, French JA, Haut SR, Higurashi N, et al. Instruction manual for the ILAE 2017 operational classification of seizure types. Epilepsia. 2017;58(4):531-42.
114. Berg AT, Millichap JJ. The 2010 revised classification of seizures and epilepsy. Continuum (Minneap Minn). 2013;19(3 Epilepsy):571-97.
115. Fiest KM, Sauro KM, Wiebe S, Patten SB, Kwon CS, Dykeman J, et al. Prevalence and incidence of epilepsy: A systematic review and meta-analysis of international studies. Neurology. 2017;88(3):296-303.
116. Aaberg KM, Suren P, Soraas CL, Bakken IJ, Lossius MI, Stoltenberg C, et al. Seizures, syndromes, and etiologies in childhood epilepsy: The International League Against Epilepsy 1981, 1989, and 2017 classifications used in a population-based cohort. Epilepsia. 2017;58(11):1880-91.
117. Scheffer IE, Berkovic S, Capovilla G, Connolly MB, French J, Guilhoto L, et al. ILAE classification of the epilepsies: Position paper of the ILAE Commission for Classification and Terminology. Epilepsia. 2017;58(4):512-21.
118. Steinlein OK, Mulley JC, Propping P, Wallace RH, Phillips HA, Sutherland GR, et al. A missense mutation in the neuronal nicotinic acetylcholine receptor alpha 4 subunit is associated with autosomal dominant nocturnal frontal lobe epilepsy. Nat Genet. 1995;11(2):201-3.
119. Imbrici P, Jaffe SL, Eunson LH, Davies NP, Herd C, Robertson R, et al. Dysfunction of the brain calcium channel CaV2.1 in absence epilepsy and episodic ataxia. Brain. 2004;127(Pt 12):2682-92.
120. Auvin S, Holder-Espinasse M, Lamblin MD, Andrieux J. Array-CGH detection of a de novo 0.7-Mb deletion in 19p13.13 including CACNA1A associated with mental retardation and epilepsy with infantile spasms. Epilepsia. 2009;50(11):2501-3.

121. Damaj L, Lupien-Meilleur A, Lortie A, Riou E, Ospina LH, Gagnon L, et al. CACNA1A haploinsufficiency causes cognitive impairment, autism and epileptic encephalopathy with mild cerebellar symptoms. Eur J Hum Genet. 2015;23(11):1505-12.
122. Epi KC. De Novo Mutations in SLC1A2 and CACNA1A Are Important Causes of Epileptic Encephalopathies. Am J Hum Genet. 2016;99(2):287-98.
123. Fletcher CF, Lutz CM, O'Sullivan TN, Shaughnessy JD, Jr., Hawkes R, Frankel WN, et al. Absence epilepsy in tottering mutant mice is associated with calcium channel defects. Cell. 1996;87(4):607-17.
124. Vetro A, Nielsen HN, Holm R, Hevner RF, Parrini E, Powis Z, et al. ATP1A2- and ATP1A3-associated early profound epileptic encephalopathy and polymicrogyria. Brain. 2021;144(5):1435-50.
125. Zhang YH, Burgess R, Malone JP, Glubb GC, Helbig KL, Vadlamudi L, et al. Genetic epilepsy with febrile seizures plus: Refining the spectrum. Neurology. 2017;89(12):1210-9.
126. Dravet C, Bureau M, Genton P. Benign myoclonic epilepsy of infancy: electroclinical symptomatology and differential diagnosis from the other types of generalized epilepsy of infancy. Epilepsy Res Suppl. 1992;6:131-5.
127. Brunklaus A, Ellis R, Reavey E, Forbes GH, Zuberi SM. Prognostic, clinical and demographic features in SCN1A mutation-positive Dravet syndrome. Brain. 2012;135(Pt 8):2329-36.
128. Berecki G, Bryson A, Terhag J, Maljevic S, Gazina EV, Hill SL, et al. SCN1A gain of function in early infantile encephalopathy. Ann Neurol. 2019;85(4):514-25.
129. Heron SE, Grinton BE, Kivity S, Afawi Z, Zuberi SM, Hughes JN, et al. PRRT2 mutations cause benign familial infantile epilepsy and infantile convulsions with choreoathetosis syndrome. Am J Hum Genet. 2012;90(1):152-60.
130. Koch H, Weber YG. The glucose transporter type 1 (Glut1) syndromes. Epilepsy Behav. 2019;91:90-3.
131. Gil-Perotin S, Jaijo T, Verdu AG, Rubio P, Mazon M, Gasque-Rubio R, et al. Epilepsy, status epilepticus, and hemiplegic migraine coexisting with a novel SLC4A4 mutation. Neurol Sci. 2021;42(9):3647-54.
132. Paucar M, Granberg T, Lagerstedt-Robinson K, Waldenlind E, Petersson S, Nordin L, et al. SLC1A3 variant associated with hemiplegic migraine and acetazolamide-responsive MRS changes. Neurol Genet. 2020;6(4):e474.
133. Kovermann P, Kolobkova Y, Franzen A, Fahlke C. Mutations associated with epileptic encephalopathy modify EAAT2 anion channel function. Epilepsia. 2022;63(2):388-401.
134. Ayata C, Lauritzen M. Spreading depression, spreading depolarizations, and the cerebral vasculature. Physiological reviews. 2015;95(3):953-93.
135. Cain SM, Bohnet B, LeDue J, Yung AC, Garcia E, Tyson JR, et al. In vivo imaging reveals that pregabalin inhibits cortical spreading depression and propagation to subcortical brain structures. Proc Natl Acad Sci U S A. 2017;114(9):2401-6.
136. Tang C, Unekawa M, Shibata M, Tomita Y, Izawa Y, Sugimoto H, et al. Characteristics of cortical spreading depression and c-Fos expression in transgenic mice having a mutation associated with familial hemiplegic migraine 2. Cephalalgia. 2020;40(11):1177-90.
137. Pottkamper JCM, Hofmeijer J, van Waarde JA, van Putten M. The postictal state - What do we know? Epilepsia. 2020;61(6):1045-61.
138. de Curtis M, Avoli M. GABAergic networks jump-start focal seizures. Epilepsia. 2016;57(5):679-87.
139. Tamim I, Chung DY, de Morais AL, Loonen ICM, Qin T, Misra A, et al. Spreading depression as an innate antiseizure mechanism. Nat Commun. 2021;12(1):2206.
140. Ahern CA, Payandeh J, Bosmans F, Chanda B. The hitchhiker's guide to the voltage-gated sodium channel galaxy. J Gen Physiol. 2016;147(1):1-24.
141. Jansen NA, Dehghani A, Linssen MML, Breukel C, Tolner EA, van den Maagdenberg A. First FHM3 mouse model shows spontaneous cortical spreading depolarizations. Ann Clin Transl Neurol. 2020;7(1):132-8.

142. Barbieri R, Bertelli S, Pusch M, Gavazzo P. Late sodium current blocker GS967 inhibits persistent currents induced by familial hemiplegic migraine type 3 mutations of the SCN1A gene. The journal of headache and pain. 2019;20(1):1-13.
143. Sutherland HG, Albury CL, Griffiths LR. Advances in genetics of migraine. J Headache Pain. 2019;20(1):72.
144. Grangeon L, Lange KS, Waliszewska-Prosol M, Onan D, Marschollek K, Wiels W, et al. Genetics of migraine: where are we now? J Headache Pain. 2023;24(1):12.
145. Rothstein JD, Dykes-Hoberg M, Pardo CA, Bristol LA, Jin L, Kuncl RW, et al. Knockout of glutamate transporters reveals a major role for astroglial transport in excitotoxicity and clearance of glutamate. Neuron. 1996;16(3):675-86.
146. Storck T, Schulte S, Hofmann K, Stoffel W. Structure, expression, and functional analysis of a Na(+)-dependent glutamate/aspartate transporter from rat brain. Proc Natl Acad Sci U S A. 1992;89(22):10955-9.
147. Schmitt A, Asan E, Puschel B, Kugler P. Cellular and regional distribution of the glutamate transporter GLAST in the CNS of rats: nonradioactive in situ hybridization and comparative immunocytochemistry. J Neurosci. 1997;17(1):1-10.
148. Rothstein JD, Martin L, Levey AI, Dykes-Hoberg M, Jin L, Wu D, et al. Localization of neuronal and glial glutamate transporters. Neuron. 1994;13(3):713-25.
149. Suarez-Pozos E, Thomason EJ, Fuss B. Glutamate Transporters: Expression and Function in Oligodendrocytes. Neurochem Res. 2020;45(3):551-60.
150. Kugler P, Beyer A. Expression of glutamate transporters in human and rat retina and rat optic nerve. Histochem Cell Biol. 2003;120(3):199-212.
151. Fahlke C, Kortzak D, Machtens JP. Molecular physiology of EAAT anion channels. Pflugers Arch. 2016;468(3):491-502.
152. Huang Z, Tajkhorshid E. Dynamics of the extracellular gate and ion-substrate coupling in the glutamate transporter. Biophys J. 2008;95(5):2292-300.
153. Watase K, Hashimoto K, Kano M, Yamada K, Watanabe M, Inoue Y, et al. Motor discoordination and increased susceptibility to cerebellar injury in GLAST mutant mice. Eur J Neurosci. 1998;10(3):976-88.
154. Wadiche JI, Kavanaugh MP. Macroscopic and microscopic properties of a cloned glutamate transporter/chloride channel. J Neurosci. 1998;18(19):7650-61.
155. Mim C, Balani P, Rauen T, Grewer C. The glutamate transporter subtypes EAAT4 and EAATs 1-3 transport glutamate with dramatically different kinetics and voltage dependence but share a common uptake mechanism. J Gen Physiol. 2005;126(6):571-89.
156. Kovermann P, Untiet V, Kolobkova Y, Engels M, Baader S, Schilling K, et al. Increased glutamate transporter-associated anion currents cause glial apoptosis in episodic ataxia 6. Brain communications. 2020;2(1):fcaa022.
157. Edvinsson L, Jansen I, Cunha e Sa M, Gulbenkian S. Demonstration of neuropeptide containing nerves and vasomotor responses to perivascular peptides in human cerebral arteries. Cephalalgia. 1994;14(2):88-96.
158. Goadsby PJ, Edvinsson L. The trigeminovascular system and migraine: studies characterizing cerebrovascular and neuropeptide changes seen in humans and cats. Annals of Neurology: Official Journal of the American Neurological Association and the Child Neurology Society. 1993;33(1):48-56.
159. Hansen JM, Thomsen LL, Olesen J, Ashina M. Calcitonin gene-related peptide does not cause migraine attacks in patients with familial hemiplegic migraine. Headache: The Journal of Head and Face Pain. 2011;51(4):544-53.
160. Octeau JC, Faas G, Mody I, Khakh BS. Making, testing, and using potassium ion selective microelectrodes in tissue slices of adult brain. JoVE (Journal of Visualized Experiments). 2018(135):e57511.
161. Tang YT, Mendez JM, Theriot JJ, Sawant PM, López-Valdés HE, Ju YS, et al. Minimum conditions for the induction of cortical spreading depression in brain slices. Journal of neurophysiology. 2014;112(10):2572-9.

162. Zerimech S, Chever O, Scalmani P, Pizzamiglio L, Duprat F, Mantegazza M. Cholinergic modulation inhibits cortical spreading depression in mouse neocortex through activation of muscarinic receptors and decreased excitatory/inhibitory drive. Neuropharmacology. 2020;166:107951.
163. Hamill OP, Marty A, Neher E, Sakmann B, Sigworth FJ. Improved patch-clamp techniques for high-resolution current recording from cells and cell-free membrane patches. Pflügers Archiv. 1981;391:85-100.
164. Lowenstein DH, Bleck T, Macdonald RL. It's time to revise the definition of status epilepticus. 1999.
165. Allen Reference Atlas – Mouse Brain [brain atlas]. Available from atlas.brain-map.org.
166. Osteen JD, Sampson K, Iyer V, Julius D, Bosmans F. Pharmacology of the Nav1. 1 domain IV voltage sensor reveals coupling between inactivation gating processes. Proceedings of the National Academy of Sciences. 2017;114(26):6836-41.
167. Prontera P, Sarchielli P, Caproni S, Bedetti C, Cupini L, Calabresi P, et al. Epilepsy in hemiplegic migraine: genetic mutations and clinical implications. Cephalalgia. 2018;38(2):361-73.
168. Bordey A, Sontheimer H. Ion channel expression by astrocytes in situ: comparison of different CNS regions. Glia. 2000;30(1):27-38.
169. O'Connor ER, Sontheimer H, Spencer DD, de Lanerolle NC. Astrocytes from Human Hippocampal Epileptogenic Foci Exhibit Action Potential–Like Responses. Epilepsia. 1998;39(4):347-54.
170. Kilb W, Kirischuk S, Luhmann HJ. Role of tonic GABAergic currents during pre-and early postnatal rodent development. Frontiers in neural circuits. 2013;7:139.
171. Farrant M, Nusser Z. Variations on an inhibitory theme: phasic and tonic activation of GABAA receptors. Nature Reviews Neuroscience. 2005;6(3):215-29.
172. Morgan JI, Cohen DR, Hempstead JL, Curran T. Mapping patterns of c-fos expression in the central nervous system after seizure. Science. 1987;237(4811):192-7.
173. Desroches M, Faugeras O, Krupa M, Mantegazza M. Modeling cortical spreading depression induced by the hyperactivity of interneurons. J Comput Neurosci. 2019;47(2-3):125-40.
174. Osteen JD, Herzig V, Gilchrist J, Emrick JJ, Zhang C, Wang X, et al. Selective spider toxins reveal a role for the Nav1.1 channel in mechanical pain. Nature. 2016;534(7608):494-9.
175. Richards KL, Milligan CJ, Richardson RJ, Jancovski N, Grunnet M, Jacobson LH, et al. Selective Na(V)1.1 activation rescues Dravet syndrome mice from seizures and premature death. Proc Natl Acad Sci U S A. 2018;115(34):E8077-E85.
176. Tottene A, Urbani A, Pietrobon D. Role of different voltage-gated Ca2+ channels in cortical spreading depression: specific requirement of P/Q-type Ca2+ channels. Channels (Austin). 2011;5(2):110-4.
177. Mesgari M, Ghaffarian N, Khaleghi Ghadiri M, Sadeghian H, Speckmann EJ, Stummer W, et al. Altered inhibition in the hippocampal neural networks after spreading depression. Neuroscience. 2015;304:190-7.
178. Knowles JK, Xu H, Soane C, Batra A, Saucedo T, Frost E, et al. Maladaptive myelination promotes generalized epilepsy progression. Nat Neurosci. 2022;25(5):596-606.
179. Richards K, Jancovski N, Hanssen E, Connelly A, Petrou S. Atypical myelinogenesis and reduced axon caliber in the Scn1a variant model of Dravet syndrome: An electron microscopy pilot study of the developing and mature mouse corpus callosum. Brain Res. 2021;1751:147157.
180. Baker EM, Thompson CH, Hawkins NA, Wagnon JL, Wengert ER, Patel MK, et al. The novel sodium channel modulator GS-458967 (GS967) is an effective treatment in a mouse model of SCN8A encephalopathy. Epilepsia. 2018;59(6):1166-76.
181. Anderson LL, Thompson CH, Hawkins NA, Nath RD, Petersohn AA, Rajamani S, et al. Antiepileptic activity of preferential inhibitors of persistent sodium current. Epilepsia. 2014;55(8):1274-83.

182. Anderson LL, Hawkins NA, Thompson CH, Kearney JA, George AL, Jr. Unexpected Efficacy of a Novel Sodium Channel Modulator in Dravet Syndrome. Sci Rep. 2017;7(1):1682.
183. Kahlig KM, Scott L, Hatch RJ, Griffin A, Martinez Botella G, Hughes ZA, et al. The novel persistent sodium current inhibitor PRAX-562 has potent anticonvulsant activity with improved protective index relative to standard of care sodium channel blockers. Epilepsia. 2022;63(3):697-708.
184. Shimamoto K, Lebrun B, Yasuda-Kamatani Y, Sakaitani M, Shigeri Y, Yumoto N, et al. DL-threo-beta-benzyloxyaspartate, a potent blocker of excitatory amino acid transporters. Mol Pharmacol. 1998;53(2):195-201.
185. Aizawa H, Sun W, Sugiyama K, Itou Y, Aida T, Cui W, et al. Glial glutamate transporter GLT-1 determines susceptibility to spreading depression in the mouse cerebral cortex. Glia. 2020;68(12):2631-42.
186. Pietrobon D, Moskowitz MA. Pathophysiology of migraine. Annual review of physiology. 2013;75:365-91.
187. Shih PY, Savtchenko LP, Kamasawa N, Dembitskaya Y, McHugh TJ, Rusakov DA, et al. Retrograde synaptic signaling mediated by K+ efflux through postsynaptic NMDA receptors. Cell Rep. 2013;5(4):941-51.
188. Sibille J, Pannasch U, Rouach N. Astroglial potassium clearance contributes to short-term plasticity of synaptically evoked currents at the tripartite synapse. J Physiol. 2014;592(1):87-102.
189. Lemaire L, Desroches M, Krupa M, Pizzamiglio L, Scalmani P, Mantegazza M. Modeling NaV1.1/SCN1A sodium channel mutations in a microcircuit with realistic ion concentration dynamics suggests differential GABAergic mechanisms leading to hyperexcitability in epilepsy and hemiplegic migraine. PLoS Comput Biol. 2021;17(7):e1009239.
190. Hires SA, Zhu Y, Tsien RY. Optical measurement of synaptic glutamate spillover and reuptake by linker optimized glutamate-sensitive fluorescent reporters. Proc Natl Acad Sci U S A. 2008;105(11):4411-6.
191. Helassa N, Durst CD, Coates C, Kerruth S, Arif U, Schulze C, et al. Ultrafast glutamate sensors resolve high-frequency release at Schaffer collateral synapses. Proc Natl Acad Sci U S A. 2018;115(21):5594-9.
192. Jensen AA, Erichsen MN, Nielsen CW, Stensbol TB, Kehler J, Bunch L. Discovery of the first selective inhibitor of excitatory amino acid transporter subtype 1. J Med Chem. 2009;52(4):912-5.
193. Erichsen MN, Huynh TH, Abrahamsen B, Bastlund JF, Bundgaard C, Monrad O, et al. Structure-activity relationship study of first selective inhibitor of excitatory amino acid transporter subtype 1: 2-Amino-4-(4-methoxyphenyl)-7-(naphthalen-1-yl)-5-oxo-5,6,7,8-tetrahydro-4H-chromene-3-carbonitrile (UCPH-101). J Med Chem. 2010;53(19):7180-91.
194. Abrahamsen B, Schneider N, Erichsen MN, Huynh TH, Fahlke C, Bunch L, et al. Allosteric modulation of an excitatory amino acid transporter: the subtype-selective inhibitor UCPH-101 exerts sustained inhibition of EAAT1 through an intramonomeric site in the trimerization domain. J Neurosci. 2013;33(3):1068-87.
195. Fitzsimons RB, Wolfenden WH. Migraine coma. Meningitic migraine with cerebral oedema associated with a new form of autosomal dominant cerebellar ataxia. Brain. 1985;108 (Pt 3):555-77.
196. Curtain RP, Smith RL, Ovcaric M, Griffiths LR. Minor head trauma-induced sporadic hemiplegic migraine coma. Pediatr Neurol. 2006;34(4):329-32.
197. Kofuji P, Newman EA. Potassium buffering in the central nervous system. Neuroscience. 2004;129(4):1045-56.
198. Theis M, Jauch R, Zhuo L, Speidel D, Wallraff A, Doring B, et al. Accelerated hippocampal spreading depression and enhanced locomotory activity in mice with astrocyte-directed inactivation of connexin43. J Neurosci. 2003;23(3):766-76.
199. Martins-Ferreira H, Nedergaard M, Nicholson C. Perspectives on spreading depression. Brain Res Brain Res Rev. 2000;32(1):215-34.

200. Lehre KP, Levy LM, Ottersen OP, Storm-Mathisen J, Danbolt NC. Differential expression of two glial glutamate transporters in the rat brain: quantitative and immunocytochemical observations. J Neurosci. 1995;15(3 Pt 1):1835-53.
201. Corbetta C, Di Ianni N, Bruzzone MG, Patane M, Pollo B, Cantini G, et al. Altered function of the glutamate-aspartate transporter GLAST, a potential therapeutic target in glioblastoma. Int J Cancer. 2019;144(10):2539-54.
202. Rothstein JD. Excitotoxicity hypothesis. Neurology. 1996;47(4 Suppl 2):S19-25; discussion S6.
203. Vecchia D, Tottene A, van den Maagdenberg AM, Pietrobon D. Mechanism underlying unaltered cortical inhibitory synaptic transmission in contrast with enhanced excitatory transmission in CaV2.1 knockin migraine mice. Neurobiol Dis. 2014;69(100):225-34.
204. Minelli A, DeBiasi S, Brecha NC, Zuccarello LV, Conti F. GAT-3, a high-affinity GABA plasma membrane transporter, is localized to astrocytic processes, and it is not confined to the vicinity of GABAergic synapses in the cerebral cortex. J Neurosci. 1996;16(19):6255-64.
205. Bottger P, Glerup S, Gesslein B, Illarionova NB, Isaksen TJ, Heuck A, et al. Glutamate-system defects behind psychiatric manifestations in a familial hemiplegic migraine type 2 disease-mutation mouse model. Sci Rep. 2016;6:22047.
206. Yuan Y, O'Malley HA, Smaldino MA, Bouza AA, Hull JM, Isom LL. Delayed maturation of GABAergic signaling in the Scn1a and Scn1b mouse models of Dravet Syndrome. Sci Rep. 2019;9(1):6210.
207. Reiber M, Miljanovic N, Schonhoff K, Palme R, Potschka H. Behavioral phenotyping of young Scn1a haploinsufficient mice. Epilepsy Behav. 2022;136:108903.
208. Wlodarczyk AI, Sylantyev S, Herd MB, Kersante F, Lambert JJ, Rusakov DA, et al. GABA-independent GABAA receptor openings maintain tonic currents. J Neurosci. 2013;33(9):3905-14.
209. Maguire JL, Stell BM, Rafizadeh M, Mody I. Ovarian cycle-linked changes in GABA(A) receptors mediating tonic inhibition alter seizure susceptibility and anxiety. Nat Neurosci. 2005;8(6):797-804.
210. Thomsen LL, Eriksen MK, Roemer SF, Andersen I, Olesen J, Russell MB. A population-based study of familial hemiplegic migraine suggests revised diagnostic criteria. Brain. 2002;125(Pt 6):1379-91.
211. Eriksen MK, Thomsen LL, Olesen J. Implications of clinical subtypes of migraine with aura. Headache. 2006;46(2):286-97.
212. Gallanti A, Tonelli A, Cardin V, Bussone G, Bresolin N, Bassi MT. A novel de novo nonsense mutation in ATP1A2 associated with sporadic hemiplegic migraine and epileptic seizures. J Neurol Sci. 2008;273(1-2):123-6.
213. Russell MB, Ducros A. Sporadic and familial hemiplegic migraine: pathophysiological mechanisms, clinical characteristics, diagnosis, and management. Lancet Neurol. 2011;10(5):457-70.
214. Choi KD, Choi JH. Episodic Ataxias: Clinical and Genetic Features. J Mov Disord. 2016;9(3):129-35.
215. Mulligan MK, Abreo T, Neuner SM, Parks C, Watkins CE, Houseal MT, et al. Identification of a Functional Non-coding Variant in the GABA (A) Receptor alpha2 Subunit of the C57BL/6J Mouse Reference Genome: Major Implications for Neuroscience Research. Front Genet. 2019;10:188.
216. Semyanov A, Walker MC, Kullmann DM. GABA uptake regulates cortical excitability via cell type-specific tonic inhibition. Nat Neurosci. 2003;6(5):484-90.
217. Engels M, Kalia M, Rahmati S, Petersilie L, Kovermann P, van Putten M, et al. Glial Chloride Homeostasis Under Transient Ischemic Stress. Front Cell Neurosci. 2021;15:735300.
218. Kovermann P, Engels M, Muller F, Fahlke C. Cellular Physiology and Pathophysiology of EAAT Anion Channels. Front Cell Neurosci. 2021;15:815279.
219. Heja L, Nyitrai G, Kekesi O, Dobolyi A, Szabo P, Fiath R, et al. Astrocytes convert network excitation to tonic inhibition of neurons. BMC Biol. 2012;10:26.

220. Pirttimaki T, Parri HR, Crunelli V. Astrocytic GABA transporter GAT-1 dysfunction in experimental absence seizures. J Physiol. 2013;591(4):823-33.
221. Cho FS, Vainchtein ID, Voskobiynyk Y, Morningstar AR, Aparicio F, Higashikubo B, et al. Enhancing GAT-3 in thalamic astrocytes promotes resilience to brain injury in rodents. Sci Transl Med. 2022;14(652):eabj4310.
222. Diaz Verdugo C, Myren-Svelstad S, Aydin E, Van Hoeymissen E, Deneubourg C, Vanderhaeghe S, et al. Glia-neuron interactions underlie state transitions to generalized seizures. Nat Commun. 2019;10(1):3830.
223. Hotz AL, Jamali A, Rieser NN, Niklaus S, Aydin E, Myren-Svelstad S, et al. Loss of glutamate transporter eaat2a leads to aberrant neuronal excitability, recurrent epileptic seizures, and basal hypoactivity. Glia. 2022;70(1):196-214.
224. Terpollili NA, Dolp R, Waehner K, Schwarzmaier SM, Rumbler E, Todorov B, et al. Ca(V)2.1 channel mutations causing familial hemiplegic migraine type 1 increase the susceptibility for cortical spreading depolarizations and seizures and worsen outcome after experimental traumatic brain injury. Elife. 2022;11.
225. Wengert ER, Wenker IC, Wagner EL, Wagley PK, Gaykema RP, Shin JB, et al. Adrenergic Mechanisms of Audiogenic Seizure-Induced Death in a Mouse Model of SCN8A Encephalopathy. Front Neurosci. 2021;15:581048.
226. Raimondo JV, Burman RJ, Katz AA, Akerman CJ. Ion dynamics during seizures. Frontiers in cellular neuroscience. 2015;9:419.
227. Bogdanov VB, Middleton NA, Theriot JJ, Parker PD, Abdullah OM, Ju YS, et al. Susceptibility of Primary Sensory Cortex to Spreading Depolarizations. J Neurosci. 2016;36(17):4733-43.
228. Aiba I, Noebels JL. Kcnq2/Kv7.2 controls the threshold and bi-hemispheric symmetry of cortical spreading depolarization. Brain. 2021;144(9):2863-78.

Appendix

A. Score sheet to assess the fulfillment of the human endpoint criteria

„Score Sheet“

Beobachtung	**Punktewertung**
I Körpergewicht	
Unbeeinflusst oder leichter (wachstumsbedingter) Anstieg	**0**
Reduktion um ≤ 5%	**1**
Reduktion um 5-8%	**5**
Reduktion um 8-10%	**9**
Reduktion um > 10%	**10**
Reduktion um > 20%	**20**
II Allgemeinzustand	
Fell glatt, glänzend, anliegend; Körperöffnungen sauber	**0**
Geringgradige Fellverschmutzung	**1**
Fell mittelgradig verschmutzt	**3**
Augen trüb, Fell verschmutzt	**5**
verklebte oder feuchte Körperöffnungen; unnormale Haltung; hoher Muskeltonus; Dehydratation:	**(6-10)**
ein Merkmal tritt auf	**6**
geringgradig (bis zu zwei Merkmale treten auf)	**7**
mittelgradig (bis drei Merkmale treten auf)	**8**
alle vier Merkmale treten auf	**10**
Krämpfe; Lähmungen; Atemgeräusche; Tier fühlt sich kalt an	**20**
III Spontanverhalten	
normales Verhalten (Schlafen, Reaktion auf Anblasen und Berührung, Neugier)	**0**
ungewöhnliches Verhalten, eingeschränkte Motorik oder Hyperkinetik (je nach Ausprägung):	**(1-5)**
geringe Verhaltensänderungen	**1**
Bewegungen gering verlangsamt/leichte Hyperkinetik	**3**
Bewegungen sind verlangsamt/Hyperkinetik	**5**
Isolation; ausgeprägte Hyperkinetik (je nach Ausprägung):	**(6-10)**
Tier vermeidet Bewegungen/Ruhelosigkeit (geringgradig)	**6**
Tier vermeidet Bewegungen/Ruhelosigkeit (mittelgradig)	**8**
Tier isoliert sich/ausgeprägte Hyperkinetik	**10**
Schmerzäußerungen; Apathie; Koordinationsstörungen; Automutilation	**20**
IV Verfahrensspezifische Kriterien	
Normales Verhalten	**0**
Neurologische Symptome: (Koordinationsstörungen, spontan auftretende Epilepsien, motorische Auffälligkeiten);	**5**
Kurzzeitige, seltene (<1 mal am Tag) spontane Anfälle, geringe Koordinationsstörungen	**5**
Häufigere Epilepsien 1-3 mal pro Tag und/oder andere Auffälligkeiten	**10**
Sehr häufige (>3 pro Tag) und lang andauernde Anfälle (> 5min)	**20**
Automutilation, Entfernen der Elektroden	**20**
Bewertung, Maßnahmen	**Punktsumme**
keine Belastung	**0**
geringe Belastung: sorgfältig weiter beobachten (ab 5 Punkten 2x tägl.), evtl. unterstützende Maßnahmen (z.B. Wärmezufuhr, Spezialfutter) und spezielle Behandlungsmethoden	**1-9**
mittlere Belastung: ggf. medizinische Versorgung einleiten (Analgesie, Antibiotikum, Infusionen etc.) länger andauernd als 24 h gilt als schwere Belastung und soll daher vorher beendet werden.	**10-19**
Schwere Belastung: Tiere werden vor Erreichen dieses Endpunktes euthanasiert.	**≥ 20**

B. Form for the assessment of a newborn litter

„Beurteilung neugeborener Wurf“*

*spätestens beim ersten Umsetzen

Haltungsort(1): FORS/Hertie Institut, gelber Bereich (Ebene 01)	Haltungsform(2) : offen
Besitzer: AG Lerche – Dr. Ulrike Hedrich-Klimosch	Herkunft(3): Taconic Biosciences
Linie (internationale Bezeichnung): Angabe erst nach Publikation der Linie notwendig! _B6;129S-*Slc1a3*^{tm1P290RCfa} Linie (interne Bezeichnung): „EAAT 1“	Besonderheiten aktuell(4): _____________ _______________________________________ _______________________________________

Bezeichnung des/r veränderten Gens/e: SLC1A3	Hintergrund d. Linie: 129S

Erwartete Eigenschaften: heterozygote Tiere: epileptische Anfälle ab der dritten Lebenswoche, Peak von P35 – P42, danach Erholung und normale Lebenserwartung

Muttertier Nr.:	Vatertier Nr.:	Wurf geboren am:	Generation:

Anzahl geboren:	Datum der Beurteilung:	Beurteilende/r:

Farbe der Neugeborenen	☐ normal	☐ Abweichungen (bitte angeben, z.B. blass)	
Aktivität der Neugeborenen	☐ normal	☐ Abweichungen (bitte angeben, z.B. auffallende Unruhe)	
Größe, Entwicklung d. Neugeborenen	☐ homogen	☐ inhomogen	Gewicht ☐ normal ☐ reduziert ☐ gesteigert
Milk Spot	☐ vorhanden	☐ nicht vorhanden	
Pflege durch das Muttertier	☐ normal	☐ Abweichungen (bitte angeben, z.B. Vernachlässigung, Kannibalismus)	
Sonstige Auffälligkeiten			

(1) Angabe Institut und Raum	(4) z.B.: Lärm wg. Baustelle, Bestandssanierung, Umzug von Räumen etc.
(2) z.B. IVC, „offener“ Käfig, Filtertop, Isolator etc. gegebenenfalls Hygienestatus angeben	
(3) Name Züchter, externes Labor etc.	

C. Official form for the assessment of animals at the time point of weaning

„Beurteilung Wurf beim Absetzen“

Haltungsort(1): FORS/Hertie Institut, gelber Bereich (Ebene 01)	Haltungsform(2) : offen
Besitzer: AG Lerche – Dr. Ulrike Hedrich-Klimosch	Herkunft(3): Taconic Biosciences
Linie (internationale Bezeichnung): Angabe erst nach Publikation der Linie notwendig! B6;129S-*Slc1a3*^{tm1P290RCfa} ___________________ Linie (interne Bezeichnung): „EAAT 1“	Besonderheiten aktuell(4):____________________ ____ ____

Bezeichnung des/r veränderten Gens/e: SLC1A3	Hintergrund d. Linie: 129S

Erwartete Eigenschaften: heterozygote Tiere: epileptische Anfälle ab der dritten Lebenswoche, Peak von P35 – P42, danach Erholung und normale Lebenserwartung

Muttertier Nr.:	Vatertier Nr.:	Wurf geboren am:	Generation:

Anzahl geboren:	Anzahl abgesetzt:	Differenz geboren/abgesetzt:

Tiernummer								
Absetzdatum								
Geschlecht								
Körpergewicht								
Auffälligkeiten(5 Bitte Buchstaben (siehe Fußnote) angeben!								
Tiernummer								
Absetzdatum								
Geschlecht								
Körpergewicht								
Auffälligkeiten(5 Bitte Buchstaben (siehe Fußnote) angeben!								

Auffälligkeiten vor dem Absetzen	Datum:			
	Auffälligkeiten(5):			

(1) Angabe Institut und Raum	(4) z.B.: Lärm wg. Baustelle, Bestandssanierung, Umzug von Räumen etc.
(2) z.B. IVC, „offener“ Käfig, Filtertop, Isolator etc. gegebenenfalls Hygienestatus angeben	(5) a = keine Auffälligkeiten b = haarlose Stellen c = Kümmerer d = Bisswunden e = Mikrophthalmie f = Elefantenzähne g = Hydrozephalus h = andere (bitte benennen)
(3) Name Züchter, externes Labor etc.	

Datum	Name und Unterschrift der/des Beurteilenden